Upconversion lasers and other applications of Er^{3+}-doped fluoride crystals

Dissertation

zur Erlangung des Doktorgrades
des Department Physik
der Universität Hamburg

vorgelegt von

Francesca Moglia

aus Cremona in Italien

Hamburg
2013

Gutachter der Dissertation:	Prof. Dr. G. Huber Prof. Dr. M. Tonelli
Gutachter der Disputation:	Prof. Dr. G. Huber Prof. Dr. H. Moritz
Datum der Disputation:	25. September 2013
Vorsitzender des Prüfungsausschusses:	Prof. Dr. P. Hauschildt
Vorsitzender des Promotionsausschusses:	Prof. Dr. D. Horns
Dekan der Fakultät für Mathematik, Informatik und Naturwissenschaften:	Prof. Dr. H. Graener

Abstract

F. Moglia: *Upconversion lasers and other applications of* Er^{3+}*-doped fluoride crystals*

Upconversion lasers are unconventional sources of visible laser emission. The nonlinear upconversion process is based on the level scheme of suitable dopants, such as Er^{3+}-ions. Here, a two-photon absorption process takes place. An intermediate level is populated by the absorption of the first photon, then the second photon populates the upper laser level. In the most efficient configuration, an Er^{3+}-doped medium can emit a photon in the visible spectral range for every two consecutively absorbed infrared photons of the same wavelength.

In this work, six different Er^{3+}-doped crystals have been spectroscopically investigated in order to demonstrate their suitability for upconversion lasers. A fundamental requirement for the host material is a low effective phonon energy, which ensures that the lifetimes of the intermediate and the laser emitting levels are long enough to allow for efficient pumping and laser emission. For this reason, the host materials are all fluorides: $LiLuF_4$, LaF_3, BaY_2F_8, $BaLu_2F_8$, KY_3F_{10} and, for the first time investigated with Er^{3+}-doping, $BaYLuF_8$. In this work, the crystal recognized as most efficient for upconversion lasers is Er^{3+}:$LiLuF_4$.

Bulk laser experiments have been carried out. Upconversion laser input-output characteristics have been recorded with a Ti:sapphire laser as pump source, obtaining a maximum output power of 80 mW and a slope efficiency of 20.7%. The results are comparable to those obtained in the same setup but using a direct pumping scheme, by substituting the pump source with a frequency-doubled optically-pumped semiconductor laser emitting at nearly half of the wavelength of the Ti:sapphire laser. In pure cw regime, a maximum output power of 35 mW has been achieved with a slope efficiency of 9.2%. It represents the first demonstration of a cw erbium-based laser directly pumped in the blue spectral range. Moreover, experiments with simultaneous pumping with two different wavelengths have been carried out to realize so-called dual-wavelength upconversion lasers.

Furthermore, Er^{3+}-doped fluoride crystals can be interesting host materials for lasers emitting in the 1.6-µm spectral range, where many applications in telecommunication and medicine are possible and greenhouse gases can be detected via LIDAR techniques. The laser experiments under inband-pumping at 1.5 µm, with different Er^{3+}:doped $LiLuF_4$ and $BaYLuF_8$ crystals yielded a maximum emission output power of 1.4 W and a slope efficiency of 19% with respect to the incident pump power. Laser operation at different emission wavelengths has been demonstrated. In particular, emission at $\lambda = 1610\,\text{nm}$ could be obtained using a 1.25 at.% Er^{3+}-doped $LiLuF_4$ crystal, which is especially interesting for the detection of CO_2. The first laser operation in Er^{3+}:$BaYLuF_8$ and the first inband-pumped laser operation at 1.6 µm in Er^{3+}:$LiLuF_4$ have been realized.

To obtain cw upconversion lasers, a second requirement is a high pump intensity in the crystal, which can be achieved in the thin-disk-laser configuration as well as in waveguide lasers. Thin-disk-laser and waveguide-laser experiments have been performed with 1.3 at.% Er^{3+}-doped $LiLuF_4$ samples. The experiments resulted in the first crystalline green upconversion waveguide laser. Performance has been improved to achieve up to 10 mW of output power with a slope efficiency of 3%. The internal losses are less than 0.5 dB/cm, very promising for future applications.

Kurzfassung

F. Moglia: *Upconversion-Laser und weitere Anwendungen Erbium-dotierter Fluoridkristalle*

Upconversion-Laser sind unkonventionelle Quellen sichtbarer Laseremission. Der nichtlineare Upconversion-Prozess basiert auf dem Niveauschema geeigneter Dotierionen wie Erbium, welches im dreiwertigen Zustand typischerweise ein langlebiges mittleres Energieniveau aufweist. Durch Absorption eines Photons wird zunächst dieses Niveau, und in einem weiteren Absorptionsschritt das obere Laserniveau besetzt. Im günstigsten Fall führt die aufeinanderfolgende Absorption zweier Photonen der gleichen Wellenlänge zur Emission von einem Photon im sichtbaren Spektralbereich.

Im Rahmen dieser Arbeit wurden sechs unterschiedliche Er^{3+}-dotierte Kristalle spektroskopisch untersucht, um ihre Eignung als Upconversion-Lasermaterial zu prüfen. Eine wesentliche Voraussetzung hierfür ist eine niedrige effektive Phononenenergie. Sie bewirkt, dass sowohl das mittlere als auch das obere Laserniveau eine ausreichende Lebensdauer haben, um effizientes Pumpen sowie Laseremission zu gewährleisten. Daher handelt es sich bei den untersuchten Wirtsmaterialien ausschließlich um Fluoridkristalle: $LiLuF_4$, LaF_3, BaY_2F_8, $BaLu_2F_8$, KY_3F_{10}, sowie erstmalig $BaYLuF_8$ mit Er^{3+}-Dotierung. Von diesen Materialien hat sich Er^{3+}:$LiLuF_4$ als das geeignetste erwiesen.

Mit einem Ti:Saphir-Laser als Pumpquelle wurde ein Upconversion-Laser im Volumen-Kristall realisiert. Die Input-Output-Kurven (maximale Ausgangsleistung von 80 mW und differentielle Wirkungsgrad von 20,7%) wurden verglichen mit denen von direkt im blauen Spektralbereich gepumpten cw Erbium-basierten Laser (maximale Ausgangsleistung von 35 mW und differentieller Wirkungsgrad von 9,2% beim reinen Dauerstrichbetrieb), die im Rahmen dieser Arbeit erstmals realisiert werden. Zusätzlich wurden durch gleichzeitiges Pumpen mit zwei verschiedenen Wellenlängen sogenannte Zweiwellenlängen-Upconversion-Laser demonstriert.

Neben der Realisierung sichtbarer Laserstrahlung sind Er^{3+}-dotierte Fluoridkristalle auch für Laser mit Wellenlängen um 1,6 µm für Anwendungen in Telekommunikation, Medizin sowie für die Detektion von Treibhausgasen mittels LIDAR von großem Interesse. In $LiLuF_4$ und $BaYLuF_8$ mit verschiedenen Er^{3+}-Dotierungen wurden Ausgangsleistungen von bis zu 1,4 W und differenzielle Wirkungsgrade von 19% gegenüber der einfallenden Pumpleistung erzielt. Laserbetrieb konnte bei verschiedenen Wellenlängen gezeigt werden. Insbesondere wurde Laseremission eines 1,25% Er^{3+}:$LiLuF_4$ Kristalls bei $\lambda = 1610\,\mathrm{nm}$ demonstriert, einer Wellenlänge die besonders geeignet für die Detektion von CO_2 ist. Im Rahmen dieser Arbeit wurde erstmalig Laserbetrieb eines Er^{3+}:$BaYLuF_8$ sowie inband-gepumpter Laserbetrieb bei 1,6 µm in Er^{3+}:$LiLuF_4$ gezeigt.

Neben Laserexperimenten im Volumkristall wurden Upconversion-Scheibenlaser und Wellenleiternlaser-Experimente durchgeführt, um eine hohe Pumpintensität im Kristall zu ermöglichen. Beide Varianten wurden mit 1,3% Er^{3+}:$LiLuF_4$-Kristallen erprobt. Dabei konnte der erste kristalline grün emittierende Upconversion-Wellenleiterlaser mit bis zu 10 mW Ausgangsleistung und einem differenziellen Wirkungsgrad von 3% realisiert werden. Die internen Wellenleiterverluste sind mit weniger als 0,5 dB/cm sehr vielversprechend für zukünftige Auswendungen.

Contents

List of Figures

List of Tables

1 Introduction and Remarks

1.1 Introduction

The demand for lasers operating in the visible spectral range is increasing strongly due to a multitude of possible applications such as display technology, which is one of those with the broadest market. Visible lasers are also an important tool in medicine, for both diagnosis and treatment. Moreover, they are the basis of a variety of investigation techniques and visible laser emission is particularly important for fundamental research, in quantum optics, biophotonics and spectroscopy [Dou98, Hän99, Kna04, Lap11].

Upconversion lasers can fulfill the demand of visible lasers while offering a further advantage: they can be pumped by infrared laser sources which are typically more available and versatile than pump sources in the short wavelength range. Moreover, infrared lasers can deliver a higher output power and the more advanced development allows for lower production costs.

A second advantage of upconversion lasers is that they offer the possibility to achieve short-wavelength emission without the use of additional non-linear frequency conversion systems. This is possible because they rely on the non-linearity of the upconversion process itself. It allows very efficiently for an intermediate excited state to be excited further into an even higher state either via Excited State Absorption (ESA) or interionic processes. The level emitting in the visible spectral range is populated most efficiently when the energy level scheme allows for two subsequent excitations by photons of the same wavelength. In the framework of this thesis, this process is defined as "single-wavelength upconversion".

Upconversion pumping and consequent laser operation is mediated by materials (in this cases fluorides) doped with different rare-earth ions, mostly Pr^{3+} [Sch04], Tm^{3+} [Heb92], Nd^{3+} [McF88] and Ho^{3+} [All90]. This work focuses on materials doped with the Er^{3+}-ion which was the first ion to be studied in upconversion lasers [Joh71].

The most interesting emission wavelength of upconversion lasers based on Er^{3+}-ions is in the green spectral range, at around 550 nm. The most efficient pumping scheme to obtain it is the consecutive absorption of two photons at a wavelength in the range of 970 nm [Heu06].

A major part of this work is devoted to the spectroscopic investigation of new materials which can allow for upconversion lasers at room temperature. First an introduction to the theory of lasers and intraionic and interionic processes, such as ESA and Energy Transfer Upconversion (ETU), is given in Chap. 2, followed by the description of the applied crystal growth techniques in Chap. 3.

Materials for upconversion lasers have to fulfill a fundamental requirement, which is a low effective phonon energy. This avoids a detrimental fast non-radiative decay of the two fundamental energy levels for the process: the intermediate level, which is first excited and allows for ESA, and the laser emitting level. A class of materials which can satisfy this demand is the fluorides. Six different fluoride hosts are introduced in Chap. 4 and a detailed spectroscopic analysis of the respective Er^{3+}-doped systems is reported in Chap. 5. The investigation focuses on the feasibility of the different hosts for single-wavelength upconversion lasers which is determined by the ESA cross sections. Furthermore, a study of the dynamics of the most important energy levels for the process, as well as the calculation of absorption, emission and gain cross sections are included.

In order to reach the lasing threshold of an upconversion laser, an exceptionally high fluence on the sample is needed. Considering that this thesis focuses on continuous wave (cw) experiments, a needed high fluence can be translated into a needed high intensity. To achieve this, two alternative approaches are presented in Chap. 6: the thin-disk laser geometry and laser operation in waveguides inscribed into the laser medium, in both cases Er^{3+}:$LiLuF_4$.

Upconversion lasers can also be realized when two pump sources operating at different wavelengths are available, that allow for the population of the laser emitting level. The so-called dual-wavelength upconversion laser will be briefly introduced in Chap. 6, together with the description of experiments using a Ti:sapphire laser and Distributed Bragg Reflector tapered diode lasers (DBR-TDLs) as pump sources.

Additionally, Er^{3+}-doped fluoride crystals offer further possibilities as laser media thanks to novel pump sources currently available. In Chap. 6, an Er^{3+}:$LiLuF_4$-based laser emitting in the green spectral range is presented, which is directly pumped by recently developed frequency-doubled optically pumped semiconductor lasers (2ω-OPSLs) emitting in the blue spectral range. This represents the first cw erbium-based laser directly pumped in the blue spectral range.

Another innovative pump source is the erbium-based fiber laser emitting in the 1.5-µm spectral range. With this device, different Er^{3+}-doped fluoride materials have been inband-pumped in order to obtain laser emission at a wavelength of 1.6 µm. Lasers emitting in this spectral range are useful for the detection of the greenhouse gases CO_2 and CH_4 via LIDAR techniques and also in telecommunications and medicine.

In Chap. 7, a summary of the results and a report of the encountered problems are given, along with suggestions for possible improvements and further investigations.

1.2 Remarks - Erratum

Due to the wrong specification of the doping concentration of a sample of Er^{3+}:$LiLuF_4$ (AC2 in Tab. A.2 contains 1.25 at.% instead of 0.5 at.% of Er^{3+}-ions), relative absorption and emission cross sections reported in the preliminary version of this work suffer from a miscalculation. This influences various results concerning Er^{3+}:$LiLuF_4$.

For this reason, corrections in comparison to the preliminary version have been reported here in the official version as follows:

Figures: 5.2a and 5.45a (in these two cases the highest peak show a higher resolution than before); 5.6a and 5.46a (in this last case the error factor is reduced because of the wrong upload of the figure in the original version); 5.17a and 5.47a; 5.17b and 5.47b; 5.18 and 5.48; 5.35 and 5.50; 5.38a and 5.52a; 5.38b and 5.52b; 5.41a and 5.53a; 5.41c and 5.53c; 5.41e and 5.53e; 6.2; 6.5; 6.6; 6.19; 6.22b; 6.23c.

Tables: 5.4; 6.2; A.2; D.1; F.1.

In the new text: Pp. I-III; pp. 71-72; p. 76; pp. 90-92; pp. 116-120; p. 127; pp. 134-137; pp. 139-141; pp. 146-147; p. 153; pp. 155-156; p. 174; pp. 179-180; pp. 182-183; p. 185; p. 187; p. 193; p. 204; p. 207. In comparison to the preliminary version, all the pages are between zero and four pages forward.

Furthermore, an exchange of the two polarizations was present in the preliminary version of Fig. 5.17c. The mistake has been corrected and consequently all the **y**-axes of Fig. 5.17 have been homogeneously rescaled.

2 Fundamentals

In this chapter, an introduction to the physical principles which describe the effects of rare-earth-ions in crystals will be given, and a thorough analysis of the concept of upconversion, especially in erbium-doped fluorides, will be carried out. Principles of laser operation will be also introduced.

More exhaustive explanations concerning the theoretical aspects here reported and references can be found in books such as [Wyb65, Tay72, Di 74, Hüf78, Gos00].

2.1 Rare earth ions in crystals

Lanthanides belong to the rare-earth ions group, which means the elements lanthanum (atomic number 57) through lutetium (atomic number 71). Due to similar external electronic configuration, scandium (atomic number 21) and yttrium (atomic number 39) are also members of this category. Nevertheless, these two ions are not optically active in crystals but the similarity with the lanthanides renders them optimal to be substituted via the doping process.

The electronic configuration of the lanthanides corresponds to the one of xenon with an extra occupied 6s shell, plus possibly one electron belonging to the 5d shell and a variable number of electrons in the 4f shell. More precisely, the configuration reads $[\mathrm{Xe}](4\mathrm{f})^n(5\mathrm{d})^x(6\mathrm{s})^2$ with:

1) $x = 1$ and $n = 0$ for lanthanum;

2) $x = 1$ and $n = 7$ for gadolinium;

3) $x = 1$ and $n = 14$ for lutetium;

4) $x = 0$ and $n = 2, \ldots 13$ for cerium through ytterbium.

In compounds, the exhibited oxidization state of the lanthanides is usually +3. In the case of group 4), the electrons given to the surrounding ligands are the two occupying the 6s shell plus one belonging to the 4f shell. Lanthanum, gadolinium and lutetium tend to lose as well the two 6s-electrons but rather than one of the f-electrons, the one belonging to the 5d shell. This configuration is favored by the stability advantages gained by having an empty, half-full or full f shell. Partially for the same reason, it is probable to find also an oxidization either +2 or +4 in ions such as europium, ytterbium and cerium.

In all these configurations, the 5s and 5p orbitals stay fully occupied and possess a higher radial extension then the 4f shell, consisting in a shield from the external environment. For this reason, the crystal-field impact on 4f → 4f-transitions is strongly attenuated and can be evaluated as a small perturbation, leading to a minimal variation of the position of the discrete energy levels of the lanthanides in different host materials. When 5d-electrons are involved in the transitions, typically the shield is not active and the crystal field can strongly influence them. Consequently, a broadening of the emission or absorption peaks into bands can be registered.

In the framework of this thesis, only the spectra connected to the presence of relatively small amounts of Er^{3+}-ions have been considered, as substitutes exclusively for Y^{3+}-, Lu^{3+}- and La^{3+}-ions in six different fluoride-based crystal hosts.

2.1.1 Free-ion model and interaction with the crystal field

When the shield offered by the full s and p shells on the 4f electrons is considered and at the same time the polarization effect induced by the incomplete 4f orbital on the internal shells can be evaluated as a small perturbation, the free-ion model can be applied.

In order to describe the system, the time-independent Schrödinger equation can be separated in an angular and a radial parts. The complete solution can give information about the energy levels of the 4f-electrons, their order and the selection rules which define whether a transition is allowed or not.

In the free-ion approximation, the Hamilton operator which can be applied in order to describe the system of an atom with N electrons corresponds to:

$$\begin{aligned} H &= T + V_{\mathrm{en}} + V_{\mathrm{ee}} + V_{\mathrm{so}} = \\ &= -\frac{\hbar^2}{2m}\sum_{i=1}^{N}\nabla_i^2 - \sum_{i=1}^{N}\frac{Ze^2}{2r_i} + \sum_{i<j}^{N}\frac{e^2}{4\pi\epsilon_0 r_{ij}} + \sum_{i=1}^{N}\zeta(r_i)\mathbf{s}_i\cdot\mathbf{l}_i, \end{aligned} \tag{2.1}$$

where e, m and N are the charge, the mass and the number of electrons in the 4f shell, respectively; r_i is the radial coordinate of the i-th electron, $r_{ij} = |\mathbf{r}_i - \mathbf{r}_j|$ the relative position of the i-th electron with respect to the j-th one; $\mathbf{s}_i$ and $\mathbf{l}_i$ are the spin and the angular momentum of the i-th electron; $\zeta(r_i)$ is the function of spin-orbit coupling; Ze is the nuclear charge.

In a preliminary analysis, only the first two terms in Eq. (2.1) can be considered and $H = H_0 = T + V_{\mathrm{en}}$. The electrons of the 4f orbitals are influenced only by their own kinetic energy and by their electrostatic interaction with the nucleus. Following the so called *central-field approximation*, an effective nuclear charge Z^*e is responsible for this interaction and it represents the effect of the shielded nucleus and $(N-1)$ electrons embedded in the internal full symmetric shells. This approximation originates by the Hartree-Fock method and determines a completely spherically symmetric potential. In this kind of approximation, hydrogenoid states such as: $\psi(r_i, \theta_i, \phi_i) = R_{nl}(r_i)Y_l^{m_l}(\theta_i, \phi_i)$ are eigenstates of H_0, where $Y_l^{m_l}(\theta_i, \phi_i)$ are spherical harmonics, $R_{nl}(r_i)$ radial functions and n, l and m_l quantum numbers.

Nevertheless, the Pauli exclusion principle has still to be imposed. To overcome this difficulty, the Hartree-Fock method suggests as solution Ψ_0 of H_0 a product of single electron wavefunctions $\psi_i = \psi(n_i, l_i, m_l, m_s)$, where n_i is the principle quantum number, l_i the angular momentum, m_l the magnetic quantum number and m_s the spin quantum number, but the energy eigenvalues depend only on n_i and l_i because they are degenerate with respect to m_l and m_s.

When the central-field approximation is abandoned, the non-radially-symmetric effects can start to be considered as perturbations, namely the Coulomb repulsion between electron pairs V_{ee} and the spin-orbit coupling V_{so} in Eq. (2.1). The function of spin-orbit coupling $\zeta(r_i) = \frac{\hbar^2}{2m^2c^2r_i}\frac{dU(r_i)}{dr_i}$ represents the interaction between the angular momentum and the spin in a Coulomb field, where $U(r_i)$ is the potential experienced by electron i.

To calculate the eigenstates and eigenvalues of the hamiltonian H, it is necessary to establish the impact and the relative influence of V_{ee} and V_{so}.

$V_{\mathrm{ee}} >> V_{\mathrm{so}}$ is valid for light atoms and it means that the angular momenta and the spin momenta can combine among each other, in the same category: $\mathbf{L} = \sum_i \mathbf{l}_i$, $\mathbf{S} = \sum_i \mathbf{s}_i$ and $\mathbf{L}$ and $\mathbf{S}$ can couple to the total angular momentum $\mathbf{J} = \mathbf{L} + \mathbf{S}$. The interaction between $\mathbf{L}$ and $\mathbf{S}$ is called *L-S coupling* or *Russell-Saunders coupling.*

$V_{\mathrm{ee}} << V_{\mathrm{so}}$ applies to atoms with a high atomic number, where the momenta of the single electrons couple to form an individual total angular momentum $\mathbf{j}_i = \mathbf{l}_i + \mathbf{s}_i$; consequently, the total angular momentum reads: $\mathbf{J} = \sum_i \mathbf{j}_i$ and causes the so-called *j-j coupling.*

$V_{\mathrm{ee}} \sim V_{\mathrm{so}}$ is the situation which is valid for rare-earth ions with an intermediate atomic number. The two potentials are comparable and the eigenstates are linear combinations of L-S states with the same total angular momentum $\mathbf{J}$. In this way, a multiplet is $(2J+1)$ times degenerate and it is described by the notation ${}^{2S+1}L_J$. The important quantum numbers are n, L, S, m_s and m_j, where m_j is the component of $\mathbf{J}$ along the quantization axis. This case describes the so-called *intermediate coupling* and, on the contrary of the previous two situations, it cannot be solved via perturbative approximations.

In order to give an exhaustive description of the effects of rare-earth ions in a crystal, it is finally necessary to consider the influence of the crystal field, which means the consequences of the presence of other ions located at the crystalline lattice sites. The field can be interpreted as electrostatic and not homogeneous. It is produced by the charge distribution which mostly affects the open 4f shell, compared to the complete ones. This last perturbative contribution to be added to H is called H_{Stark} and reads:

$$H_{final} = H + H_{\mathrm{Stark}} = H + \sum_i \sum_l \frac{Z_l e^2}{|\mathbf{R}_l - \mathbf{r}_i|}, \tag{2.2}$$

where Z_l and $\mathbf{R}_l$ are the atomic number and the position of every ligand (lattice matrix), respectively. In this way the $(2J+1)$-degeneration of the quantic number m_j is removed and the so-called *Stark splitting* of the levels originating by the free ion model divides them in further sublevels.

When an ion is inserted in a lattice site, its symmetry is not spherical anymore, but it turns into the point symmetry dictated by the crystalline site. The number of sublevels can be directly calculated via the group theory [Tin64].

Finally, Kramers theorem establishes that if the ions have an odd number of electrons in the 4f shell (semi-integer J) a double degeneracy is maintained and the multiplet splits into $(2J+1)/2$ sublevels. If the electrons in the 4f shell are even (integer J), the splitting is $(2J+1)$ and it can lead also to the formation of a singlet. As a consequence of the

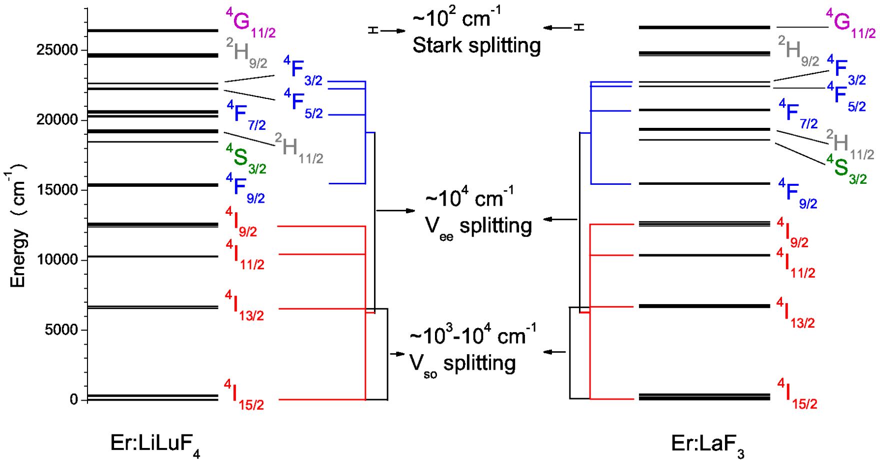

Figure 2.1: Trivalent erbium ions in $\mathrm{LiLuF_4}$ (left) and $\mathrm{LaF_3}$ (right) [Kam86, Kru64, Car72, Car86] as an example to show the similarity between Coulomb and spin-orbit interaction (10^3 - $10^4\,\mathrm{cm}^{-1}$) and the less pronounced effect of the Stark splitting ($\sim 10^2\,\mathrm{cm}^{-1}$). Different hosts cause differences, but not in the order of magnitude of the splitting.

Stark splitting, every sublevel can be identified as $^{2S+1}L_{J,\mu}$, with μ index of every Stark sublevel.

In Fig. 2.1 the erbium energy levels in two different hosts are depicted. The correspondence between the orders of magnitude of V_{ee} and V_{so} (10^3 - $10^4\,\mathrm{cm}^{-1}$) is obvious and it causes an overlap between levels. The effect of the Stark splitting is evidently smaller ($\sim 10^2\,\mathrm{cm}^{-1}$). Furthermore, the limited but still evident difference in the splitting of the levels given by different hosts is shown.

2.2 Rare earth ions and energy transfers

Rare-earth ions are interesting because of their interaction with light. After describing how the 4f energy levels of a rare-earth ion are split when embedded in a crystal host, it is possible to clarify how their population dynamically evolves. The considered processes are based on absorption and emission of light and consequent exchanges of energy among the levels. When they affect only the levels belonging to one ion, they are called *single-ion* or *intraionic* processes. When two or more ions give a contribution to the process, they are called *multiple-ion* or *interionic* processes. In this last case, when a process of transfer of energy takes place between two ions, the ion which is excited at the beginning is called *donor* and the one which receives the excitation is called *acceptor*.

Furthermore, when a transition takes place and has fluorescence as consequence, it is called *radiative* and the luminescence can be registered and studied in order to obtain information about the process. When a transition has no fluorescence as effect, it is *nonradiative* and it is governed mostly by either phonons or impurities inside the crystal.

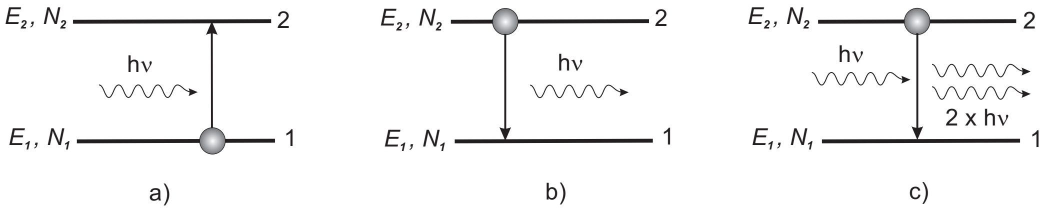

Figure 2.2: Possible intraionic processes for rare-earth-ions in a simplified two-level system. a) Absorption (GSA/ESA). b) Spontaneous emission. c) Stimulated emission.

2.2.1 Intraionic processes

In this section an overview about the most common intraionic processes is reported. To simplify the explanation, it will be considered that at room temperature the thermalization of the sublevels is fast enough to define a multiplet as a single level [Yen64]. A representation of the processes is depicted in Fig. 2.2.

Ground State Absorption (GSA) and Excited State Absorption (ESA)

In a simple picture where only two energy levels of an ion are considered, one at energy E_1 below a second at energy E_2, initially level 1 is occupied. Nevertheless, photons with energy equivalent to $\Delta E = E_2 - E_1 = h\nu$ can be absorbed and consequently level 2 becomes occupied. When level 1 corresponds to the ground state of the ion, the process is called Ground State Absorption (GSA); when level 1 is an energetically higher level, different from the ground state level, the process is called Excited State Absorption ESA (see Fig. 2.2 a)).

With N_i being the population of the i-th energy level and F an incident flux of photons, the change in time t of the population N_1 of level 1 is described by:

$$\left(\frac{dN_1}{dt}\right)_{\text{abs}} = -\sigma_{12} F N_1, \tag{2.3}$$

where the flux F is defined by the intensity $I = Fh\nu$ of the photons and σ_{12} is the absorption cross section from level 1 to level 2.

Stimulated emission and amplification

If level 2 is populated, photons of energy ΔE can also stimulate the excited ion to consequently emit identical photons in direction, frequency, phase, and polarization (see Fig. 2.2 c)). Thus, this stimulated emission process induces a population change of N_2 according to:

$$\left(\frac{dN_2}{dt}\right)_{\text{SE}} = -\sigma_{21} F N_2, \tag{2.4}$$

where σ_{21} is the emission cross section.

When the degeneracy is identical, $\sigma_{12} = \sigma_{21} = \sigma$ [Ein16]. Therefore, if the population change is evaluated for both energy levels such as in a two-level system, the photon flux change through a crystal of thickness dz can be calculated with:

$$\frac{dF}{dz} = \sigma_{21} F N_2 - \sigma_{12} F N_1 = \sigma F (N_2 - N_1). \tag{2.5}$$

In order to obtain amplification, the photon flux change in time must be positive, which means $N_2 > N_1$, the condition of inversion. In absence of (at least) a third energy level, the extreme reachable condition is $N_2 = N_1$, which means that to obtain laser inversion a two-level system is insufficient.

Spontaneous emission

When without any external influence the energy accumulated in a high energy level (e. g. level 2 in fig. 2.2 b)) is transferred to a lower energy level (e. g. level 1) and photons are emitted, the process is called spontaneous emission and the population of the upper level changes according to:

$$\left(\frac{dN_2}{dt}\right)_{\mathrm{sp}} = -AN_2 = -\frac{N_2}{\tau_{\mathrm{sp}}}, \tag{2.6}$$

with the spontaneous emission lifetime τ_{sp} of the level N_2 defining the Einstein coefficient A.

Beyond the two-level system, when only radiative decay is considered in a multilevel system, the population of level i has the possibility to decay in all the lower k levels and $\tau_{\mathrm{sp},i}$, lifetime of level i, is defined by:

$$\frac{1}{\tau_{\mathrm{sp},i}} = A = \sum_{j=1}^{k} A_{ij} = \sum_{j=1}^{k} \frac{1}{\tau_{ij}}, \tag{2.7}$$

where A_{ij} is the Einstein coefficient for a pair of energy levels i (higher) and j (lower).

In order to estimate the relevance of the decay channel $i \to l$ over the other possible $(k-1)$, the branching ratio β_{il} is defined as follows:

$$\beta_{il} = \frac{A_{il}}{\sum_{j=1}^{k} A_{ij}} = \frac{A_{il}}{A}. \tag{2.8}$$

Selection rules

When optical radiation is emitted by rare-earth-doped crystals, the four identified dominant sources [Vle37] are:

a) forced dielectric dipole transitions induced by odd terms of the crystal field, when not centrosymmetric;

b) forced dielectric dipole transitions induced by odd terms of lattice vibrations;

c) allowed magnetic dipole transitions;

d) allowed electric quadrupole transitions.

This result is a consequence of the selection rules predicted by *Laporte* [Lap25] and the influence of the crystal field.

The Laporte rules specified for f shells read:

1) $\Delta l = \pm 1$;
2) $\Delta S = 0$;
3) $|\Delta L| \leq 2l = 6$;
4) $|\Delta J| \leq 2l = 6$;
5) $J = 0 \nRightarrow J' = 0$.

Transitions in the UV - IR region due to rare-earth doping in crystals are typically of 4f → 4f - kind and parity rules would prevent them from having a dielectric-dipole origin. Nevertheless, with allowed magnetic-dipole transitions being six orders of magnitude less probable than allowed electric-dipole ones, the forced electric-dipole transitions are still the most prominent ones.

Nonradiative transitions

A high relevance is given to *phonon-assisted* nonradiative transitions, because of their potential to quench radiative transitions when the aim is to obtain laser emission in a rare-earth doped crystal. Further effects due to phonons which can be experimentally detected are: disappearance of fluorescence originating in high Stark levels, a shortening of the radiation lifetime with decreasing energy gap between two levels, and a general temperature dependency of the radiative lifetime of an energy level.

This happens because when two levels are considered and the ion is excited in the upper level, it is possible that instead of decaying into the lower level radiatively, a certain number of phonons are emitted. The energy for different phonon modes is crystal-dependent. Vibronic spectra can define these modes [Yen64, Coh68], they can be measured and Raman spectroscopy is the most common technique. The result of the investigation is either the highest-energy mode, which can be identified at the so-called *cut-off phonon energy*, or the effective phonon energy, which can be a convolution of the phonon spectrum.

If the energy gap can be bridged by only four phonons having the cut-off phonon energy, it has been experimentally proven [Ris67, Ken02] that $\tau_{\mathrm{R}} \approx \tau_{\mathrm{NR}}$ (radiative and non-radiative lifetime) and the fluorescence is strongly quenched. When instead of 25% of the energy gap the phonon cut-off energy is between 10 and 25% (4 to 10 involved phonons), the radiative decay is detectable. For wider energy gaps, the multiphonon relaxation is negligible.

One of the first attempts to give a simplified version of phonon theory has been reported by *Huang and Rhys* in 1950 [Hua50], but the interpretation which follows is mostly the fruit of the work of *Rieseberg and Moos* [Ris68, Moo70].

If it is assumed that for 4f electrons in rare-earth ions the phonon-electron coupling is weak, the constant α which defines the strength of the electron-phonon coupling can be considered small. Phonons behave like bosons, following the Bose-Einstein statistics, so the temperature- and energy-gap-dependent nonradiative transition rate $W_{\mathrm{NR}}(\Delta E, T)$ can be calculated and reads:

$$W_{\mathrm{NR}}(\Delta E, T) = W_0\, e^{-\alpha\, \Delta E} \left(1 - e^{-\frac{\hbar\omega_{\text{cut-off}}}{KT}}\right)^{-p}. \tag{2.9}$$

In this equation, W_0 and α are dependent on the host material and p represents the number of phonons which can bridge the energy gap $\Delta E = p\, \hbar\omega_{\text{cut-off}}$. In this approximation, it is considered that only one phonon mode is active, corresponding to the cut-off energy, rather than to the effective energy. When the cut-off energy phonons are extremely weak, it is possible to replace them with the second highest-energy phonons, without compromising the approximation [Web67a, Web73, Shi83].

For all the transitions which present both fluorescence and multiphonon relaxation, the effective lifetime of the upper level τ_{eff} is a result of the combination of the radiative and non-radiative contributions as follows:

$$\frac{1}{\tau_{\mathrm{eff}}} = \frac{1}{\tau_{\mathrm{R}}} + \frac{1}{\tau_{\mathrm{NR}}}, \tag{2.10}$$

where τ_{R} is the simplified version for a two-level-system of $\tau_{\mathrm{sp},i}$ defined in Eq. (2.7) and $\tau_{\mathrm{NR}} = \frac{1}{W_{\mathrm{NR}}}$.

The effective lifetime can be calculated from the decay curve of the fluorescence intensity $I(t)$ as follows:

$$I(t) = I_0\, e^{-\frac{t}{\tau_{\mathrm{eff}}}}. \tag{2.11}$$

2.2.2 Interionic processes

When in a crystal the concentration of rare-earth ions is sufficiently high, the average distance among them decreases and the probability of interaction increases. Although the average Er^{3+}-doping concentration adopted in the framework of this thesis is relatively low (less than 1.5 at.%), interionic processes have been identified.

Energy transfers of this kind involve at least two states of different ions. They can be either resonant, which means the interaction is only among the ions, without need of coupling to the lattice, or non-resonant, which implies the contribution of phonons, expanding the variety of possible processes.

The effects of these cooperative processes can be either radiative or non-radiative, and have mostly the consequence of suppressing laser emission, but also of favoring new pumping mechanisms.

A model for the study of the transfer rate for resonant interionic processes has been developed by *Förster and Dexter* [För48, För49, Dex53].

Förster focused on the multipolar interaction between rare-earth ions, in a similar approach to the one valid for intraionic processes in Sect. 2.2.1, considering an overlap between the fields induced by the donor (D) and the acceptor (A). The transfer rate between them $W_{\mathrm{A,D}}$ can be calculated via an Hamilton operator:

$$H_{\mathrm{int}} = \sum_{i,j} \frac{e^2}{|r_{\mathrm{D},i} - r_{\mathrm{A},j}|}, \tag{2.12}$$

which expresses the electrostatic interaction between the electronic clouds of an electron i of the donor and an electron j of the acceptor, at a distance $R_{\mathrm{A,D}} = |r_{\mathrm{D},i} - r_{\mathrm{A},j}|$.

To determine $W_{\mathrm{A,D}}$, a multipole expansion in Cartesian coordinates is calculated and the proportionality to the distance R between the electrons results as follows:

- $H_{\mathrm{int}} \sim 1/R^3 \Rightarrow W_{\mathrm{A,D}} \sim 1/R^6$, for electric dipole-dipole interaction;
- $H_{\mathrm{int}} \sim 1/R^4 \Rightarrow W_{\mathrm{A,D}} \sim 1/R^8$, for electric dipole-quadrupole interaction;
- $H_{\mathrm{int}} \sim 1/R^5 \Rightarrow W_{\mathrm{A,D}} \sim 1/R^{10}$, for electric quadrupole-quadrupole interaction.

This sequence excludes *a priori* the contribution of magnetic dipole interaction, considered orders of magnitude smaller than the electric ones.

Additionally, *Dexter* analyzed the problem of the interionic processes evaluating the contribution of the exchange interaction. This kind of coupling is based on the direct overlap of the electron wavefunctions and it is limited to distances of a few angstroms, therefore unlikely in the erbium-doped crystal studied in the framework of this thesis. Nevertheless, when active, its strength is comparable to the one of the electric dipole-dipole interaction.

The aim of both the studies has been to give a possible explanation to the missing pure exponential behavior of fluorescence intensity decay when interionic processes take place. The transfer rate W_{DA} is evaluated for these cases and, in analogy to Eq. (2.11), $I(t)$ evolves as:

$$I(t) = I_0\, e^{-\left(\frac{t}{\tau_{\mathrm{eff}}} + W_{\mathrm{DA}}\, t\right)}. \tag{2.13}$$

In the following subsections, the most relevant resonant interionic processes for this work will be introduced and briefly described. A representation of all the interactions is depicted in Fig. 2.3.

Energy migration

When an excitation is resonantly and completely transferred from a donor to an acceptor of the same type starting in its ground state, the process is called energy migration (see Fig. 2.3 a)). This is not necessarily a loss, but the probability that the energy is trapped by an impurity and turns into a non-radiative process increases if this energy is able to travel for long distances inside the crystal.

Cross-relaxation

In a cross-relaxation process (CR), the excitation of the donor is only partially yielded to an acceptor. At the end of the interaction, both the ions are in an excited state (see Fig. 2.3 b)). This process can determine losses when the initial state of the donor corresponds to the emitting level of a laser. Nevertheless, in some laser systems, cross-relaxation functions as efficient population mechanism (e.g. 2-µm thulium lasers [Fan88, Han88, Koo11]). The term “cross-relaxation” is traditionally employed when donors and acceptors are ions of the same kind, but the definition can be extended to different ions.

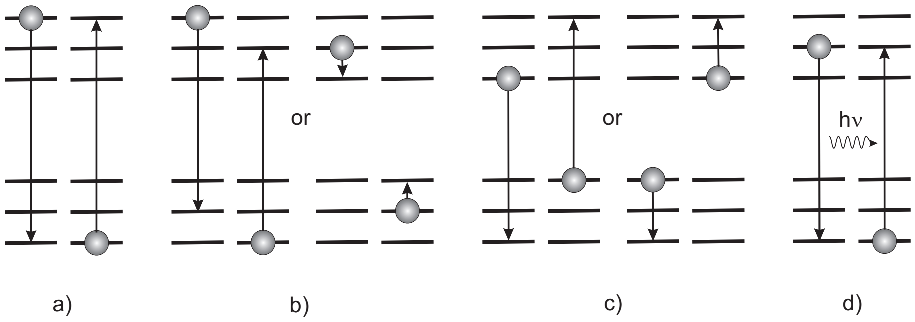

Figure 2.3: Relevant interionic processes for Er^{3+}-ions. a) Energy migration. b) Cross-relaxation. c) ETU. d) Reabsorption.

Energy Transfer Upconversion - ETU

This process resembles a cross-relaxation, but it necessarily begins with both ions in an excited state. When part of the excitation is lost by the donor, the final state of the acceptor is energetically higher than the initial one of the donor (see Fig. 2.3 c)). Upconversion can be a detrimental effect for laser emission when it is a source of losses of photons from either the pumping or the emitting level. Nevertheless, it can be favored in order to depopulate the final laser level and increase the efficiency (e.g. 3-µm erbium lasers pumped at 970 nm [Pol90a, Jen96, Li12]) or directly used as pump mechanism to obtain shorter laser wavelengths than the pump wavelength, without non-linear frequency conversion systems, when not only the ESA-pumping in single-ion scheme is active (e. g. praseodymium- and erbium-doped fluorides for visible emission [Whi91, San97, Sch04], for further details see Sect. 2.4).

Reabsorption

When an excitation from a donor decays radiatively, the emitted photon can be directly absorbed by the acceptor, typically of the same type (see Fig. 2.3 d)). This is a process which mostly has detrimental effects. In the case of laser emission at the wavelength of the reabsorbed photon, the incident power which determines the laser threshold can be increased (especially in three- and quasi-three-level lasers, as described in Sect. 6). In spectroscopic measurements, reabsorption can cause errors in the estimation of the radiative lifetime of a manifold and of the emission cross sections [Küh07].

2.3 The laser

LASER is an acronym for *Light Amplification by Stimulated Emission of Radiation.* The name clarifies the need of the amplification of the radiation at the wavelength of the desired laser.

As stated in Sect. 2.2.1:

1) amplification depends on the realization of population inversion;

2) more than two levels are needed to obtain inversion.

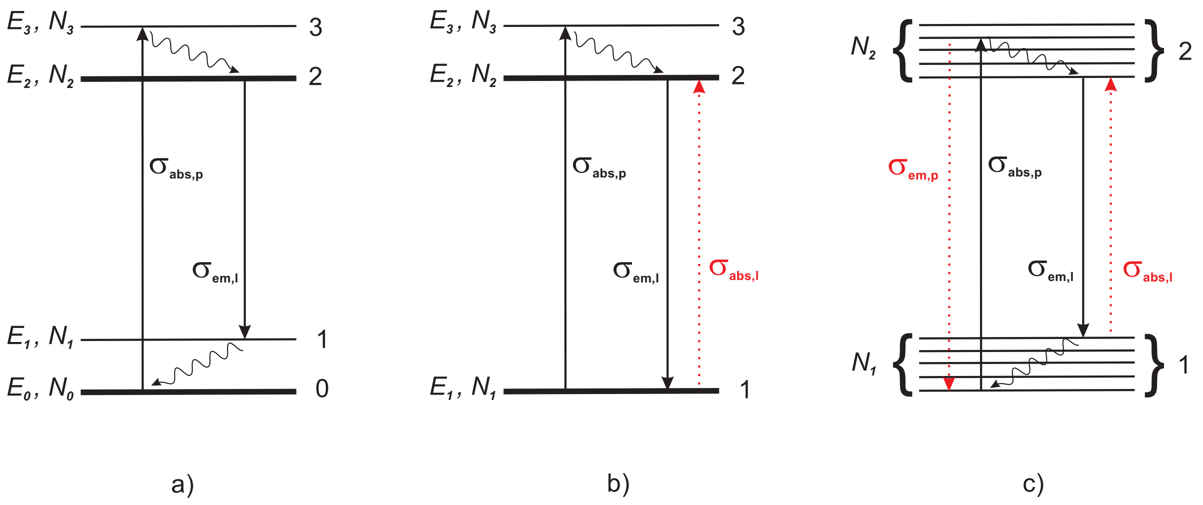

Figure 2.4: The three possible laser schemes. Thick lines denote the levels which are considered populated in the calculation of the rate equations. Sinusoidal arrows highlight fast nonradiative decays. Red and shaded transitions show the possible detrimental reabsorptions or emissions which increase the threshold pump power for the lasing process. a) Four-level scheme. b) Three-level scheme. c) Quasi-three-level scheme.

Technically, the basic elements needed to build a laser are:

- an *active medium*, which allows the laser transitions, defining the emission wavelength;
- a *pumping mechanism*, which includes a pumping source able to excite the ions or molecules of the active medium;
- an *optical feedback system*, which is typically a resonator with partially reflective mirrors, able through the feedback to stimulate the emission of photons.

When they are all present, the light field is amplified in the resonator and the portion which can escape, due to the partial reflectivity of the mirrors, constitutes the laser beam.

In this work, the only involved active materials are Er^{3+}-doped insulating materials (fluoride crystals).

Consequently, the three possible energy level schemes will be explained, all of them being involved in the framework of this thesis. A representation of the three systems is depicted in Fig. 2.4.

2.3.1 Laser schemes

The four-level laser is the scheme where population inversion is obtained the easiest. As definition, the four levels must be at an energy distance much higher than $E_T = kT$ and can be considered as single energy levels, although in reality each of them may be a thermally populated multiplet (see Fig. 2.4 a)).

With these assumptions, all the ions are in the ground state 0 in Fig. 2.4 a), defining a population density N_0. When an excitation source is available, photons can excite the ions from level 0 to level 3, defining a density population $N_3 \neq 0$. As a condition on the scheme, from this energy level a fast non radiative decay must take place, in order to populate energy level 2, with a population density corresponding to N_2. In inversion and laser emission level 2 and 1 are involved, where the former is depopulated via emission of photons on the advantage of the latter, determining a population density N_1. For a successful laser action, a second condition is applied: level 1 is rapidly nonradiatively depopulated in favor of level 0. Due to the efficiency in the depopulation of levels 1 and 3, it can be considered that the total density of dopant active ions N_{dop} corresponds to:

$$N_{\mathrm{dop}} = N_0 + N_2. \tag{2.14}$$

If under these conditions the inversion requisite 1) is readapted to the nomenclature of the four levels, the inversion N reads:

$$N = N_2 - N_1 = N_2. \tag{2.15}$$

Under these conditions, the reabsorption of e laser photon is avoided and the scheme results as being the most convenient of the three.

When the scheme changes to a three-level laser, level 0 and level 1 coincide because they are thermally coupled ($\Delta E \sim kT$) and typically a Boltzmann distribution governs the population dynamics (picosecond-regime population organization) (see Fig. 2.4 b)). Nevertheless, the fast nonradiative relaxation between levels 3 and 2 is still valid and the population density N_3 is negligible. In this case, detrimental reabsorption of laser photons from level 1 to 2 is possible.

If the easiest quasi-three-levels scheme is considered, also the level 2 and 3 coincide because they are thermally coupled. In this picture, only two multiplets are involved and the laser levels are four of the present Stark sublevels, a pair per multiplet (see Fig. 2.4 c)). Typically, the laser transition takes place between the lowest Stark sublevel of multiplet 2 and one of the highest Stark sublevel of multiplet 1. In this way, it strongly resembles a four-level scheme.

Rate equations for the quasi-three-levels scheme

In order to describe the time evolution of the population density of the energy levels, the rate equations which govern the quasi-three-levels scheme will be evaluated. Successively, a brief analysis of the differences to the other two systems will be carried out.

The conditions to be imposed read as follows: the laser oscillation works as single mode and the energy density distribution of the pump and of the laser inside the medium have the same size and form. Consequently, a space-independent approximation is considered (zero-dimensional case).

For the quasi-three-levels scheme Eq. (2.14) reads:

$$N_{\mathrm{dop}} = N_1 + N_2. \tag{2.16}$$

If W_{p} stands for the pump rate, q for the number of photons in the laser mode and σ_{em} and σ_{abs} are the emission and the absorption cross sections at the laser wavelength, respectively, the population density of level 2 evolves in time such as:

$$\frac{\mathrm{d}N_2}{\mathrm{d}t} = W_\mathrm{p}N_1 - \frac{qc}{A_\mathrm{l}L'}(\sigma_\mathrm{em}N_2 - \sigma_\mathrm{abs}N_1) - \frac{N_2}{\tau_\mathrm{eff}}, \tag{2.17}$$

where A_l is the area of the laser mode inside the medium and $L' = L + (n-1)l$ is the effective length of the resonator, considering the refractive index n of the crystal, the distance between the mirrors L and the length of the crystal l [Sve98].

Furthermore, the temporal evolution of the number of photons inside the resonator can be estimated:

$$\frac{\mathrm{d}q}{\mathrm{d}t} = \frac{qlc}{L'}(\sigma_\mathrm{em}N_2 - \sigma_\mathrm{abs}N_1) - \frac{qc\gamma}{L'}. \tag{2.18}$$

In this equation, $\gamma = \gamma_\mathrm{int} + (\gamma_1 + \gamma_2)/2$ is the total logarithmic loss per pass, which is composed by the logarithmic internal losses $\gamma_\mathrm{int} = -\ln(1 - L_\mathrm{int})$ and the output coupling losses at the mirrors $\gamma_i = -\ln(1 - T_i)$, with T_i as output coupling transmissions of the mirrors and L_int as the internal losses. In the case of small losses, the internal losses per round trip Γ_int can be approximated as being two times the logarithmic internal losses γ_int.

A relation between the output power P_out of the laser and q in Eq. (2.18) can be found and reads:

$$P_\mathrm{out} = \frac{\gamma_2 c}{2L'}\, h\nu_\mathrm{L}\, q, \tag{2.19}$$

where the energy of a laser photon $h\nu_\mathrm{L}$ is mentioned.

Once the critical inversion is reached, a linear relationship between P_out and the pump power P_p can be established:

$$P_\mathrm{out} = \eta_\mathrm{sl}(P_\mathrm{p} - P_\mathrm{thr}), \tag{2.20}$$

where η_sl is the slope efficiency and P_thr the threshold pump power.

If $\mathrm{d}q/\mathrm{d}t = 0$ from Eq. (2.18) is set, the threshold inversion density N_thr can be calculated as:

$$N_\mathrm{thr} = \frac{\gamma}{\sigma_\mathrm{abs} l} \tag{2.21}$$

Consequently, P_thr reads:

$$P_\mathrm{thr} = \frac{\gamma h\nu_\mathrm{p}}{\eta_\mathrm{p}\tau_\mathrm{eff}}\,\frac{A_\mathrm{l}}{(\sigma_\mathrm{abs} + \sigma_\mathrm{em})}\left(1 + \frac{N_\mathrm{dop}}{N_\mathrm{thr}}\right), \tag{2.22}$$

where η_p is the pump efficiency and $h\nu_\mathrm{p}$ the energy of a pump photon.

Equations (2.20) and (2.22) determine the characterization of the laser. Simultaneously, the slope efficiency η_sl includes further efficiencies related to the overlap, the output coupling and the quantum efficiency, respectively:

$$\eta_\mathrm{sl} = \eta_\mathrm{p}\, \eta_\mathrm{ol}\, \eta_\mathrm{OC}\, \eta_\mathrm{qe}, \tag{2.23}$$

where η_ol is the overlap or transverse efficiency defining the fraction of the pumped channel, $\eta_\mathrm{OC} = \gamma_2/(2\gamma)$, and the laser quantum efficiency corresponds to $\eta_\mathrm{qe} = h\nu/h\nu_\mathrm{p}$.

Comparison with three- and four-level schemes

In comparison, the three-level laser scheme depicted in Fig. 2.4 b), has a level 3, whose population can be neglected because of the fast decay into level 2. Since the ground state corresponds to the lower laser level, the two cross sections σ_{em} and σ_{abs} are equal in Eq. (2.17) and Eq. (2.18) and similarly a relatively high power is needed to reach inversion.

In the four-level scheme, an advantage is given by the presence of a level 1 and a level 0 in Fig. 2.4 c) because the inversion is reached more easily than in a quasi-three-level laser. As a consequence, the threshold pump power is lower. Furthermore, if in Eq. (2.17) and Eq. (2.18) N_1 is renamed N_0, the equations are still valid, with $\sigma_{\mathrm{abs}} = 0$ because this is the only scheme where reabsorption is not possible and consequently it is demonstrated to be the most convenient laser scheme.

2.4 Upconversion in Er^{3+}-doped fluorides

As it will be explained in Chap. 4, Er^{3+}-doped fluorides are suitable for laser transitions in a wide spectral range.

Laser experiments which were object of this thesis can be grouped as follows:

- upconversion-pumped green laser (laser wavelength $\lambda_{\mathrm{l}} \sim 550\,\mathrm{nm}$), with the pump wavelength $\lambda_{\mathrm{p}} \sim 975\,\mathrm{nm} \Longrightarrow$ three-level laser scheme;
- upconversion-pumped green laser ($\lambda_{\mathrm{l}} \sim 550\,\mathrm{nm}$), with two different pump wavelengths in the range $790\,\mathrm{nm} < \lambda_{\mathrm{p}} < 985\,\mathrm{nm} \Longrightarrow$ different three-level laser schemes;
- upconversion-pumped infrared laser ($\lambda_{\mathrm{l}} \sim 850\,\mathrm{nm}$), with $\lambda_{\mathrm{p}} \sim 975\,\mathrm{nm} \Longrightarrow$ four-level laser scheme;
- visible-laser-pumped green laser ($\lambda_{\mathrm{l}} \sim 550\,\mathrm{nm}$), with $\lambda_{\mathrm{p}} \sim 485\,\mathrm{nm} \Longrightarrow$ three-level laser scheme;
- inband-pumped ($\lambda_{\mathrm{l}} \sim 1.6\,\mathrm{\mu m}$ laser), with $\lambda_{\mathrm{p}} \sim 1.54\,\mathrm{\mu m} \Longrightarrow$ quasi-three-level laser scheme.

This section is focused on the laser transitions based on an upconversion-pumping scheme, such as the first three mechanisms of the previous list.

In Fig. 2.5, the three single-wavelength upconversion schemes which have been recognized as most effective in pumping the $^4\mathrm{S}_{3/2}$-muliplet of erbium are depicted. Upconversion as a pumping process involves at least two photons or excitations (see Figures 2.3c) and 2.5) to efficiently populate higher energy levels. Successively (often after a fast relaxation), the upper laser level can be populated and consequently laser emission at a wavelength shorter than the pumping wavelength can be obtained. Ideally, the upper laser level has a relatively long lifetime, in order to build a sufficient inversion for the laser process to take place. The intermediate levels should have an even longer lifetime, to maintain a high efficiency of population of the higher levels.

Occasionally, or when the scheme is based on pumping via different wavelengths, simultaneously, it can be that the laser emission wavelength is nevertheless longer than

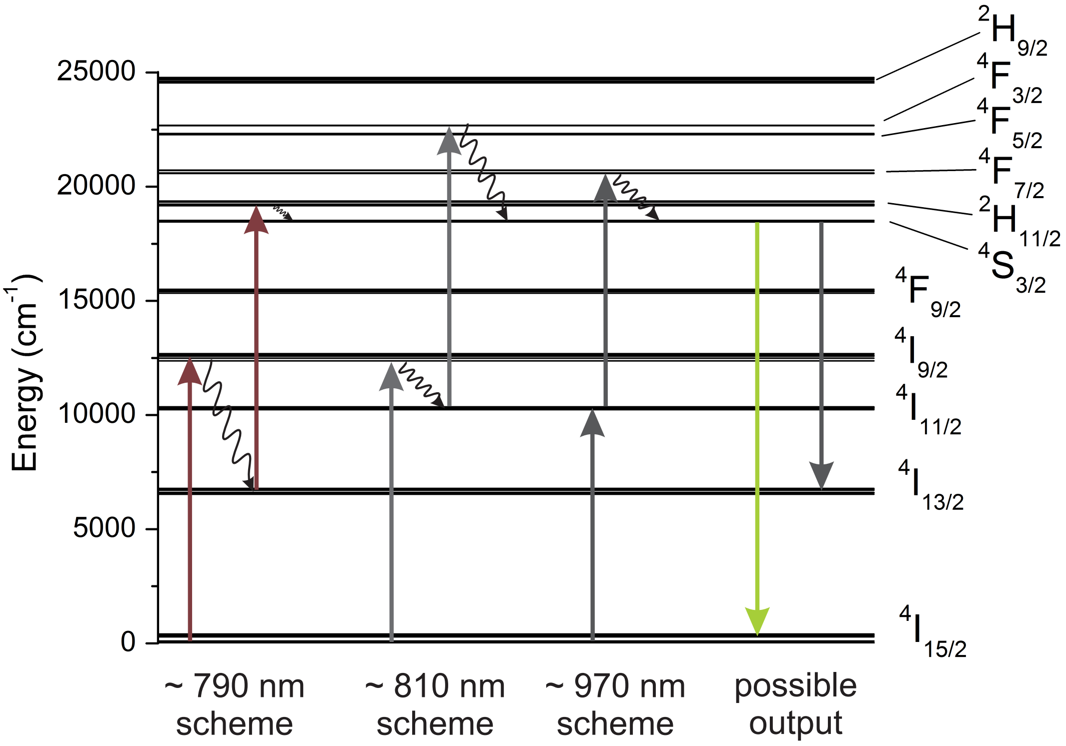

Figure 2.5: Possible single-wavelength upconversion laser pumping schemes (single-ion GSA/ESA mechanism) in erbium-doped fluorides. The energy level scheme refers to Er^{3+}:BaY$_2$F$_8$ [Bar05]. Sinusoidal arrows refer to nonradiative relaxations. The scheme based on a ~ 790 nm beam has the $^4I_{13/2}$-multiplet as metastable intermediate level. Both the schemes based on ~ 810 nm and ~ 970 nm beams share the $^4I_{11/2}$-multiplet as metastable intermediate level. One possible output is in the green spectral range, at ~ 550 nm, in a three-level laser configuration. The second possible output considered in this work is in the IR spectral range, at ~ 850 nm, in a four-level laser configuration.

one or more wavelengths involved in the pumping process. In this case, the name can differentiate from *upconversion laser* to *upconversion-pumped laser*.

This definition is valid also when codoping is imposed, which generally means that one kind of ion represents the sensitizer of the pumping (or donor) and the second the emitting ion (activator or acceptor) which is efficiently pumped. Ytterbium, due to its simple energy level scheme, its high efficiency in being pumped with well-available 1 µm-sources and in transferring its excitation to other rare-earth ions, is the most widespread sensitizing ion [Auz66, Ovs66, Joh71, San96].

All the experiments which have been pursued in the framework of this thesis can be defined as *upconversion-laser* experiments, because none of the pumping wavelengths is shorter than the obtained laser emission wavelength.

The rare-earth ions typically involved in upconversion lasers are Er^{3+} [Joh71], Tm^{3+} [Ngu89], Nd^{3+} [McF88], Ho^{3+} [All90] and Pr^{3+} [Koc90], because they offer a wide selection of metastable multiplets.

In the last fifty years, since the first studies on upconversion processes, the interest has grown and a multitude of review publications on the topic is available, although they present different interpretations [Auz73, Sch96, Jou99, Gam01, Auz04, Suy05a].

Historically, the first attempt to describe an ESA process is attributed to *Bloembergen* [Blo59], who immediately recognized the ability of the system as infrared quantum counter.

Nevertheless, systematic studies about the process of upconversion have been published only seven years later, simultaneously by *Ovsyankin and Feofilov* [Ovs66] and *Auzel* [Auz66].

The advent of the first upconversion laser dates 1971, and it is particularly important for this work because it was a visible (in the red spectral range) infrared-pumped laser, hosted by a codoped Er^{3+},Yb^{3+}:BaY_2F_8 crystal, together with a green laser based on Ho^{3+},Yb^{3+} codoping in the same matrix. Nevertheless, both lasers could operate only at low temperature (77 K) and in a pulsed regime [Joh71].

Surprisingly, because of the shortened lifetime of the emitting level by relatively high energetic phonons, the first cw upconversion laser has been a 1 at.% -doped Er:$YAlO_3$, still operating at low temperature [Sil87]. Nevertheless, better results have been obtained only one year later with Er^{3+}:$LiYF_4$ [Len88]. In 1989 the first diode-pumped upconversion laser in the same crystal has been realized [Ton89].

Successively, thanks to the availability of always more powerful diode lasers and Ti:sapphire lasers, it has been possible to obtain upconversion lasers also at room temperature and the first ones have been again erbium-doped fluorides (namely $LiYF_4$ and KYF_4) together with YAG, which has shown much worse performances than the other two crystal hosts [Bre93b].

Further interesting results concern the realization of blue and green emission with an erbium-based $LiYF_4$ crystal, pumped with a Ti:sapphire laser at $\sim$ 970 nm [Heb90] and the possibility of obtaining short-wavelength lasers also pumping at 1.5 µm, such as in Er^{3+}:CaF_2 [Pol86] and Er^{3+}:$LiYF_4$ [Xie92a, Xie92b].

Upconversion lasers are more easily achieved at low temperature because of the higher cross sections and longer lifetimes of the energy levels. Nevertheless, single-wavelength-pumping upconversion lasers are more interesting and attractive for industrial and research applications if operating at room temperature. Furthermore, in this case, the spectroscopic features are broader and establishing a wavelength overlap between GSA and ESA is easier.

As mentioned in Sect. 2.2.2, upconversion belongs to the family of interionic processes. Nevertheless, when it is considered as mechanism to pump a laser, different processes can be involved and the main upconversion pumping strategies are four [Auz73, Auz04]:

- **GSA/ESA** is an intraionic process, where two photons are successively absorbed: the first photon populates via GSA a metastable level which then can be excited by the second photon, via ESA, in a higher state. The photons can be of the same wavelength, but also of two different ones. Three examples of single-wavelength upconversion in an Er^{3+}-based system via ESA pumping are depicted in Fig. 2.5.

- **ETU**, Energy Transfer Upconversion, resembles the same process described formerly as interionic process. One ion is the sensitizer (donor) and one the activator (acceptor). In the first step, both have been excited via GSA. Subsequently, a non-radiative energy transfer takes place which simultaneously promotes the activator to a higher excited state, due to the energy offered by the donor, which relaxes to the ground state (see Fig. 2.3c)). The ions can be of the same kind or different, such as typically Yb^{3+}-ion as donor, together with another effective lasing rare earth ion. A relatively high concentration of potential interacting ions is needed for efficient ETU.

- **Cooperative processes** are typically taking place in case of high doping concentration or clustering and they are considered for the interpretation of concentration quenching effects [Auz82, Auz04]. When clusters are present, the formation of new levels may be experimentally observed. They are so-called *pair levels*. When two resonant states are coupled, their degeneracy is removed and the connection between the consequently new-born level and the parental single-state level is highlighted by a certain shift between their spectroscopic features. The effects of this interaction are typically a few orders of magnitude lower than those due to the previous processes.

- **PA**, Photon Avalanche, is a third kind of interionic process characterized by an efficient energy transfer via cross-relaxation (CR) which populates a metastable state of the acceptor and subsequently induces an ESA process. Furthermore, PA processes are identified by a threshold: when the excitation power is lower than the threshold level, the upconverted fluorescence is weak and an ordinary absorption regime of the pump power is registered. Above threshold, the emitted fluorescence increases exponentially and the medium absorbs the pump power much more strongly. A lengthening of the time needed to reach the steady state conditions is also recognized when the incident power approaches the threshold. Less strictly than in cooperative processes but as much as in ETU mechanisms, PA is more effective when a consistent concentration of rare earth ions is present [Jou99]. An example of avalanche mechanism is reported in Sect. 2.4.2, with reference to Fig. 2.6.

2.4.1 GSA/ESA and ETU processes

These are the two processes mainly responsible for upconversion pumping in low erbium-doped fluoride crystals. Unfortunately, it is not straightforward how to distinguish the two contributions, especially when both are present.

Namely, one is a single-ion process, while the other is a two-ion process. When a medium is relatively low doped, it is more probable that only a GSA/ESA pumping process is active. The probability of the participation of ETU increases with the doping concentration, until ETU and cooperative processes become dominant. In every host the onset of multiple-ion processes can be at different conditions. Most of the reports found in literature establish the limit of doping concentration of Er^{3+}-ions in fluorides where ETU becomes a relevant effect already at 1 at.% or lower (e. g. [Zie70, Rub86, Pol96a]).

Reliable information about which pumping mechanism prevails can be found in time-dependent emission measurements and excitation and emission spectra [Rub86, Pol00, Gam01, Suy05a, Suy05b].

In the case of time-dependent measurements, it is possible to distinguish between a pure GSA/ESA pumping scheme from a mixed one with ETU when the decay curve of the fluorescence after a short pumping pulse is analyzed. In the first case, the curve shows a pure exponential decay after an instantaneous pump. If $N(t)$ is the population of the emitting level, τ its decay time and N(0) the population at $t = 0$:

$$\frac{\mathrm{d}N}{\mathrm{d}t} = -\frac{N(t)}{\tau} \quad \Rightarrow \quad N(t) = N(0)e^{-\frac{t}{\tau}}. \tag{2.24}$$

This is valid for both Stokes- and anti-Stokes-fluorescence, which means for both pump beams at a shorter wavelength than the emission and at a longer wavelength than the emission. It is not possible to have any information about the intermediate metastable level, in the case of anti-Stokes-fluorescence.

When ETU is present, it is typically evident in the dynamic of the activator which is observed. This process is much slower than the short pump pulse used for the experiment (generally a few nanoseconds). The energy transfer shows a rise in the transient, followed by a decay. With rate equations, this effect can be interpreted such as the population were a consequence of a fast decay of a higher energy level in a Stokes-fluorescence.

In the Stokes-fluorescence case, $N_2(t)$ is the population of a level 2 higher than the emitting level 1, whose population $N_1(t)$ is governed by the equation:

$$\frac{\mathrm{d}N_1}{\mathrm{d}t} = -\frac{N_1}{\tau_1} + A_{21}N_2 \quad \text{with} \quad N_1(0) = 0, \tag{2.25}$$

where A_{21} represents the transition probability from level 2 to 1. The solution for $N_1(t)$ is then:

$$N_1(t) = \frac{\tau_1\, \tau_2\, N_0\, A_{21}}{(\tau_1 - \tau_2)} \left(e^{\left(-\frac{t}{\tau_1}\right)} - e^{\left(-\frac{t}{\tau_2}\right)} \right). \tag{2.26}$$

The correct interpretation of eq.(2.26) is:

- if $\tau_2 < \tau_1 \quad \Rightarrow$ the fluorescence originated in level 1 shows first a rise with a time constant equal to τ_2 and then an exponential decay with time constant equal to τ_1;
- if $\tau_2 > \tau_1 \quad \Rightarrow$ the opposite of before: the fluorescence originated in level 1 shows first a rise with a time constant equal to τ_1 and then an exponential decay with time constant equal to τ_2.

An upconversion system can be interpreted like an anti-Stokes fluorescence is taking place. In this case, it is considered that an energy transfer process from the lower level 1 to the higher level 2, with a transfer rate W, takes place and the dynamic of level 2 is studied. In this situation, the rate equation for the population density N_2 reads:

$$\frac{\mathrm{d}N_2}{\mathrm{d}t} = -\frac{N_2}{\tau_2} + WN_1^2. \tag{2.27}$$

If for level 1 the population density corresponds to:

$$N_1(t) = N_1(0)e^{\left(-\frac{t}{\tau_1}\right)}, \tag{2.28}$$

at a long time after the pump pulse:

$$N_2 \approx e^{\left(-\frac{2t}{\tau_1}\right)}. \tag{2.29}$$

In upconversion systems, further information about the incidence of the different pumping mechanisms can be given by fluorescence spectra [Pol00, Gam01]. When a sample is excited by a long-wavelength pumping source, the consequent upconversion fluorescence intensity can be measured and plotted versus the incident intensity. When the representation is set on a double logarithmic scale, the number n of photons needed to excite the emitting level and the saturation of the upconversion as a non-linear process can be deduced by the slope and the general behavior of the plot.

The theory is based on the solution of rate equations which in low-phonon-energy hosts assume:

1) only one kind of doping ion, responsible for upconversion;

2) the ground state population density as a constant;

3) cw pumping via GSA;

4) the only two possible mechanisms for upconversion pumping are either ETU or GSA/ESA;

5) every excited state has a certain lifetime τ and decays predominantly radiatively to the ground state;

6) the thickness of the samples is much smaller than one absorption length α^{-1};

7) a uniform transversal distribution of the pump power.

In order to distinguish the influence of GSA/ESA from ETU and the number of photons involved in the multi-photon pumping process, it is possible to analyze the slope of the plot at relatively low incident power and compare it to that at relatively high incident pump power. The relevant possible cases for a rare earth ion embedded in a low-phonon-energy host can be summarized as follows:

- a measured slope of x indicates an upconversion process which involves n or more photons where:
    - n is the smallest integer greater than x, if x is not an integer;
    - $n = x$, if x is an integer.

- At low incident pump power, upconversion is not the relevant mechanism for the depletion of the intermediate metastable levels and the plot gives solely the information about how many photons are involved in the process. Namely, if N_i is the population density of level $i = 1, 2, \ldots n$, and P^i is the behavior of the plot: $N_i \sim P^i$.

- At high incident pump power, upconversion is the main process for the depletion of intermediate levels and the dominant upconversion mechanism can be determined observing the luminescence originated by the intermediate excited states, with a certain population density N_i, with $i = 1, 2 \ldots n-1$:
    - if ETU is the dominant process: $N_i \sim P^{1/2}$;

  - if GSA/ESA is the dominant process: $N_i \sim P^0 =$ constant.

- At high incident power, observing the luminescence from the n^{th}-level does not give further information because it is expected to be, for both GSA/ESA and ETU pumping schemes: $N_n \sim P^1$.

The attenuation in the slopes is the demonstration of an intrinsic saturation effect of upconversion, first observed in 1966 [Sin66]. The principle of conservation of energy imposes the impossibility for every non-linear process to show non-linearity up to infinite incident intensity. Consequently, any fluorescence originated by upconversion processes presents a saturation of the non-linear effect at a certain incident exciting intensity.

2.4.2 PA processes

Cooperative and PA processes are the least probable in the pumping of upconversion lasers in the erbium-doped fluoride crystals involved in this work. One main reason is the relatively low doping concentration, which is not able to support this kind of interionic processes.

PA is a non-linear process and recent theoretical studies [Guy97] confirmed a similarity to second order phase transitions, and the possibility to be treated via the Landau theory [Lan59].

One of the rare earth ions which has been mostly studied concerning PA mechanisms and the first which has been observed is praseodymium [Chi79, Koc90]. Nevertheless, it has been proven that also erbium-doped structures can exhibit PA effects at room temperature. One example is based on a pumping scheme with wavelengths of the visible spectral range (yellow and red) [Auz94, Auz95]. In these cases the host materials have been ZBLAN, a fluoride glass, and $LiYF_4$, with a relatively high erbium concentration of 5 at.% and no laser radiation has been produced, but only fluorescence.

A second example of avalanche phenomenon is reported by *Pollnau*, concerning the pump in the infrared spectral range [Pol95, Pol96a], such as the pumping wavelengths considered in this work. It is valid for both wavelengths 810 and 975 nm, because they share $^4I_{11/2}$-multiplet as intermediate metastable level (See Fig. 2.5). It is described for $1\%Er^{3+}$:$LiYF_4$, but due to the analogy with $LiLuF_4$, it could be possible in this host crystal and in other fluoride hosts, as well.

The processes which constitute the avalanche are of three types and they are depicted in Fig. 2.6 a)-e): a CR, an ETU and an ESA. The PA process shows the necessity of being initiated, namely a pure ESA pumping to populate $^4F_{7/2}$-multiplet (in the case of 975-nm pumping) and a fast nonradiative relaxation to $^2H_{11/2}$-multiplet are invoked. An equivalent initiation can be carried out by an analogous ETU process with two involved ions. In a standard PA process, this step is interpreted by a non-resonant GSA which can inefficiently populate an intermediate excited level where the characteristic ESA and CR transitions are originated.

In the present system, once $^2H_{11/2}$-manifold is populated, two CRs of the type: $(^2H_{11/2}, {}^4I_{15/2}) \rightarrow (^4I_{9/2}, {}^4I_{13/2})$ are supposed to take place (see Fig. 2.6 a)). Afterwards, one ETU process is supposed to happen (Fig. 2.6 b)): one ion in the $^4I_{13/2}$-multiplet state decays to the ground state and the gained energy is transferred to another ion, which

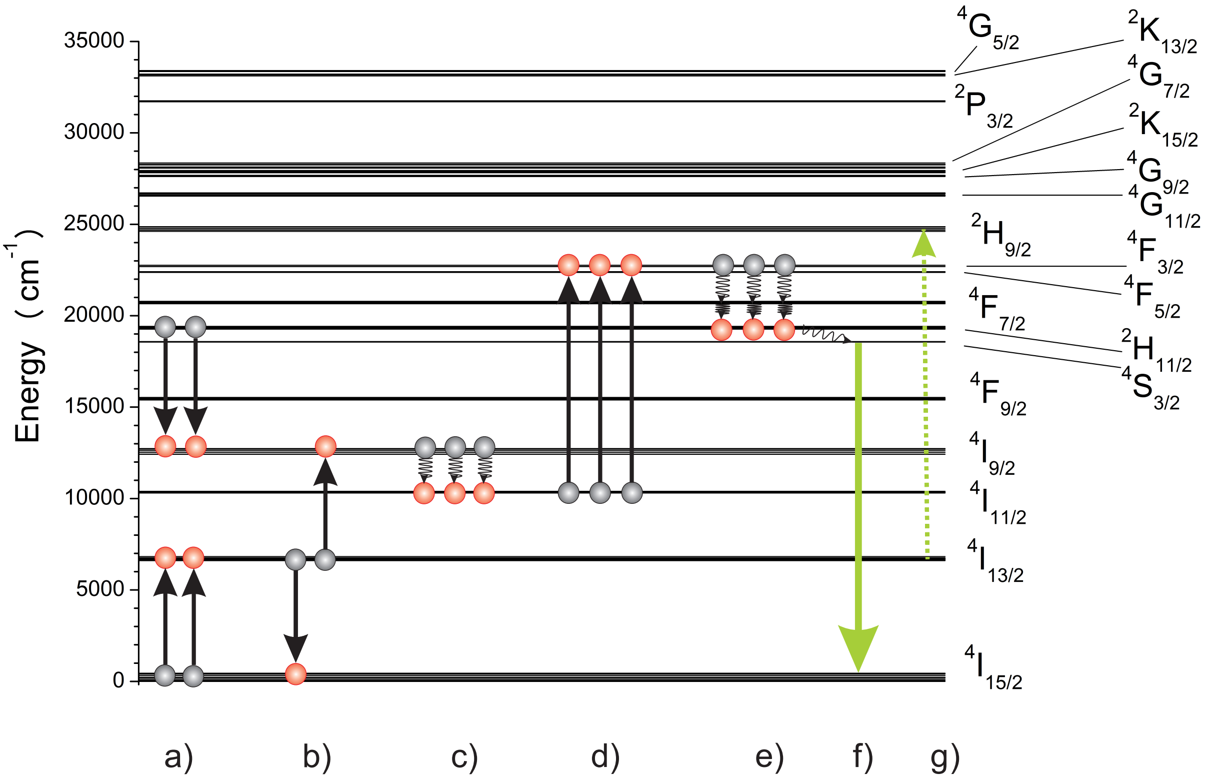

Figure 2.6: Possible avalanche process in erbium-doped fluorides, suggested in [Pol95, Pol96a]. The effect is described for Er^{3+}:LiYF$_4$ but here it is reported on the energy level scheme of Er^{3+}:LaF$_3$ [Kru64, Car72, Car86]. Grey and red spheres represent the position of the excitations before and after the transition, respectively. After ESA takes place and $^2H_{11/2}$-multiplet is populated, the avalanche process begins: a) two CR ($^2H_{11/2}$, $^4I_{15/2}$) → ($^4I_{9/2}$, $^4I_{13/2}$) take place; b) an ETU process follows: one ion in the $^4I_{13/2}$-multiplet state decays to the ground state and the gained energy is transferred to another ion, which can be promoted from the $^4I_{13/2}$-manifold to the $^4I_{9/2}$-manifold. c) Successively, the three excitations populating $^4I_{9/2}$-manifold can fast nonradiatively decay into the $^4I_{11/2}$-state, in order then to be pumped up to $^4F_{3/2}$-multiplet via three ESA processes (d) transition). e) The three excitations can then rapidly non-radiatively decay into the $^2H_{11/2}$- manifold, concluding the cycle with a net gain of $3/2 = 1.5$. f) $^2H_{11/2}$ and $^4S_{3/2}$ are thermally coupled and a laser transition to the ground state can take place, at ~550 nm. g) A reabsorption process as ESA between the metastable $^4I_{13/2}$- and $^2H_{9/2}$-levels can eventually affect the laser operation.

can be promoted from the $^4I_{13/2}$-manifold to the $^4I_{9/2}$-manifold. In this phase, three excitations are available in $^4I_{9/2}$-state which can fast non-radiatively decay into $^4I_{11/2}$-state (Fig. 2.6 c)) and create a convenient triple occupation to be converted in a triple occupation of $^4F_{3/2}$-multiplet, via three ESA processes (Fig. 2.6 d)). Three successive fast non-radiative decays into $^2H_{11/2}$- manifold conclude the cycle, yielding a total gain of excitation of $3/2 = 1.5$ (Fig. 2.6 e)).

The lasing level is expected to be the $^4S_{3/2}$-multiplet, which is strictly thermally coupled with the $^2H_{11/2}$-manifold (Fig. 2.6 f)). When the laser emission is in the green spectral range, a detrimental reabsorption process as ESA (or ESR, Excited State Reabsorption) in the transition $^4I_{13/2} \rightarrow {}^2H_{9/2}$ can take place (Fig. 2.6 g)).

When the doping concentration of erbium is increased already at 2 at.% , some further intraionic parasitic processes become relevant, such as the reabsorption of the green laser wavelength in the transition $^4I_{13/2} \rightarrow {}^2H_{9/2}$, making laser emission impossible. The required threshold for the onset of an avalanche process is also recognizable at a certain incident pump power, in laser experiments [Pol95, Pol96a].

Simulations to obtain the solution of the rate equations establish the need of such interionic processes in order to support the pure intraionic ESA pumping scheme and to reach the inversion [Pol96a]. Nevertheless, in this work PA processes have not been considered as main responsible of upconversion pumping, because of the relatively low concentration of Er^{3+}-ions in the considered crystals.

Avalanche processes have been identified also in other erbium-doped crystal hosts, such as BaY_2F_8 [McF94], but the relatively high doping concentration of 5 at.% can be the main responsible for the onset of this effect.

3 Crystal growth of fluorides

As it will be explained in Chap. 4, fluorides are among the most suitable hosts for Er^{3+}-ions when the interest is focused on upconversion-pumped processes. Moreover, they are suitable to be grown via the Czochralski technique, generally at temperatures below 1000 °C.

In this chapter, an introduction to this crystal growth method and a variation of the so-called Nacken-Kyropoulos technique will be explained.

More than a hundred years ago, the first detailed descriptions of crystal growth methods were starting to be published. Currently, a few of them are successfully applied in modern facilities which still recall the ancient approaches. One of the most popular techniques still in use is applied in this work. Further details about the methods and the principles of the crystal growth can be also found in [Lau70, Wil88, Pam75].

3.1 Czochralski technique

In 1918 J. Czochralski published his work concerning the growth of metallic crystals [Czo18]. In the following years, this method was variously modified to satisfy the demands of other kinds of materials, including rare earth-doped insulators for optical applications. A prototype of a Czochralski facility is depicted in Fig. 3.1.

This technique, also called *crystal pulling*, has the merit of being able to produce large single-crystal boules, with a low level of defects.

Some of its characteristics are:

- a *liquid-solid* technique, because it implies starting with molten materials;
- a *conservative, normal freezing* method, because material is never either added or removed from none of the phases, except by the crystallization process;
- a *crucible-based* technique, because a crucible is needed to locate the starting materials;
- a *real time* technique, able to control dimensions during the growth, generally by continuously observing either the diameter size or the weight.

At present, extremely efficient facilities are able to grow high-quality semiconductors, in particular silicon and compounds, such as GaAs [Lin87, Neu01]. The huge demand of these materials on the market has stimulated the development of the technique in order to reduce the content of defects in the crystals and shorten the growth duration. For example, numerical simulations of the whole process have gained a main role in the *a priori* determination of the optimal working parameters, trying to face the still major

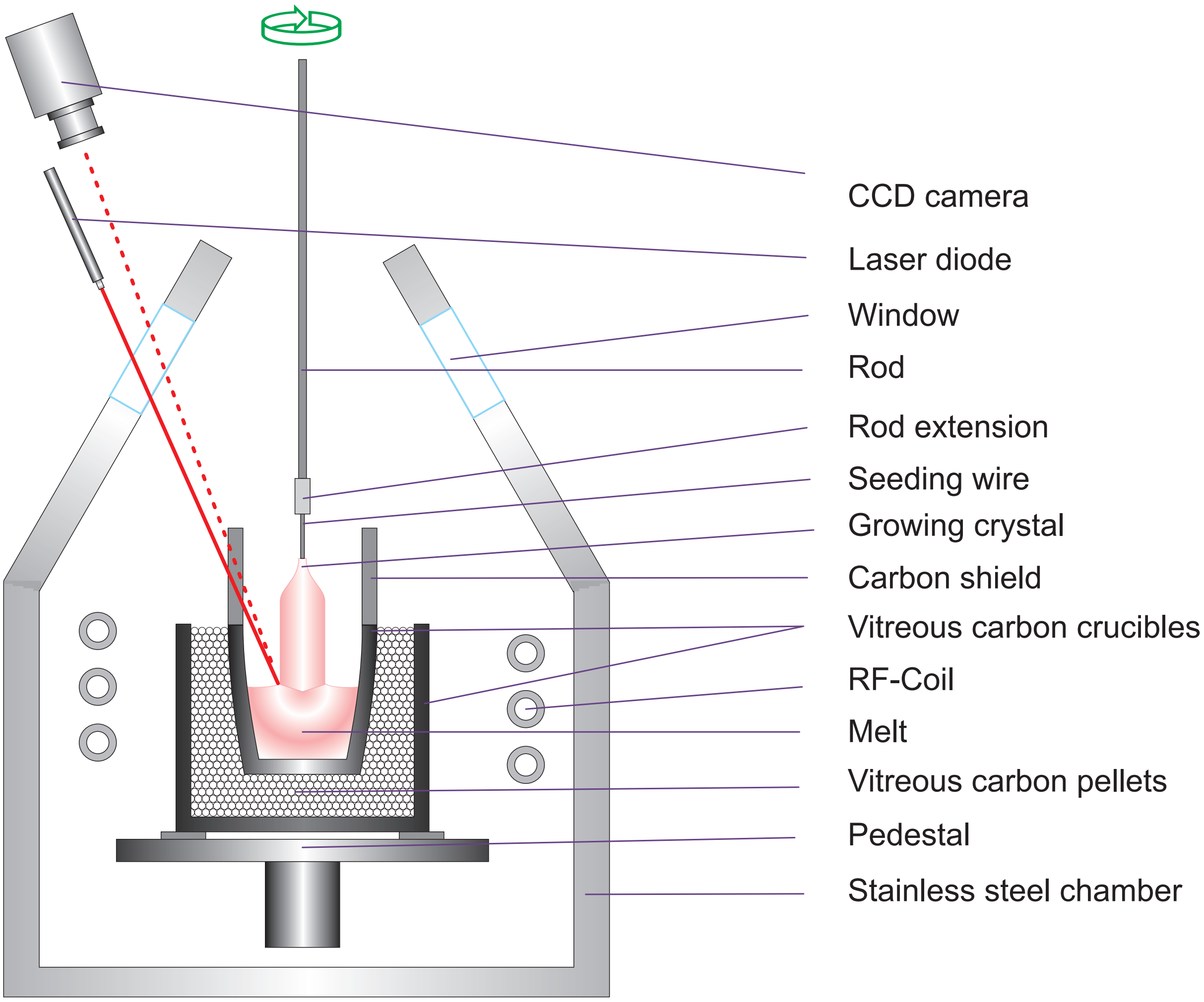

Figure 3.1: Prototype of a Czochralski facility. All the peculiarities of the facility active at the Institut für Laser-Physik (ILP) explained in the text are present, and a *real time* equipment, based on checking the diameter of the growing crystal, via laser reflexes at the meniscus, is added.

challenge of the quantitative prediction of the convective flow in the melt, during the crystal growth [Mül07].

The basic principles of the Czochralski growth are simple: an appropriate amount of the starting materials is placed in a crucible. Heat is then provided until the melting temperature is reached and when the materials are completely molten, a suitable wire (non-reacting and having a higher melting temperature than the growing crystal) can be lowered until it gets in contact with the surface. If the conditions are suitable, at the contact point the temperature is low enough to start the nucleation of a crystalline structure around the tip of the rod which, from this moment on, is slowly lifted by a rod, generally under rotation. As a result of the pulling, continuously more material reaches the solidification temperature and it can grow as a single crystal after the first nuclei.

For a higher quality of the resulting crystals and to choose their crystallographic orientation, it is recommendable to substitute the wire with a so-called *seed*, which is generally an undoped little portion of a crystal identical to the one which is grown and helps the organization of the first nucleus in the correct order and a faster creation of a single crystal.

Crystals do not grow at the thermodynamic equilibrium and the kinetics which governs the process is very complex.

During the growth, the diameter of the boule can be controlled mainly by adjusting two parameters: the heating power and the pulling rate. In this way, the *meniscus* of the growth front is influenced, that is the curvature of the upper surface of the molten material, interfaced with the growing crystal. Depending on the angle, it can be distinguished whether the crystal diameter is increasing or decreasing. When the desired size is reached, it is possible to maintain it constant, if the specific angle of the meniscus for stationary growth is also preserved.

In order to homogenize the temperature and keep the solid-liquid interface clean from impurities, the crystal is put in rotation. This allows for a finer tuning of the diameter size than the simple change of the heating power and it introduces further parameters to be adjusted.

A more practical way to increase the quality of the crystal and reduce dislocations or polycrystallinity is the so-called *necking* technique. This consists in reducing the thickness of the grown crystal, maintaining it small for a relatively short time and then starting to slowly increase it again. This can be repeated several times. This process limits the size of the crystal to a few nuclei which can more easily organize in the correct structure and mistake-free further grow .

3.1.1 Facilities and their peculiarities

To improve understanding of the Czochralski growth process, the three different facilities which have contributed to this work are introduced:

First, the facility 1) will be described and afterwards some important differences with respect to the other two will be emphasized.

1) the fluoride crystal growth facility at the Institut für Laser-Physik (ILP) in Hamburg, Germany;

2) the facility of the company *AC Materials* in Tarpon Springs, USA;

3) the facility at the University of Pisa, Italy.

At the ILP, the raw materials are located in a conical crucible with an internal volume of 17 ml, which is placed in a second larger cylindrical crucible (49 mm in height and 50 mm in diameter), filled with pellets with 2 mm in diameter. The composing material of the crucible as well as the pellets is vitreous carbon. The pair of crucibles is then positioned on a carbon pedestal, as represented in Fig. 3.2. In

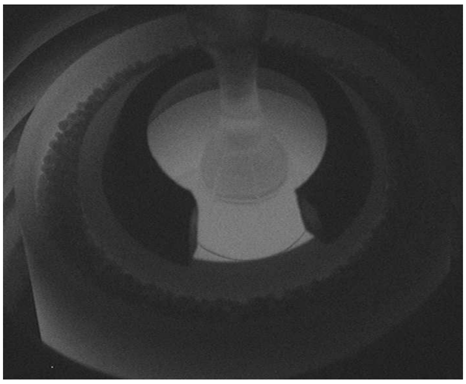

Figure 3.2: View inside the chamber via a CCD camera at the Hamburg facility. The carbon double-crucible and pellets system is placed inside the RF-coil and the growing crystal-melt interface is visible through a slit in the carbon shield.

order to avoid a strong temperature gradient which can easily cause cracks in the growing crystal, a 1-cm high carbon shield is placed on top of the inner crucible. Around these components the RF-coil (radio frequency) is fastened; it is made of six windings with an internal diameter of 5.9 cm. The heat is induced thanks to a generator supplied by *Hüttinger* (*TIG 5/300*), able to operate at a frequency between 30 and 300 kHz and at a nominal maximum power of 5 kW.

Vitreous carbon is suitable as composing material because it combines a very high sublimating temperature (it is burning-resistant up to 3000 °C [HTW06]) and a very low reactivity with fluoride substances, at least at relatively low temperatures. Furthermore, vitreous carbon is characterized by a relatively weak electric conductivity which leads to a *skin depth* thick enough to not significantly reduce the RF field through the walls of the first crucible, and to let the material inside heat up.

The skin depth is usually defined as the penetration depth of electrical current into metals. The real value corresponds to the depth where the current has dropped to a certain amount (usually $1/e = 37\%$) compared to its original value at the surface. When the material is not a conductor, the skin depth is high (in this case 3.8 mm) and if the vitreous carbon walls are thin (in this case 1.85 mm for the outer crucible), most of the RF field can be coupled inside [Ric08].

All the elements described so far are placed in a vacuum chamber of about 20 l of volume, provided with two windows. Through one of them and thanks to a slit in the carbon shield on the internal crucible, the growing process can be observed with a CCD camera interfaced with a computer. Fig. 3.2 is an example of a picture detected by the CCD camera. The pulling rod is placed on the upper part and it is able to reach the center of the inner crucible. The extension to seed the growth can either be a platinum or iridium wire, or a seed crystal. This chamber allows a vacuum level up to 10^{-5} mbar, when evacuated with a turbomolecular pump (supplied by *ILMVAC*). Most of the components of the chamber are made of stainless steel to ensure sustainability against the fluoride compounds.

Figure 3.3: Chamber for Czochralski crystal growth at the University of Pisa. The distinction between the upper area, equipped with a large window, separated by a valve from the lower main chamber is shown.

The other two facilities have some distinct differences. The first one is the heating technique: resistive instead of RF. Furthermore, as composing material in the chamber, typically carbon is present in reduced amounts (only the resistive coil is made of graphite). Crucibles and the extensions of the rod are made of platinum and shields to reduce the heat at the external parts are made of molybdenum, when the temperature to be reached are not too elevated. The chambers are also different, as shown in Fig. 3.3. They consist of two different parts: a lower one, where the crucible is placed, and a smaller upper one, separated by a valve, where some exchanges can be carried out during the growth process, without the materials in the main chamber being contaminated. These facilities can also sustain a higher vacuum limit of 10^{-7} mbar. Moreover, they are supplied with a *real time* equipment. During the crystal growth, a laser diode is pointed to the interface between the crystal and the melt. From the reflexes, which are registered by a CCD camera, a computer program can deduce the present crystal diameter and consequently adapt the heating.

None of these facilities is able to implement a fine tuning of the growth by a variation either of the rotation or the pulling rate which generally stay constant during the whole process. In Pisa and Tarpon Springs it is possible to clean the surface of the molten material of impurities which are always present when the melting point is reached, by lowering a platinum net to the surface of the melt. Successively, without changing either the temperature or the atmosphere inside the main chamber, the net can be pulled up to the secondary area and removed, after the communication valve has been closed.

The chamber depicted in Fig. 3.1 can be considered an optimization of the ILP facility with a *real time* equipment.

3.1.2 Growth preparation and the chamber atmosphere

The purity of the starting materials and the growth atmosphere play a major role in the crystal growth process. The strong electronegativity of an F^--ion together with the similarity between its atomic radius an the one of an O^{2-}-ion, make the substitution of F^- with O^{2-} during the crystal growth highly efficient, degrading the quality and eventually the laser performance of the products. Thus O^{2-} represents the worst impurity in fluoride crystals.

Nowadays, commercially available starting materials can reach a purity up to 5 N or even 6 N (either $< 0.001\,\%$ or $< 0.0001\,\%$ of impurity content). Depending on both the possibilities which the facilities allow and the experience of the operators, three main working strategies regarding the pre-treatment of the raw materials and filling gas in the chamber are possible:

a) pre-treatment of the raw materials using HF and filling the chamber with a mixture of an inert gas and CF_4, possibly containing also HF (no optimum vacuum required) [Gug63, Asa66, Joh71, Wen99, Shi01, Rei12b];

b) pre-treatment of the raw materials using HF, reaching a very high vacuum level in the chamber, with pre-pumping (higher than 10^{-6} mbar) and refilling with an inert gas (mostly argon) [Wel64, Ton10, Tur11];

c) HF-free pre-treatment including NH_4HF_2, filling the chamber with a mixture of an inert gas and CF_4 [Tho61, Naf73, Jou01, Dou03].

Pre-fluorination processes and fluoride gases at the ILP

To support the technique a), adopted in the framework of this thesis, a wide selection in the literature can be found [Sob02]. *Guggenheim* was the first who described the use of HF at all stages of the high-temperature-treatment of fluorides [Gug61, Gug63]. Nevertheless, the consecutive improvements to the strategy are well described in a collection of papers of *Pastor* [Pas74, Pas75a, Pas75b, Pas76a, Pas76b, Pas80]. They range from the exclusive use of HF to the test of other reactive materials, like CF_4, teflon ($(C_2F_4)_n$) and BF_3, in order to apply an always more effective reactive atmosphere processing technique (RAP). *Pastor et al.* are also owner of one of the first patents regarding growth of fluoride crystals [Pas76c].

The factor which mostly influences the choice of the gas mixture in the chamber is the most probable kind of impurity which can contaminate the melt and consequently the produced crystal. The major problem is the so-called *pyrohydrolysis* of fluorides, namely the reaction with water vapors at high temperature. It has been observed [Ran96, Bal99, Shi01, Ran02a] that traces of oxygen or moisture lead to the formation of highly reactive OH^- radicals which easily enter the structure as substitutional defects. They can be detected by absorption measurements in the range from 2630 to 2880 nm. Moreover, also complexes can be formed, namely three groups:

- $M(OH)_2$, derived from the interaction with further free divalent contaminating ions M^{2-} (M = Mg, Mn, or Ti); observable in the range from 2770 to 2880 nm;
- HCO^-, originated by traces of carbon included in the crystal and typically appearing as absorption peaks between 3425 and 3510 nm;
- hydrogen oxides H_xO_y ($x = 1, 2$ and $y = 1, 2$) detectable in a wide range from 2500 to 4170 nm.

CF_4 is expected to well react with water, following the reaction:

$$CF_4 + 2H_2O \longrightarrow CO_2 + 4HF. \tag{3.1}$$

Eq. 3.1 shows that CF_4 is not only efficient in removing moisture, but also in producing HF at the same time. This gas reacts with oxyfluorides which usually melt at a higher temperature than the oxygen-free fluorides, and stay on the surface of the melt during the crystal growth process. The strongest reactions of HF occur with $M(OH^-)$ or $M(O^{2-})$, but none with water. For these reasons, the two gases are expected to be complementary agents: CF_4 is efficient against water presence in the chamber but not against HCO^- or $M(OH)_2$; in the letter case, HF is more effective. Nevertheless, in [Mai09] it is explained that in the usual fluoride growth temperature range (800 - 900 °C), CF_4 is in chemical equilibrium with reactive F and all the CF_x (x = 3, 2, 1). When the density of oxidized components is low, they can be fluorinated also without the support of HF.

However, when a high quantity of HF is needed and the one produced by the reaction between CF_4 and water is not enough, it is possible to add HF to the mixture from the beginning. *Pastor et al.* [Pas75a] explained that hydrolysis, which causes hydroxide contamination during crystal growth processes, is a chemical reaction based on the

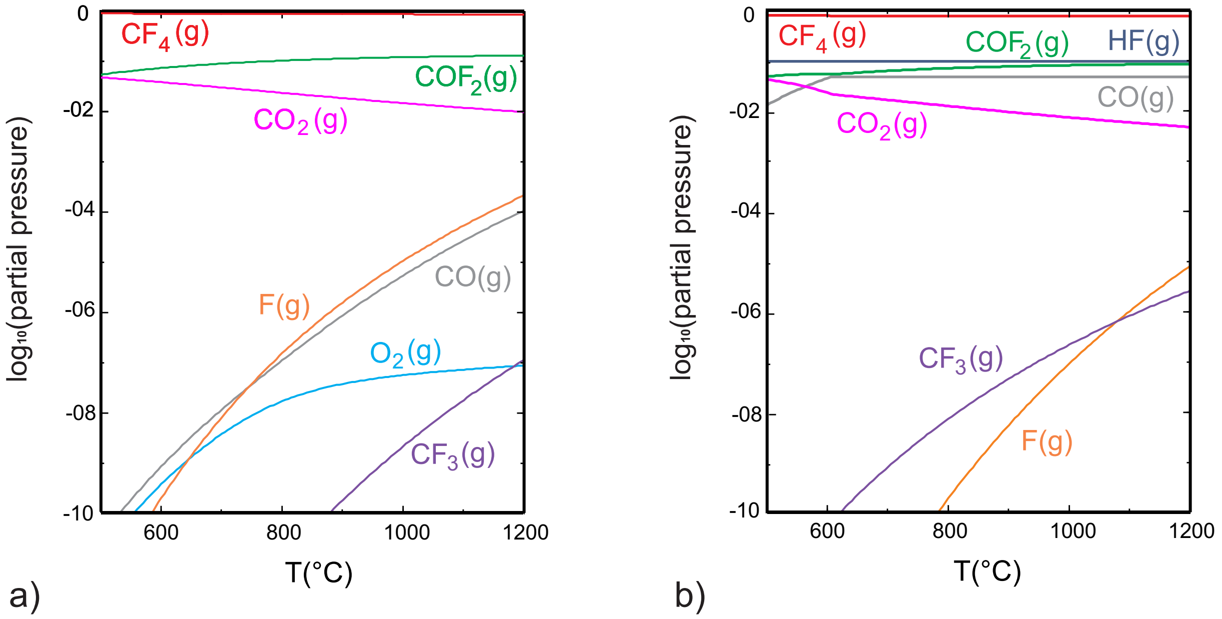

Figure 3.4: Predominance (Ellingham) diagram simulated by D. Klimm, *IKZ* (*Leibniz-Institut für Kristallzuchtung*, Berlin, Germany) via *FactSage* program [Kli12]. It is valid only at conditions of equilibrium. a) Case when only CF_4 is present to fluorinate Y_2O_3. b) Case when also H_2 is added and HF can be created for an improved fluorination capability.

unavoidable presence of water traces and it implies:

$$F^-(c) + H_2O(g) \longrightarrow OH^-(c) + HF(g), \tag{3.2}$$

where the F^- ion and OH^- are in the condensed state (c) and HF and water in the gaseous state (g). From the equilibrium relation, the concentration ratio C of F^- to OH^- is given by:

$$C = K\ i_{RAP} = K\ \frac{P(H_2O)}{P(HF)}. \tag{3.3}$$

In this way, the ratio between the two partial pressures of water and HF results in the index of reactive atmosphere processing. When the concentration of HF is high, i_{RAP} decreases and consequently C decreases as well, leading to a low concentration of hydroxides in the crystal.

Nevertheless, a simulated predominance diagram can explain in a more detailed way which phenomena take place. In Fig. 3.4 two situations are plotted: in a) fluoride raw materials are placed in the chamber in a pure CF_4-atmosphere and a hypothetically considered small oxidization is represented by Y_2O_3 (when structures containing yttrium are grown); in b) a certain amount of H_2 is added to the CF_4. Taking into account that in this diagram equilibrium conditions are considered, the simulated partial pressure of the gases are close to the real ones only at temperatures far above room temperature, starting at e. g. 500 °C. At this point, the high concentration of CO_2 and CO in the gas mixture in Fig. 3.4b) compared to Fig. 3.4a) shows that CF_4 is able to fluorinate Y_2O_3 according to:

$$2Y_2O_3 + 3CF_4 \longrightarrow 4YF_3 + 3CO_2. \tag{3.4}$$

Then, depending on the presence of H_2, the following can happen: if H_2 is present

$$CO_2 + H_2 \longrightarrow CO + H_2O, \tag{3.5}$$

$$O_2 + 2H_2 \longrightarrow 2H_2O; \tag{3.6}$$

otherwise

$$2CO_2 \longrightarrow 2CO + O_2. \tag{3.7}$$

COF_2 originates from further reactions with CF_4 and, when H_2 is present, O_2 can be involved in the creation of water, and consequently it is absent in Fig. 3.4b), according to Eq. (3.6).

Around the usual melting temperature of fluorides, reactive CF_3 and F barely start to be created and they do not play an active role in the chemistry of the system. At the same time, the partial pressure of CF_4 is always high, up to the maximum temperature shown of 1200 °C and the same is for HF, when H_2 is present. The only crystal considered in this work which can probably benefit from the presence of F and CF_3, extrapolating the diagram to higher temperatures, is LaF_3, which exhibits a melting temperature of almost 1500 °C.

Although in [Mai09] the conclusion is that the best way to grow fluorides is to fill the chamber with 100 % of CF_4, at the ILP the amount considered enough to have high quality crystals is 40 % of it in Argon. The purity of the starting materials and of the gases (also 5 N purity) is also very important.

It is evident that the procurement of high-quality materials is the first step for a successful crystal growth. A way to obtain impurity-free fluorides is to pre-fluorinate oxides in a platinum reactor, at high temperature, using HF as fluorinating agent. After this process, it is recommendable to handle the products the least possible. This procedure is followed by the company *AC Materials*, owner of the facility 2) previously described, and suppliers of the starting materials for the growth of the crystals involved in the framework of this thesis.

At the ILP, following the procedure a), prior to every growth session, a fluorination process has been performed. This was based on HF only when old materials were used, as in this case a high oxygen contamination could be expected due to the long storage in air. When CF_4 is present, HF is created adding a suitable amount of molecular hydrogen H_2.

After evacuating the chamber via the turbomolecular pump and a few hours of baking at ~ 500 °C (in order to remove residual oxygen and water), the chamber has been filled with either pure CF_4 or a mixture of CF_4 and argon (40 % CF_4) or one of CF_4, argon and hydrogen (7 %, 89 % and 4 %, respectively). The fluorination process has been performed for up to 7 h, at a temperature of a few hundreds of degrees Celsius below the melting temperature of the starting materials, with a continuous exchange flow of the gases between 5 and 10 l/h. This procedure has been repeated every time the crucible has been refilled, typically twice per crystal growth process. Indeed, due to the small size of the crucibles, after reaching the melting temperature, the chamber has been cooled and evacuated prior opening, and the crucible refilled with new raw material. Typically, a third of the volume can be gained after melting, and the amount of material reaches, for example in the case of $LiLuF_4$ crystals, a total weight of 80 g.

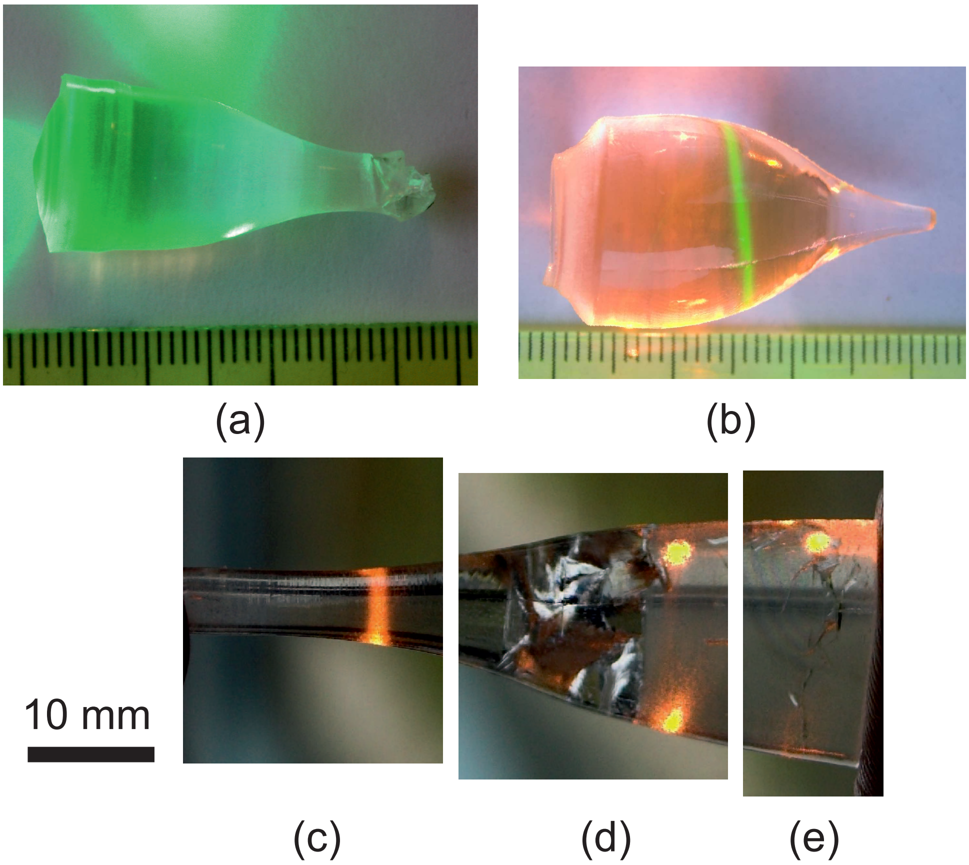

Figure 3.5: Test of crystal quality with laser pointers. a) High-quality undoped $LiLuF_4$ F boule (Tab. A.1) is checked with a green laser pointer and no scattering is visible. b) In high-quality 1.3%$Er:LiLuF_4$ H boule (Tab. A.1), two different laser pointers are used: orange scattering on the left is absent, but green light causes fluorescence on the right. The 1% $Er:BaY_2F_8$ Q boule (Tab. A.4) is checked with an orange laser pointer. c) In the neck: scattering is high. d) In the middle: scattering centers are less numerous. e) In the bottom: scattering is absent.

At the moment a growth process starts, or every time the material is melted, the atmosphere in the chamber (i.e. the gas content) has to be chosen. The mixture of gases already mentioned regarding the pre-fluorination of the raw materials were also those kept in the chamber during the whole growth process (although in most cases the content of CF_4 was lowered, even to 10-15%).

Furthermore, either a steady atmosphere or a certain gas flow for a dynamic atmosphere can be chosen. An exhausting valve ensures a slight positive pressure inside the chamber in order to avoid suction of air. The pre-fluorination processes have been performed with a certain flow. During the actual growth process, the valve was closed and the atmosphere has been kept static.

Detection of defects

To detect visible inclusions, a grown crystal is commonly tested by shining a laser beam through its volume and observing the scattered light [Bel91], as shown in Fig. 3.5. Nevertheless, precaution must be taken if the doping ion has a complicated level scheme. For example, either Er^{3+}- or Ho^{3+}-ions , when included in a crystal, lead to numerous possible absorption peaks and consequent fluorescence.

The wavelength of the easiest available laser pointers on the market are mostly matching these absorption peaks and often it is not possible anymore to distinguish between scattered light and fluorescence. When a crystal is undoped, such as the $LiLuF_4$ in Fig 3.5a), also a green laser pointer at 532 nm can be used and if the crystal has a good quality, no light is scattered.

For Er^{3+}-doped crystals a safe region from absorption is the one in the yellow to orange spectral range. For this reason, the quality of the crystals was tested with a 593 nm laser beam.

Fig. 3.5c)-e) allows to understand how the laser beam has been employed to show the decreasing amount of impurities along a self-grown $Er{:}BaY_2F_8$ boule. In a), the neck of the crystal is tested and a relatively high level of scattering is evident. Moving towards the bottom of the boule, the scattering decreases (Fig. 3.5b)), until it almost completely disappears (Fig. 3.5c)).

In Fig. 3.5b), a comparison of the consequences of using the green and the orange laser pointer on an Er^{3+}-doped crystal are demonstrated in the same boule: the orange beam (on the left) is not scattered, meaning a good quality of the crystal, while the green laser beam is absorbed and fluorescence is emitted at a slightly longer wavelength (on the right). Although macroscopic inclusions are not present, the green fluorescence could be interpreted as scattering.

In absorption measurements performed with a *Varian Cary 5000 UV-Vis-NIR* spectrophotometer, covering the wavelength range from 200 to 3200 nm, the occurrence of $M(OH)_2$ and H_xO_y was examined. Unfortunately, the operating wavelength range of the device did not extend to longer wavelengths. Therefore, in particular HCO^- impurities could not be detected. However, HCO^- inclusions are not expected due to the extremely weak interaction between fluorides and the carbon crucibles mentioned before.

The results of the absorption measurements for seven different $LiLuF_4$ samples are plotted in Fig. 3.6. The reported spectrum is in the range 2700-2850 nm, where the only resolvable peak was detected, precisely at 2765.5 nm, in only two crystals. This could correspond to the fingerprint either of a general OH^- inclusion or of a H_xO_y complex [Coc81] (e. g. HO_2 from *HITRAN Database*). Although this wavelength is very close to the range where $M(OH)_2$ can be detected, the low probability of contamination of the starting materials renders this option unlikely. Furthermore, the two samples which have shown the absorption peak have been cut from two very first boules which have been grown. For these growth runs a low percentage of CF_4 /Ar (only 10 %), no flux of the atmosphere, no extra-quantity of LiF as starting material (the reason will be explained in detail in Chap. 4) and no pre-fluorination process have been employed, although at that time the only ErF_3 available was relatively old and probably affected already by oxidization.

Alternative crystal growth conditions

As mentioned before, under a high vacuum conditions, fluorides can be grown with non-aggressive gases. Inert gases are preferable, because they reduce the possibility of inter-

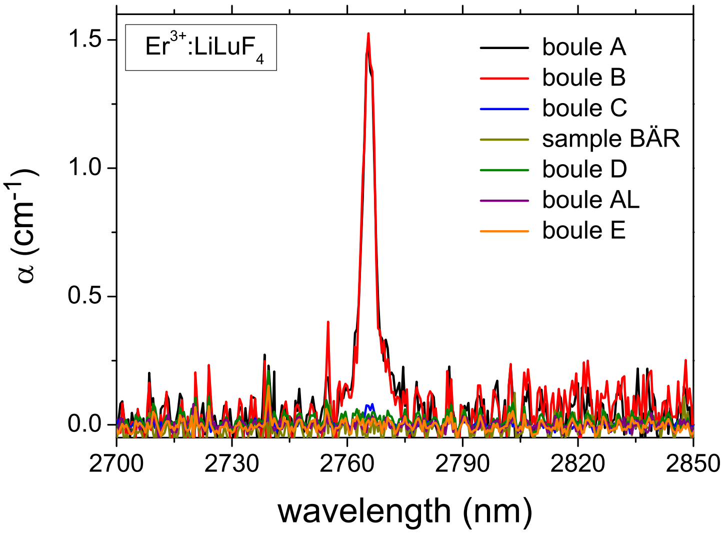

Figure 3.6: Absorption measurements for the detection of defects. The seven Er^{3+}:LiLuF$_4$ crystals represented do not show any absorption peak in the measurable range of the spectrophotometer (up to ~3000 nm), with the exception of boules A and B, which exhibit an absorption peak at 2765.5 nm due to oxygen inclusions. The spectrum has a relatively high level of noise because of the vicinity to the limit of measurability and the low signal. It was recorded with a data interval of 0.5 nm, an averaging time of 3 s and a spectral resolution (SBW) of 1.5 nm. More information about the crystals cited are summarized in Tables A.1 and B.1

.

action with the growing material, still maintaining a slight over-pressure ($P \gtrsim 1$ atm) in the chamber. A typical gas that is chosen by *AC Materials* and the operators in Pisa is high purity (5 N) argon. This, together with a vacuum higher than 10^{-7} mbar and 5 N or 6 N quality raw materials, ensures a very low probability of contamination in the grown crystal [Jen06].

The third option which also avoids to employ a dangerous and highly corrosive gas such as HF, is to perform a pre-fluorination with ammonium bifluoride, NH_4HF_2. HF can perform an efficient fluorination process directly on high purity oxides (4 N or 5 N), but this ammonia-based substance is also suitable for the same process. In [Dou03] it is suggested to mix the starting oxide material (namely R_2O_3) with liquid NH_4HF_2 at 150 °C in order to activate the following reaction:

$$NH_4HF_2 + R_2O_3 \longrightarrow RF_3 + NH_4F + H_2O. \qquad (3.8)$$

At this temperature water evaporates and, when the fluorination process is completed, NH_4F is removed via pyrolisis at 650 °C, in neutral atmosphere. The crystal growth can then start in an evacuated chamber refilled with CF_4, which is efficient in removing the last spurious traces of H_2O, following Eq. (3.1).

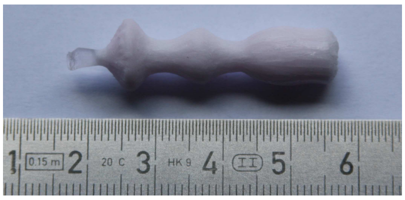

Figure 3.7: Er:LiLuF$_4$ failure grown after an inefficient evacuation of the chamber: high-purity starting materials, reducing atmosphere and a seed as growth starter could not avoid the complete oxidization of the boule.

Independently of the chosen gases and fluorination process, it is clear that a starting high level vacuum, at least higher than 10^{-4} mbar, is essential. In Fig. 3.7 a picture of an Er:LiLuF$_4$ boule is shown. Due to a leakage of the chamber, a high vacuum could not be obtained prior to the growth process. Despite the reducing atmosphere and the seed crystal which was employed, the grown structure was completely oxidized.

3.2 Variation of the Nacken-Kyropoulos technique and the seedless cooling down method

A modified Nacken-Kyropoulos technique and the seedless cooling down method resulted, in certain cases, to be a good alternative to the Czochralski technique for the crystal growth of fluorides. They can be easily implemented in the same facility and help overcoming some problems which occasionally arise.

The Nacken-Kyropoulos approach is the one named after the two scientists who independently developed it more than 80 years ago [Nac15], [Kyr26]. In this case the starting phase is the same as in the standard Czochralski technique: the chamber should be very well evacuated, the high-purity raw materials can be fluorinated and then, with either a static or a dynamic atmosphere, the growth can start. The raw materials can be melted and a seed crystal can be dipped into the melt. At this point, instead of slowly pulling and rotating, it is enough to decrease slowly the temperature and let the crystallization proceed from the first nucleus generated by the contact between the colder seed and the melt and let it propagate into the whole volume of the melt. Nevertheless, with this method, there is a lack of control of the crystallization process, because the intense thermal radiation can cause a relatively sudden crystallization at the surface. A further drawback is the contact of the growing structure with the crucible walls, which induces stress and enhances polycrystallinity. Fortunately, fluorides exhibit very low adhesiveness to carbon crucibles, which reduces significantly this last problem.

Instead of using a seed crystal, a bottleneck can also be grown, as it is often done with the Czochralski technique. By the application of the Nacken-Kyropoulos method, crystal samples can be easily obtained in the cases the Czochralski technique was troublesome, namely when difficulties in pulling the material or maintaining the contact between the melt and the growing crystal occurred.

Alternatively, it is possible to start the growth by making contact with a wire instead of a seed or even without any contact and simply cooling down (seedless method). Nevertheless, this last technique is even less controllable than the Nacken-Kyropoulos method.

In the framework of this thesis, the seedless cooling down method was systematically applied only to grow one kind of structure: LaF$_3$. In Fig. 3.8, the present setup is depicted.

The problems which have been encountered during the growth of LaF$_3$ are an unusually high melting temperature for fluorides and a very strong evaporation of the raw materials starting at a temperature slightly below the melting point. Further information can be found in Chap. 4. In the literature, different experiences can be found: in [Fuk10] a report of the growth of large Czochralski grown boules, without evaporation phenomena, is included. But in [Shi04], a spontaneous-nucleation strategy, similar to the seedless coling down method has been chosen.

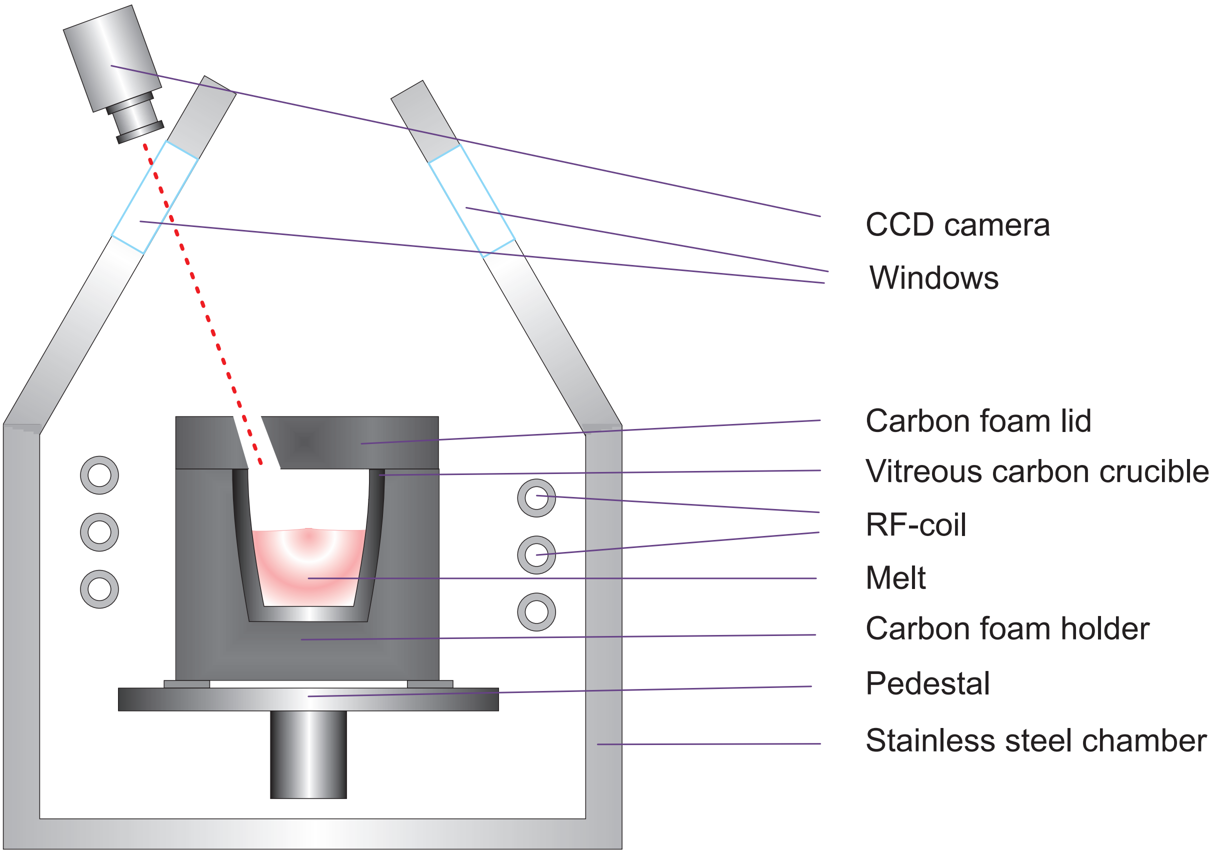

Figure 3.8: Seedless cooling down facility adopted to grow LaF_3 crystals. Neither wires nor seeds are used and a carbon foam lid is used in order to prevent the evaporation of the raw materials. A slit in the lid allows for observing the surface via a CCD camera .

LaF_3 crystals melt close to 1490 °C [Por62] and with the carbon insulation that is usually employed in the Czochralski facility at the ILP, only temperatures up to $\sim$ 1200 °C can be reached. In order to optimize the insulation, the usual double-crucible system with carbon pellets has been replaced by a cylindrical, hollow, carbon-foam-made holder for the 17 ml crucible. This foam is normally used as complementary material in the chamber. This structure can suitably fill the space inside the RF-coil, inducing a higher impedance and reducing the skin depth of the field, with a total result of a higher temperature reached in the crucible. In this way, temperatures above 1600 °C can be reached with the same facility. After many growth sessions, all the components of the chamber have demonstrated to withstand these high temperatures, except for the vitreous carbon crucibles, which exhibit faster degradation. This is confirmed in [Sob02], where it is stated that CF_4 above 1400 °C reacts with graphite and a burning process is accelerated. Furthermore, for the attempts of pulling LaF_3 crystals, it is necessary to substitute platinum with iridium wires, which melt at a higher temperature and does not react with fluorides.

A more crucial difficulty, still to be completely solved, is the evaporation of the material. When the optimal temperature for growing is reached, a strong, visible evaporation begins. As a consequence, a large amount of residue is deposited on the walls and windows of the chamber. The growing crystallites cover the surface of the melt much faster than the desired crystallization from the melt. This is the reason why no bottleneck can be grown.

A circumvention of the evaporation can be accomplished covering the surface of the melt with a lid made of carbon foam. A slit has been cut in the lid in order to observe the surface of the material with the camera and realize when the melting point is reached. The evaporation is not only limited because of the decreased free volume over the surface. A reduction originates also from the decreased diffusion through the slit and it is evident due to the diminished deposit growing on the internal side of the lid.

The diagrams depicted in Fig. 3.4 state that CF_4 in the chamber can generate a higher amount of reactive F and CF_3 at this higher temperature. They are able to more efficiently protect the growing crystal from inclusions than for other fluorides, but at the same time the presence of a lid quenches this positive influence.

4 Crystalline hosts for the Er^{3+}-ion

Despite the partial shield of 5s and 5p shells, the crystal field, depending on its symmetry and strength, influences the position of the barycenter of a manifold and the position of the single Stark sublevels. In this way, the transition probability is affected, implying a variation of the lifetimes of the energy levels up to an order of magnitude [Cor09]. Furthermore, the Boltzmann population of the levels in the multiplets can greatly influence the performance of a quasi-three-level laser, mostly regarding its threshold.

Another important feature of a crystal structure is its intrinsic phonon energy which determines the probability of the non-radiative decays. Depending on the possible multiphonon relaxations, the fluorescence lifetime of some energy levels can undergo a shortening process, down to a real quenching of some relatively low-energy transitions.

Finally, also the thermomechanical features of a host have a major influence on the performance of a laser, especially at high output power and for short pulses applications. The last tendencies in science are to match the broad emission lines of nowadays well-developed and powerful laser diodes and to push the realization of short pulses down to the femtosecond range [Hub10].

For upconversion lasers based on Er^{3+}-ions, the host has to allow for a relatively long-living $^4S_{3/2}$-multiplet, as emitting level, and $^4I_{11/2}$-level, as intermediate pumping level. Furthermore, the quasi-three-level laser is favored by a relatively strong crystal field, enlarging the separation of the Stark sublevels, decreasing the laser threshold.

4.1 Overview on the potential of fluorides

The main category of insulating materials which are widely used as host materials for solid-state laser fabrication is the oxides. One of the alternative group is the fluorides. Although the importance of thermomechanical characteristics for high power applications would mostly lead to an advantage for oxides, there is no absolute best structure which is feasible for every situation.

The role of this chapter is to show how fluorides can be advantageous in many cases and in relation to the experiments involved in this work, especially those based on upconversion.

More specifically, what is usually recognized as promising for oxides is their high thermal conductivity, their hardness, which makes them easier to handle and polish, their less critical crystal growth. Moreover, oxides show a stronger crystal field leading to a larger Stark splitting for rare-earth-ion manifolds, lowering the threshold of quasi-three-level lasers.

On the other hand, fluorides are usually characterized by:

- a lower phonon frequency, which decreases the probability of non-radiative multiphonon relaxations, increases the luminescence quantum efficiencies and more transitions in the relatively long wavelength IR region are possible for lasing;

- as a consequence of a low phonon energy, longer lifetimes of the laser emitting levels, allowing higher energy storage useful for the q-switching laser regime;
- a higher bandgap which together with the low phonon energy determines a wider transparency range (possibly from the VUV to the 10-µm region);
- a negative thermo-optic coefficient which in lasers reduces the thermal-lensing effect and improves the beam shape and the stability at high average pump power;

Nevertheless, some characteristics lead to a lower suitability for industrial applications, because, when compared to oxides, fluorides suffer from:

- a critical crystal growth conditions (required high vacuum attainable in the chamber, need of aggressive gases. . . See Chap. 3)
- lower thermal conductivity;
- higher brittleness;
- higher thermal expansion, which means higher sensitivity to thermal shocks and fractures;
- hygroscopicity (occasionally).

When the history of solid-state lasers is briefly considered, in a few cases, rare-earth-doped fluoride crystals have offered advantages, if compared to other rare-earth-doped crystals.

For example, with the aim of the realization of a broadly tunable, direct solid state UV-laser, cerium has often been found embedded in fluoride hosts, such as $LiLuF_4$ [Dub94] and $Li(Sr,Ca)AlF_6$ [Dub93, Pin94, Cou04].

These crystals, in order to obtain widely tunable and short-pulses lasers in the short infrared range, can also be doped with Cr^{3+} [Pay88, Pay89, Gäb98, Uem00], despite the fact that chromium is more often used in oxide hosts or in its divalent and tetravalent form.

For the realization of scintillators and lithographic imaging, a wide transparency in the UV and VUV spectral range is required. Ce^{3+}, Nd^{3+}, Eu^{3+} and Tb^{3+} are the most commonly involved ions, embedded in the above mentioned hosts and LaF_3 [Jou03, Dor90, Sar02].

Another rare-earth ion proven to be very efficient in a fluoride host, either as visible laser or as frequency doubled in the UV range, is Pr^{3+} in $LiYF_4$ [Est77, Ric04, Gün11a, Gün11b].

Nowadays, an outstanding success in terms of efficiency and short pulses generation at 1 µm of wavelength involves the implementation of the thin-disk geometry, using, after a fist development of Yb:YAG, the sesquioxides as hosts for Yb^{3+}-ions, due to their extraordinary thermomechanical properties [Pet02, Pet07, Pet09b, Sar12]. Nevertheless,

Yb^{3+} in $LiYF_4$ can give a wide tuning range of 25 nm [Kaw01]. It can be also applied in the thin disk lasers [Fre11] and it is supposed to determine less losses due to cooperative luminescence, compared to oxides [Weg95, Ben04].

Nd-doped crystals are well-known mostly for their possible four-level-laser operation at 1 µm. After the first demonstration of a cw-laser in Nd:$LiYF_4$ [Pol82], a comparison with the results obtained with the most commonly used Nd:YAG was possible: despite a lower emission cross section in both polarizations, a lower threshold and double of the TEM_{00}-laser power were exhibited by Nd^{3+} embedded in the fluoride host. The negative thermal lensing of $LiYF_4$, caused by the negative change of refractive index with increasing temperature, plays the most important role in decreasing the overall thermal lensing effect during laser operation. Furthermore, when frequencies lower than 2 kHz in q-switched 1-µm lasers are needed, Nd^{3+} in $LiYF_4$ has a pulse energy capability two times higher than in YAG [Lee12]. Nowadays, Nd:YAG is the most efficient laser (e. g. [Bar98]), but a more than two times longer lifetime of the upper-laser level in $LiYF_4$ [Pol82] favors efficient q-switched laser emission. For example, frequency-doubled Nd:$LiYF_4$ lasers are commercially available for pumping ultrafast (femtosecond-regime) Ti:sapphire-based amplifiers [Coh11], but depending on the application, the choice made in industry between YAG and $LiYF_4$ is still open [Lee12].

A system that so far has exhibited high efficiency in the range of 2 µm emission wavelength is the Tm^{3+}-Ho^{3+} laser. Either when the host is codoped, or the two ions are singly embedded, oxide crystals are mostly preferred (e. g. [Koo11]). Nevertheless, in fluoride structures such as $LiYF_4$, an efficient energy transfer between Tm^{3+}- and Ho^{3+}-ions has been measured (compared to the back-transfer Ho^{3+}- to Tm^{3+}-ion, the transfer coefficient is 30% higher than in YAG [Pay92, Wal97]) and lower detrimental upconversion losses in q-switched operation have been shown [Rus96, Vie02]. Furthermore, in KYF_4, Tm^{3+}- and Ho^{3+}-ions present a wider laser tunability than in oxide hosts [Gal04a, Gal04b].

When singly doped with Tm^{3+}-ions, fluoride materials can also show very high slope efficiencies [Est90, Sch09]. Moreover, Tm:$LiLuF_4$ has been recently applied in a thin-disk-laser module with encouraging results [Sto12]. Additionally, $LiYF_4$ has been compared to YAG also concerning Ho^{3+}- based lasers for infrared q-switched emission at 2 µm and recognized as more promising referring to a higher slope efficiency, a lower threshold and a longer upper level lifetime [Chi71, Chi72].

A host which is also suitable for laser applications, due to its particularly high thermo-mechanical characteristics and relatively simple and high quality crystal growth, is CaF_2. The charge compensation which is needed when a trivalent rare-earth ion substitutes Ca^{2+} can appear as a drawback. In reality, this leads to a broadening of the absorption and emission peaks, and to a consequent widening of the tunability range, like in Tm:CaF_2 [Cam04].

Due to the very wide transparency range of fluorides, applications further in the mid-IR are possible. For example, Dy^{3+} in $LiYF_4$ has proven to be suitable for a laser at 4.34 µm [Bar91].

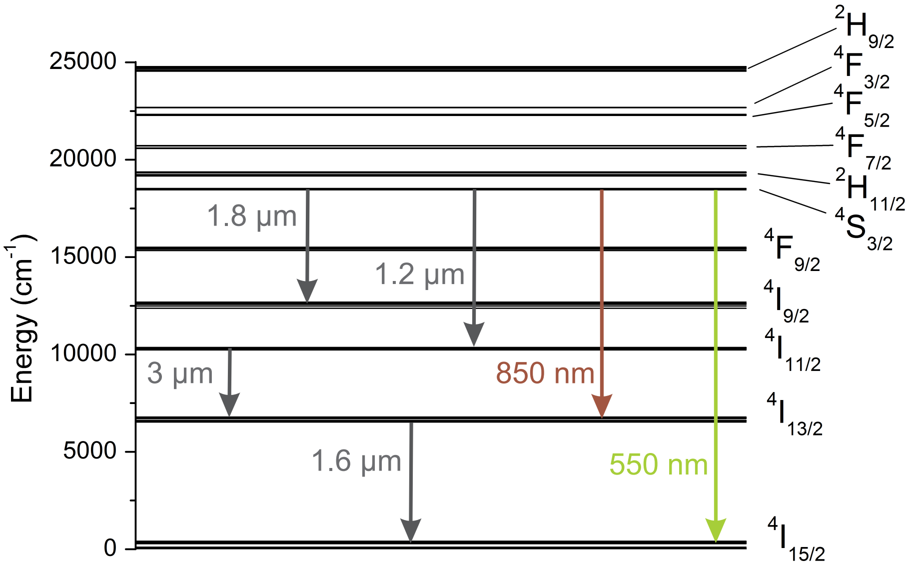

Figure 4.1: Er^{3+}:BaY$_2$F$_8$ level scheme and possible laser transitions [Bar05].

4.2 Er^{3+}-doped fluorides as optically active materials

This section represents a summary of the features of Er^{3+}:fluorides as laser emitters at different wavelengths.

Due to the complex energy level scheme which characterizes it, the Er^{3+}-ion is capable of a big variety of transitions which can satisfy many different requests in terms of applications. The most successful lasers, possible to be realized at room temperature, will be shortly introduced and they are represented in Fig. 4.1.

Starting from the mid-IR region, the longest wavelength which erbium can support as a laser transition is around 3 µm. The respective transition is $^4I_{11/2} \longrightarrow {}^4I_{13/2}$. In order to realize a four-level laser, the emitting level can be directly pumped at around 970 nm, via well-available semiconductor pump sources. A problem that can occur is a failure in obtaining a true cw-behavior, considering that generally the lifetime of the final level is more than double of the one of the emitting level (i. e. ∼10 ms and 4 ms in fluoride hosts). A way to overcome this inconvenience is to enhance transitions which depopulate the final level. It has been proven [Jen96, Li12] that a relatively high doping concentration promotes the upconversion process $^4I_{13/2} + {}^4I_{13/2} \longrightarrow {}^4I_{15/2} + {}^4I_{9/2}$, shortening the $^4I_{13/2}$-lifetime. At the same time, it quenches a detrimental upconversion of the pump wavelength up to the $^4S_{3/2}$-manifold. In this way, efficiencies higher than the quantum limit are reachable, in a true cw-operation. Although thermal issues can be more detrimental than in other laser transitions, fluoride crystals, especially LiYF$_4$, are widely used in 3-µm lasers [Kin87, Jen96].

The following shorter-wavelength emission which can be obtained with Er^{3+}-ion in laser operation, but not as much pursued as the previous one, is the 1.7 - 1.8 µm [Bar86]. The involved transition is $^4S_{3/2} \longrightarrow {}^4I_{9/2}$ and the hardest problem concerns the competition with the other possible ones, as well starting from $^4S_{3/2}$-manifold, but emitting at shorter wavelengths.

Another transition which has been widely studied for laser development, especially in fibers [Gil91], is $^4I_{13/2} \longrightarrow {}^4I_{15/2}$, at 1.5 - 1.6 µm. A pioneering technique which has been frequently applied in order to pump efficiently Er^{3+}-ions, especially in this spectral range, is codoping with Yb^{3+}-ions. Depending on the host, ytterbium can absorb in the range of 915-980 nm, where semiconductor diodes are well available, and transfer the energy to erbium [Sok00]. Nevertheless, power scaling is limited by the transfer efficiency and by the presence of residual 1-µm emission of which Yb^{3+}-ions are responsible, limiting the usual eye-safety of the 1.5-µm radiation. In singly-doped erbium materials, the transfer process is avoided and diode lasers at around 970 nm can still be implemented. However, as already mentioned, this pump process suffers from upconversion to higher levels. Furthermore, it has a high quantum defect which limits severely the efficiency and the power-scaling possibilities and increases the thermal load [Qui91].

The quantum defect is lower when resonant inband-pumping is applied. Nowadays, with the advent of powerful fiber lasers and novel diode systems based on InGaAsP/InP, the $^4I_{13/2}$-manifold can be directly pumped [Bra11b, Gar05]. When laser operation is performed in crystalline hosts, the aim of power scalability favors the choice of oxides, due to their advantageous stronger crystal field in quasi-three-level transitions. Nonetheless, fluorides have been also investigated [Sch93] and can be suitable for q-switched operation, because of the longer lifetime of the $^4I_{13/2}$- manifold, enabling the material to store a greater amount of energy.

At even shorter wavelengths, a second transition emitted by $^4S_{3/2}$-manifold has to be considered. It is characterized by a wavelength of 1.2 µm, and the $^4I_{11/2}$- manifold as terminating level. Compared to the other transitions starting from the $^4S_{3/2}$- manifold, the one at 1.2 µm has low emission cross sections and in laser operation it has the limitation of a ten-times longer lifetime of the final level with respect to the emitting one, compromising the true cw operation. In order to pump the emitting manifold, upconversion excitation schemes have been proposed [Pol89], but the most efficient pump involves Yb^{3+}-codoping. It implies an energy transfer process in upconversion which simultaneously depletes the $^4I_{11/2}$-level of erbium, allowing cw operation at 1.234 µm [Heu96]. Considering the higher efficiency of upconversion pumping of the $^4S_{3/2}$-manifold, this transition is more conveniently studied in fluoride crystals. For the same reason, also the Er^{3+}-emissions at 550 nm and at 850 nm are mainly studied in fluoride hosts and they are described in Sect. 2.4, and Chap. 6.

4.3 Investigated crystals

This work is focused on emitting processes involving upconversion of infrared into green light in Er^{3+}-doped crystals. Only some hosts allow this process, in particular those in which the intermediate manifold $^4I_{11/2}$ features a sufficiently long lifetime.

As already mentioned in Chap. 2, phonons are the main source of non-radiative depopulation of manifolds in rare-earth-doped crystals. In this work only fluoride hosts are considered because of their intrinsic low phonon energy.

Furthermore, it is important to maintain a relatively long lifetime of the green emitting level $^4S_{3/2}$: when the doping concentration is high, cross-relaxation and energy transfer processes become more probable and frequent, depleting quickly this manifold. It has been proven that when the lifetime of the $^4S_{3/2}$ state is around 400 µs, the best compromise between the efficiency of the upconversion process and the cross sections of ground-state and excited-state absorptions is reached [Heu02a, Sch04, Heu06].

Finally, typically the reabsorption process is not to be excluded in ground-state lasers, supported by an absorption cross section different than zero at the laser wavelength (see Chap. 2, [Hei94]).

As a consequence, the optimal erbium doping concentration level is around 1 at. %, the one featured by most of the crystals presented in this work.

Although in the easiest double-step upconversion pumping the wavelengths allowing for the first and second step might be different (i. e. [Sil87, McF88, Heb92]), the main advantage of most erbium-doped fluoride crystals is the possibility of being pumped by a single source emitting close to 970 nm and lase in the green spectral range, even at room temperature [Whi91, McF91, Heu02b].

A more precise motivation for the choice and a detailed description of the crystalline hosts which fulfill the previous requirements is reported in the following.

4.3.1 Lithium-lutetium fluoride - $LiLuF_4$

$LiLuF_4$ is a well-known crystal for laser applications (e. g. [Heu06, Liu08, Sto12] and references therein) and it is isomorphic to yttrium-lutetium fluoride ($LiYF_4$).

$LiLuF_4$ has an uniaxial tetragonal structure like $LiYF_4$ which is represented in Fig. 4.2a. The optic axis corresponds to the **c**-axis. The volume of the fundamental cell V_{cell} is also reported in the picture. For further details about the crystallographic and optical classification, see App. C.

$LiLuF_4$ shares some qualities with $LiYF_4$, but also shows advantages which distinguish the two structures. A few of their technical characteristics in comparison with other hosts are summarized in Tab. B.1.

The first property which favors $LiLuF_4$ regards the crystal growth. During the growing process, more precautions must be taken for a fluoride more than an oxide and some restraints are present (as explained in Chap. 3). A further complication which affects the growth of $LiYF_4$ crystals is having an *incongruent* melting behavior.

In the literature, two different interpretations of the crystal growth of $LiYF_4$ are present: one considers the growth eutectic [Pas75b, Abe76, Ben01, San12], while the second peritectic [Tho61, Gab68, Sha69, Uhr77, Pol80, Sha91, Lar03]. The letter interpretation is the one represented via the phase diagram in Fig. 4.2b, where an extra-amount of LiF in the melt is needed in order to have a sole crystallization of $LiYF_4$, without inclusions of solidified YF_3. This means that the composition of the crystal does not correspond to the one of the melt.

On the other hand, $LiLuF_4$ shows an *eutectic* behavior (see Fig. 4.2c, where the melt composition can be stoichiometric. An extra-amount of LiF is needed to compensate the fraction which is lost via evaporation during the growth, due to its higher vapor pressure

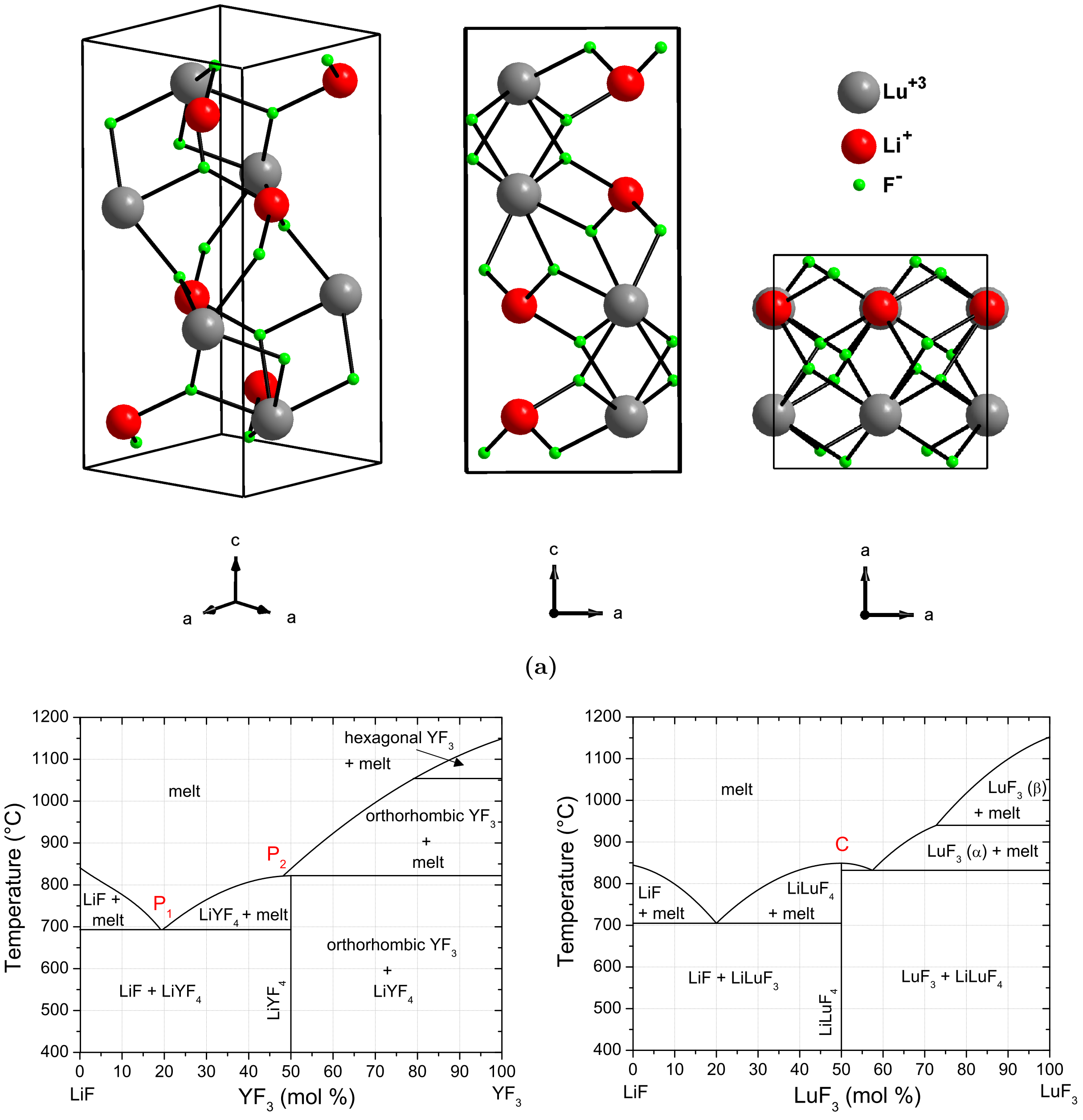

(a)

(b) (c)

Figure 4.2: (a) Three different views of the structure of $LiLuF_4$, depending on the orientation of **a**- and **c**-axis. $V_{cell} = 286.43$ Å^3 [Gar93]. (b) Phase diagram of $LiYF_4$ showing that an extra-quantity of LiF is needed to grow $LiYF_4$ at the peritectic point P_2. P_1 is the eutectic point, at 19 mol % YF_3 [Tho61, Pol80]. (c) Phase diagram of $LiLuF_4$: it grows at the monotectic point C [Har83, Ric08].

compared to LuF_3 [Jan97, Ben04, San05]. This results in an advantage in growing $LiLuF_4$ rather than $LiYF_4$.

Further difficulties regarding the crystal growth of $LiYF_4$ are reported, illustrating the advantageous growth properties of $LiLuF_4$. For example, *Harris et al.* [Har83] specify seeding problems of the growth of $LiYF_4$. Difficulties in obtaining large boules, avoiding cracks or supercooling phenomena can also be a major obstacle [Jon75, Rog97]. Typically, a precise estimation of the necessary amount of LiF in the melt and the use of highly purified starting materials and atmosphere contribute in the reduction of these risks during the growth.

Furthermore, *Cockayne et al.* [Coc81] verified also a higher mechanical hardness in $LiLuF_4$, rendering it easier to polish, compared to $LiYF_4$. Moreover, a lower difference in the thermal conductivity and thermal expansion along each of the crystal axes characterizes $LiLuF_4$, with respect to $LiYF_4$, with an advantage in homogeneity as response to heat [Agg05]. In general, higher crystal quality, expected for $LiLuF_4$ crystals, implies higher resistance to laser-induced damage (e. g. [Bar98]).

An example of Er^{3+}:$LiLuF_4$ boule grown in the framework of this thesis is depicted in Fig. 4.3.

A fundamental difference derived from including either Y^{3+} or Lu^{3+}, lies on the consequent variations of the induced crystal field. The effective ionic radius of Lu^{3+} is shorter than the one of Y^{3+}. This results in a stronger crystal field in $LiLuF_4$, inducing a larger Stark splitting in a given manifold. Thus, in the case of ground-state lasers, a lower thermal population of the laser terminating level is expected, together with a better performance of the laser.

The differences between the two hosts become more specific when they are doped with different rare-earth ions, depending on the application they are implied for.

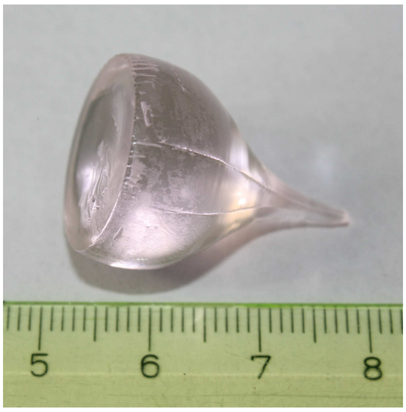

Figure 4.3: 1.3% Er^{3+}:$LiLuF_4$,G in Tab. A.1.

When pumping schemes in the UV spectral range are involved, Ce^{3+} can be used as doping ion. It has been proven (e. g. [Lim88, Dub94, Sar95, Niz07]) that Ce^{3+}-doped $LiYF_4$ compared to $LiLuF_4$ has a higher tendency to *solarize*, which means to experience stepwise multiphoton ionization by intense UV pumping. An explanation for the occurring of solarization at higher energies for $LiLuF_4$ compared to $LiYF_4$ is the broader band gap of the first (11.5 eV) compared to the second one (10 eV) [Lar03]. This depends on the fact that in isomorphs the 4f-ground-states of rare-earth dopants tend to be at the same energy above the top of the valence band. Furthermore, the stronger splitting verified in Lu^{3+}-based crystals is amplified in levels belonging to the 5d configuration, which are only slightly shielded from the crystal field influence, compared to 4f-levels. In Er^{3+}-doped crystals, this results in a shift to longer wavelength of absorption and emission spectrum and to an increase of the cross sections at the typical pumping wavelengths. In this way a $LiLuF_4$ crystal can be enriched with lower doping concentrations, in comparison to $LiYF_4$, reducing the photochemical instability in terms of probability of color centers formation.

Different theoretical and experimental works [Fil94, Jan97, Ben01, Wal04] have demonstrated that improvements are obtained in substituting $LiYF_4$ with $LiLuF_4$ as host material also when they are codoped with Ho^{3+} and Tm^{3+}. When laser oscillation at 2.06 µm is stimulated, Tm,Ho:$LiLuF_4$ shows a lower threshold and a better slope efficiency than Tm:Ho:$LiYF_4$.

The consequences of choosing $LiLuF_4$ instead of $LiYF_4$ as host crystal have a major role for this work when the doping ion is erbium. The advantage on the thermal population when the Stark splitting is larger for both emitting and ground multiplet is present also in Er^{3+}:$LiLuF_4$ compared to Er^{3+}:$LiYF_4$ [Sch04].

Furthermore, the aptitude of these hosts for upconversion lasers focuses the attention on their characteristic phonon energy. The larger mass of lutetium- compared to yttrium-ions contributes to a lower phonon energy for $LiLuF_4$ ($E_{\text{phonon cut-off}} < 430\ \text{cm}^{-1}$ instead of $E_{\text{phonon cut-off}} = 458\ \text{cm}^{-1}$ [Sal97]). A higher phonon energy possibly causes a shortening of the lifetimes of the laser emitting level. At room temperature, in the case of 1%Er:$LiLuF_4$ and 1%Er:$LiYF_4$, the lifetime of $^4S_{3/2}$ is 30 µs shorter in $LiYF_4$ (370 instead of 400 µs [Heu02a]). Moreover, the long lifetime of the intermediate $^4I_{11/2}$-multiplet needed in the upconversion process is more efficiently preserved when the phonon energy of the host material is low. Finally, $LiLuF_4$ profits also by its characteristic GSA and fluorescence cross sections, both higher than in $LiYF_4$ [Sch04, Heu02b].

Nevertheless, a possible disadvantage of $LiLuF_4$ compared to $LiYF_4$ is the higher cost of LuF_3 compared to YF_3. Furthermore, the smaller radius of Lu^{3+} can occasionally disturb its replacement with other rare-earth doping ions with a larger radius, limiting the segregation coefficient. This is not the case for Er^{3+}-ions, having in 8-fold coordination an ionic radius only 0.03 Å longer than Lu^{3+}-ions (1.14 Å instead of 1.11 Å [Kam90a]).

Crystal growth of Er^{3+}:$LiLuF_4$ boules

Eleven boules of $LiLuF_4$ have been successfully grown in the framework of this thesis. Ten of them were Er^{3+}-doped, with a concentration in the melt between 1 at. % and 1.3 at. %; only one was an undoped boule. Data about all the boules which have been grown are summarized in Tab. A.1.

The aim of this series of crystal growths was the determination of the optimal set of parameters concerning:

- the ratio of the components to be molten,
- the composition of the atmosphere in the chamber during the growth,
- the quality of the vacuum which could be reached after the pre-growth evacuation,
- the influence of adopting a seed crystal.

The weight of starting material was always ∼ 60 g, following the reaction:

$$LiF + LuF_3 \longrightarrow LiLuF_4. \tag{4.1}$$

The parameters regarding the pulling process itself have not been varied. Previous experience with fluoride crystal growth of fluorides has been considered as a reference [Ton10]. On account of this, the rotation speed and the pulling velocity have been kept 5 rpm and 0.5 mm/h, respectively, although further experiences claim the possibility of a faster pulling for such materials (e. g. [Ric08]).

The post-pulling cooling time needs to be long enough to avoid sudden drops of temperature which could lead to fractures in the grown crystal. On this purpose, the average cooling rate has been always slower than 35 °C/h, but also faster than 16 °C/h, which means the cooling period was always between 24 and 50 h. It has been shown with the last grown $LiLuF_4$ boule (K, in Tab. A.1) that a cooling rate above 100 °C/h causes fractures in the crystal, which prevents from obtaining large samples. It is also important to remind that the cooling rate can be defined only as an average value, because the cooling process could not be driven by a temperature decline, but by a power decline of the generator. The temperature has approximately a linear behavior with respect to the generator power at low power, but it relaxes to a much slower increase at higher power. The behavior is dependent on the insulation in the chamber (see Chap. 3).

The crystal growth experiments revealed that a seed crystal is not essential. When the quality of the raw materials is high, the amount of CF_4 in the atmosphere can be less then 100% and a further addition of HF is not strictly necessary. An efficient compromise in the gas mixture composition is 40% of CF_4 in a neutral gas (argon or nitrogen), as demonstrated in the growth of other types of fluoride crystals (see App. B.1). A dynamic atmosphere is not mandatory during the whole growth process, but a few hours of gas flowing, while reaching the melting point, is recommendable to decrease the unavoidable content of moisture and oxygen in the chamber. An extra amount of LiF in the starting material ensures that evaporation losses are not detrimental for the growth process.

4.3.2 Lanthanum fluoride - LaF_3

Another crystal which has very promising characteristics for upconversion processes is LaF_3. Most interesting is its particularly low phonon energy, having its cut-off at 340 cm^{-1} [Yen64, Buc96], the lowest one among all the crystals investigated in this work. This low phonon energy has a positive influence in maintaining the metastability of the $^4I_{13/2}$-manifold, needed for erbium-upconversion lasers.

Starting already in the 1920s [Oft29], a long scientific debate took place in order to verify the real structure of LaF_3 [Man64, Cas64, deR66, Tho66, Gre83, Max85, Zal85]. The solution chosen as most reliable to this question is a slightly distorted version (twinning model [Udo08]) of the centrosymmetric system $P\bar{3}c1$, called tysonite. It can be optically treated as a hexagonal structure, which also means uniaxial, with the **c**-axis corresponding to the optic axis. Three possible visualizations of the structure are depicted in Fig. 4.4.

Interest for Er^{3+}:LaF_3 arose in the early 1960s, when *Krupke and Gruber* performed spectroscopy and laser experiments at 1.6 µm [Kru63, Kru64]. A few years later, the contribution of *Weber* concerning spectroscopy and non-radiative decay had been published [Web67b, Web67a]. With Pr^{3+}-doping, stimulated emission in the green spectral range was already shown in 1963 [Sol63]. Further spectroscopy studies have been pursued concerning almost all the lanthanides as doping ion, with particular attention paid for Ce^{3+}, Nd^{3+} and Tm^{3+} (e. g. [Asa66, Eli73, Hea76, Yan76, Yan78]). Laser emission could be also reached in Ce^{3+}: and Nd^{3+}:LaF_3 [Ehr80, Way85, Fan89].

A further main feature of this host material and partially a consequence of the ex-

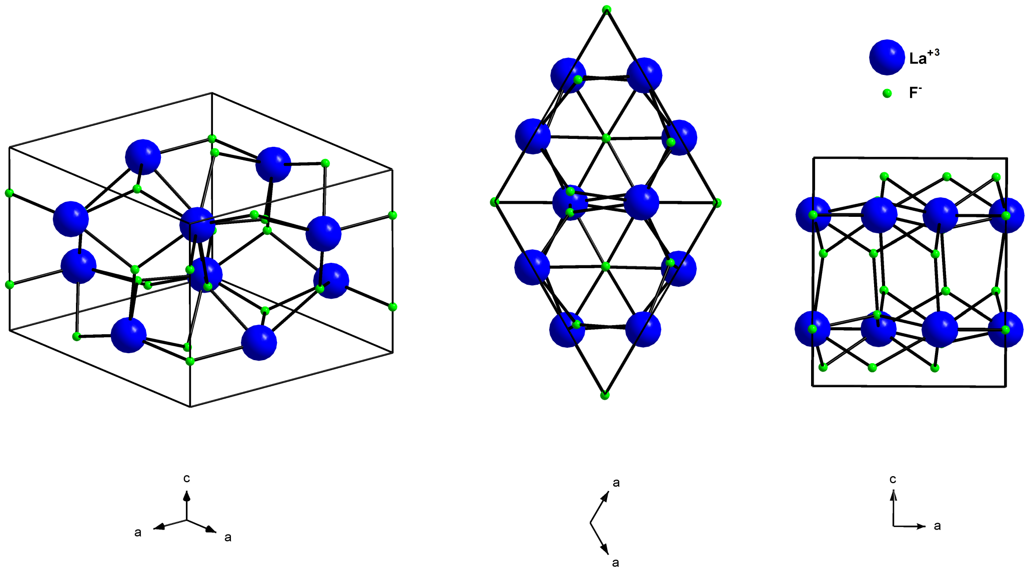

Figure 4.4: Three different visualizations of the structure of LaF_3, depending on the orientation of **a**- and **c**-axis. $V_{cell} = 329.26\,Å^3$, if the trigonal unit is considered (six formula units per fundamental cell) [Udo08].

tremely low phonon energy, is a very wide transparency, corresponding to 0.18 - 12 µm [Moo66]. Also a strong Stark splitting has been recognized as typical of rare-earth doped LaF_3 crystals [Kum04].

Moreover, absorption and emission spectral features of most of rare-earth-doped LaF_3 have a characteristic broadness which typically does not feature 4f-4f transitions. This is due to large amplitude thermal vibrations. La^{3+} has a relatively long ionic radius and when it is replaced by typically smaller rare-earth ions, they can suffer from wide oscillations around the equilibrium position, giving rise to a stronger interaction with the crystal field, a broadening of emission or absorption peaks and general smoothing of the spectra [Som73, Buc96]. Due to its particularly short ionic radius, Er^{3+} shows prominently this effect in LaF_3. A sufficient broadness of the emission spectra renders the laser material promising for wavelength tuning or short-pulses generation.

As already clarified in Chap. 3, suitable parameters for an efficient Czochralski crystal growth of LaF_3 have not been determined, yet. After the solution of the initial problem of the comparatively high melting temperature of ∼ 1490 °C using a different insulation in the chamber, the evaporation process which starts in the proximity of the melting temperature remains still a major issue. Although different attempts have been performed to obtain a single crystal boule via Czochralski growth, due to this evaporation process, none was successful. The usual procedure is based on the seedless cooling down method, with a a particular attention paid for the cooling rate and strategy.

In the framework of this thesis, in total five different growth processes of Er^{3+}:LaF_3 have been initiated and details can be found in Tab. A.3. All involved ∼ 60 g of raw materials, which means powder of LaF_3 with a proportioned quantity of ErF_3. The crucible has always been refilled two times per growth. The first crystal growth L was necessary to obtain samples for spectroscopy and laser experiments, via pure seedless cooling down method. The static atmosphere contained 15% of CF_4 in argon and the average cooling rate was ∼ 18 °C/h, performed in a single ramp. The following Czochralski growth processes represented attempts to avoid the evaporation. After the failure of contacting and pulling either with a wire (iridium) or with a seed crystal, the Nacken-Kyropoulos technique and the seedless cooling down method have been applied.

In order to increase the size of the crystalline samples, the cooling ramp has been split in two different regimes: one particularly slow ramp across the solidification temperature region and a faster ramp down to room temperature. For the last growth attempt P (see Tab. A.3), a first very slow ramp between 1 and 2 °C/h was necessary to overcome the crystallization temperature range of $\Delta T \sim$ 60 °C, around 1490 °C. After the crystallization has taken place, the cooling could be accelerated up to ∼ 35 °C/h, in order to reach room temperature in roughly 40 h.

Unfortunately, prolonging the duration of the apparatus at very high temperatures in contact with CF_4 has detrimental effects. The elements which suffer the most are the carbon crucibles. They typically can be implied only for one growth and a large amount of carbon powder is deposited on the surface of the melt. A solution to remove at least this source of inclusions would be substituting the crucibles with expensive iridium crucibles. From the experience arisen also with Pr^{3+}- and Ho^{3+}-doped LaF_3 [Rei12b, Rei12a], the seedless cooling down method has lately given improved results, in terms of size and quality of crystal samples, applying a slow cooling ramp slower than 1 °C/h.

Crystal growth processes

Figure 4.5: 0.6% Er:LaF_3 sample belonging to L (see Tab. A.3).

It has been shown that Ho^{3+}- and Er^{3+}-doped crystals can hardly show a better quality than those doped with Pr^{3+}, due to the size of the ions. If the effective ionic radii are compared (for the simplicity of traceability of data [Kam90a] in 8-fold coordination, instead of the real 9-fold coordination in LaF_3) Pr^{3+} has a very similar size compared to La^{3+}: 1.28 Å effective radius, instead of 1.32 Å. On the contrary, Er^{3+} and Ho^{3+} exhibit respectively 1.14 Åand 1.16 Å as effective radius. As previously clarified, the difference of almost 15% implies pronounced broadness and smoothness of the spectroscopic spectra of LaF_3 crystals doped with these ions. Furthermore, a very low segregation coefficient and a general difficulty in building the crystalline LaF_3 structure can be recognized. As a proof of this, in the literature crystal growths of large boules of LaF_3 are more frequently reported when the crystal is doped with large ions, like Nd^{3+} or Eu^{2+} and Ca^{2+}, with 1.26 Å, 1.39 Åand 1.26 Å, respectively as effective ionic radius, in 8-fold coordination [Fuk10, Shi04, Kam90a, Kru64]. During the seedless cooling down method, the strong tendency of fragmentation and the inhomogeneous distribution of doping ions in the crystals render difficult to establish a rule for the ability in ions segregation. Nevertheless, two of the samples extracted from the process L are much less doped then the nominal doping concentration, namely 0.6% and 0.4%, instead of 1.3% of Er^{3+}-ions and these data confirm the intrinsic solubility limit of Er^{3+} in LaF_3 of 1% measured by *Jones and Shand* [Jon68]. The first of the two samples is depicted in Fig. 4.5.

Further improvements for the optimization of the crystal growth of LaF_3 have been identified.

One of them suggested in literature [Jon68] is the setting of an over-pressure of the atmosphere in the chamber, considerably higher than the one normally kept against oxygen flux from the outside, in order to impede evaporation of the raw materials. Unfortunately, the ILP facility does not allow an internal relative pressure higher than 3 bars. On account of this, a crystal growth attempt has been performed at a relative internal pressure of ~ 2.5 bars, which has shown a visible reduction of the quantity of the evaporated material [Rei13c].

Reduction of the evaporation can lead to the possibility of employment of a crystal seed, as in a Nacken-Kyropoulos crystal growth, and as final aim to perform a Czochralski growth.

4.3.3 Barium-yttrium fluoride - BaY_2F_8

The relevance which BaY_2F_8 has in upconversion-laser history is dictated by the fact that the first lasers ever realized in this host material were *Johnson* and *Guggenheim´*s erbium-based upconversion lasers, at the same time also first upconversion lasers ever, in the red and green spectral range, but at T = 77 K [Joh71, Joh72] . The interest for this Er^{3+}-doped crystal started even earlier [Gug69] and increased in the following 40 years,

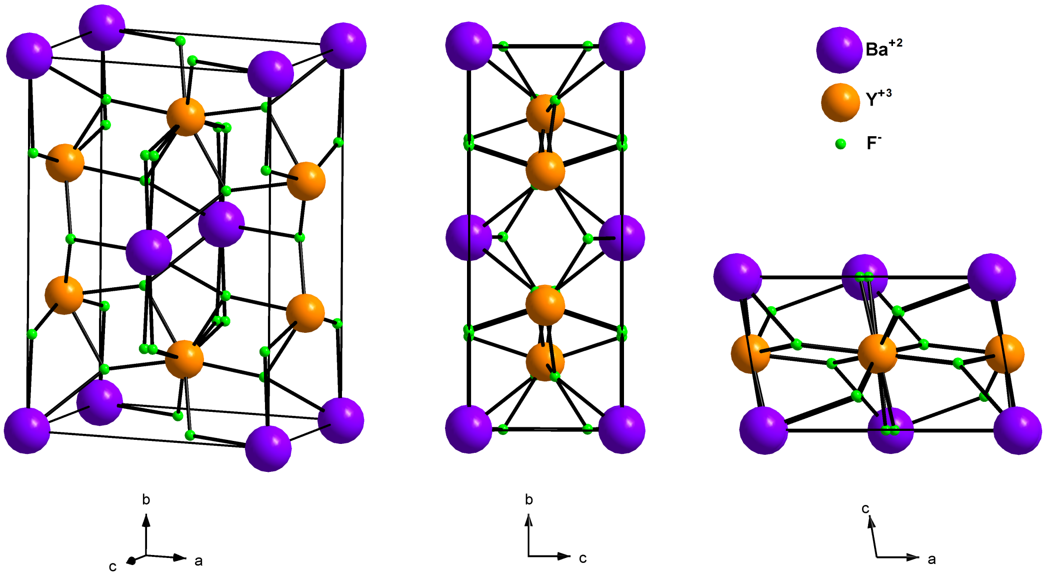

Figure 4.6: Three different views of the structure of BaY_2F_8, depending on the orientation of **a**-, **b**- and **c**-axis. In the third view the angle $\beta = 99.7°$ between **a**- and **c**- axis is evident. $V_{cell} = 308.78\,\text{Å}^3$ [Gui93].

extending from the transitions originating from the $^4S_{3/2}$-manifold to others, especially to those allowing laser emission at 1.5 µm and 3 µm [Kam90b, Pol90b, Kno92, McF94, Pol96b, Bar05, Toc07]. Interest for this host material has developed thanks to its property as scintillation and laser material, also when doped with other rare-earth ions, such as Nd^{3+} [Kam83, Kam93a, Agn04], Tm^{3+}-Ho^{3+} [Cor02] and Pr^{3+}-Yb^{3+} [Osi03b].

One of the main features which BaY_2F_8 shows compared to other laser hosts is a particularly low cut-off phonon energy of only $\sim 415\,\mathrm{cm}^{-1}$ [Kam90b, Gui93]. A low phonon energy advantages upconversion-pumped processes, especially reducing the multiphonon-decay rate of the emitting levels. This renders BaY_2F_8 more attractive than $LiYF_4$ when doped with Pr^{3+}- Yb^{3+} or Er^{3+}, for both visible and 3 µm emission [Kno92, Osi03b, Osi03a]. Specifically for green emission in Er^{3+}: BaY_2F_8, the radiative lifetime of $^4S_{3/2}$-manifold, for 1% -doping concentration, corresponds to 370 µs in $LiYF_4$ while to 630 µs in BaY_2F_8 [Kno92, Heu02a], still impressive if the cation densities are compared.

Furthermore, BaY_2F_8 can be preferable to $LiYF_4$ also when doped with other ions. For example, BaY_2F_8 shows a wide cw-tunability in the 2-µm range when doubly doped with Tm^{3+} and Ho^{3+} (89 nm) [Cor02] and in mode-locked operation [Gat07]. The tunability range has been demonstrated to be very wide also in Tm^{3+}- doped BaY_2F_8 (245 nm) for a 1.9-µm laser [Col06a, Col06b].

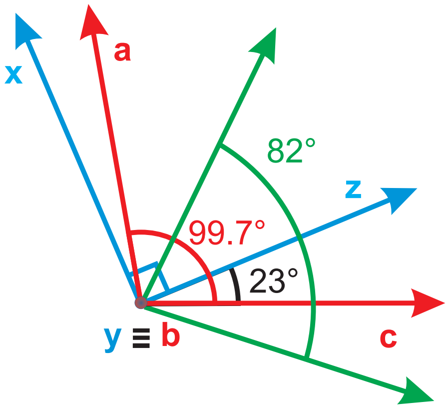

Figure 4.7: Crystallographic, refractive-index and optic axes in BaY_2F_8. The correspondence between **b**- and **y**- axes and the mismatch-angle of 23° between the first two systems are depicted [Din92, Bai11]. The optic axes are depicted in green. They are separated by roughly 82° and the **z**- axis represents the bisectrix of the angle [McA63, Gun13].

A complication which affects the work with BaY_2F_8 boules is the need of a crystal orientation due to its $C\frac{2}{m}$-monoclinic biaxial structure (see Fig. 4.6). On the other hand, the effective advantage given by biaxial crystals against thermal lensing for relatively high-power lasers still motivates to pursue research with this kind of crystals. The presence of two optic axes implies the adoption of an X-ray diffraction technique and the orientation of the different systems is depicted in Fig. 4.7. In this case the angles between the crystallographic axes are: $\alpha = \gamma = 90°$ and $\beta = 99.7°$ [Gui93]. Furthermore, the **y**- axis coincides with the **b**-axis and the angle of mismatch between the two systems of reference is 23° [Din92, Bai11]. The optic axes (green) lie in the same **x**-**z**-plane, an angle of roughly 82° separates them and the **z**- axis is the bisectrix of the angle [McA63, Gun13].

Consequently, an accurate spectroscopic analysis of rare-earth-doped BaY_2F_8 crystals requires the performance of at least three differently polarized measurements, if the refractive-index coordinate system is considered as a reference (see also Chap. 5 and App. C).

So far, with Er^{3+}:BaY_2F_8 green laser emission via infrared upconversion pumping at room temperature could not be realized, yet.

Crystal growth process

Nevertheless, in literature several problems have been notified in growing crack-free boules. One interpretation is that the high temperature which determines the creation of α-$BaLu_2F_8$ exists also for the yttrium-based crystals (see Fig. 4.8) and has to be avoided with strictly precise stoichiometric proportions of the starting materials [Kam98a]. A second explanation is connected to the anisotropy of the thermal expansion coefficients which can cause strains and tensions during the crystal growth process [Bar93, Tur11].

Only one boule of erbium-doped BaY_2F_8 has been grown in the framework of this thesis and it is depicted in Fig. 3.5 as crystal-quality-test boule. The chosen atomic doping concentration of Er^{3+} substituting Y^{3+} has been 1 at.%, in a total mass of material of 60 g, following the reaction:

$$BaF_2 + 2YF_3 \longrightarrow BaY_2F_8. \tag{4.2}$$

The crystal has been grown via Czochralski-growth and further details are summarized in Tab. A.4.

To increase the quality of the resulting crystal, the starting material has been treated with a fluorination process based on CF_4 and HF. Nevertheless, the quality test shows the presence of inclusions. A possible explanation for this is that the fluorination treatment was not sufficient to compensate the deterioration especially of BaF_2 due to a long exposure to air. Nevertheless, the progressive improvement of the quality along the crystal growth axis is a signal of the effectiveness of the fluorination process.

To rely on a high-quality oriented sample, all the spectroscopic and laser experiments have been carried out with a 1% Er^{3+}-doped BaY_2F_8 crystal grown and oriented via X-ray diffractometry (Laue method, see Sect. 5.1) at the Pisa facility.

Further attempts with the crystal growth of BaY_2F_8 at the ILP facility have not been performed, but from this single try no fundamental restraints emerged. Recommendations for a next attempt would be either using higher quality starting materials, or the performance of a more thorough fluorination. Moreover, the initiation of the crystal growth with an oriented seed would not only cause an improvement of the quality of the crystal, but for monoclinic structures it would also determine the orientation of the boule.

4.3.4 Barium-lutetium fluoride - $BaLu_2F_8$

$BaLu_2F_8$ exhibits very similar crystallographic properties compared to BaY_2F_8.

The first experiments with this material were also performed by *Johnson* and *Guggenheim* [Gug69]. While these authors claimed $BaLu_2F_8$ to be isostructural to BaY_2F_8, with only two Y-ions substituted by Lu-ions, later it has been revealed that $BaLu_2F_8$ exhibits polymorphism [Tka73, Gre81, Sob82]. Indeed, $BaLu_2F_8$ presents two different phases called α- and β-$BaLu_2F_8$ which belong to two different sets of parameters in the phase diagram during the crystal growth. As it is shown in Fig. 4.8, when 2/3 of the total amount of starting material consist of YF_3 and the rest 1/3 of BaF_2, a congruent crystal growth can start at $\sim 950\,^\circ$C. When the temperature is slowly decreased, the first encountered phase is α-$BaLu_2F_8$, which shows an orthorhombic symmetry. At $\sim 910\,^\circ$C the onset of the monoclinic β-$BaLu_2F_8$ starts and the phase is stable till room temperature.

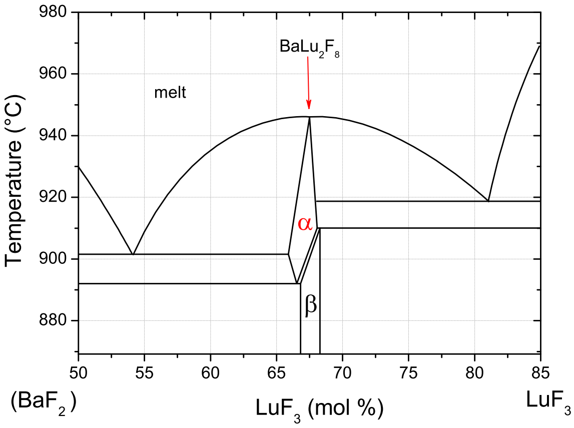

Figure 4.8: Detail of the phase diagram of BaLu$_2$F$_8$. Around the quantity-proportion of 2:1 between LuF$_3$ and BaF$_2$, in a range of almost 60 °C below the crystallization point, it is possible to obtain orthorhombic α-BaLu$_2$F$_8$. In order to freeze this symmetry, it is necessary to cool down fast (see text) to suppress the $\alpha \rightarrow \beta$ transition. Monoclinic β-BaLu$_2$F$_8$ is the phase which prevails until room temperature when a typical slow cooling ramp is initiated [Sob82, Kam98a].

Polymorphism causes problems in obtaining both the phases. When α-BaLu$_2$F$_8$ is desired, in order to freeze the phase and not incur the β-phase, it is necessary to decrease rapidly the temperature, at a minimum rate of 10°C/min [Kam98a]. This rate is clearly much faster than the recommended cooling rates in order to avoid cracks in the boule. This remains a major issue in the crystal growth of orthorhombic BaLu$_2$F$_8$. Nevertheless, the $\alpha \leftrightarrow \beta$ phase transition is detrimental also for the quality of grown monoclinic BaLu$_2$F$_8$. Fortunately, typically BaR_2F$_8$ (R =Y and all the elements between Dy and Lu in the periodic table) experiences a considerable supercooling which allows the overcome of the phase transition [Kam98a].

Unfortunately, the α-modification is metastable at room temperature and when the crystal is heated, already at ~350 °C the $\alpha \rightarrow \beta$ transition begins, together with a deterioration of the crystal [Kam98a]. This characteristic is clearly not ideal for a laser crystal.

In the past, mostly *Kaminskii et. al* were involved in research concerning BaLu$_2$F$_8$. In general, the most successful experiments have been carried out with Er^{3+}-Yb^{3+} and Er^{3+}-ions [Kam98b, Wen99], but also with Ce^{3+}- [Spi99] and Nd^{3+}- doping ions [Kam96b, Wen00]. Upconversion processes were mostly the center of interest.

In the literature, some discrepancies can be found among the sets of crystallographic data concerning the fundamental cell of α-BaLu$_2$F$_8$. Nevertheless, the most recent papers (*Kaminskii*´s series, [Bli91]) agree in confirming the presence of eight formulas per unit cell (instead of twenty-four [Gre81]). Furthermore, for α-BaLu$_2$F$_8$, the presence of two distinct rare-earth dopant sites has been confirmed for Er^{3+}- and Nd^{3+}-ions [Wen99, Wen00].

The distinction originates from the crystallographic inequivalence of two Lu^{3+}-sites. Both are located in LuF$_8$-polyhedra, which means in a configuration where a Lu-ion is surrounded by eight F-ions, like depicted in Fig. 4.9. The peculiarity is only a slight difference in the distance between Lu- and F-ions. For the so-called A-site, the Lu-F

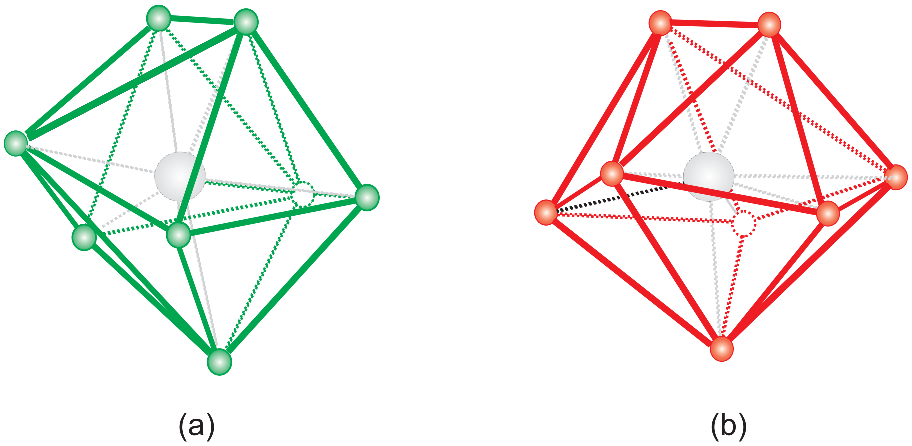

Figure 4.9: Different A- and B-LuF$_8$-polyhedra present in BaLu$_2$F$_8$ structure are depicted in (a) and (b), respectively. The black bond is the only relatively long one (+ 0.4 Å instead of ± 0.1 Å, compared to the average Lu-F-bond length) which determines the lower spherality of B-LuF$_8$ compared to A-LuF$_8$ [Kam98a].

bonds have a variation between minimum and maximum length of only 0.1 Å, while for the so-called B-site the variation is wider, corresponding to 0.4 Å. This determines a stronger approach to the spherical symmetry for the A-LuF$_8$-polyhedra compared to the B-LuF$_8$-polyhedra, although for both sites an absence of symmetry C$_1$ is valid [Kam98a].

A consequence of this discrepancy is a different and stronger Stark splitting determined by the least symmetrical polyhedron (B), when Lu^{3+}-ion is substituted by the doping ion. This was proven by *Wenger et al.* for Er^{3+}- and Nd^{3+}-doping, determining the different splitting after low-temperature spectroscopy. The results for Er^{3+}-levels are displayed in Fig. 4.10. In this case, every site determines a $(2J+1)/2$-splitting, for a total of $(2J+1)$ levels per multiplet. Consequently, it is presumed that two sites lead to twice the density of states in α-BaLu$_2$F$_8$ and possibly increase the upconversion efficiency. In [Wen99] an ETU rate[1] four times larger in Er^{3+}:BaLu$_2$F$_8$ than in Er^{3+}:LiYF$_4$ is reported.

Further advantages not strictly connected to the presence of two doping sites have been discovered concerning erbium-doped α-BaLu$_2$F$_8$. One of those is a low cut-off phonon energy corresponding to $\sim 400\,\text{cm}^{-1}$, even lower than the typical one for BaY$_2$F$_8$ ($\sim 415\,\text{cm}^{-1}$) [Kam90b, Gui93, Kam98a], convenient for upconversion processes. Nevertheless, at the same doping concentration, the radiative lifetime $\tau(^4\text{I}_{11/2})$ in Er^{3+}:BaLu$_2$F$_8$ is 20% shorter than in Er^{3+}:BaY$_2$F$_8$ [Kam98a].

Another characteristic which distinguishes α-BaLu$_2$F$_8$ from other erbium-doped hosts is a concentration quenching process starting at higher doping concentrations. The experience with Er^{3+}:LiLuF$_4$ [Heu02a, Sch04, Heu06] in laser experiments and spectroscopic data from LiYF$_4$ and BaY$_2$F$_8$ [Kno92] confirm that the optimal doping concentration is not much higher than 1%. When it is increased to a few percent, a dramatic decrease of the radiative lifetime is detected. It decreases by almost 90% for the $^4\text{S}_{3/2}$- and $^4\text{I}_{11/2}$-manifolds, due to favored non-radiative processes, such as cross-relaxation. In contrast, in the case of Er^{3+}:BaLu$_2$F$_8$, it has been shown [Wen99] that changing the erbium-doping

---

[1] Energy Transfer Upconversion, a process which is explained in detail in Chap. 2.

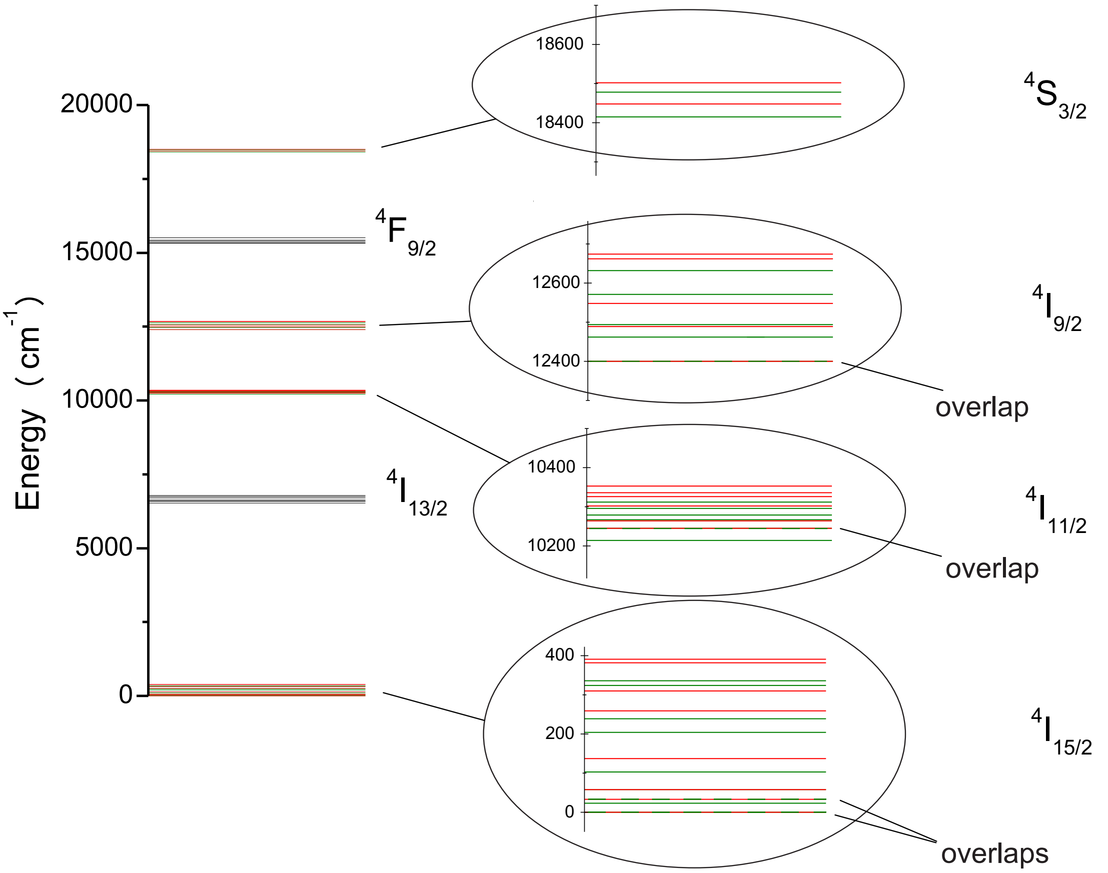

Figure 4.10: Energy level splitting caused by A- and B-site in Er^{3+}:$BaLu_2F_8$. The first six manifolds of Er^{3+} are represented. The A-site- and B-site-manifolds are depicted in green and red, respectively. They have been calculated in [Wen99] for the four most important multiplets for upconversion processes. In four cases there is an overlap between two levels belonging to the two different sites. For completeness, the $^4I_{13/2}$- and $^4F_{9/2}$-multiplets of Er^{3+}:BaY_2F_8 are reported in black [Kam90b].

concentration from 1% to 4.5% leads to a shortening of the two lifetimes of much less than 10% . Considering the relatively high incident fluence needed to reach the threshold in upconversion lasers, the possibility of increasing the doping concentration without depleting the important multiplets becomes a very appealing characteristic, even if a compensation has to be considered when the cation density in the different host materials is calculated.

It is still an open question how exactly the dynamics evolves concerning energy transfer between the two A- and B- sites, especially considering the four overlaps of levels highlighted in Fig. 4.10 [Wen99].

Crystal growth process of $BaLu_2F_8$ samples

In order to obtain samples of Er^{3+}:α-$BaLu_2F_8$, only one crystal growth attempt has been performed. As highlighted in the phase diagram in Fig. 4.8, in order to freeze the orthorhombic α-$BaLu_2F_8$ structure, it is necessary to adopt a very fast cooling rate of 10 °C/min [Kam98a]. This, starting from the melting point of ∼ 945 °C, corresponds to a cooling time of less than 100 min. This condition, connected to a failed attempt to grow a boule in the Czochralski facility, caused the growth of only very small samples, very hard to orientate. Considering the limited concentration quenching effect and the segregation coefficient for RE^{3+}-ions of ~ 0.9, a corresponding amount of 5.5% of ErF_3 has been introduced in a total of 60 g of starting BaF_2 and LuF_3 in the same proportions dictated by Eq. (4.2), with LuF_3 substituting YF_3. Nevertheless, considering the failed Czochralski-growth attempt, an EDX measurement [2] defined a presence of $(7 \pm 1)\%$ of Er^{3+}-ions in the main sample used for spectroscopic experiments.

A summary of the parameters which characterize the crystal growth attempt of Er^{3+}:$BaLu_2F_8$ is reported in Tab. A.5.

4.3.5 Barium-yttrium-lutetium fluoride - $BaYLuF_8$

$BaYLuF_8$ is a mixed structure of BaY_2F_8 and $BaLu_2F_8$, at 50%.

The aim of using a mixed host is typically to create a certain degree of disorder which can broaden absorption and emission peaks and eventually extend either the tunability range or the emission band, in order to produce short-pulses lasers. Examples of these processes with Yb^{3+}-doped crystals are reported in [Kis06, Bae09]. In the literature, comparisons of the thermomechanical properties and laser performances of different intermediate and unmixed rare-earth-doped materials can be found (e. g. Nd^{3+}-doped vanadates [Qin03]).

At the origin of the investigation of Er^{3+}:$BaYLuF_8$ is the aim of connecting the advantages and at the same time avoiding the problems that can be found either in BaY_2F_8 or $BaLu_2F_8$.

Regarding the crystal growth, the same issues explained in the Sections 4.3.3 and 4.3.4 arose.

The only reported experiments with RE^{3+}:$BaYLuF_8$ concern Ho^{3+}- [Bai11], Nd^{3+}- [Tur11], and Nd^{3+}-Tm^{3+}-doping [Pej12].

A direct comparison between Nd^{3+}- doped BaY_2F_8 and $BaYLuF_8$ could be pursued. The results confirm the possibility of $BaYLuF_8$ being grown with less risks of cracking, but no fundamental differences in the spectroscopic characteristics, when compared to Nd:BaY_2F_8 [Tur11], could be detected.

Considering phenomena such as multi-siting and delayed concentration quenching which are present in Er^{3+}-doped $BaLu_2F_8$ [Kam98a], the aim of the investigation of Er^{3+}-doped $BaYLuF_8$ is to find similar effects when 50% of LuF_3 is substituted with YF_3. Unfortunately, the previously cited papers tend to prove a stronger resemblance of $BaYLuF_8$ to the BaY_2F_8-structure, than to the one belonging to $BaLu_2F_8$. A confirmation of this can be found already at the X-ray diffraction test of an undoped sample, where the monoclinic structure with very similar cell parameters emerges [Tur11].

A further relevant investigation, already partly performed with double Nd^{3+}-Tm^{3+}-doped crystals by *Pejchal et al.* [Pej12], would be a systematic inspection of the effects of mixing in a series of $BaY_{2-x}Lu_xF_8$ crystals, with $0 < x < 2$. It is expected that at a certain value of $2 > x > 1$ the similarities of the structure to $BaLu_2F_8$ increase while the stability of BaY_2F_8 is maintained.

---

[2] Energy-Dispersive X-ray spectroscopy, performed at the facility available in Hamburg, Germany.

Together with the structure parameters, for $BaYLuF_8$ also the different orientation of crystallographic and refractive index axes has the same character as in BaY_2F_8. Consequently, the Figures 4.6 and 4.7, connected explanations and comments can be considered valid also for $BaYLuF_8$ crystals.

Although any accurate measurement of cell parameters has been performed, all the authors previously cited kept parameters belonging to BaY_2F_8 also for $BaYLuF_8$, mostly motivated by the extreme similarity of spectroscopic results.

When the hypothesis of similarity is not taken into account, it is possible to apply the so-called Vegard's approximation [Veg21]. When it has been introduced by *Vegard*, it was intended as an empirical rule which describes, at constant temperature, an existing linear variation with composition of crystal lattice parameters of a structure, when two of statistically distributed atoms or ions are one with the other continuously substituted. In literature, it is possible to find experimental confirmations of this law (e. g. $LiY_{1\text{-}x}Lu_xF_4$ [Ran02b]). Nevertheless, further experiences [Fon76, Den91, Jac07] have demonstrated that, rather than a law, it can be considered as an approximation with several conditions to be observed. For example, the mismatch between the two different ions/atoms should be less than 5% and some further modifications of the fundamental rule, often based on statistical physics principles, can extend the validity of the approximation. A typical effect which confirms it is a progressive shift of the peaks in spectroscopic spectra, proportional to the composition.

In the case of the sequence BaY_2F_8- $BaY_{2\text{-}x}Lu_xF_8$ - $BaLu_2F_8$, the mismatch of the Y^{3+} and Lu^{3+} radius is $\sim 4.3\%$ and it seems the Vegard's approximation is applicable. In this way, if lattice parameters of BaY_2F_8 and $BaLu_2F_8$ are considered as two empirical points, a linear intrapolation individuates the expected parameters for a certain $BaY_{2\text{-}x}Lu_xF_8$. The case taken into account is $BaYLuF_8$ with $x = 1$. Considering the low availability of data concerning β-$BaLu_2F_8$, the parameters in use in the approximation are taken from [Gre81], although it is defined that the unit fundamental cell contains six $BaLu_2F_8$-units, instead of the expected two. The most reliable data for BaY_2F_8 have been measured by *Kaminskii et al.* (e.g. [Kam98a]) and were used in the calculation.

Nevertheless, some observations have to be made. It has been verified that the structure of α-$BaLu_2F_8$ is completely different from the one of BaY_2F_8 and $BaYLuF_8$, and this implies the choice of parameters concerning β-$BaLu_2F_8$, also monoclinic, to be the most appropriate one. Moreover, the real expected shift of the peaks in spectroscopic spectra, such as absorption and fluorescence measurements, has not been proven for RE^{3+}:$BaYLuF_8$ in the previously cited papers. Finally, it is confirmed that $BaLu_2F_8$ has a larger unit cell containing eight instead of two molecules, like in BaY_2F_8. This suggests the probability of a sudden change of structure for a certain x in the formula, for $1 < x < 2$ which renders the Vegard's approximation not anymore valid.

In conclusion, in this work the results of the Vegard's approximation have been used for the definition of the possible cell parameters and consequently for the calculation of the density of cations, as summarized in Tab. B.1. This affects the calculation of absorption cross sections present in Chap. 5.

Samples of Er^{3+}:$BaYLuF_8$ involved in this work

At the ILP facility no $BaYLuF_8$-boules have been grown.

The spectroscopic measurements and laser experiments have been carried out with one 0.5%-erbium-doped $BaYLuF_8$ sample grown by *AC Materials* at the USA facility and one 1.3%-erbium-doped $BaYLuF_8$ sample grown at the Pisa facility. Further information concerning these two crystals is summarized in Tab. A.6.

4.3.6 Potassium-yttrium fluoride - KY_3F_{10}

The group of crystals derived from the system KF-YF_3 contains five members. The orthorhombic K_2YF_5 and the monoclinic K_3YF_6 and K_2YF_7 have been very seldom considered (e. g. [Car74, Dub90, Gus06]). The one which had the most success so far, especially in the last twenty years, is KYF_4. Its most efficient application is as 2-µm-laser host for Tm^{3+}- Ho^{3+} thanks to the broad tunability it makes possible [Mar03, Gal04a, Gal04b]. Moreover, this host has been recognized as efficient upconverter for visible emission when doped with Er^{3+} and it shows multi-siting similar to Er^{3+}:α- $BaLu_2F_8$ [Bou99, Yin02, Par10]. Furthermore, Er^{3+}:KYF_4 can lase in the 3-µm spectral range [Die98] and remarkably, it has been, together with Er^{3+}: $LiYF_4$ and YAG, the first crystal showing upconversion-pumped laser green emission at room temperature [Bre93b]. However, the crystal growth of boules of KYF_4 can be problematic, due to its incongruent-peritectic aptitude. Furthermore, researchers do not yet agree about the definition of its trigonal structure, being either disordered, or ordered but simply multisite [Syt91, LeF92, San04].

The only member of this family of crystals showing a cubic symmetry is KY_3F_{10}.

As previously mentioned, most of the attention for this host was paid in the twenty-first century. In the seventies, only spectroscopic experiments and theoretical calculations were carried out mostly by *Porcher and Caro* on Eu^{3+}-doped samples [Bor71, Por76, Por78a, Por78b, Car79] and in the eighties the first laser experiments have been performed [Abd87a]. On the whole, apart from an interesting work about samarium-doped KY_3F_{10} [Wel99, Wel00, Yam00], the most successful experiments carried out with KY_3F_{10} crystals have been those involving Tm^{3+} and Pr^{3+} as doping ions. When Tm^{3+}-ions are sensitized by Yb^{3+}-ions, it has been demonstrated that the energy-transfer efficiency in KY_3F_{10} is much higher than in other fluorides, such as BaY_2F_8 and $LiYF_4$ [Bra00]. Nevertheless, KY_3F_{10} can lase also when singly-doped with Tm^{3+}-ions [Bra01]. Although Yb^{3+}-ions are helpful sensitizers also for Pr^{3+}-doped KY_3F_{10} [Kim07], very promising results have been obtained with singly-doped Pr^{3+}:KY_3F_{10}, either in the visible or in the UV spectral range after frequency-doubling conversion [Yos05, Cam07, Ric08, Xu11, Don12]. Recently, also Ho^{3+}:KY_3F_{10} crystals have shown laser oscillation at 2 µm [Sch13].

A wide research about erbium-doped KY_3F_{10} has not yet been developed. The first pioneering experiments with Yb^{3+}-ions as sensitizers for upconversion processes date back to 1979 [Car79]. Afterwards, low- and room-temperature spectroscopy has been carried out in the eighties on singly-doped Er^{3+}:KY_3F_{10} samples [AF85, Abd87b]. More recently, some further spectroscopic experiments have been performed [Hey98, Dia03] and finally the Stark splitting diagram has been defined and an exhaustive study of the possible transitions realized [Bou06].

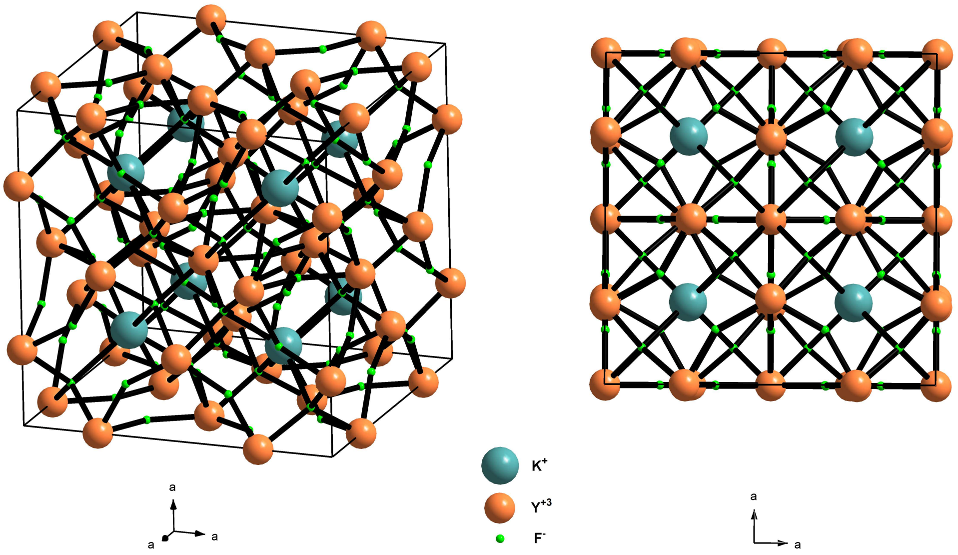

Figure 4.11: Two different views of the structure of KY_3F_{10}. It is cubic and V_{cell} = 1542.00(23) Å^3 [Grz02].

As earlier mentioned, KY_3F_{10} is the only cubic structure of the KF-YF_3 system and for this reason it has been tested as crystal host for Er^{3+}-ions in the framework of this thesis as sole example and reference in a comparison with uni- and biaxial structures. Two visualizations of the fundamental cell of KY_3F_{10} are depicted in Fig. 4.11.

The crystal growth is congruent and relatively easy because of the absence of phase transitions. The thermomechanical properties, the wide transparency and the optical damage threshold are in the range of the other fluorides considered so far in this work [Kim07]. Nevertheless, KY_3F_{10} has the advantage of a remarkably strong Stark splitting, enhancing upconversion processes and quasi-three-level laser operation [Hey98]. Furthermore, the peaks in absorption and emission spectra of RE^{3+}:KY_3F_{10} are usually broad and this can favor the resonance between ESA- and GSA-peaks in upconversion processes.

However, the evaluation of the cut-off phonon energy of KY_3F_{10} is problematic. In the literature, it is not possible to find unambiguous data, but only values which range between 380 and 602 cm^{-1} [Bra01, Mar01, Sil05, Kim07]. *Mortier et. al* are the only authors showing Raman spectra which recognize as cut-off phonon energy an amount equivalent to 495 cm^{-1} [Mor91]. Consequently, in the present work this is the value which has been considered valid. Evidently, KY_3F_{10} presents a slightly higher phonon energy than typical fluoride hosts and this could be detrimental for the stability of the intermediate manifold in upconversion processes.

Crystal growth process of KY_3F_{10}-boules

Due to the limited information concerning Er^{3+}:KY_3F_{10}, the doping concentration in the melt which has been chosen for the crystal growth is based on data related to Er^{3+}:KYF_4. Considering the disordered/multisite and trigonal nature of KYF_4, the differences compared to KY_3F_{10} are expected to be high. Nevertheless, information about Er^{3+}:KYF_4 can be still meaningful. The effect of the concentration quenching in Er^{3+}:KYF_4 regarding the lifetime of $^4S_{3/2}$-multiplet has not been clearly defined [Bou99, Yin02, Par10]. Evaluating the rate of reduction of green photoluminescence moving from low to room temperature and the lifetime measurements for high erbium-concentrations at low temperatures, it is possible to extrapolate a probable reduced strength of the concentration quenching phenomenon in this host crystal. For this reason, the only attempt of growth of an Er^{3+}:KY_3F_{10} boule has been performed adding the equivalent of 2 at.% of ErF_3 to an amount of YF_3 and KF following the reaction:

$$KF + 3YF_3 \longrightarrow KY_3F_{10}. \tag{4.3}$$

The Czochralski-growth process has been carried out successfully in CF_4-HF atmosphere and seeded with a platinum wire. A particularly reducing atmosphere has been chosen in order to compensate the decreased quality of the KF starting material, because of a long storage. In order to reach the moderate melting temperature of 1030 °C of KY_3F_{10} [Cha93], the insulation with the double crucible system filled with carbon pellets could be adopted (see Chap. 3). For further information about the crystal growth parameters see Tab. A.7.

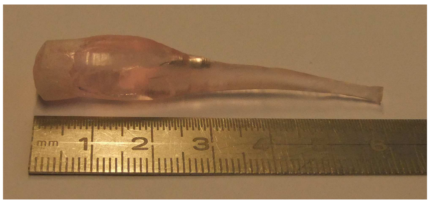

Figure 4.12: 2% Er^{3+}:KY_3F_{10} boule S in Tab. A.7.

Although the usual long cooling down rate of the boule has been implied (~ 20 °C/h), the crystal presents a certain degree of tension and stress. A picture of the boule is depicted in Fig. 4.12. The long neck is not perfectly cylindrical and with smooth surface, but it rather shows an irregular diameter and an anomalous torsion which evolves in a fracture in the central part of the boule. The quality of the neck and of the central part is fair but scattering centers are present. At the bottom the surface is opaque and the crystal quality turns worse. Samples for spectroscopic investigations could be extracted.

4.4 Further possible fluoride hosts for Er^{3+}-ions

In the framework of this thesis, other crystal hosts had been recognized as suitable for Er^{3+}-ions and upconversion laser. Unfortunately, the crystal growth attempts did not succeed and a further development of experiments has to be considered as an outlook of this work.

In the following, a brief introduction to the peculiarities of these hosts will be presented, focusing on the advantages when they are Er^{3+}-doped and the problems to be overcome during the crystal growth sessions. They have all been chosen because of a certain connection with LaF_3, in the attempt of skipping the evaporation problem during the crystal growth (see Sect. 4.3.2 and Chap. 3). Namely, they are YF_3, LuF_3 and $KLaF_4$.

Yttrium fluoride - YF_3

Apart from the crystal growth, a problem which has been encountered during the work with LaF_3 was the extremely high difference of ionic radius between Er^{3+}-ions and La^{3+}-

ions (in 8-fold coordination, $r_{La^{3+}} = 1.32\,\text{Å}$, $r_{Er^{3+}} = 1.14\,\text{Å}$ [Kam90a]). This can cause a very low segregation coefficient and a general instability also at low doping concentration, which can impede the single crystal growth.

A similar structure which offers a reduced ionic radius of the cation is YF_3 (in 8-fold coordination, $r_{Y^{3+}} = 1.16\,\text{Å}$ [Kam90a]). Furthermore, it has been recognized [Som73] that a low symmetry of the cation substituted by the rare-earth-ion weakens the parity-forbidding effect of the electric dipole 4f-4f-interaction. Consequently, this favors the efficiency of the conversion from infrared to visible light in Yb^{3+}-Er^{3+} codoped materials and it is confirmed for singly Er^{3+}-doped ones. YF_3 (and LuF_3 as well) presents a C_s point symmetry [Dor00] at the cation position, the lowest offered by the crystal hosts in the framework of this thesis.

Moreover, a detailed analysis of Gd^{3+}-doped LnF$_3$ (Ln = Y, Tb, Dy, Er, Yb, Lu, La, Ce, Pr, Nd) summarized in [Lag04] underlines the superior laser aptitude as host material of LnF$_3$ when Ln = Y, Lu, compared to Ln = La. Nevertheless, a comparative study of the three hosts in the form of polycrystalline films [Buc96] shows opposite characteristics concerning erbium-doping and photoluminescence at 1.5 µm, which means stronger Stark splitting and longer lifetime of the $^4I_{13/2}$-multiplet in Er^{3+}:LaF$_3$, when compared to Er^{3+}:YF$_3$ and Er^{3+}:LuF$_3$.

Furthermore, a thorough study of erbium-doped YF_3 [Zie70] has demonstrated a remarkable aptitude as infrared upconverter for the production of visible radiation. On this purpose, an ideal doping concentration of $\sim 1\%$ is confirmed. In this way, the ion-pairs relaxation is limited and the importance at this doping concentration of both single-ion ESA-processes and ETU can be highlighted (see Chap. 5). Although nothing similar is mentioned in [Zie70], *Sommerdijk et al.* [Som74] claimed to have demonstrated a multi-siting effect in Pr^{3+}:YF$_3$ which is not excluded to be active when erbium is embedded instead of praseodymium.

As a consequence of all the previous considerations, a crystal growth attempt of YF_3 has been carried out with a doping concentration of 1.3 at. % . In order to reach the high melting temperature of $\sim 1387\,°C$ [Sok01], the carbon-foam insulation has been used (see Chap. 3). A fluorinating flow of 40% CF_4 in nitrogen has been activated for the time needed to reach the melting point.

A complication which affects the growth of YF_3 single crystals (and of LuF_3 as well) is a phase transition which occurs at $\sim 1050\,°C$ [Tho66, Sob76, Lag04]. It is a transition from the high-temperature α-YF$_3$ hexagonal phase to the room-temperature β-YF$_3$ orthorhombic phase. Nevertheless, a boule could be pulled, as it can be seen in Fig. 4.13a, with no occurrence of evaporation processes. From an external view, the quality of the crystal cannot be defined because of the opacity of the walls and traces of carbon powder. Unfortunately, an unexpected sudden drop of current impeded the usual slow cooling down ramp and the boule has been extracted as totally polycrystalline. The starting material has been considered suitable for the crystal growth because of the low hygroscopicity of YF_3.

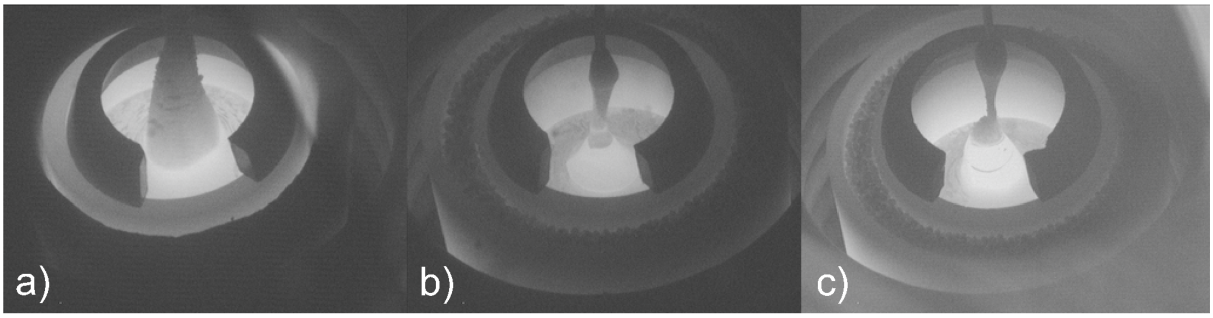

Figure 4.13: Three different Czochralski crystal growths. In a) a growing YF_3 boule is depicted; the extracted crystal was ceramic/polycrystalline. In b) a growing LuF_3 boule is represented; the crystal was not centered on the axis of rotation: the neck broke and the crystal melted in the remaining molten material. In c) a second growing LuF_3 boule is depicted; after the extraction from the chamber it was also found to be polycrystalline.

Lutetium fluoride - LuF_3

Another material of the group $Ln\mathrm{F}_3$ suitable for hosting Er^{3+}-ions is LuF_3.

In this case, some of the advantages mentioned for YF_3 are still valid, and further already considered in Sect. 4.3.1 about working with $LiLuF_4$ instead of $LiYF_4$, are once again well-grounded. The ionic radius of Lu^{3+}-ion is shorter than Y^{3+}-ion, but only of a few angstroms (in 8-fold coordination: $r_{Lu^{3+}} = 1.11\,Å$[Kam90a]) and this causes a stronger crystal-field influence on the 4f-4f-transitions and a consequent wider Stark splitting of the sublevels inside a manifold, possibly favoring quasi-three-level laser operation. Furthermore, as a rough estimation, Lu^{3+}-ions, having a higher mass, are expected to determine a lower cut-off phonon energy for LuF_3 in comparison to YF_3. Nevertheless, it is shown via polarized Raman spectra by *Lage et. al* [Lag04] that the cut-off energies are very similar and the lowest one belongs to YF_3 ($514\,\mathrm{cm}^{-1}$, instead of $528\,\mathrm{cm}^{-1}$ for LuF_3).

Two attempts of crystal growth of Er^{3+}:LuF_3 have been performed. The chosen doping concentration has been 1.3 at. % . The melting temperature is considerably lower than in YF_3 (1182 °C [Sob76] instead of 1387 °C), thus the ordinary insulation has been adopted (see Chap. 3) and it can be seen in Fig. 4.13 b, c, compared to Fig. 4.13 a. The purity of the starting material has been evaluated high enough to skip a pre-fluorination process and the crystal growths have been carried out in a static atmosphere of 40% CF_4 in nitrogen. Finally, a cooling down ramp of the boule of $\sim 15\,°\mathrm{C/h}$ has been chosen. Unfortunately, the boule was polycrystalline.

The reason of the polycrystallinity of the boules of YF_3 and LuF_3 grown in the framework of this thesis resides in the phase transition which both hosts encounter at $\sim 1050\,°\mathrm{C}$. In the growth of α-$BaLu_2F_8$ a fast cooling has been performed in order to maintain the high-temperature phase. In this case the situation is opposite: there is no interest in keeping a high-temperature hexagonal phase, and the attempt is to set the room-temperature orthorhombic phase for both the hosts. The exclusive way to maintain the monocrystallinity shown during the pulling until room temperature is reached, is to overcome completely the phase transition. In principle, this is the harder the closer the phase-transition temperature is to room temperature. Fortunately, for both hosts the phase transition happens at a relatively short temperature interval from the melting temperature.

For these reasons, the mixture of the raw materials with a third relatively low-temperature melting and non-reactive substance should decrease the overall melting temperature below the phase-transition one. This has been already tested and successfully performed by adding LiF to the raw materials [Rot93, Gue01, Lag04]. LiF represents a perfect candidate because its melting temperature is extremely low compared to YF_3 and LuF_3 (845 °C [Cac10]). The recommended proportions vary between 20% and 45% , relatively to the sum quantity of LiF and the chosen host material.

Nevertheless, the phase transition can be overcome by a flux growth [Bri73], lowering the melting point and leading to a crystallization directly in the desired phase, but that is not part of the research performed in this thesis.

Potassium-lanthanum fluoride - $KLaF_4$

This material has not been widely investigated, but in the last years its aptitudes as upconverter phosphor in nanocrystal form, when doped with Er^{3+}-or Er^{3+}-Yb^{3+}-ions, have been shown [Tya10, Ahm12, Liu12].

The crystal growth is challenging because the phase diagram presents an incongruent point and an eutectic point [Der48, TT61, Buk65, Abd97]. Additionally, the structure can be either a high-temperature cubic symmetry or a more thermodinamically stable low-temperature hexagonal symmetry [Zac48, Heb73, Tya10], although *Kodama et al.* claimed they obtained cubic crystalline samples with a slow cooling down ramp [Kod98].

From the published data, it is not clear whether the most efficient host for Er^{3+}-ions upconverted emission is either cubic or hexagonal $KLaF_4$ [Tya10, Das11, Ahm12, Liu12]. Nevertheless, the best upconversion-phosphor ever studied until now in terms of green-to-red fluorescence ratio is double Er^{3+}-Yb^{3+}-doped $NaYF_4$ [Men72, Suy05a, Mai07]. It has a similar structure, it can be grown as well in such two symmetries and it showed better performances in the hexagonal form.

Generally, $KLaF_4$ presents further advantages as host for Er^{3+}-ions. It has been recognized that it shows multi-siting [Tya10, Das11, Ahm12, Liu12] and it is expected to have a relatively low phonon energy. Nevertheless, data regarding the cut-off energy are discordant: a theoretical study estimates a value of $\sim 470\,\mathrm{cm}^{-1}$ [Gro03], while a low resolution Raman spectroscopic measurement determines a value of $383\,\mathrm{cm}^{-1}$ [Ahm12]. Furthermore, *Tyagi et al.* measured an unusual inverse concentration quenching, where the green fluorescence lifetime from the transition $^2H_{11/2} \rightarrow {}^4I_{15/2}$ increases with increasing doping concentration [Tya10].

Considering the previous information, a crystal growth attempt has been performed. The doping concentration for Er^{3+}-ions corresponded to 3 at. % in a mixture according to:

$$\mathrm{KF} + \mathrm{LaF_3} \longrightarrow \mathrm{KLaF_4}, \tag{4.4}$$

in order to reach the eutectic point in the phase diagram at about 700 °C [Der48]. The atmosphere has been maintained static and composed of 40% CF_4 in nitrogen and the ordinary double-crucible insulation has been adopted (see Chap. 3). Considered the previously mentioned advantages of the hexagonal symmetry, a slow cooling ramp of $\sim 11\,^\circ\mathrm{C/h}$

has been initiated. Unfortunately, adding KF massively reduced the crystallization temperature compared to the one of pure LaF_3, but it did not hinder its evaporation. Successively, no samples could be extracted, because the material was diffusively ceramic or polycrystalline.

A possible reason for the failure of the crystal growth attempt is the phase transition between the cubic and the hexagonal phase.

The status of the research about $KLaF_4$ single crystals suggests that near-future investigations will not go further than spectroscopic analysis of relatively low quality crystal samples.

5 Spectroscopy

The identification of an erbium-doped crystal as possible efficient upconverter of infrared light into the visible spectral range depends strictly on a detailed spectroscopic investigation.

In this chapter, GSA and emission spectra will be presented, together with ESA and gain spectra. For a few erbium-doped hosts, the behavior of the upconverted fluorescence has been analyzed in relation to the incident exciting power. For every kind of performed measurement the relevant experimental setup will be described.

5.1 Crystal orientation

Most of the host crystals investigated in this work have no cubic structure and need to be correctly oriented for polarization-dependent spectroscopy.

If the crystal is uniaxial (see App. C), white statistically polarized light and a system of two crossed polarizers is enough to determine the orientation of the **c**-axis. In this setup, the crystal is positioned between the two polarizers. The first polarizer encounters as first the unpolarized white light and allows only light vibrating parallel to the polarizing direction for passing through. The second polarizer, typically called *analyzer*, is positioned with its polarizing axis perpendicular to the axis of the first polarizer and determines the extinction of the light [Nel11]. When a crystal is positioned between the two polarizers and it is rotated along the direction of the light, the transmission of the light can change.

If the crystal is isotropic, the direction of vibration is not modified by the crystal and none of the possible crystal rotations alters the transmission of the light through the setup, corresponding to zero transmission. If the crystal is not isotropic, it shows birefringence and, depending on the position of the axes under rotation of the crystal, some light can pass through the analyzer.

If the crystal is uniaxial, when the light is passing through the crystal and its optic axis is along the direction of light, it appears isotropic and the transmission of the setup is independently on the rotation angle of the crystal holder equal to zero. When the axis is not parallel to the direction of light, it can pass the analyzer. The intensity is dependent on the rotation of the crystal.

Moreover, a conoscopic lens can give further information about the direction of the crystal axis, via the observation of the emerging interference figure, when it is positioned between the crystal and the analyzer.

When the crystal is biaxial, a mere analysis of the polarization changes of the transmitted light is usually not enough to determine precisely the position of the optic axes.

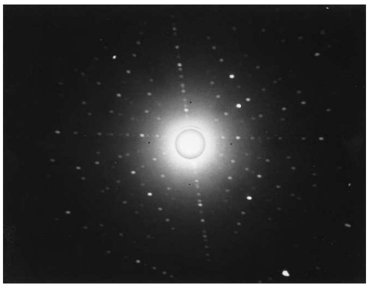

Figure 5.1: X-ray diffraction pattern of a 1% europium-doped BaY_2F_8 crystal detected via Laue technique [Mog08].

In the framework of this thesis, for an accurate orientation of the crystals, a diffractometric method based on the Laue technique has been applied. This method determines a X-ray diffraction pattern (see Fig. 5.1) depending on the symmetry of the crystal encountered by a collimated spectrally broad X-ray beam. The crystal does not need to be moved because certain wavelengths in the beam are able to satisfy the condition of constructive interference dictated by the Bragg law [Ash76].

From the facility at the ILP, a diffractometer based on the Laue technique is accessible (as courtesy of *HASYLAB*, part of the Deutsche Synchrotron, *DESY* facility). A very similar device is as well available at the laboratories in Pisa. It consists of a high voltage *HT* X-ray source *PW1830/40* and a copper tube by *Philips* in connection with a diffraction photocamera *Laue Camera 801/802* by *Huber* working in back-reflection. The maximum applicable voltage is 60 kV and the maximum current is 60 mA. The single crystal as target of the X-ray beam can be mounted on a goniometer head, which allows a positioning in space with a sensitivity of 0.1 °. Suitable applied voltage, current and X-ray exposition time vary in relation to the host material. Once a pattern is obtained (e. g. such as displayed in Fig. 5.1), the coordinates of the diffraction peaks in the wave vector reciprocal space can be used to calculate the lattice parameters in real space. Computer programs such as *Orient Express* can perform the analysis of the patterns. Typically, a few diffraction patterns observed with different orientation of the target are enough to establish the real position of the crystallographic axes in the crystal and consequently to define in which directions a sample can be cut and polished for either polarization-dependent spectroscopic or laser experiments. In this way, a sample can be oriented either in the crystallographic or in the refractive-index system (see App. C).

5.2 Absorption spectra

Transmission spectra of erbium-doped crystals have been recorded via a *Varian Cary 5000 UV-Vis-NIR* spectrophotometer, sensitive in the spectral range 175 - 3300 nm.

In order to obtain ground state absorption spectra, the Beer-Lambert law can be applied:

$$I^{\kappa}(\lambda, d) = I_0^{\kappa}(\lambda)\mathrm{e}^{-\alpha^{\kappa}(\lambda)d}, \tag{5.1}$$

where d is the thickness of the sample, $I_0^{\kappa}(\lambda)$ is the incident intensity, and $\alpha^{\kappa}(\lambda)$ is the absorption coefficient, depending on the polarization κ. Consequently:

$$\alpha^{\kappa}(\lambda) = \frac{1}{d}\ln\frac{I_0^{\kappa}(\lambda)}{I^{\kappa}(\lambda, d)}. \tag{5.2}$$

If the doping ion density n_{dop} is known, the ground state absorption cross section $\sigma_{\mathrm{GSA}}^{\kappa}(\lambda)$ can be calculated as:

$$\sigma_{\mathrm{GSA}}^{\kappa}(\lambda) = \frac{\alpha^{\kappa}(\lambda)}{n_{\mathrm{dop}}}. \tag{5.3}$$

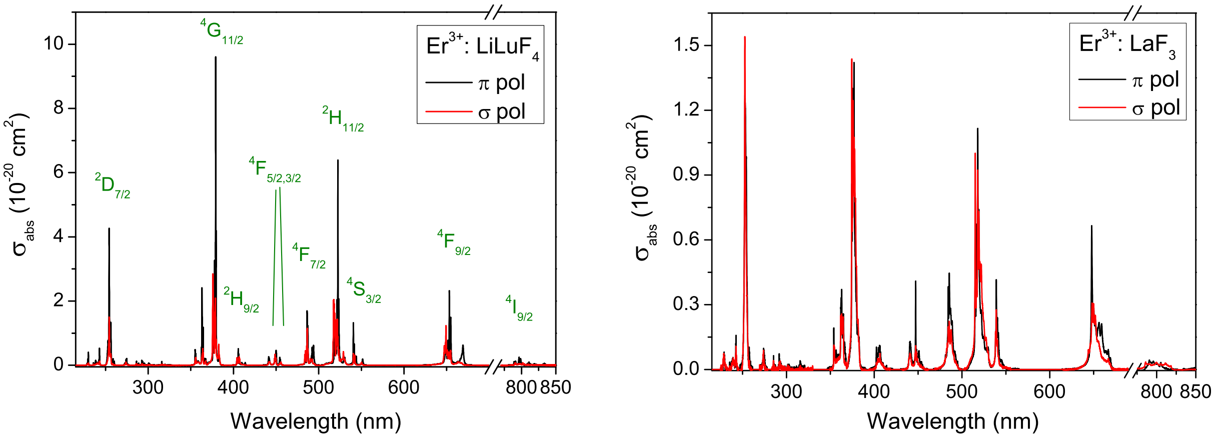

(a) (b)

Figure 5.2: Polarization-dependent absorption cross sections at room temperature of 1.25 at.% Er^{3+}:$LiLuF_4$ (a) and 0.6 at.% Er^{3+}:LaF_3 (b), in the wavelength range 215 - 850 nm. The absorption lines in this spectral range correspond to the transitions between the Er^{3+}-ion ground state $^4I_{15/2}$ and different excited states. In (a), the final energy levels of the dominant transitions are displayed [Die63, Weg00]. For a complete list of cross sections in both polarizations and involved energy levels in Er^{3+}:$LiLuF_4$, see Tab. D.1.

5.2.1 Measurement results

In the following, room-temperature polarization-dependent absorption spectra of erbium-doped crystals will be discussed. They will be sorted by the wavelength range, showing mainly the absorption cross sections in the visible spectral range and at around 970 nm to demonstrate the potential for upconversion-pumping. Additionally, absorption in the 1.5 µm spectral range has been investigated to determine the feasibility of pumping at $\lambda = 1535$ nm for the realization of a 1.6-µm laser.

Absorption spectra in the UV and visible spectral range up to 850 nm

In this section the absorption spectra recorded at room temperature in the range 215 - 850 nm are presented.

Most of the measurements have been performed with a spectral resolution of 0.15 nm. Only for Er^{3+}:LaF_3, in order to increase the signal-to-noise ratio, the resolution in the spectral range 775 - 850 nm was 0.75 nm.

Fig. 5.2a shows the absorption spectrum of Er^{3+}:$LiLuF_4$. This Er^{3+}-doped host exhibits the highest cross sections of all investigated crystals (to compare with Tab. D.1). The final energy levels for the transitions from the ground state $^4I_{15/2}$ exploiting the highest cross sections are named. As in other erbium-doped uniaxial hosts, the highest absorption cross sections are mainly in π-polarization. In $LiLuF_4$, the highest absorption peak is at $\lambda = 379.2$ nm in π-polarization, corresponding to the transition $^4I_{15/2} \rightarrow {}^4G_{11/2}$, with an absorption cross section of $9.6 \cdot 10^{-20}\,\mathrm{cm}^2$. The InGaN laser diodes available for laser experiments could be tuned via variation of the temperature to reach the highest peak of the transition $^4I_{15/2} \rightarrow {}^4F_{5/2}$ at $\lambda = 450.0$ nm. The corresponding cross section is

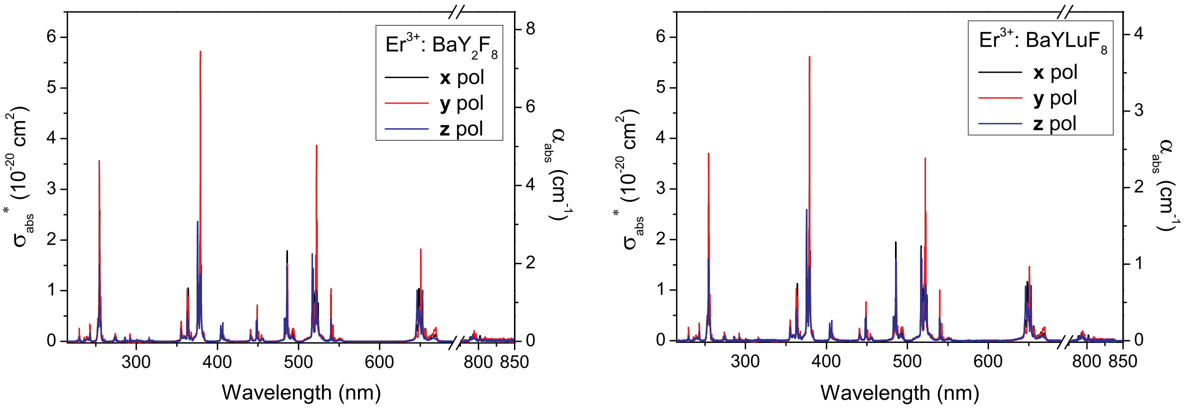

(a) **(b)**

Figure 5.3: Polarization-dependent absorption coefficients and estimated cross sections at room temperature of a 1.0%Er^{3+}:BaY_2F_8 a) and a 0.5% Er^{3+}:$BaYLuF_8$ b) in the wavelength-range 215 - 850 nm. The cross sections are limited to be an estimation (signed with $*$) strictly correlated to the employed samples due to the missing correspondence between the refractive-index-coordinate-system and the system based on the optic axes and the **y**-axis.

$0.46 \cdot 10^{-20}\,\mathrm{cm}^2$. At the operating wavelength of the available more powerful 2ω-OPSL[1] for laser experiments ($\lambda = 486.15\,\mathrm{nm}$), the absorption cross section in both polarizations is around $0.40 \cdot 10^{-20}\,\mathrm{cm}^2$.

Nevertheless, also at the typical laser emission wavelengths which have been detected during laser experiments (540.6, 551.6 and 552.6 nm, see Chap. 6), non-negligible absorption cross sections, possibly causing reabsorption losses have been measured (see Chap. 2). The corresponding cross sections are $1.3 \cdot 10^{-20}$, $0.18 \cdot 10^{-20}$ and $0.04 \cdot 10^{-20}\,\mathrm{cm}^2$, respectively.

As a direct comparison, in Fig.5.2b the absorption spectrum of Er^{3+}:LaF_3 is displayed. The superiority of π-polarization is not pronounced and the cross sections are in general four times smaller than in $LiLuF_4$. Indeed, the maximum is detected in σ-polarization at 252.6 nm, with a cross section of $1.5 \cdot 10^{-20}\,\mathrm{cm}^2$. As explained in Sect. 4.3.2, when Er^{3+}-ions substitute La^{3+}-ions in LaF_3, the transition lines are much broader than in other hosts. This line broadening partly results in lower peak cross sections, but allows for easier addressing of the emission peak of pump sources in laser experiments.

In laser experiments with a pump source in the blue spectral range, the highest absorption cross sections are addressed in π-polarization. InGaN laser diodes can be tuned to 447.2 nm, where Er^{3+}:LaF_3 has an absorption cross section peak of $0.41 \cdot 10^{-20}\,\mathrm{cm}^2$. For the available 2ω-OPSL at 486.15 nm, the absorption cross section is $0.28 \cdot 10^{-20}\,\mathrm{cm}^2$.

In Fig. 5.3 the absorption spectra of Er^{3+}:BaY_2F_8 and Er^{3+}:$BaYLuF_8$ are reported.

Unfortunately, the desired broadening of the peaks in the mixed crystal $BaYLuF_8$ for the aim of producing short-pulses lasers does not take place and the two spectra are extremely similar to each other.

As explained in App. C, monoclinic crystals are biaxial crystals where the two optic axes lie in the **x**-**z** plane perpendicular to the **y**-axis, separated by an angle $2V$ characteristic for every crystal. In the monoclinic crystals BaY_2F_8 (and probably the same or similar in

---

[1] frequency-doubled optically pumped semiconductor laser

$BaYLuF_8$), the angle $2V$ can be calculated with Eq. (C.1) and it roughly corresponds to 82° (see Chap. 4). The spectroscopic investigations on Er^{3+}:BaY_2F_8 and Er^{3+}:$BaYLuF_8$ have been performed following the refractive-index coordinates system, which means every measurement has been performed with the **E**-vector (electric field) of the light parallel to one of the three direction **x**, **y** and **z** of the indicatrix. Therefore, to describe the absorption spectrum with the Beer-Lambert equation (Eq. (5.1)) a sum of two exponential terms has to be taken into account, due to the projection on the desired axis of the contribution from both optic axes. If approximations cannot be performed, when a summation of Beer-Lambert exponential terms is involved, the result is dependent on the thickness of the crystal in every direction, rendering the absorption coefficients and the cross sections only an estimation strictly related to the analyzed sample.

Furthermore, an efficient test to prove the impact of the angle-dependency of the cross-sections is to perform always two measurements in the same polarization, having the **B**-vector (magnetic field) and the **k**-vector parallel to both the other two refractive-index axes in the two different ways. When samples of different sizes are available, it is possible to distinguish the contributions of the two components solving a differential equation system.

Nevertheless, cross sections have been estimated and it is worth to remind from Chap. 4 that the volume of the fundamental cell of $BaYLuF_8$ has been estimated from the lattice constants and calculated via the Vegard law [Veg21], keeping the same angle β and two unit formulas per cell typical of the structure of BaY_2F_8. This causes a pessimistic estimation for the absorption cross sections, if compared to the strategy of keeping the same cell parameters of BaY_2F_8. This is caused by the fact that the presence of Lu^{3+}-ions instead of Y^{3+}-ions renders the volume cell larger and therefore causes a decrease in the calculated cross sections.

The estimated cross sections in Er^{3+}:BaY_2F_8 and Er^{3+}:$BaYLuF_8$ are slightly lower than in $LiLuF_4$, but of the same order of magnitude. The highest estimated cross sections are mostly in **y**-polarization.

The displacement of the peaks between Er^{3+}:BaY_2F_8 and Er^{3+}:$BaYLuF_8$ in the significant spectral areas is either not existing or extremely low (0.05 nm, which is also the wavelength step of the measurement device) and the differences in estimated cross sections are marginal.

For the visible spectral range, a fourth polarization-dependent measurement, as twin of one of the first three, has been performed for biaxial crystal hosts. No differences have been recorded in comparison to the twin-polarization. As a consequence, only three polarization-dependent curves per host are presented and a comparison between every polarization-dependent spectrum in the two host crystals can be performed.

The highest estimated cross section is for both crystals at 379.1 nm and it corresponds to $5.7 \cdot 10^{-20}\,\mathrm{cm}^2$ in Er^{3+}:BaY_2F_8 and $5.6 \cdot 10^{-20}\,\mathrm{cm}^2$ in Er^{3+}:$BaYLuF_8$. One of the light differences of the spectrum is the ratio between the main peaks of the two groups at around 250 nm and 520 nm. In **y**-polarization, BaY_2F_8 has a higher estimated cross section at 522.10 nm ($3.9 \cdot 10^{-20}\,\mathrm{cm}^2$) than at 254.40 nm ($3.6 \cdot 10^{-20}\,\mathrm{cm}^2$); while $BaYLuF_8$ has a lower cross section at 522.15 nm ($3.6 \cdot 10^{-20}\,\mathrm{cm}^2$) than at 254.40 ($3.7 \cdot 10^{-20}\,\mathrm{cm}^2$). At the possible pumping wavelengths with InGaN diode lasers the absorption peaks of Er^{3+}:BaY_2F_8 and Er^{3+}:$BaYLuF_8$ are shifted only by 0.05 nm and the cross sections in

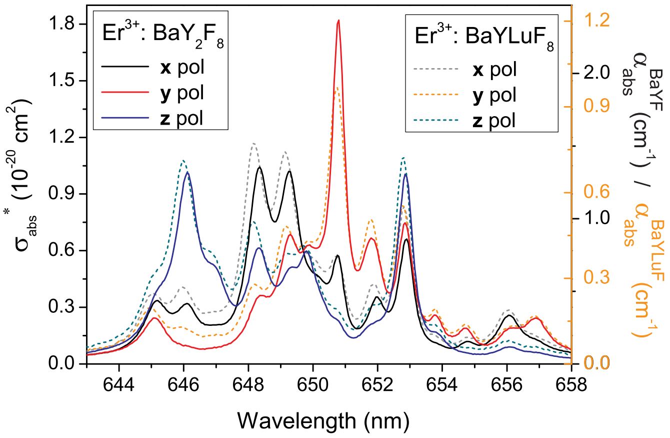

Figure 5.4: Comparison of estimated cross sections between 1 at.% Er^{3+}:BaY_2F_8 and 0.5 at.% Er^{3+}:$BaYLuF_8$ in the wavelength range of 650 nm. In this spectral range, if compared to others, a slightly higher displacement of some peaks in the same polarization is detectable and a more consistent differences in the absorption coefficients and estimated cross sections are evident. The cross sections are an estimation (signed with an $*$) due to the different missing correspondence between the refractive-index-coordinate-system and the system based on the optic axes and the **y**-axis.

y-polarization slightly advantage $BaYLuF_8$ (Er^{3+}:BaY_2F_8: $0.71 \cdot 10^{-20}\,\mathrm{cm}^2$ at 448.95 nm and Er^{3+}:$BaYLuF_8$: $0.77 \cdot 10^{-20}\,\mathrm{cm}^2$ at 448.90 nm). Also at the emission wavelength of the 2ω-OPSL (486.15 nm) Er^{3+}:$BaYLuF_8$ exhibits higher estimated cross sections in **y**-polarization: $1.1 \cdot 10^{-20}\,\mathrm{cm}^2$ instead of $0.97 \cdot 10^{-20}\,\mathrm{cm}^2$ in Er^{3+}:BaY_2F_8.

The only spectral range where slightly more significant variations between the two crystals are detected is around 650 nm and an enlargement of the area can be found in Fig. 5.4. All the six polarization-dependent curves are reported and can be compared to each other. The absence of significant broadening in $BaYLuF_8$ is evident. Nevertheless, for a few peaks a more consistent difference in estimated cross sections and especially a displacement in the wavelength is noticeable. For example, one of the peaks in **z**-polarization has a maximum at 646.00 nm in $BaYLuF_8$, which is at 646.10 nm in BaY_2F_8; while another peak in **x**-polarization has a maximum at 648.15 nm in $BaYLuF_8$, which is at 648.35 in BaY_2F_8.

In Fig. 5.5a, the absorption spectrum of Er^{3+}:$BaLu_2F_8$ is depicted. The absorption cross sections represent only an estimation. The crystal is uniaxial and the difficulties in correctly orienting it, because of the low quality and small dimension of the sample, have impeded the performance of the needed polarization-dependent measurements. Furthermore, erbium in this host presents double siting and the impossibility to distinguish between the contribution of each site is another reason to rely on the absorption coefficient α instead of the absorption cross sections.

The estimated cross sections are much lower than those reported for Er^{3+}:BaY_2F_8 and Er^{3+}:$BaYLuF_8$ in Fig. 5.3 and none of these spectra or a convolution of them recorded for these two hosts resembles the unpolarized measurement of Er^{3+}:$BaLu_2F_8$. The highest absorption coefficient in the 7% doped sample is detected at 378.9 nm and corresponds to $13.7\,\mathrm{cm}^{-1}$. In the region of possible pumping with InGaN diode lasers, the highest absorption coefficient is $2.39\,\mathrm{cm}^{-1}$ at 449.2 nm. In laser experiments with the 2ω-OPSL emitting at 486.15 nm, the available absorption coefficient corresponds to $6.47\,\mathrm{cm}^{-1}$, which

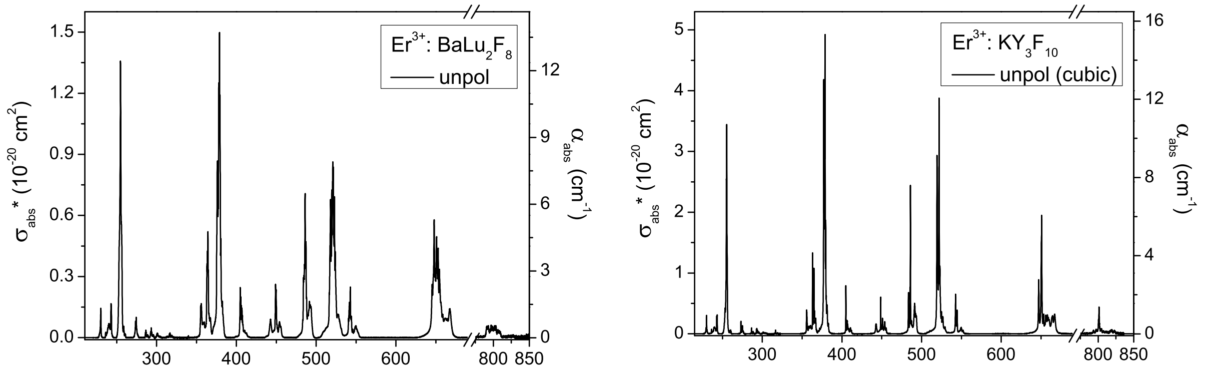

(a) **(b)**

Figure 5.5: Room temperature absorption spectra of Er^{3+}:$BaLu_2F_8$ (unpolarized) (a) and Er^{3+}:KY_3F_{10} (b). The shown cross sections can be considered only as an estimation for different reasons. Er^{3+}: $BaLu_2F_8$ is an uniaxial crystal and it should exhibit σ- as well as π-polarization. Furthermore, it presents double siting and it is not proven which contribution comes from which of the two sites. KY_3F_{10} is a cubic crystal but the doping concentration of 2 at.% refers to the melt and has not been measured in the samples used for the spectroscopic investigations. For these reasons, not only the cross sections $\sigma^\star$ but also the absorption coefficient α is plotted.

is also the absorption maximum in the Er^{3+}-ion transition $^4I_{15/2} \rightarrow {}^4F_{7/2}$ (see Fig.5.2a as a reference of the transitions).

Fig. 5.5b shows the absorption spectrum of Er^{3+}:KY_3F_{10}. The absorption cross sections are, like in Er^{3+}:$BaLu_2F_8$, only an estimation, but in this case surely pessimistic because it has been considered that the 2 at.% Er^{3+} doping in the melt has been entirely incorporated in the grown crystal and consequently in the extracted sample for spectroscopy. Considering the much lower doping concentration than in $BaLu_2F_8$, the potential in KY_3F_{10} appears higher because of the slightly higher absorption coefficients. For example, the maximum is found to be 15.3 cm^{-1} at 378.80 nm. Furthermore, the expected pessimistic estimation of the absorption cross sections leads to an evaluation of the real cross sections, which can reach the same size of those measured in crystals such as Er^{3+} BaY_2F_8 and even $LiLuF_4$. In laser experiments with InGaN diode lasers, the highest absorption coefficient is found to be 1.88 cm^{-1} at 448.7 nm. Further laser experiments with the 2ω-OPSL pump source at 486.15 nm could rely on an absorption coefficient of 3.84 cm^{-1}.

Absorption spectra in the IR spectral range

In this section all the room temperature absorption spectra in the range 930 - 1050 nm and 1400 - 1650 nm for the six different Er^{3+}-doped hosts involved in this work are presented.

The resolution of the measurements has been 0.6 nm in most cases. In the range 930 - 1050 nm in Er^{3+}:LaF_3, it was 0.75 nm in order to improve the signal-to-noise ratio and in Er^{3+}:KY_3F_{10} it was 0.3 nm.

In Fig.5.6a, the absorption cross sections of Er^{3+}:$LiLuF_4$ are depicted. Also in the IR spectral range, π-polarization is dominant and more favorable for absorption in laser experiments. The two highest peaks in the 1-µm range are at 971.8 and 968.8 nm, with

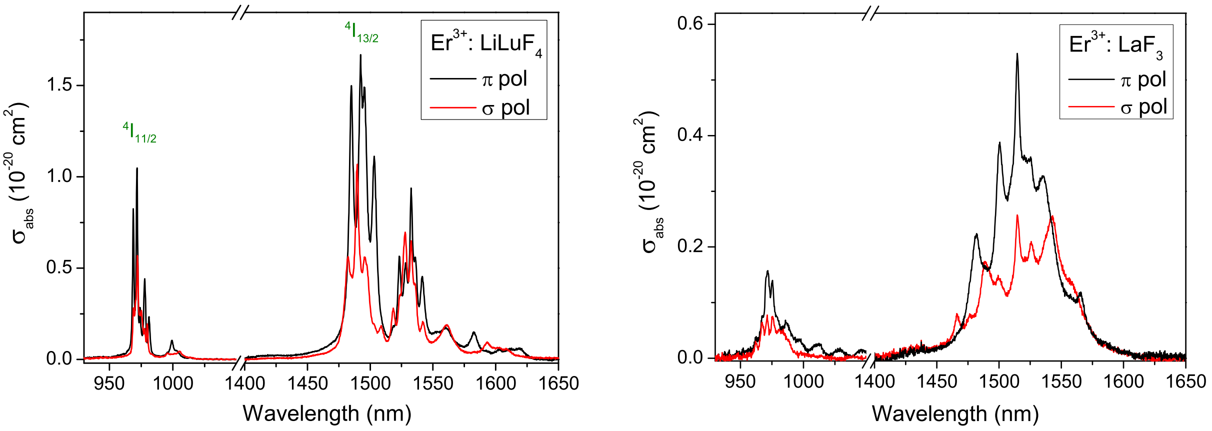

(a) (b)

Figure 5.6: Polarization-dependent absorption cross sections at room temperature of Er^{3+}:$LiLuF_4$ (a) and Er^{3+}:LaF_3 (b). In (a) the final energy levels of the two transitions from the ground state $^4I_{15/2}$ are labeled.

an absorption cross section of $1.0 \cdot 10^{-20}$ and $0.83 \cdot 10^{-20}$ cm^2, respectively. In the 1.5-µm range, the absorption cross sections are higher and the highest peak is at 1492.4 nm, corresponding to a value of $1.7 \cdot 10^{-20}$ cm^2. Nevertheless, laser experiments could be performed with a fiber laser as pump source, emitting at 1535 nm. At this wavelength the absorption cross section in Er^{3+}:$LiLuF_4$ is equal to $0.53 \cdot 10^{-20}$ cm^2.

Fig. 5.6b illustrates the absorption cross sections of Er^{3+}:LaF_3. Also in this spectral range, the lower cross sections of Er^{3+}:LaF_3 compared to Er^{3+}:$LiLuF_4$ are confirmed and the broadening of the peaks is even more evident than in the visible spectral range. Nevertheless, in contrast to the visible spectral range, π -polarization is strongly higher than σ-polarization in LaF_3. The quality of the spectra are lower due to a lower signal-to-noise ratio because of the lower doping concentration in the sample. Furthermore, oscillations are caused by ethalon effect in the π-polarization in the range 1000 - 1050 nm. In the 1-µm range the highest peaks are at 971.8 and 975.5 nm, with a corresponding absorption cross section of $0.16 \cdot 10^{-20}$ and $0.14 \cdot 10^{-20}$ cm^2, respectively. In the 1.5-µm range, where the absorption cross sections are higher, the highest peak is at 1514.6 nm, with $\sigma_{abs} = 0.55 \cdot 10^{-20}$ cm^2. At 1535 nm, the working wavelength of the available pump laser for laser experiments, the absorption cross section is equal to $0.33 \cdot 10^{-20}$ cm^2.

Fig. 5.7 shows the estimated absorption cross sections of Er^{3+}:BaY_2F_8 and Er^{3+}:$BaYLuF_8$. As for the visible spectral range, the estimated cross sections and the shape of the peaks are very similar in these two hosts, and the estimated cross sections are lower than in $LiLuF_4$, although less severely in the 1-µm range than in the 1.5-µm range. Furthermore, the absorptions in **y**-polarization are less dominant than in the visible spectral range. Especially in Er^{3+}:BaY_2F_8 in Fig. 5.7a, the evidently lower signal-to-noise ratio for **y**-polarization is due to an inhomogeneity of the dimensions of the crystal Pi1 along the three axes (see in Tab. A.4 the ratio of the two edges $y/x > 2$).

In the 1-µm spectral range, the estimated peak cross section is in **y**-polarization, at 968.6 and 968.4 nm in Er^{3+}:BaY_2F_8 and Er^{3+}:$BaYLuF_8$, corresponding to a value of $0.93 \cdot 10^{-20}$ and $0.88 \cdot 10^{-20}$ cm^2, respectively. The second highest peak is in **z**-polarization

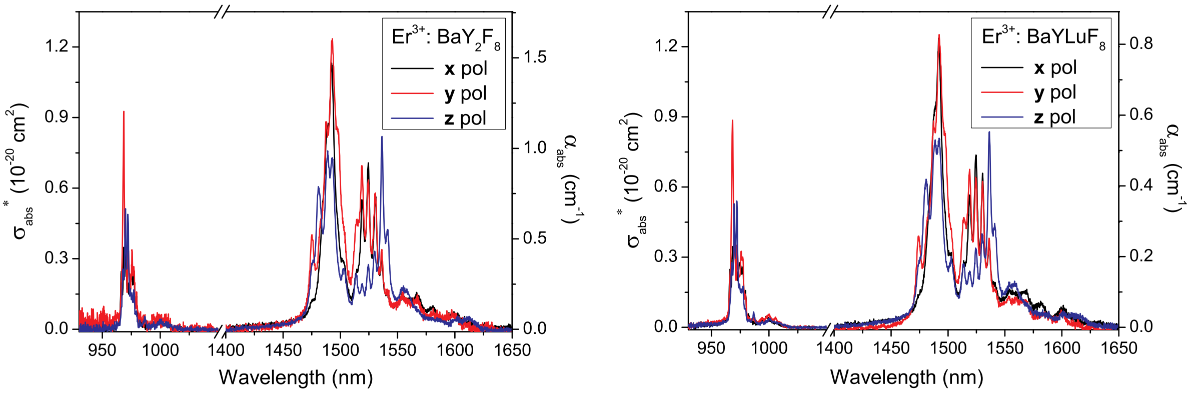

(a) (b)

Figure 5.7: Room-temperature polarization-dependent absorption cross sections of Er^{3+}:BaY_2F_8 (a) and Er^{3+}:$BaYLuF_8$ (b). As explained in the text and in Fig.5.3, the cross-sections are only an estimation.

is placed at 970.0 nm in Er^{3+}:BaY_2F_8 and at 972.0 nm in Er^{3+}:$BaYLuF_8$, corresponding to an estimated absorption cross section of $0.51 \cdot 10^{-20}$ and $0.54 \cdot 10^{-20}\,cm^2$, respectively.

In the 1.5-µm spectral range, effects due to the different orientation of the optic axes with respect to the refractive-index coordinates system are evident. If the crystals are investigated with the **E**-field parallel to a refractive index axis, the two twin measurements with the **B**-field and the **k**-vector in the two possible different combinations of parallelism with respect to the other two refractive index axes display differences.

Although some significant differences due to the different host affect the local absorption maxima around 1490 nm (in **y**-polarization for both hosts, in Er^{3+}:BaY_2F_8: $\lambda_{peak} = 1493.0\,nm$, $\sigma_{abs} = 1.2 \cdot 10^{-20}\,cm^2$; in Er^{3+}:$BaYLuF_8$: $\lambda_{peak} = 1492.2\,nm$, $\sigma_{abs} = 1.3 \cdot 10^{-20}\,cm^2$), the strongest differences due to the position of the optic axes are present in the region 1510 - 1540 nm, where the operating wavelength of the available fiber laser for laser experiments is located.

The three measurements needed to resolve the absorption spectra of monoclinic crystals present in this work, have been always tested with a fourth measurement which represented a repetition of an earlier measurement, but with exchanged parallelism of the **B**-field **k**-vector, keeping the parallelism of the **E**-field with respect to the same refractive-index axis. In the spectral ranges so far presented, this test measurement has always matched the correspondent twin measurement, but not in the wavelength region of 1510 - 1540 nm.

With a double measurement in **z**-polarization of BaY_2F_8 this effect has been recognized. A monoclinic crystal with six polished side faces to investigate this behavior was AC3 (see Tab. A.6 of Er^{3+}:$BaYLuF_8$ crystals). The results of the absorption measurements with incident light in two different directions are shown in Fig. 5.8. The spectra are grouped by couple of same electric polarizations, with indicated each direction of the incident light **k** and direction of the magnetic field **B**.

It has to be highlighted that the previously displayed spectra for Er^{3+}:BaY_2F_8 and Er^{3+}:$BaYLuF_8$ have been chosen to be comparable to each other, also regarding the direction of **k** and **B**.

The estimated cross sections at the emission wavelength of the pump laser for inband-

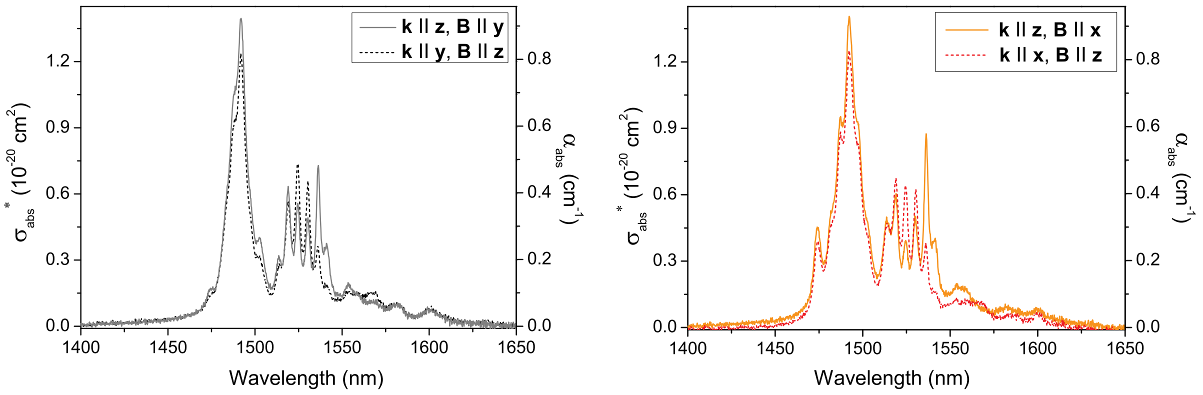

(a) $\mathbf{E} \parallel \mathbf{x}$ **(b)** $\mathbf{E} \parallel \mathbf{y}$

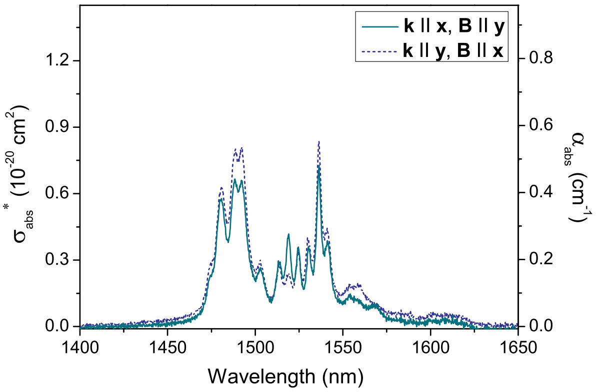

(c) $\mathbf{E} \parallel \mathbf{z}$

Figure 5.8: Comparison of absorption coefficients and estimated cross sections in 0.5 at.% Er^{3+}:$BaYLuF_8$ for the same electrical polarization, but different orientation of the **k**-vector and of the magnetic field **B** of the incident light. In (a), **x**-polarization is shown, with the two possible combinations of **k** and **B** along **y** and **z**. In (b), **y**-polarization is shown, with the two possible combination of **k** and **B** along **x** and **z**. In (c), **z**-polarization is shown, with the two possible combination of **k** and **B** along **x** and **y**. The cross sections are an estimation as explained in the text and in Fig. 5.3

pumping (1535 nm), in both hosts, for the different orientation of the crystals, is always included between $0.31 \cdot 10^{-20}\,\mathrm{cm}^2$ (in Er^{3+}:BaY_2F_8 **x**-polarization) and $0.85 \cdot 10^{-20}\,\mathrm{cm}^2$ (in Er^{3+}:$BaYLuF_8$ **y**-polarization), which is higher than in Er^{3+}:$LiLuF_4$.

Considering the availability of a second Er^{3+}:$BaYLuF_8$ sample Pi2 (details summarized in Tab. A.6) with different sizes and Er^{3+}-doping concentration in comparison to crystal AC3, absorption cross sections in this spectral range have been estimated and the results are only 10-12% different. This proves that, also in the region where orientation differences emerge, a strong dependency on the size of the sample cannot be observed. This can be considered valid for a standard sample size, with a volume either smaller or comparable to $1\,\mathrm{cm}^3$.

Fig.5.9a shows the estimated unpolarized absorption cross sections and absorption coefficient of Er^{3+}:$BaLu_2F_8$. In this spectral region, the reduction of the estimated cross sections compared to other host crystals is less severe and the two highest peaks in the 1-µm region are located at 971.6 and 972.2 nm, with an absorption coefficient equal to 2.91 and $1.99\,\mathrm{cm}^{-1}$, respectively. In the 1.5-µm region, the highest absorption peak is

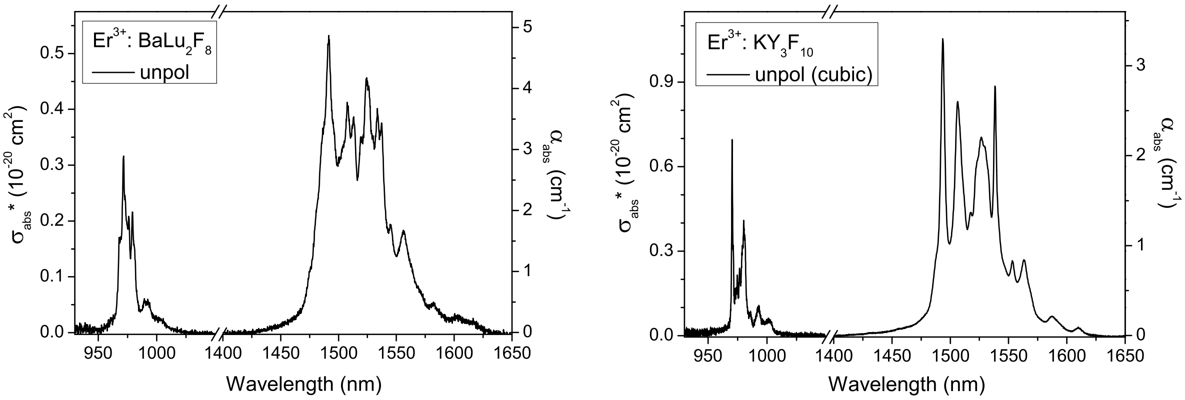

(a) **(b)**

Figure 5.9: Room-temperature absorption spectra of 7 at.% Er^{3+}:$BaLu_2F_8$ (unpolarized) (a) and 2% Er^{3+}:KY_3F_{10} (b). The cross sections are labeled with a $*$ because of the same reasons explained in Fig. 5.5 they can be considered only as an estimation. Therefore, the absorption coefficient α is also reported. The scale of the estimated cross sections is a factor of two larger for Er^{3+}:KY_3F_{10} than for Er^{3+}:$BaLu_2F_8$.

located at 1491.6 nm, with an absorption coefficient of 4.87 cm^{-1}. At the laser wavelength of the pump laser for inband-pumped experiments (1535 nm), the absorption coefficient corresponds to 3.23 cm^{-1}. In this host the difference in absorption coefficient in the 1400-nm range with respect to the 1500-nm range is not pronounced, as in Er^{3+}:LaF_3.

In Fig. 5.9b), the estimated absorption cross sections and absorption coefficients of Er^{3+}:KY_3F_{10} are reported. Also in this case the order of magnitude of the estimated absorption cross sections are slightly lower than in other host crystals, but higher than in Er^{3+}:$BaLu_2F_8$. For a direct comparison, the scale of the cross sections is exactly a half in Er^{3+}:$BaLu_2F_8$ with respect to Er^{3+}:KY_3F_{10}. In the 1-µm region, the highest maxima of Er^{3+}:KY_3F_{10} are located at 970.3 and 980.2 nm, with a correspondent absorption coefficient of 2.18 and 1.29 cm^{-1}, respectively. In the 1.5-µm region, the highest absorption peak is at 1493.6 nm, with an absorption coefficient of 3.28 cm^{-1}. At the operation wavelength of the pump laser for inband-pumped laser experiments (1535 nm), the absorption coefficient is 1.35 cm^{-1}.

5.3 Fluorescence and emission cross sections measurements

Fluorescence measurements are important in this work to obtain two distinct results: emission cross sections in different spectral ranges and the dependence of the upconverted green fluorescence as a function of the incident infrared exciting beam.

5.3.1 Emission cross sections

Two different methods can be applied to calculate emission cross sections. The so-called reciprocity method, based on the theory of McCumber (McC) [McC64], derives the emission cross sections from the absorption cross sections, when the energy of every Stark level of the involved multiplets is known. The β-τ or Füchtbauer-Ladenburg method (FL) [Hub75, Aul82, Mou86, Wal98] is based on the knowledge of the complete fluorescence spectra and the radiative lifetime of the considered manifold.

Reciprocity or McCumber method

The method described by McCumber represents a generalization of the equality of cross sections in a simple atomic two-level system postulated by Einstein [Ein16] to a complex multi-level system.

If the energy level structure is known, it is possible to define the Stark occupation of a certain energy level f_i as:

$$f_i = \frac{g_i}{Z}\,\mathrm{e}^{\left(-\frac{E_i - E_0}{kT}\right)}, \tag{5.4}$$

where g_i and E_i are degeneration and energy of the level, respectively and E_0 the energy of the lowest Stark level of the manifold. T and k are the temperature and the Boltzmann constant, while Z represents the partition function of the manifold, defined as:

$$Z = \sum_i g_i\,\mathrm{e}^{\left(-\frac{E_i - E_0}{kT}\right)}. \tag{5.5}$$

If the principle of equality of atomic cross sections σ_{at} is valid, the occupation of the involved Stark levels of the lower and upper manifold f_{l} and f_{u} are related to the absorption (σ_{GSA}) and emission cross sections (σ_{em}) as follows:

$$\sigma_{\mathrm{GSA}} = f_{\mathrm{l}}\,\sigma_{\mathrm{at}} \qquad \text{and} \qquad \sigma_{\mathrm{em}} = f_{\mathrm{u}}\,\sigma_{\mathrm{at}}. \tag{5.6}$$

If the polarization dependence κ for non-isotropic host materials is added and the absorption cross sections are known, the emission cross sections can consequently be calculated via the following equation:

$$\sigma_{\mathrm{em}}^{\kappa,\,\mathrm{McC}}(\lambda) = \sigma_{\mathrm{GSA}}^{\kappa}(\lambda)\,\frac{Z_{\mathrm{l}}}{Z_{\mathrm{u}}}\,\mathrm{e}^{\left(-\frac{E_{\mathrm{ZL}} - \frac{hc}{\lambda}}{kT}\right)}, \tag{5.7}$$

where the partition functions of the lower and upper manifold are identified as Z_{l} and Z_{u}, respectively and the energy difference between the two lowest Stark levels of the two manifolds is represented by the energy E_{ZL}. Additionally, c is the speed of light and h the Planck constant [McC64].

Füchtbauer-Ladenburg method

If polarization-dependent fluorescence spectra $I^{\kappa}(\lambda)$ can be measured, and the radiative lifetime τ_{R} defined in Eq. (2.10) can either be measured or estimated, the emission cross sections can be evaluated via the Füchtbauer-Ladenburg equation:

$$\sigma_{\mathrm{em}}^{\kappa,FL}(\lambda) = \frac{\beta_{i,l}}{8\pi\,c\,\tau_{\mathrm{R}}\,(n^{\kappa}(\lambda))^2}\,\frac{\lambda^5\,I^{\kappa}(\lambda)}{\frac{1}{3}\sum_{\xi}\int \lambda^{\star}\,I^{\xi}(\lambda^{\star})\,\mathrm{d}\lambda^{\star}}, \tag{5.8}$$

where the auxiliary index ξ indicates every kind of polarization κ and $\beta_{i,l}$ is the branching ratio defined in Eq. (2.8). The wavelength-dependent refractive index $n^{\kappa}(\lambda)$ for every polarization κ is also required.

Typically, both methods are efficient in a different way for different parts of the spectral range.

The emission spectra calculated via the McCumber theory show an increased noise in the long-wavelength region, originated by the lower absorption cross sections due to a limited occupation of the upper Stark levels of the lower multiplet. Furthermore, the exact energy of every Stark level must be known and typically the literature offers different versions for one ion embedded in the same host crystal.

On the contrary, fluorescence spectra, on which the Füchtbauer-Ladenburg equation is based, are affected by reabsorption which can never be completely avoided and causes an attenuation of emission peaks, especially in the short-wavelength spectral region. Furthermore, the value of τ_{R} has always to be considered with a relatively wide error bar. Finally, every fluorescence spectrum needs a calibration spectrum, detected via illumination with the radiation from a grey body at roughly 2600 K and in case of polarization-dependent spectroscopy, the orientation of the optic axes and of the polarizer can be source of further inaccuracy.

As a consequence, the most reasonable way is to illustrate the emission-cross-section spectra calculated with the McC method, as well as those calculated via FL method. Alternatively, a combination of both can be performed. Namely, the accuracy of the McCumber-derived spectra in the short-wavelength range can be used to scale the Füchtbauer-Ladenburg results in the long-wavelength range of the spectrum. This should be performed before the onset of the noise, preferably not at a high peak, where it is more probable to suffer from reabsorption. Subsequently, from this point, the long-wavelength range spectrum can be represented by the scaled Füchtbauer-Ladenburg results. A further representation could be the ratio of the two spectra, which shows in which spectral range the reabsorption is active and the factor which distinguishes the cross sections derived via the two methods.

The setup employed to perform fluorescence measurements will be described in Sect. 5.3.2 and is represented in Fig. 5.11.

Fluorescence lifetime measurements

Information on the radiative lifetime of energy levels of rare earth ions are essential to determine the laser-emission capabilities.

In the case of upconversion processes in erbium-doped materials, special attention is paid for the radiative lifetimes of both the potential laser emitting $^4\mathrm{S}_{3/2}$-level and the intermediate metastable $^4\mathrm{I}_{11/2}$-level.

Furthermore, the knowledge of the radiative lifetime of a manifold is essential to apply the Füchtbauer-Ladenburg method for the calculation of emission cross sections.

The general high uncertainty which surrounds radiative lifetime data in the literature

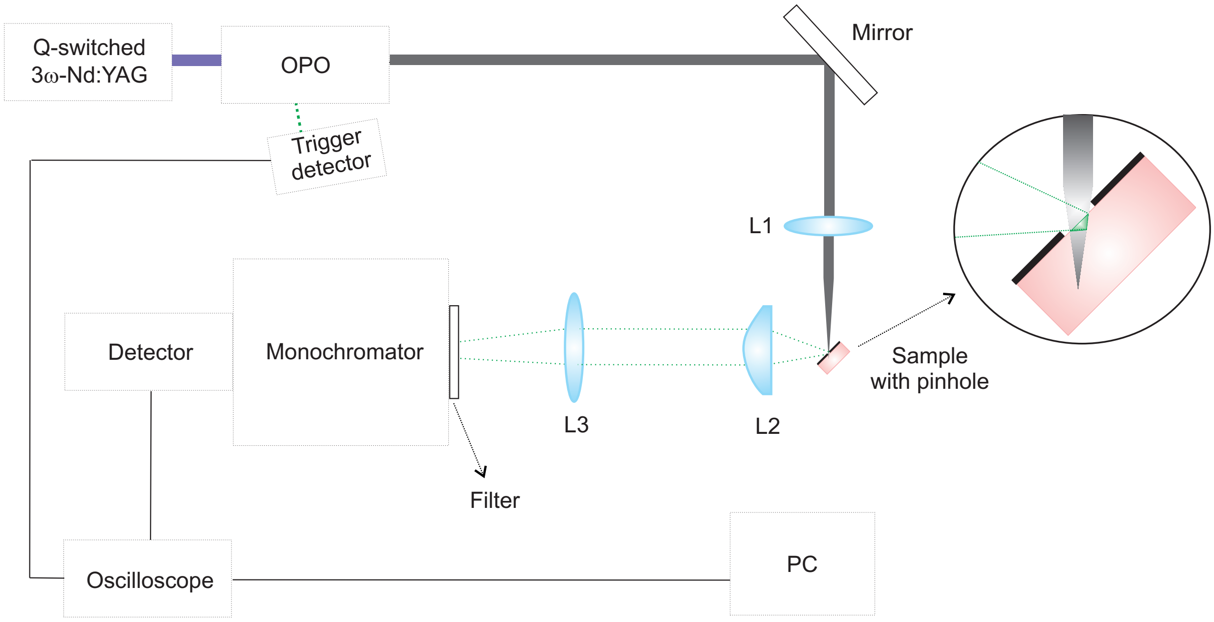

Figure 5.10: Setup for the performance of fluorescence lifetime measurements and enlargement of the sample where the pinhole method is applied [Küh07].

is founded on either the estimation nature of calculations[2] or the width of the error bars which characterizes every measurement.

In this work, when radiative lifetime data have been not deduced from the literature, they have been measured via the detection of fluorescence decay curves.

Mainly, this kind of measurements can be affected by reabsorption, namely radiation-trapping, which results in an elongation of the measured lifetime. This effect is amplified by a overlap between absorption and emission spectra and by a high doping concentration in the sample. For these reasons, the measurements have been performed on relatively low-doped, thin samples. Furthermore, the application of the pinhole method [Küh07] can ideally return the radiation-trapping-free lifetime.

The setup to perform fluorescence lifetime measurements is depicted in Fig. 5.10.

The excitation source was the third harmonic of a Q-switched Nd:YAG laser, pumping two different kinds of optical parametric oscillators (OPO) in a system by *Solar LS*, tunable in a wide spectral range, from the UV to the near IR. The repetition rate was 10 Hz, the pulse energy was of a few millijoules and the pulse duration < 20 ns, which means much shorter than the shortest measured lifetime (generally more than hundreds of microseconds). When the pinhole method has been employed, the excitation pulses were illuminating only the portion of the sample behind the pinhole, without being hardly focused by the lens L1 (see enlargement in Fig. 5.10). The available diameters of the pinholes were between 0.5 and 2.5 mm, in steps of 0.1 mm. The fluorescence has been collimated and imaged by lenses L2 and L3 onto the slits of a 0.5 m-SPEX monochromator equipped with a 500 nm-blazed grating with 1200 lines per millimeter. Residual pump light has

---

[2] Radiative lifetime data can be estimated via methods such as Judd-Ofelt theory [Jud62, Ofe62]. The results are fruit of approximations to be taken into account when the data are implied in further calculations.

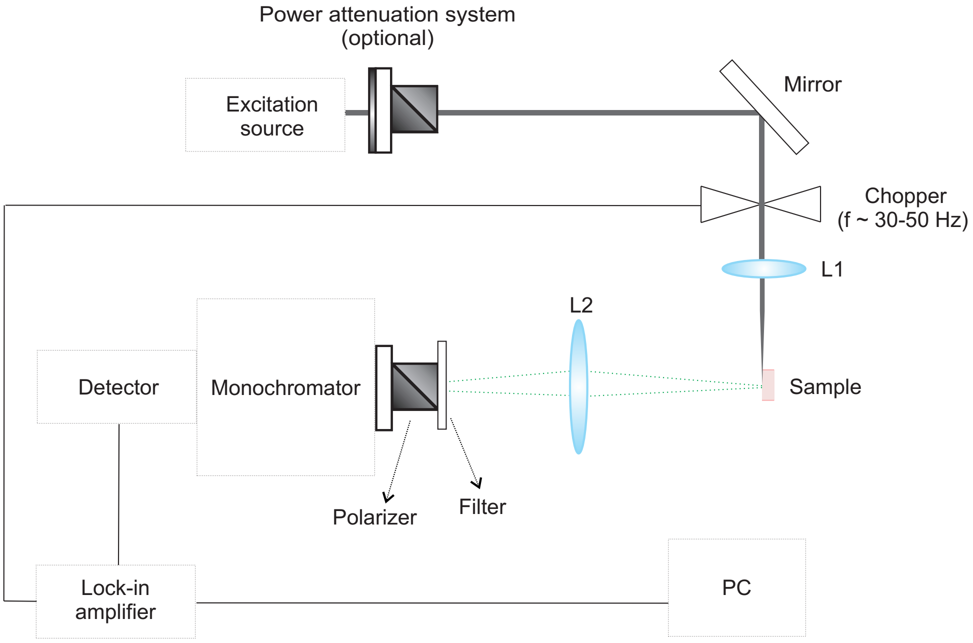

Figure 5.11: Setup to perform fluorescence measurements.

been blocked via either filters or dichroic mirrors. The wavelength-selected fluorescence could be detected by either a S1-photomultiplier, sensitive in the spectral range between 350 nm and 1 µm, or a photomultiplier tube (PMT) by *Hamamatsu*, sensitive in the spectral range 1-1.7 µm. The output signal has been recorded by an oscilloscope (*LeCroy* 9630 Dual 600MHz, 5Gs/s) and averaged over 500 - 1000 decay curves, in order to improve the signal-to-noise ratio. A Si-photodiode (trigger detector) has been employed to detect a signal from the OPO as a reference for the oscilloscope.

As stated in Chap. 2, the expected decay curve of an energy level has the shape of an exponential, where τ_{R} can be deduced using the formula:

$$I(t) = I_0\, \mathrm{e}^{-\frac{t}{\tau_{\mathrm{R}}}}\,. \tag{5.9}$$

5.3.2 Excitation-power-dependent upconversion fluorescence

As stated in Sect. 2.4, analyzing the slope of upconversion fluorescence vs exciting power on a double logarithmic scale can give information about the dominant process which governs the upconversion phenomenon.

Unfortunately, when the upconversion has only two steps (like in the case of infrared-pumping at ~970 nm), such a distinction of processes cannot be detected observing the green fluorescence. Nevertheless, for a few erbium-doped hosts, this measurement has been performed in order to detect the change of slope between relatively low and relatively high incident power and check the absolute value of the slopes of the two ramps.

The setup to perform the detection of the fluorescence as a function of excitation power resembles the setup used to record fluorescence spectra and it is depicted in Fig. 5.11.

The excitation source, depending on the fluorescence spectral range to address, has been of two types. One was a cw Ti:sapphire laser by *Spectra Physics* pumped by the second harmonic of a Nd:YVO$_4$ laser, tunable between 750 nm and 1 µm, emitting a maximum output power of ~3.5 W. The second excitation source was an InGaN diode laser emitting at ~450 nm with a maximum output power of 1.6 W. These two lasers also served as pumping sources in the laser experiments described in Chap. 6.

The excitation source has been focused onto a small portion of the sample via the lens L1, in order to limit reabsorption. Subsequently, the fluorescence from the crystal has been imaged through the lens L2 onto the slits of a 1-m SPEX monochromator. When polarization-dependent measurements have been carried out, a Glan-Taylor polarizer has been interposed between the monochromator and the sample. Furthermore, either a filter or a dichroic mirror was used to block spurious excitation light. Depending on the fluorescence wavelength range, the grating was either a 500-nm or 1-µm blazed, with either 1200 or 600 lines per millimeter. Either a Si- or a Ge-photodiode has been employed as detector for either emission in the visible-1 µm spectral range or fluorescence at around 1.6 µm. In order to improve the signal-to-noise ratio of the signal, the fluorescence has been transferred to a lock-in amplifier (*Stanford Research Systems SR 810 DSP*). To benefit from the lock-in system, the excitation beam has been periodically interrupted employing a chopper located in front of the focusing lens L1, set on a frequency of 30 - 50 Hz and adopted as a reference signal.

5.3.3 Measurement results

In this subsection all the emission measurements will be summarized, sorted by the Er^{3+}-doped host crystal. When possible, the results from the McCumber and Füchtbauer-Ladenburg of the same spectral region will be directly compared. If the Füchtbauer-Ladenburg is applied with measured lifetimes, also the data concerning the lifetime measurements will be briefly discussed. For a non-standard analysis of a few fluorescence decay curves, see Sect. 5.4.

Moreover, the results of the upconversion fluorescence as function of the excitation power will be shown.

Emission spectra and fluorescence lifetime measurements

Er^{3+}:LiLuF$_4$

The main role of LiLuF$_4$ in this thesis leads to a more specific study of the spectroscopic aspects of Er^{3+}-ions in this host.

The Füchtbauer-Ladenburg method, described in Sect. 5.3, implies the knowledge of the branching ratios for the analyzed transition. These have been calculated by *Bär* [Bär00] via the Judd-Ofelt method and are reported in Tab. 5.1.

The polarization-dependent refractive indices, for LiLuF$_4$ and all the other hosts involved in this work, have not been measured. Therefore, the data present in the literature have been used to calculate the emission cross sections. These values for each crystal host are summarized in Tab. B.1.

For Er^{3+}:LiLuF$_4$, the radiative lifetime of the three manifolds $^4S_{3/2}$, $^4I_{11/2}$ and $^4I_{13/2}$ have been measured on a 1%-doped sample. The pinhole method has been applied. Most of the excitations have been inband, which means that the emitting multiplet was directly

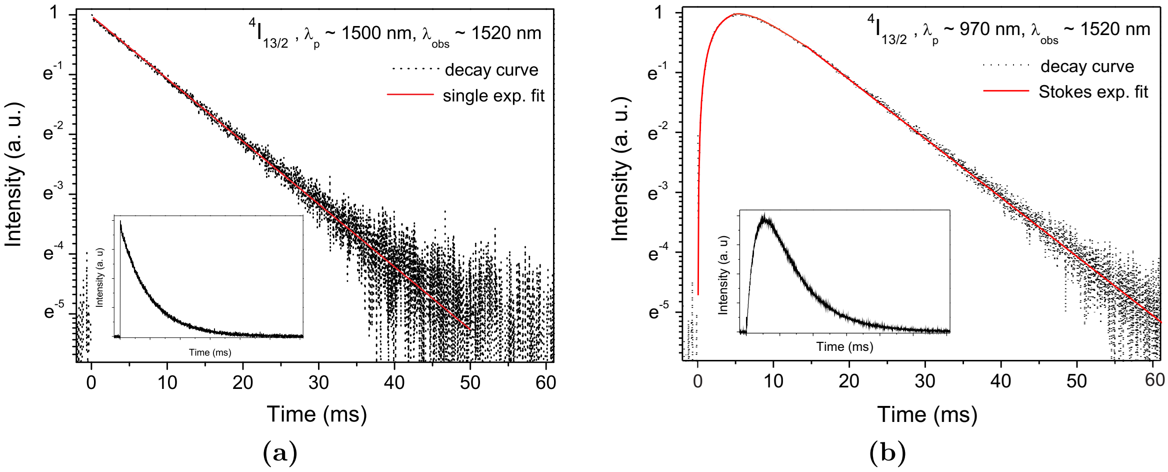

Figure 5.12: Exponential decay curves of the $^4I_{13/2}$-multiplet in 1 at.% -doped Er^{3+}:LiLuF$_4$. In (a), the multiplet is inband-pumped at ~1500 nm and the same exponential curve is represented in semilogarithmic scale with an exponential fit and on linear scale in the inset. In (b), the excitation at ~970 nm reaches first the $^4I_{11/2}$-multiplet and only after its decay the $^4I_{13/2}$-manifold can be populated. Therefore, a smooth increase of the fluorescence signal is detected, depending on the lifetime of $^4I_{11/2}$-manifold [Rub86]. The same curve is depicted on semilogarithmic scale with the correspondent double-exponential fit, and on linear scale in the inset.

excited by the pumping source tuned at a slightly shorter wavelength than the fluorescence one. A summary of the pumping schemes is reported in Fig. E.1a.

For the $^4S_{3/2}$-multiplet a comparison study has been performed: the lifetime has been measured observing both the fluorescence in the green spectral range, which populates the ground state, and the one at 850 nm, which is still originated by the $^4S_{3/2}$-multiplet but populates the $^4I_{13/2}$-manifold, in order to demonstrate that the two measured lifetimes coincide. Furthermore, a comparison study of the dynamic of the $^4S_{3/2}$- and the $^4I_{13/2}$-multiplet has been carried out when the excitation is given via upconversion, at around 970 nm, and via inband-excitation, respectively.

In Fig. 5.12, the decay process $^4I_{13/2} \rightarrow {}^4I_{15/2}$, observed at 1530 nm, for inband-excitation, at roughly 1500 nm, as well as for excitation at roughly 970 nm is reported. As expected, the curves show an exponential behavior and the measured radiative lifetime corresponds to 9.7 ms. When the multiplet is directly pumped, as shown in Fig. 5.12a, the signal decays exponentially right after the excitation is given. In Fig. 5.12b, the

Transition	Spectral region	$\beta_{i,j}$
$^4S_{3/2} \rightarrow {}^4I_{15/2}$	550 nm	0.6678
$^4S_{3/2} \rightarrow {}^4I_{13/2}$	850 nm	0.2773
$^4S_{3/2} \rightarrow {}^4I_{9/2}$	1.7 µm	0.0327
$^4S_{3/2} \rightarrow {}^4I_{11/2}$	1.2 µm	0.0219
$^4S_{3/2} \rightarrow {}^4F_{9/2}$	3 µm	0.0003

Table 5.1: Branching ratios of the multiplet $^4S_{3/2}$ in Er^{3+}:LiLuF$_4$, calculated via Judd-Ofelt method [Bär00] and spectral region of the consequent fluorescence.

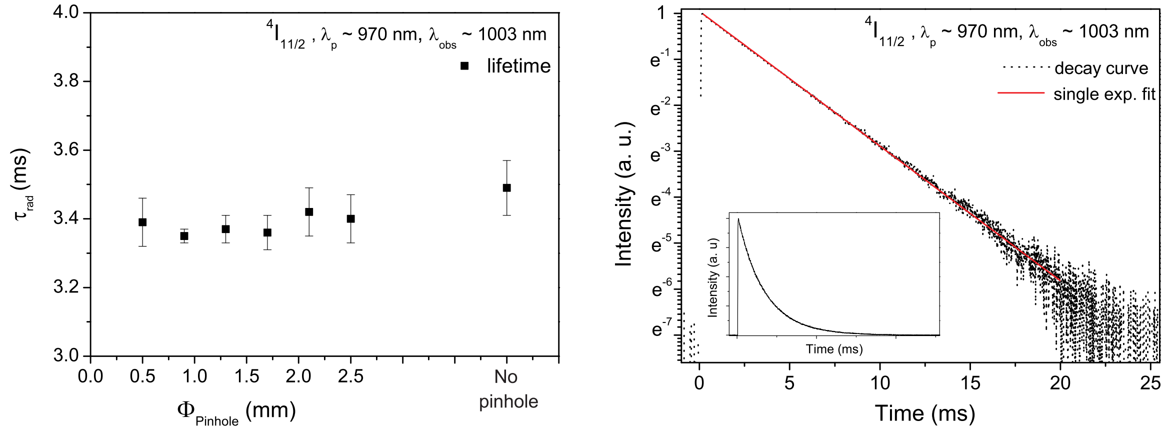

(a) (b)

Figure 5.13: Radiative lifetime of the $^4I_{11/2}$-multiplet in 1 at.%-doped Er^{3+}:LiLuF$_4$. In (a), the results of the pinhole measurements with six different pinhole diameters are reported. For comparison, the result obtained with the same sample but without pinhole is also shown. In (b), an example of the exponential decay curve of the multiplet (no-pinhole measurement), fitted by an exponential curve, is reported on semilogarithmic scale. In the inset the same decay curve is reported on linear scale.

excitation populates first the above $^4I_{11/2}$-manifold in a time comparable to its lifetime. Therefore, the excitation does not appear as a δ-function as in the case before. After the $^4I_{13/2}$-manifold has been populated, it is still possible to calculate approximately the same value of radiative lifetime from an exponential decay curve. This behavior is explained in [Rub86] and in Chap.2. As a confirmation, the whole curve has been successively fitted with a double-exponential function of the form:

$$y = A\mathrm{e}^{-x/t_1}(1 - B\mathrm{e}^{-x/t_2}) \tag{5.10}$$

which determines both the lifetime values of roughly 2 ms, corresponding quite precisely to the lifetime of the $^4I_{11/2}$-manifold, and 9.7 ms, the lifetime of the $^4I_{13/2}$-manifold.

The lifetime of $^4I_{11/2}$-multiplet has been tested with the pinhole method and the results are reported in Fig. 5.13a. The excitation wavelength was ∼970 nm and the observed fluorescence at 1003 nm, corresponding to the decay process $^4I_{11/2} \rightarrow {}^4I_{15/2}$. Six different sizes of pinhole have been employed and every lifetime value corresponds to an average over different measurements, with an error bar of three standard deviations. No significant increase of the lifetime could be observed when increasing the pinhole diameter. Therefore, reabsorption effects can be neglected. This means that the extrapolation to an ideal pinhole diameter of 0 mm was not necessary, but an average radiative lifetime has been calculated and it corresponds to 3.4 ms. Nevertheless, the lifetime value derived from measurements without the pinhole shows a slight increase, still included in the error bar of the other values. In Fig. 5.13b, an example of one clearly single-exponential decay curve on semilogarithmic scale and the respective exponential fit are represented. In the inset the same curve is shown on linear scale.

For the determination of the radiative lifetime of the $^4S_{3/2}$-multiplet, the pinhole method has been applied to fluorescence decay curves originating from different transition channels. Both curves originated from the depopulation of the same multiplet, but they have been detected at different wavelengths: ∼550 nm for the $^4S_{3/2} \rightarrow {}^4I_{15/2}$

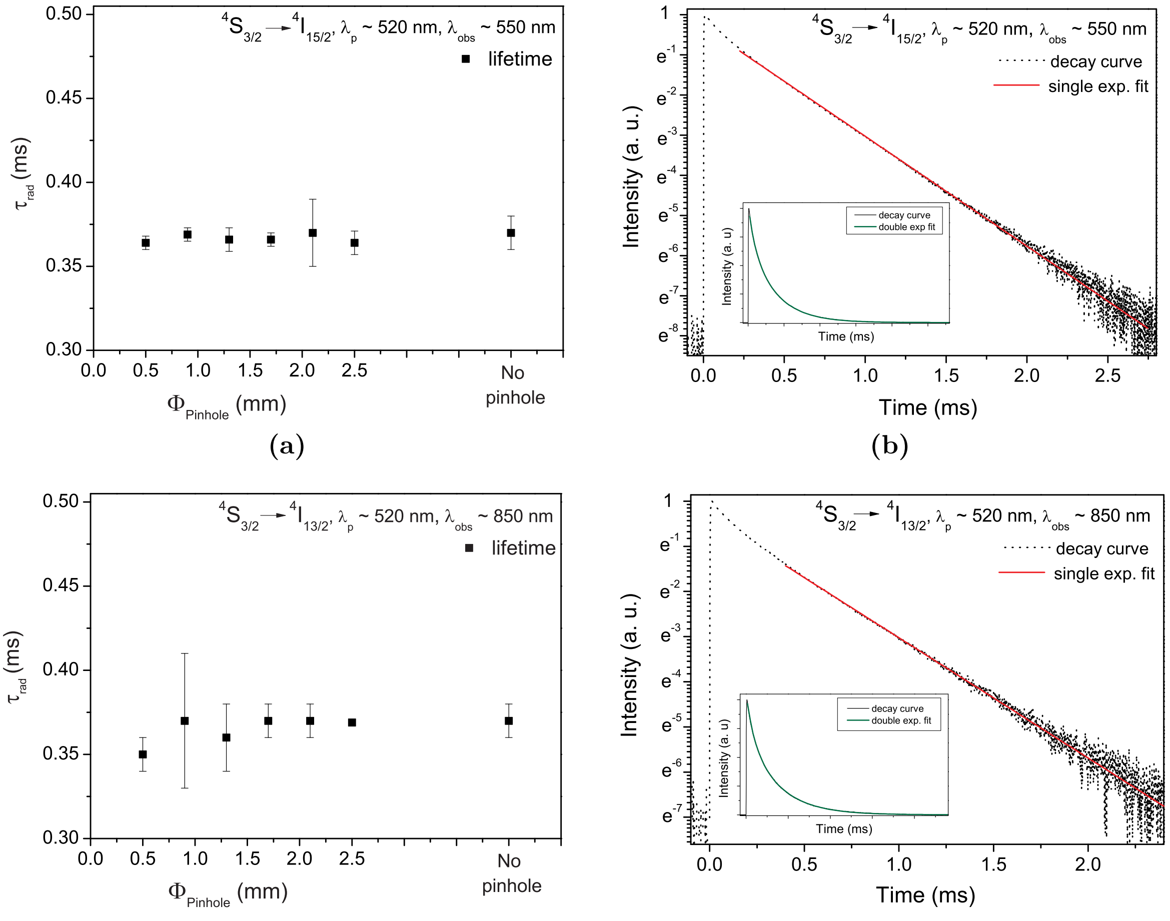

(a) (b)

(c) (d)

Figure 5.14: Radiative lifetime of the ${}^4S_{3/2}$-multiplet in 1 at.% -doped Er^{3+}:$LiLuF_4$. In (a) and (c), the results of the applied pinhole measurements with six different diameters are reported for fluorescence at roughly 550 and 850 nm, respectively. In (b) and (d), examples of decay curve at the two different wavelengths are depicted (ϕ_{pinhole} = 2.1 mm and 2.5 mm, respectively)). For both the behavior is not purely single exponential and in the semilogarithmic scale the single exponential fit is calculated with a delay of ~ 300 µs. Alternatively, in the insets, a double exponential decay fit is performed on the same decay curves in linear scale.

transition and ~ 850 nm for the ${}^4I_{13/2} \rightarrow {}^4I_{13/2}$ transition. The pumping source was in both cases tuned to ~ 520 nm. The results are reported in Fig. 5.14. In Fig. 5.14a, the lifetime of the ${}^4S_{3/2}$-manifold is determined with six different pinhole sizes, detecting the fluorescence decay at ~ 550 nm. In Fig. 5.14c, the same kind of results are reported for the fluorescence decay at ~ 850 nm. The results of the pinhole methods are the same, in the limit of the error bars: no reabsorption effects are evident and it is possible to calculate the lifetime of the ${}^4S_{3/2}$-multiplet as average of the data observed at different wavelengths, converging to τ =0.37 ms. Also the data corresponding to the absence of pinhole resemble the results obtained with the pinhole method. In the figures 5.14b and 5.14d, an example of decay curve is reported for the two different fluorescence wavelengths.

It has to be noticed that the decay curve is not purely single exponential. Therefore, the single-exponential fit has been calculated only for the tail of the curve, starting roughly

300 µs after the excitation pulse. The insets of both figures represent a possible alternative fit with a double-exponential decay curve. For both, one decay time represents the decay time of the $^4S_{3/2}$-multiplet, as deduced via the delayed single exponential decay, while the second decay time corresponds to a value of $\tau_2 \sim 90\,\mu s$. It can be excluded that the decay of the $^2H_{11/2}$ energy level has an influence on this, because this is thermally coupled to the $^4S_{3/2}$-multiplet and a phonon-induced non-radiative decay is expected in the picosecond time-regime. Nevertheless, the longer-living energy levels below the $^4S_{3/2}$-manifold (e. g. $^4I_{11/2}$- and $^4I_{13/2}$-multiplets have a lifetime in the order of a few milliseconds) could be populated as a consequence of radiative decay. This would cause, via ESA or ETU, the population of higher levels, which would recycle partly the pump energy, alternatively partially populating, via fast decay, the $^4S_{3/2}$-manifold. This processes could be characterized by a time scale in the order of the second lifetime τ_2 of the double-exponential fit. ESA measurements do not exclude this possibility.

An interesting study which can be carried out concerning the lifetime of the $^4S_{3/2}$-manifold, involves the upconversion pumping at $\sim$970 nm, to be compared to the ordinary direct pump in the green spectral range. The results of this measurement are depicted in Fig. 5.16. Also in this case, no reabsorption effects could be observed during the measurement of the radiative lifetime and an average value could be calculated. Nevertheless, the results are quantitatively different. The radiative lifetime of the $^4S_{3/2}$-multiplet after the upconversion pumping scheme has been determined to be 1.25 ms. This time value is much longer than the one measured with direct pumping and almost one half the lifetime of the intermediate $^4I_{11/2}$ pumping level. A similar effect has been encountered also in the very similar material Er^{3+}:LiYF$_4$ [Rub86] where Stokes- and anti-Stokes-fluorescence are analyzed. In this case, the explanation has been found in an interionic energy transfer process (ETU) most probably involving only pairs of ions.

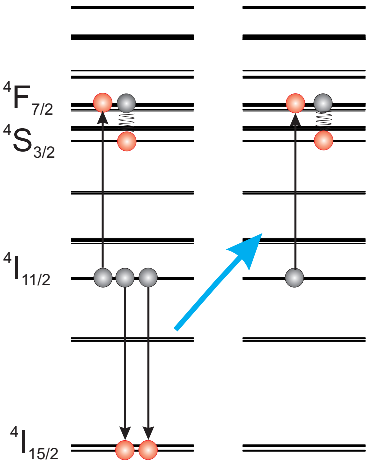

Figure 5.15: ESA pumping (left) and possible ETU (left to right) in Er^{3+}:LiLuF$_4$. Grey and red spheres represent the position of the excitations before and after the transition, respectively. In this way, the $^4S_{3/2}$-multiplet is populated as long as the $^4I_{11/2}$-manifold decays.

In order to motivate the extraordinary long lifetime measured for the $^4S_{3/2}$-manifold, the following energy transfer has been suggested: $^4I_{11/2}$, $^4I_{11/2} \rightarrow {}^4F_{7/2}$, $^4I_{15/2}$ and it is depicted in Fig. 5.15. The $^4S_{3/2}$-multiplet would be populated by a fast decay from the $^4F_{7/2}$-multiplet. The connection between the lifetime of $^4S_{3/2}$ and $^4I_{11/2}$-manifolds relies on the feeding process of $^4S_{3/2}$, supposed to last as long as the $^4I_{11/2}$-multiplet decays (see Sect. 2.4). In this picture, also an intraionic ESA process is depicted. If the population densities N_S and N_I of the two manifolds are considered in the rate equation, it is possible to write:

$$\frac{dN_S}{dt} = -\frac{N_S}{\tau_S} + W_1 N_I^2, \tag{5.11}$$

where $\tau_S = 0.37$ ms and W_1 is the transfer rate (in unit of cm^3/s). If $N_I(t) = N_I(0)e^{-\frac{t}{\tau_I}}$,

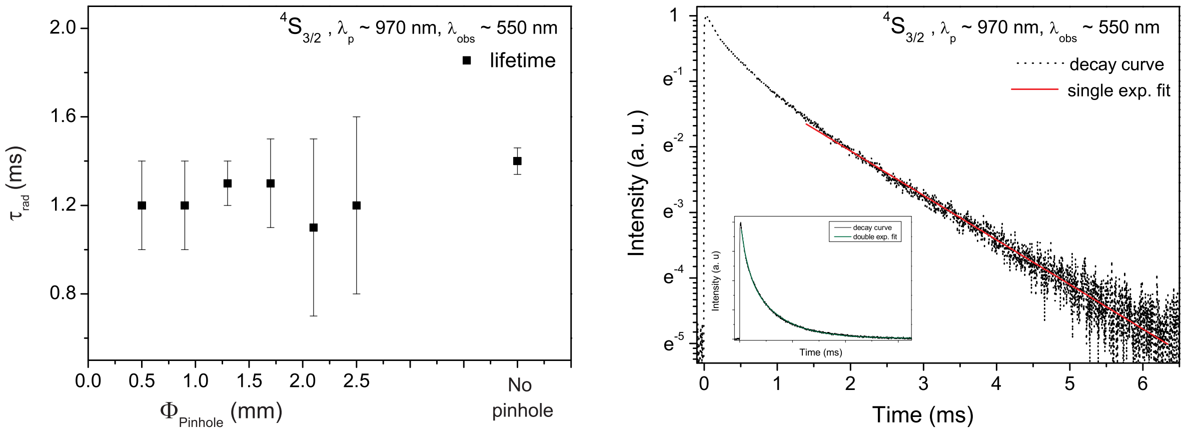

(a) **(b)**

Figure 5.16: Radiative lifetime of the $^4S_{3/2}$-multiplet in 1% -doped Er^{3+}:$LiLuF_4$ when upconversion-pumped. In (a), the results of the pinhole measurements with six different diameters are reported. For a comparison, the result obtained with the same sample but without pinhole is also shown. In (b), one decay curve (from the no-pinhole measurement), fitted by a delayed exponential curve, is reported on semilogarithmic scale. In the inset the same decay curve is reported on linear scale and fitted by a double exponential decay.

with $\tau_I = 3.2\,\mathrm{ms}$, the Eq. (5.11) would have as solution:

$$N_S(t) \approx e^{-\frac{2t}{\tau_I}}. \tag{5.12}$$

Actually, the measured lifetime in this case is less than a half of τ_I, but it could be considered as a rough estimation.

Moreover, another observation concerns the first part of the curve, where, despite the involvement of different energy levels, no rising of the curve (such as in Fig. 5.13b) is visible in Er^{3+}:$LiYF_4$, while a very slight one is visible in Er^{3+}:$LiLuF_4$. This could be the fingerprint of the ESA process causing the upconversion pumping, which is an intraionic process, when the curve has no rise. Consequently, the time-dependent measurement of upconversion-pumped fluorescence of a manifold could be an efficient and easy method to obtain an indication of the kind of process involved in the pumping scheme (either intra- or interionic) and for the doping-concentration-threshold for the onset of the interionic processes.

Another difference in comparison to Er^{3+}:$LiYF_4$ [Rub86] is found in the shape of the measured decay curve, which for Er^{3+}:$LiLuF_4$ is depicted in Fig. 5.16b. On the contrary of what reported in [Rub86], the decay curve in Er^{3+}:$LiLuF_4$ is not single exponential but it can be fitted by a double exponential decay, as depicted in the inset in linear scale of Fig. 5.16b. The first lifetime of this double exponential decay is the one measured for the $^4S_{3/2}$-manifold, equal to 1.25 ms and the second lifetime ~ 250 µs. A possible explanation for this could be once again the involvement of ETU processes. For this reason, all the lifetimes measured with the pinhole method reported in Fig. 5.16a, have been evaluated as single exponential decay curves with a delay of roughly 1.5 ms.

In the approximation which leads to the results in Equations (5.11) and (5.12), the transfer rate W_1 has to be considered dependent on a constant distance between the ions, expressing the possibility of only one kind of pair of neighbor Er^{3+}-ions. Further non-single-exponential and rising effects can be attributed to other kinds of Er^{3+}-ions pairs.

Finally, to obtain reliable values of radiative lifetimes which do not include further effects, direct pumping is recommendable.

The radiative lifetime of the $^4S_{3/2}$-multiplet has been measured and demonstrated to become longer, if the doping concentration is reduced. As expected, when the distance among the doping ions is large, there are less probabilities for interionic processes which reduce the lifetime of the energy levels. For two samples respectively 0.2 % and 0.5% doped, the radiative lifetime of the $^4S_{3/2}$-multiplet has been measured and it corresponds to 0.44 and 0.42 ms, respectively. Nevertheless, these two samples have not been tested with the pinhole method and they had a higher thickness compared to the 1% -doped sample. In conclusion, as a compromise and following the results published in the literature (i.e. [Heu02a]), for emission cross sections, calculated via the Füchtbauer-Ladenburg, a radiative lifetime of $\tau = 0.40$ ms has been adopted.

In Fig. 5.17 the emission cross sections in three different spectral ranges are represented. They are all derived from the radiative decay from the same Er^{3+}-multiplet $^4S_{3/2}$. More precisely, the green fluorescence is consequence of the $^4S_{3/2} \rightarrow {}^4I_{15/2}$ decay, the emission around 850 nm is caused by the $^4S_{3/2} \rightarrow {}^4I_{13/2}$ transition and the $^4S_{3/2} \rightarrow {}^4I_{11/2}$ decay is responsible for the spectra at 1.2 µm. A fourth transition starting from the $^4S_{3/2}$-manifold can be detected at around 1.7 µm [Bar86, Pol89, Pol97], but the low sensitivity of the setup in this spectral range did not allow for the detection of the fluorescence. Furthermore, an even less intense transition is $^4S_{3/2} \rightarrow {}^4F_{9/2}$, resulting in emission around 3 µm.

In Figures 5.17a and 5.17b, the polarization-dependent emission cross sections of Er^{3+}:$LiLuF_4$ in the green spectral range are illustrated. The additional green line represents the ratio McC/FL of the spectra calculated with the FL and the McC methods, respectively. The main characteristic is the low factor which distinguishes the two spectra, which can be deduced by the average of this green line. The average factor is around 0.5, and it tends to increase with increasing wavelength in π-polarization. In this case, the difference could be enhanced by an underestimation of the radiative lifetime. Nevertheless, the structures present in this spectral range and around 540 and 550 nm have to be recognized as consequence of reabsorption which affected the emission measurements, fundamental for the FL method. In π-polarization, the strongest reabsorption is caused by the absorption peak at 540.7 nm, while in σ-polarization by the absorption peak at 542.3 nm. Furthermore, it is not excluded that in σ-polarization residues of π-polarization are present (e. g. peak at 551.5 nm).

Due to the not comparable resolution of the spectra (0.36 nm for the FL spectra and 0.15 nm for the McC spectra), it would be anyway not possible to estimate the accuracy of the lifetime value which has been used for the calculations of the FL spectra. In conclusion, although the McC results can suffer from an imprecise definition of the Stark levels (taken from [Kam86]), they have to be considered as the reliable ones for the calculation of gain spectra. Only starting at 553.3 nm for π-polarization and at 554 nm for σ-polarization, the FL spectra will be scaled to the McC results and will substitute them, in order to avoid the high signal-to-noise ratio of the region.

From the $^4S_{3/2}$-multiplet, also the emission spectra around 850 nm and 1.2 µm could be recorded with a resolution of 0.6 nm and the emission cross sections have been calculated

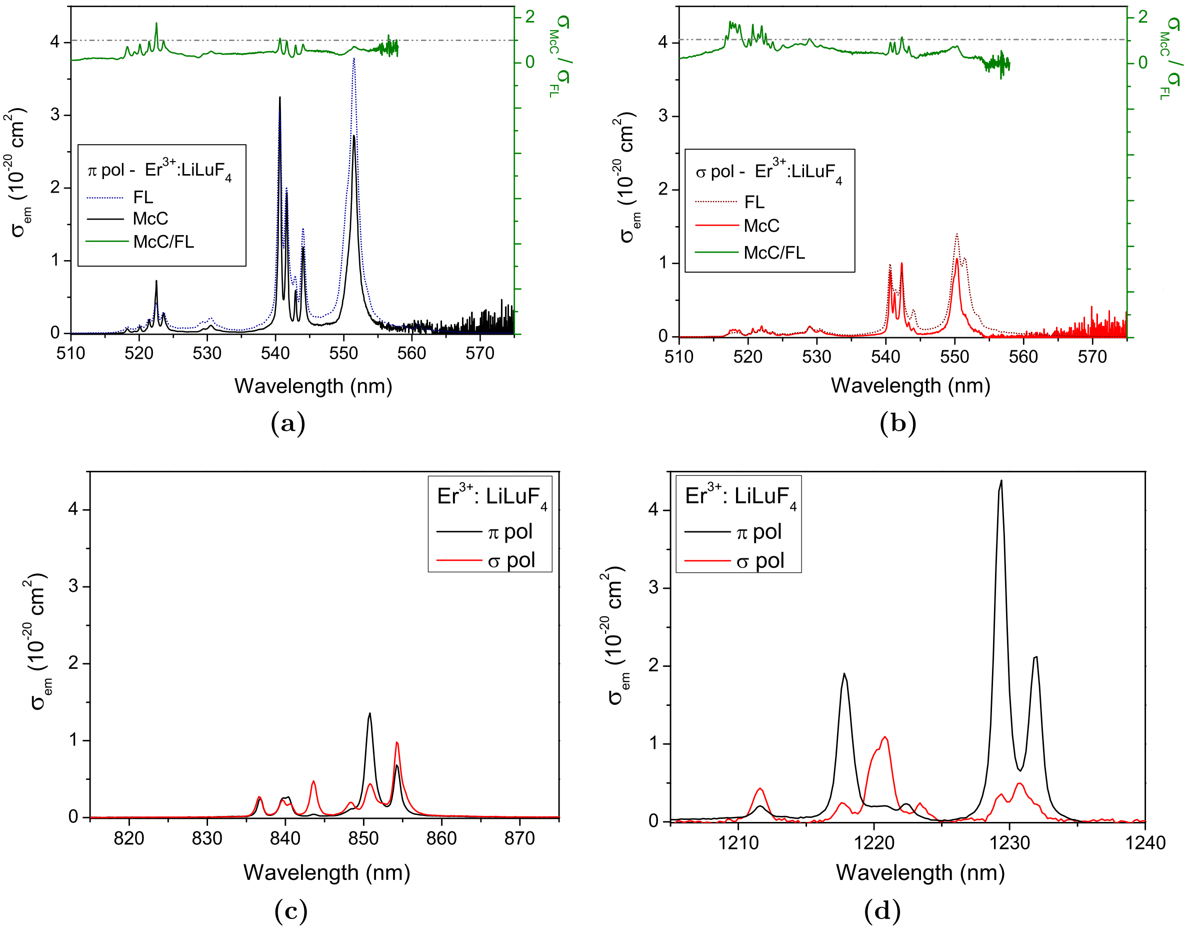

(a) **(b)**

(c) **(d)**

Figure 5.17: Emission cross sections of transitions starting from the ${}^4S_{3/2}$-multiplet in Er^{3+}:LiLuF$_4$. In (a) and (b), a comparison between the results calculated with the FL (with 1 at.% Er^{3+}:LiLuF$_4$) and McC (with 1.25 at.% Er^{3+}:LiLuF$_4$) methods (energy level scheme based on [Kam86]) is shown in π- and σ-polarization, respectively. On the right vertical axis the ratio of the two curves McC/FL is shown. This curve has been limited to 558 nm in order to hide the divergence due to the low signal-to-noise ratio of the McC curve. In both polarizations, the reliable spectra are those derived with the McC method. In (c) and (d), the results obtained around 850 nm and 1.2 µm, respectively, with the FL technique are depicted for both the polarizations.

via the Füchtbauer-Ladenburg method. Considering the four-level-structure of the energy levels involved in these transitions and the missing possibility to establish the absorption cross sections from the two final manifolds, a comparable spectra via reciprocity method could not be calculated. The emission cross sections are in the same order of magnitude than in the green spectral range.

Emission cross sections in Er^{3+}:LiLuF$_4$ have been calculated also in the 1.5 µm-range and they are reported in Fig. 5.18.

The difference between the results obtained via the FL and the McC method are much reduced in comparison to the visible spectral range. Furthermore, a difference in spectral resolution is still present (0.6 nm for the absorption spectra and 0.45 nm for the emission spectra) but less severe than in the visible spectral range and such a difference in spectral resolution is anyway not relevant in a spectral region where the peaks are broader.

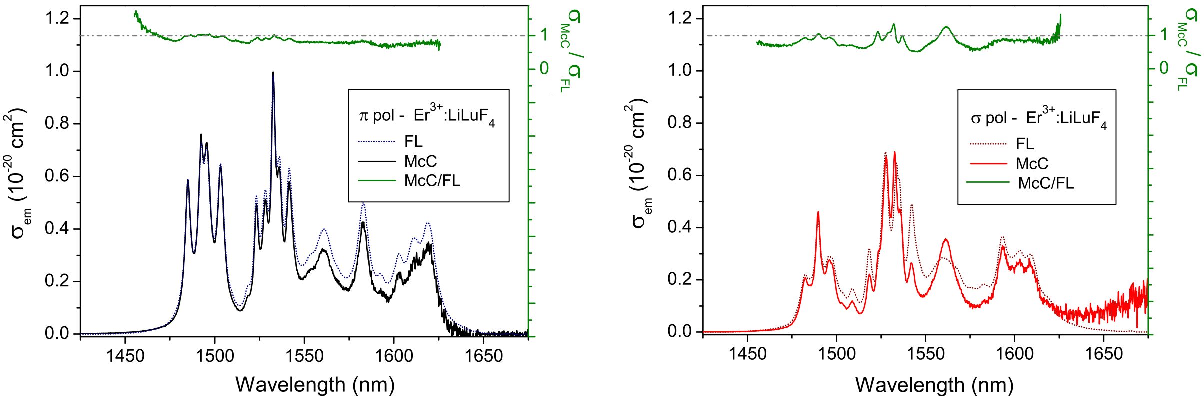

(a) **(b)**

Figure 5.18: Polarization-dependent emission cross sections of the transition $^4I_{13/2} \rightarrow {}^4I_{15/2}$ in Er^{3+}:LiLuF_4. The cross sections have been calculated from the emission spectra of a 1.3 at.% -doped Er^{3+}:LiLuF_4 crystal (FL) and the absorption spectra of a 1.25 at.% -doped Er^{3+}:LiLuF_4 crystal (McC). On the right vertical axis the ratio of the two curves McC/FL is shown. This curve has been limited to 1645 nm in order to hide the divergence due to the low signal-to-noise ratio of the McC curve. In both polarizations, the reliable spectra are those derived with the McC method.

The ratio McC/FL has in this case an average value closer to one than for the green spectral range in the two polarizations. The emission cross sections calculated from the absorptions were stronger in π-polarization than in σ-polarization. Nevertheless, the fluorescence signal was stronger in σ-polarization. This discrepancy has been corrected with the known ratio between the two polarization-dependent absorption spectra. Reabsorption effects are relevant and equally strong in both the peaks around 1490 nm and 1530 nm. In σ-polarization the McC/FL ratio is similar, but contrary to the π-polarization, the reabsorption effects are stronger also for the peak at 1560 nm.

As a consequence, also in this case it is not possible to estimate the quality of the lifetime measurement of the $^4I_{11/2}$-multiplet. For the calculation of the gain cross sections, the McC version of the emission cross sections will be considered, with the replacement only of the part after 1585 nm where the high signal-to-noise ratio of the rescaled FL measurements is needed.

Er^{3+}:LaF_3

For Er^{3+}:LaF_3, attention has been paid for the lifetime of the $^4S_{3/2}$-multiplet and the $^4I_{11/2}$-multiplet. Five sets of measurements have been performed at five different pumping wavelengths on two different crystals, at 0.6 at.% and 0.43 at.% of doping concentration. The pumping schemes are summarized in Fig. E.1b.

For the $^4I_{11/2}$-multiplet, five different pinhole sizes have been employed together with a measurement for the sample without any pinhole. The results are reported in Fig. 5.19. No strong reabsorption effects are detected, especially considering the relatively short lifetime measured in the case without pinhole, as shown in Fig. 5.19a. The data are averaged over results of single-exponential fits. The final value corresponds to 12.6 ms. This is roughly 13% longer than the value reported by *Weber* [Web67b]. An example of the observed single-exponential decay curve is reported in Fig. 5.19b: once it is plotted

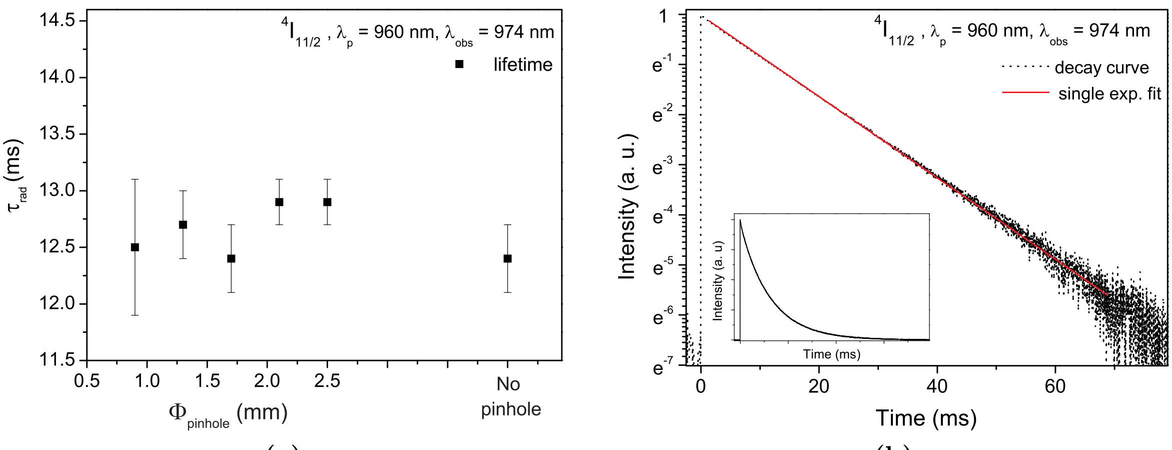

(a) (b)

Figure 5.19: Radiative lifetime of the $^4I_{11/2}$-multiplet in 0.6 at.% -doped Er^{3+}:LaF_3. In (a), the results of the pinhole measurements with five different diameters are reported. For comparison, the result obtained with the same sample but without pinhole is shown. In (b), an example of the exponential decay curve of the multiplet (from the no-pinhole measurement), fitted by an exponential curve, is reported on semilogarithmic scale. In the inset the same decay curve is reported on linear scale.

on semilogarithmic scale, while in the inset the same curve is represented in linear scale.

Considering the lifetime of the $^4S_{3/2}$-manifold, the fluorescence has always been observed in the green spectral range, more precisely at 539 nm. The pinhole method has been applied for the measurements with the excitation wavelengths of 520 nm and 483 nm. The results of the measurements performed with an excitation wavelength of 520 nm are reported in Fig. 5.20. Despite the extremely low doping concentration of the samples, all the decay curves were not single exponential. A double exponential fit has been calculated in all cases. The longest of the two resulting lifetimes has been considered as the effective lifetime of the $^4S_{3/2}$-multiplet, corresponding always to the value obtained via a linear fit in semilogarithmic scale of the tail of the decay curve. For the 0.6 at.% -doped sample, the value of the short lifetime was mostly included between 200 and 265 µs. As a difference compared to what obtained with Er^{3+}:$LiLuF_4$, here some effects of reabsorption are present. This is a remarkable result because the Er^{3+}-ions density in these LaF_3 samples is lower than in a 1 at.% Er^{3+}:$LiLuF_4$. Therefore, a linear fit and an extrapolation to a diameter of the pinhole corresponding to 0 mm has been calculated, obtaining a value of 0.65 ms. The presence of stronger reabsorption problems than in $LiLuF_4$, is also proven by the higher difference between the lifetimes measured with the pinholes and the data obtained in a bulk sample (see Fig. 5.20a). The lifetime measured without pinhole is 0.83 ms. This value fits very well to the data reported by *Weber* [Web67b]. Nevertheless, the value considered as reliable and adopted as lifetime of the $^4S_{3/2}$-manifold in the calculation of emission cross sections via the Füchtbauer-Ladenburg method, is the result of the pinhole method, because it is believed to be a reabsorption-free value.

Furthermore, especially in the decay curves measured with pinholes with relatively large diameters, a non-δ-shaped population of the level is evident, but in a much reduced way than in Fig. 5.12b. If a double-exponential decay fit as in Eq. (5.10) is performed, or, alternatively, a single-exponential fit of the rising ramp, a result of roughly 15 µs for the lifetime (or the short lifetime in the double-exponential decay fit) is obtained. This

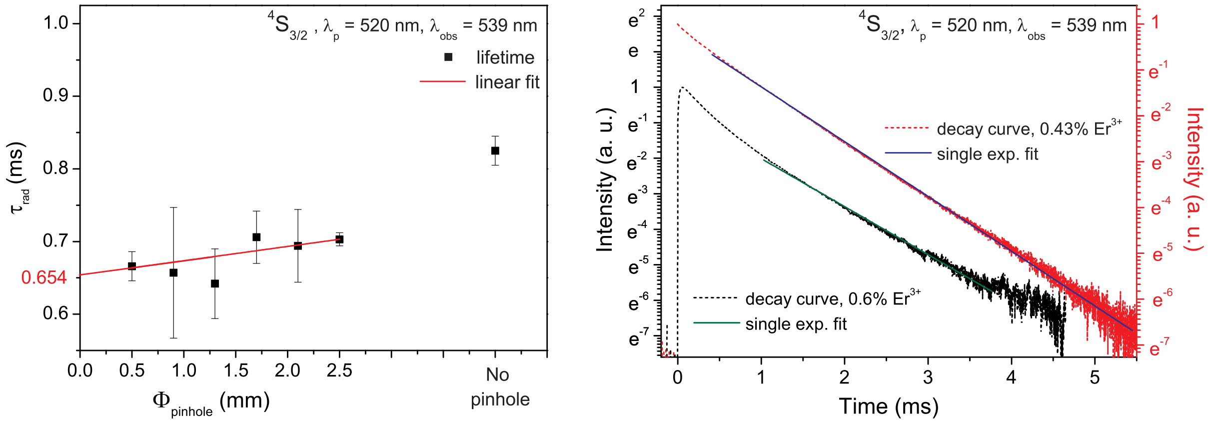

(a) (b)

Figure 5.20: Radiative lifetime of the $^4S_{3/2}$-multiplet in Er^{3+}:LaF_3. In (a), the results of the pinhole measurements with six different diameters are reported. These measurements have been performed with a 0.6 at.% Er^{3+}-doped crystal. As a comparison, the result obtained without pinhole is also shown. A linear fit has been performed in order to extrapolate the reabsorption-free lifetime value for a zero-diameter pinhole. In (b), two examples of the decay curves of the multiplet, fitted by a delayed exponential curve, are reported on two different semilogarithmic scales. The red curve has been measured without pinhole on the 0.43 at.% Er^{3+}-doped sample and results less strongly double-exponential (the blue linear fit can be performed after a short delay with a good correspondence), while the black curve has been measured with a 2.1 mm-wide pinhole in the 0.6 at.% -doped sample and shows a stronger double-exponentiality (the green linear fit can be performed only on a delayed, short portion of the curve)

cannot represent an influence of the $^2H_{11/2}$-multiplet, which can be directly pumped at 520 nm, because it is expected to decay non-radiatively. A possible explanation for this could be connected to the double-exponential effect in the decay curves: if a recycling of excitation is sustained by lower energy levels via ETU processes, a delayed population of the $^4S_{3/2}$-multiplet could be a consequence.

Finally, in Fig. 5.20b two different exponential curves are reported, in order to show the stronger double-exponential effects and the more pronounced non-δ of the rise evident in the curve measured in the 0.6% -doped LaF_3 crystal, in comparison to the decay curve measured in the bulk of a second sample, which is a 0.43 at.% Er^{3+}-doped crystal. Here the single-exponential fit can be performed already less than 1 ms after the pump pulse, instead of after 1.5 ms for the curves measured with pinhole and the other sample. For clarity in showing the two curves, two different intensity scales have been adopted.

The pinhole method has been applied again, varying the excitation wavelength to 483 nm. Seven different sizes of pinholes have been used on the 0.6% -doped sample, and a measurement has been performed also without any pinhole. The results are represented in Fig. 5.21a and they are partly surprising: in this case, no significant reabsorption effects are noticeable, and an average lifetime has been calculated from the eight available values, which nevertheless is less than 5% different than the previous one (0.68 ms instead of 0.65 ms). Furthermore, the decay curves show a similar strong double-exponential behavior as before, therefore the lifetimes of the $^4S_{3/2}$-multiplet have been once more considered as the longest of the two resulting values. The direct excited manifold in this case is $^4F_{7/2}$, and the rising ramp typical of Stokes-fluorescence is visible, with a single-exponential behavior with a lifetime of ~15 µs. In [Web67b], the lifetime of the

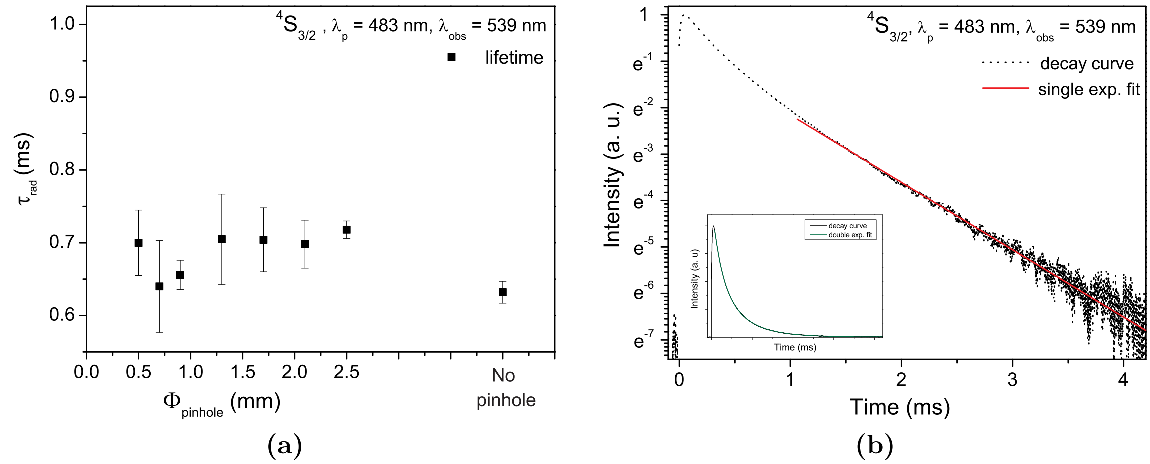

Figure 5.21: Radiative lifetime of the $^4S_{3/2}$-multiplet in a 0.6% -doped Er^{3+}:LaF_3 when pumped at 483 nm. In (a), the results of the pinhole measurements with seven different diameters are reported. As a comparison, the result obtained without pinhole is shown. No reabsorption effects are evident and the an average value of 0.68 ms has been calculated. In (b), an example of the decay curve of the multiplet, fitted by a delayed single-exponential curve, is reported on semilogarithmic scale (curve from the no-pinhole measurement). In the inset, the same curve is depicted on a linear scale and fitted by a double-exponential curve. In doing so, the longest lifetime corresponds to the lifetime obtained in the main graph.

$^4F_{7/2}$-multiplet is measured with the same technique (observing the rising ramp of the decay curve of a lower energy level, when the $^4F_{7/2}$-multiplet is directly pumped) but at a temperature of 77 K where the authors recognized a lifetime shorter than 5 µs. A room-temperature measurement reported in [Pol96a] for Er^{3+}:$LiYF_4$ for the $^4F_{7/2}$-multiplet defines a lifetime of 5 µs. In Fig. 5.21b, an example of decay curve showing the delayed population (rising ramp) and a double-exponential decay behavior is depicted. The main graph is in semilogarithmic scale and it shows the possibility of performing a single-exponential fit after 1.5 ms from the population of the multiplet. The same lifetime value of 0.65 ms is obtained if a double-exponential fit is performed and the longest of the two resulting lifetimes is considered to be valid. This is represented for the same curve, on linear scale, in the inset of Fig. 5.21b.

In the case the excitation light was at 405 nm, the fluorescence at 539 nm was not sufficient to perform measurements with a pinhole. The results (see Fig. 5.22a) show an even stronger double-exponential behavior which, together with the low signal, does not allow to find a straightforward connection with a delayed single-exponential fit. Nevertheless, the average of the longest lifetime resulting from a multitude of double-exponential fits matches the previously mentioned lifetimes with an inaccuracy of $\sim 15\%$. Two further results which suggest the possibility of a different dynamics coordinating the recycling of excitation via ETU processes with the pump tuned at 405 nm, are a longer rising time of the ramp for the population of the $^4S_{3/2}$-multiplet ($\sim$ 22 µs) and a longer second lifetime derived from the double-exponential fit ($\sim$ 300 µs). Following the same rule of Stokes-fluorescence, the lifetime measured on the rising ramp could represent the lifetime of the $^2H_{9/2}$-multiplet, addressed directly by the pumping wavelength, although this manifold and all those located between it and the $^4S_{3/2}$-multiplet are all usually considered as thermally coupled. For comparison, in [Web67b] a value between 30 and 40 µs can be extracted

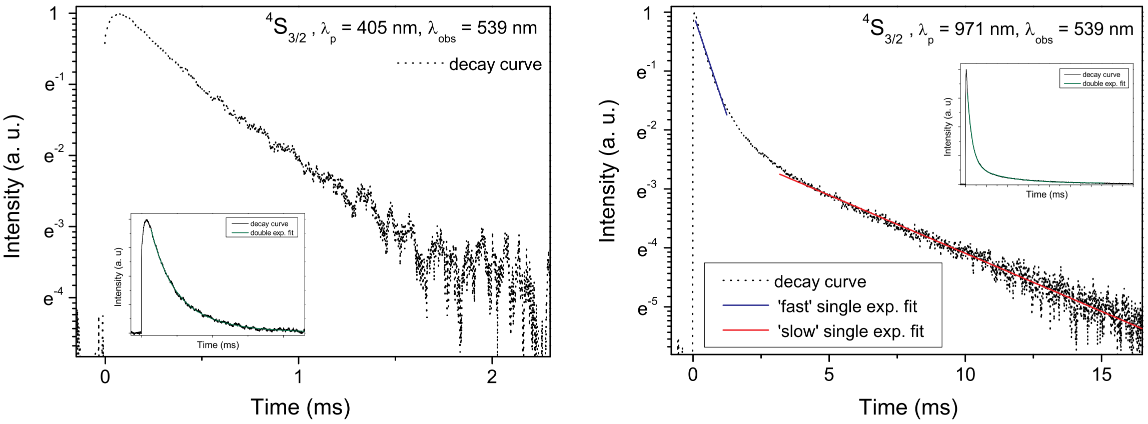

(a) (b)

Figure 5.22: Decay curves of the $^4S_{3/2}$-multiplet in a 0.6% -doped Er^{3+}:LaF$_3$, when pumped at 405 nm and 971 nm. In (a), an example of the decay curve of the $^4S_{3/2}$-multiplet, when pumped at 405 nm, is reported on semilogarithmic scale. A single-exponential fit of the tail was not possible, therefore, in the inset, a double-exponential fit of the same curve on a linear scale is represented. In (b), an example of the decay curve of the $^4S_{3/2}$-multiplet, when pumped at 971 nm, is reported on semilogarithmic scale. Two linear fits are reported: a short-living one in the first milliseconds of time and a long-living one in the following time range. A double-exponential fit of the same curve on a linear scale is also represented. The two lifetimes values do not correspond to each other for the two different ways of calculation.

by a plot of lifetimes in Er^{3+}:LaF$_3$ in function of temperature, while in Er^{3+}:LiYF$_4$ it is reported to be 10 µs ([Pol96a]). As a conclusion, 22 µs is a plausible value for the lifetime of the $^2H_{9/2}$-multiplet in Er^{3+}:LaF$_3$.

As in the case of Er^{3+}:LiLuF$_4$, a few measurements have been carried out in order to show the behavior of the green fluorescence from the $^4S_{3/2}$-manifold when it is upconversion-pumped at 971 nm. As it can be seen in Fig. 5.22b, the curve plotted on semilogarithmic scale is strongly non-single-exponential and, differently than in other cases, two distinct slopes can be measured which result in two lifetime values which do not correspond to those fitted by a double-exponential curve, represented in the inset, on linear scale. More precisely, the average values which can be measured are: 5.3 and 0.75 ms in the case of the linear fit on semilogarithmic scale and 3.5 and 0.46 ms in the case of a double-exponential fit on linear scale. The longest lifetime corresponds in this case to $\sim \tau(^4I_{11/2})/2$ (considering the value in literature and the one measured in this work, $\tau(^4I_{11/2})/2 \sim 5.5$ and 6.3 ms, respectively) and it could be explained via the same feeding-dependence of the $^4S_{3/2}$-manifold on the $^4I_{11/2}$-multiplet, as previously explained for Er^{3+}:LiLuF$_4$. At the same time, the steepest curve corresponds to a lifetime which is of the same order of magnitude of the usual radiative lifetime of the $^4S_{3/2}$-multiplet in Er^{3+}:LaF$_3$ when it is directly pumped. But this has not been measured in Er^{3+}:LiLuF$_4$, where the second lifetime was a relatively short value, attributed to ETU (see Fig. 5.16b). Furthermore, the strong non-exponentiality in Fig. 5.22b should not be that evident, if the behavior is expected to be similar to the one in Er^{3+}:LiLuF$_4$.

Part of the work in measuring the lifetime of these manifolds contributed to the calculation of emission cross sections in Er^{3+}:LaF$_3$ crystals.

For the emission cross sections of the $^4S_{3/2}$ and the $^4I_{13/2}$-multiplet calculated via the FL method, values of 0.67 ms and 15 ms, respectively have been adopted as radiative lifetime values. The first is the result of an average over the different measurements performed in this work. Nevertheless, this value is less than 70% of the one measured by *Weber* (1.1 ms, [Web67a]) and more than 30% longer than the one measured by *Krupke and Gruber* (0.5 ms, [Kru64]). The value of the radiative lifetime of the $^4I_{13/2}$-multiplet is the average of the data derived by four different publications [Web67b, Web67a, Car86, Pay92].

The branching ratios for the $^4S_{3/2}$-multiplet are also fundamental for the calculation of the emission cross sections and the adopted values are those calculated in [Web67a] and reported in Tab. 5.2. For the McC calculations, the energy level positions for the $^4S_{3/2}$, $^4I_{13/2}$ and $^4I_{15/2}$-manifolds correspond to an average of the values reported in different publications [Kru63, Kru64, Car72, Neo85, Car86].

The emission cross sections of transitions starting from the $^4S_{3/2}$-multiplet in Er^{3+}:LaF_3 are depicted in Fig. 5.23.

In the Figures 5.23a and 5.23b a comparison of the results obtained with the FL and the McC methods is represented. The curves derived from the McC spectra have been limited in extension, in order to not display the typical strong divergence of this kind of spectra in the long-wavelength region. In the case of Er^{3+}:LaF_3, differently than for Er^{3+}:$LiLuF_4$ crystals, the resemblance between the spectra derived via the two methods is much higher and on the average the ratio McC/FL is less than one. This can be originated by an underestimated radiative lifetime of the $^4S_{3/2}$-multiplet. The strongest reabsorption peaks are evident in both polarizations in the regions around 517 nm and 540 nm. If an average value of the ratio McC/FL is considered in the regions without reabsorption or excessive noise level in both polarizations, it emerges that the FL spectra are roughly 25% higher than the McC spectra. This could lead to the conclusion that the real radiative lifetime should be 25% longer than the one adopted in the FL calculations, which means it should be closer to the value proposed by *Weber* [Web67a]. Furthermore, if it is considered that the resolution of the fluorescence spectra is lower than the one of the absorption spectra needed for the McC study (0.3 nm vs 0.15 nm), the FL spectra would be expected to show even higher peaks, leading to an even lower difference between Weber's value and the one estimated as real radiative lifetime of the $^4S_{3/2}$-multiplet. This is valid only if the uncertainty of other parameters involved in the calculations (e.g. position of the energy levels, branching ratios) are considered much lower than the contribution of the value of the radiative lifetime.

Consequently, for the determination of the gain spectrum in this wavelength range, the McC spectrum will be kept as a reference until $\lambda = 541$ nm. The long-wavelength part of

Transition	Spectral region	$\beta_{i,j}$
$^4S_{3/2} \rightarrow {}^4I_{15/2}$	550 nm	0.662
$^4S_{3/2} \rightarrow {}^4I_{13/2}$	850 nm	0.268
$^4S_{3/2} \rightarrow {}^4I_{9/2}$	1.7 µm	0.028
$^4S_{3/2} \rightarrow {}^4I_{11/2}$	1.2 µm	0.020

Table 5.2: Branching ratios of the multiplet $^4S_{3/2}$ in Er^{3+}:LaF_3, calculated via Judd-Ofelt method [Web67a] and spectral region of the consequent fluorescence.

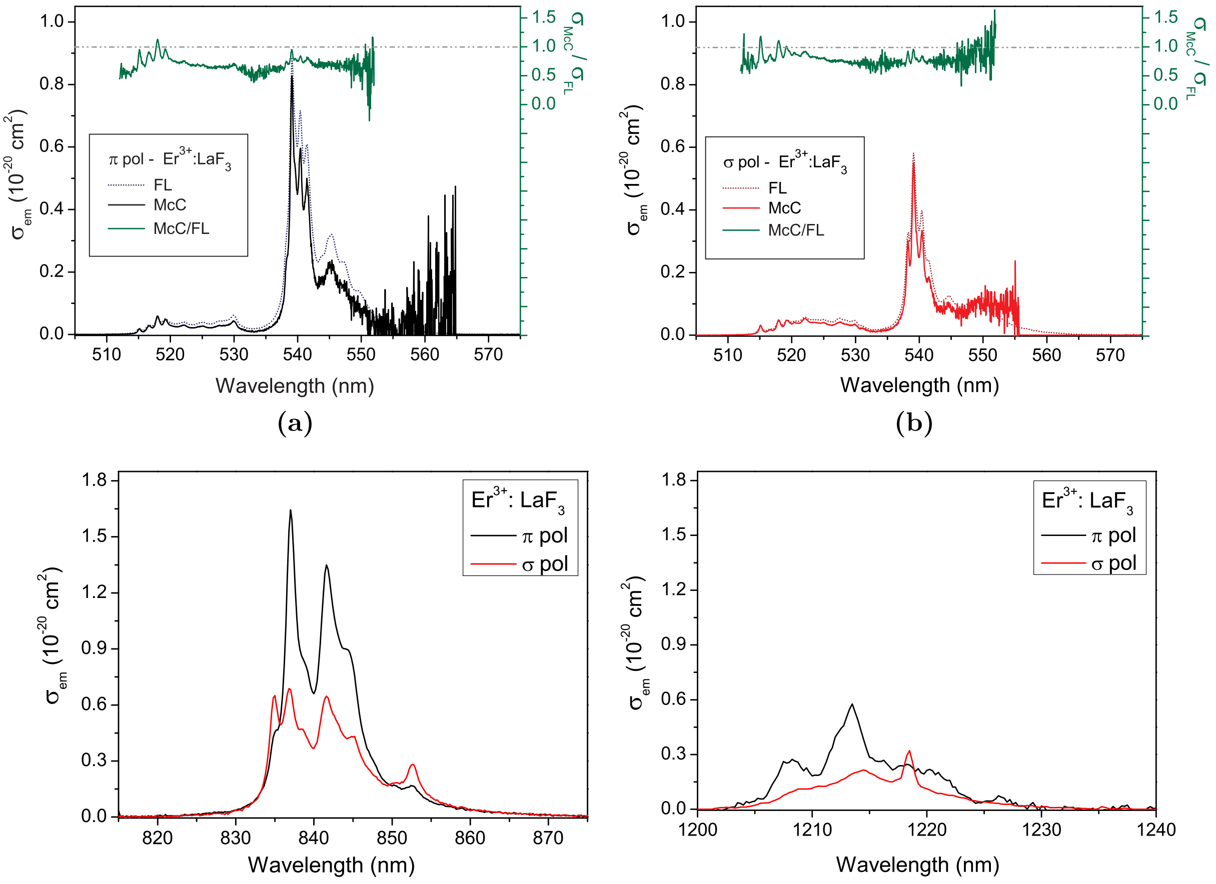

(a) (b)

(c) (d)

Figure 5.23: Emission cross sections in 0.6 at.% Er^{3+}:LaF_3 crystals from the $^4S_{3/2}$-multiplet. In (a) and (b), a comparison between the results of the FL and McC methods is shown in π- and σ-polarization, respectively. On the right vertical axis the ratio of the two curves McC/FL is shown. This curve and the McC curve have been limited in order to hide the divergence due to the low signal-to-noise ratio of the McC curve. In both polarizations, the reliable spectra are those derived with the McC method. In (c) and (d), the results obtained around 850 nm and 1.2 µm, respectively, with the FL method are depicted for both the polarizations.

the spectrum will be taken form the rescaled FL curve.

In the Figures 5.23c and 5.23d the emission cross sections from the same multiplet in the region around 850 nm and 1.2 µm, calculated via the FL method, are illustrated. These are four-level transitions and the resolution of the measurements is 0.6 nm and 0.75 nm, respectively. Compared to the results in $LiLuF_4$, also in this spectral range the cross sections in Er^{3+}:LaF_3 are lower and the highest ones are in the 850 nm region.

For Er^{3+}:LaF_3 crystals, also the emission cross sections for the transition $^4I_{13/2} \rightarrow ^4I_{15/2}$ have been calculated via both FL and McC methods.

In Fig. 5.24, both the polarizations are separately reported, showing the comparison between the results of the McC and those of the FL method. Also in this spectral range, the resemblance of the results obtained with this method is stronger than in Er^{3+}:$LiLuF_4$ and especially in σ-polarization. In this polarization, the ratio McC/FL has an average value similar to one, with the exceptions of a few regions where reabsorption is present,

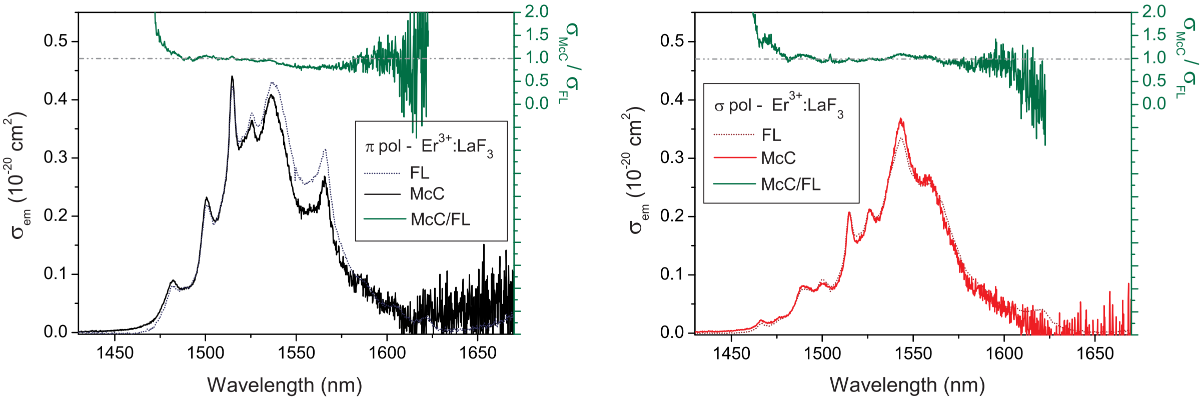

(a)

(b)

Figure 5.24: Emission cross sections in a 0.6% - and a 0.43% -doped Er^{3+}:LaF_3 from the $^4I_{11/2}$-multiplet. In (a) and (b), a comparison between the results of the FL (with the higher Er^{3+}-doped sample) and McC (with the lower Er^{3+}-doped sample) methods is shown in π- and σ-polarization, respectively. On the right vertical axis the ratio of the two curves McC/FL is shown. This curve has been limited in order to hide the divergence due to the high signal-to-noise of the McC curve. In both polarizations, the reliable spectra are those derived with the McC method.

namely around 1504 and 1543 nm. In the border regions, where divergence due to a low signal-to-noise ratio is present, the McC/FL ratio has not been shown. The results would confirm the reliability of the parameters involved in the estimations of the two spectra, included the average radiative lifetime taken from the literature. In π-polarization, reabsorption is particularly evident in certain regions, such as around 1515 nm. Also in this case, for both polarizations, the McC spectrum is considered as a reference for emission cross sections up to 1546 nm. For longer wavelengths, the FL spectrum will be scaled to the McC one, in order to avoid its artifacts due the low signal-to-noise ratio.

Er^{3+}:BaY_2F_8 and Er^{3+}:$BaYLuF_8$

To estimate the emission cross sections via the FL method for Er^{3+}:BaY_2F_8 and Er^{3+}:$BaYLuF_8$, radiative lifetime measurements have been carried out on these crystals regarding mainly the $^4S_{3/2}$- and $^4I_{13/2}$-manifolds. A few examples of detected decay curves are reported in Fig. 5.25.

To measure the decay time of the $^4S_{3/2}$-manifold, it was possible to inband-pump at 520 nm and observe the fluorescence around 550 nm. For both the crystal hosts the decay curve was not perfectly single-exponential. Nevertheless, single-exponential fits have been performed with a certain delay (0.10 and 0.70 ms, respectively for Er^{3+}:BaY_2F_8 and Er^{3+}:$BaYLuF_8$). The average radiative lifetime of the $^4S_{3/2}$-multiplet, measured without employing the pinhole method in a 1 at.% Er^{3+}-doped BaY_2F_8 crystal, gave a result of 0.58 ms, while for a 0.5 at.% Er^{3+}-doped $BaYLuF_8$ crystal the result was 0.62 ms. A mismatch of less than 10% confirms the similarity of the two crystal hosts, despite the different doping concentration, which could be the responsible of the slightly shorter lifetime in Er^{3+}:BaY_2F_8. Indeed, if the measurement is repeated in the same conditions with a 1.3 at.% Er^{3+}-doped $BaYLuF_8$, the decay lifetime results 15% shorter (0.53 ms), possibly due to concentration quenching.

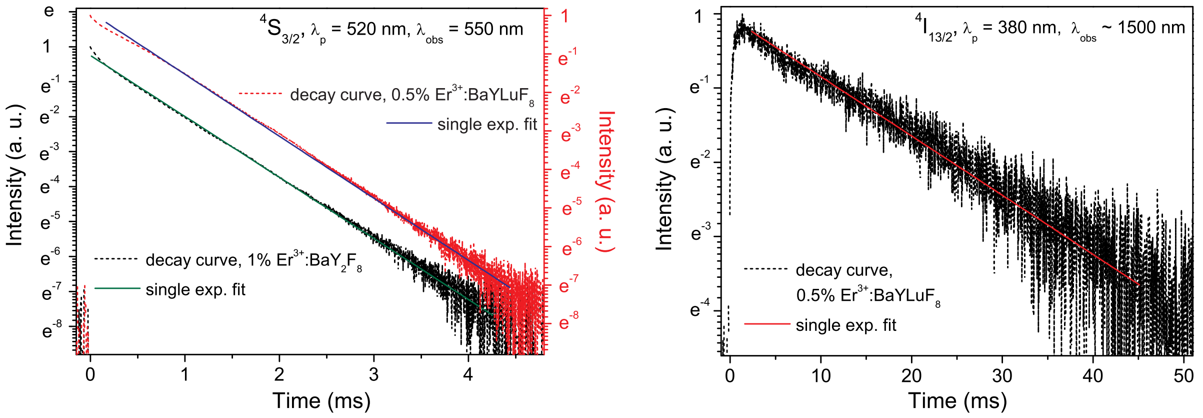

(a) (b)

Figure 5.25: Radiative lifetime of the $^4S_{3/2}$- and $^4I_{13/2}$-multiplet at 550 nm and 1.5 µm in 1% Er^{3+}-doped BaY$_2$F$_8$ and 0.5% Er^{3+}-doped BaYLuF$_8$. In (a), one example of the exponential decay curve of the $^4S_{3/2}$-multiplet in each crystal, fitted by an exponential curve, is reported on semilogarithmic scale. In (b), an example of the decay curve of the $^4I_{13/2}$-multiplet in Er^{3+}:BaYLuF$_8$ fitted by an exponential is reported.

Furthermore, Er^{3+}:BaY$_2$F$_8$ and Er^{3+}:BaYLuF$_8$ show a longer radiative lifetime of the $^4S_{3/2}$-multiplet compared to Er^{3+}:LiLuF$_4$, also because of the relative lower Er^{3+}-ions density at the same doping level. This could lead to advantages in laser experiments in the green spectral range. These results correspond to those found in literature: for low doping concentration of Er^{3+}-ions in BaY$_2$F$_8$, 630 µs, 600 µs and 0.61 ms (in the units chosen by the authors) are reported [Kno92, Kam90a, Bar05].

Regarding the radiative lifetime of the $^4I_{13/2}$-multiplet, measurements have been performed with the 0.5% -doped Er^{3+}:BaYLuF$_8$ sample. In this case, instead of inband-pumping, a wavelength in the UV region has been chosen, as reported in Fig. 5.25b. As expected, no pure single-exponential decay with a low signal-to-noise ratio has been detected. Nevertheless, a delayed linear fit on semilogarithmic scale could be performed. The average radiative lifetime value corresponds to 12.8 ms. This multiplet is typically much less severely affected by concentration quenching at these levels of doping concentration. A similar result (12.7 ms) has been obtained repeating the same kind of measurements with a 1.3 at.% -doped crystal. The values in the literature concerning Er^{3+}:BaY$_2$F$_8$ span a relatively wide range, and the value obtained in this work for Er^{3+}:BaYLuF$_8$ is compatible: 13.6 ms, 10.6 ms (but at 10% doping concentration of erbium), 16.4 ms, 10.8 ms ([Pol89, Kno92, Toc07, Bar05]). Collaborators have performed similar measurements on the 1.3 at.% -doped crystal, with a pumping wavelength of 980 nm resulting in a lifetime of 14.6 ms [Par13].

As mentioned concerning absorption cross sections, in biaxial crystals oriented along the refractive index coordinate system, polarization-dependent measurements have a dependency on the sum of two exponential terms in function of the angle between the refractive-index axis and the two optic axes. Consequently, the sum is dependent on the size of the crystal. Although the dependency can be weak, it is not *a priori* definable and therefore also in the case of emission cross sections, the results will be presented as an estimation and addressed with an asterisk.

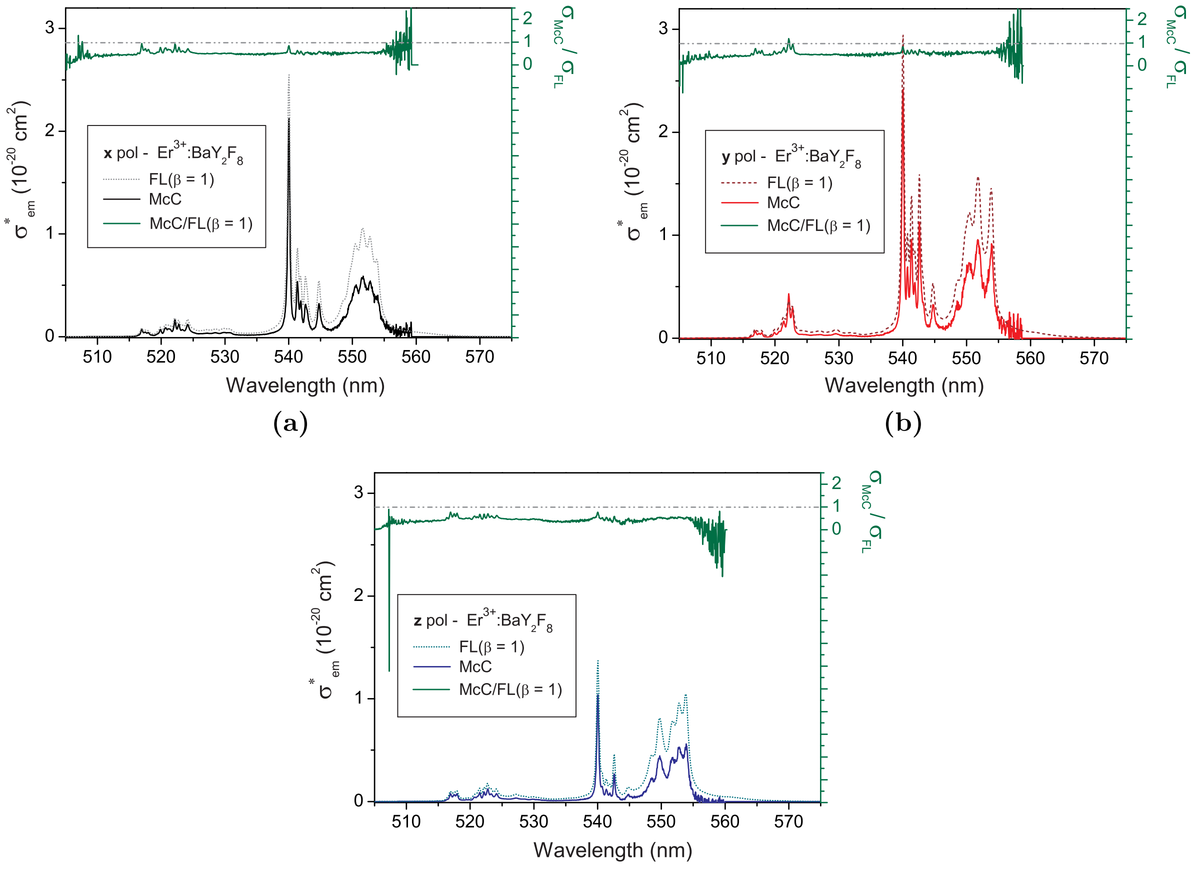

(a)

(b)

(c)

Figure 5.26: Estimated emission cross sections of the $^4S_{3/2}$-multiplet in a 1 at.% Er^{3+}-doped BaY_2F_8 crystal. The cross sections are only estimated (signed with a $*$) because of the biaxial nature of the crystal host. A comparison between the results of the FL (with branching ratio $\beta = 1$) and McC methods is shown in the three polarizations, respectively. On the right vertical axis the ratio of the two curves McC/FL is shown. The McC curves have been limited in order to hide the divergence due to the low signal-to-noise ratio. In this case, the McC/FL ratio can be used as an estimation for the unknown β value. For the three polarization-dependent measurements, the reliable spectra are those derived with the McC method.

In Fig. 5.26, the results for the estimated emission cross sections for Er^{3+}:BaY_2F_8 in the green spectral range are summarized. The three different polarization-dependent spectra are divided and a comparison between the FL and the McC methods results is shown. Differently than for the two previous crystal hosts, the branching ratio for the transition $^4S_{3/2} \rightarrow {}^4I_{15/2}$ in Er^{3+}:BaY_2F_8 is not present in literature. Therefore, in this case, the McC/FL ratio has not only the duty to show the spectral ranges where reabsorption is present, but also to give an estimation of the branching ratio β of the transition. Indeed, in the FL spectra, initially the branching ratio can be considered as $\beta = 1$. Then, from the McC/FL ratio, the real value of β for a certain transition can be evaluated. For the McC spectra, the energetic positions for the $^4S_{3/2}$-, $^4I_{15/2}$- and $^4I_{13/2}$-multiplets have been calculated as an average of the values reported in different publications [Joh71, Pol89, Kam90a, McF94, Bar05].

For **x**- and **z**-polarizations spectra, reported in Figures 5.26a and 5.26c, the reabsorption effects are stronger in the short-wavelength region around 520 nm and on the highest peak of the manifold around 540 nm. In Fig. 5.26b, the **y**-polarization spectrum is depicted. Here reabsorption is particularly strong on the peaks at ~ 522 nm and ~ 554 nm.

Considering that the McC/FL ratio is in the polarization-dependent spectra lower than one, it is allowed to assume that these values can be considered a valid approximation of β, calculating an estimated $\beta_{\text{estim.}}$ such as:

$$\beta_{\text{estim.}} = \frac{\sigma_{\text{em}}^{*McC}}{\sigma_{\text{em}}^{*FL}(\beta = 1)}. \tag{5.13}$$

Furthermore, if an average of the McC/FL ratio on the spectral regions where reabsorption is not evident is calculated, for the three polarizations the results are similar and the average value is 49%. If the two FL spectra in **x**- and **z**-polarization are matched to the respective McC spectra in the long-wavelength range, where reabsorption is not expected to have influence, the β value can be raised to 55%. If the β known for the two previous crystal hosts is considered as a reliable reference (0.668 and 0.662 in Er^{3+}:LiLuF_4 and Er^{3+}:LaF_3, respectively), a deviation of more than 15% is evident. Nevertheless, considering the maximum possible accuracy reachable in this kind of estimations, a β of 55% is eligible. For the calculation of gain spectra, the McC spectrum will be kept as a reference up to either 535 nm or 585 nm (depending on the polarization), where then the rescaled FL spectrum will be adopted. Moreover, in [Bar05] the spontaneous emission coefficients A_{il} between i- and l-multiplets in Er^{3+}:BaY_2F_8 introduced in Sect. 2.2.1 are summarized. If the measured radiative lifetime of the $^4\text{S}_{3/2}$-multiplet 0.58 ms is adopted as parameter in Eq.(2.7), the branching ratio for the transition $^4\text{S}_{3/2} \rightarrow {}^4\text{I}_{15/2}$ can be calculated via Eq. (2.8) and a value of 79% is obtained. This value renders the estimation of β via derivation from combined FL and McC methods even less reliable. Nevertheless, uncertainty in any Judd-Ofelt calculation is also relatively high.

Considering that the exact position of the energy levels and the branching ratios in Er^{3+}:BaYLuF_8 are unknown, no emission cross sections have been calculated. Nevertheless, a direct comparison with the results in Er^{3+}:BaY_2F_8 can be carried out. The three polarization-dependent fluorescence spectra in the green spectral range, normalized at the maximum in **x**-polarization are reported in Fig. 5.27.

The absorption spectra, apart from slight differences in the position of a few peaks, are very similar to each other, when the same polarizations for every host are compared to each other. Quantitatively, the $\sigma^*_{\text{abs}}(\text{BaY}_2\text{F}_8)/\sigma^*_{\text{abs}}(\text{BaYLuF}_8)$ ratio is roughly 90% for all the three polarizations, even up to 95% for **y**-polarization. Nevertheless, the ratio of the Boltzmann population of the involved multiplets can still be different. In the case also the Boltzmann populations were similar, a very similar McC spectrum would be expected for Er^{3+}:BaYLuF_8 when compared to Er^{3+}:BaY_2F_8, which means similar peak emission cross sections in the order of $1 - 3 \cdot 10^{-20}\,\text{cm}^2$.

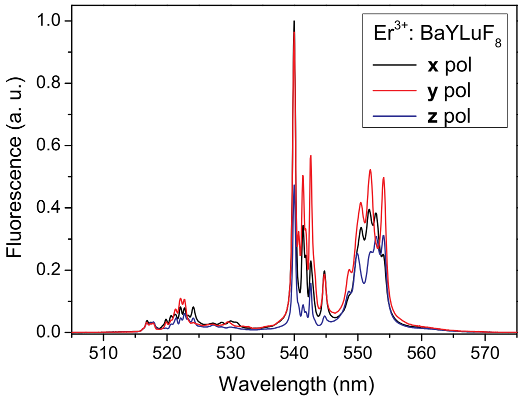

Figure 5.27: Polarization-dependent fluorescence spectrum of a 0.5 at.% Er^{3+}-doped $BaYLuF_8$ in the green spectral range. The emission cross sections could not be estimated because of the unknown branching ratio and the uncertainty about the exact position of the energy Stark levels of the involved multiplets.

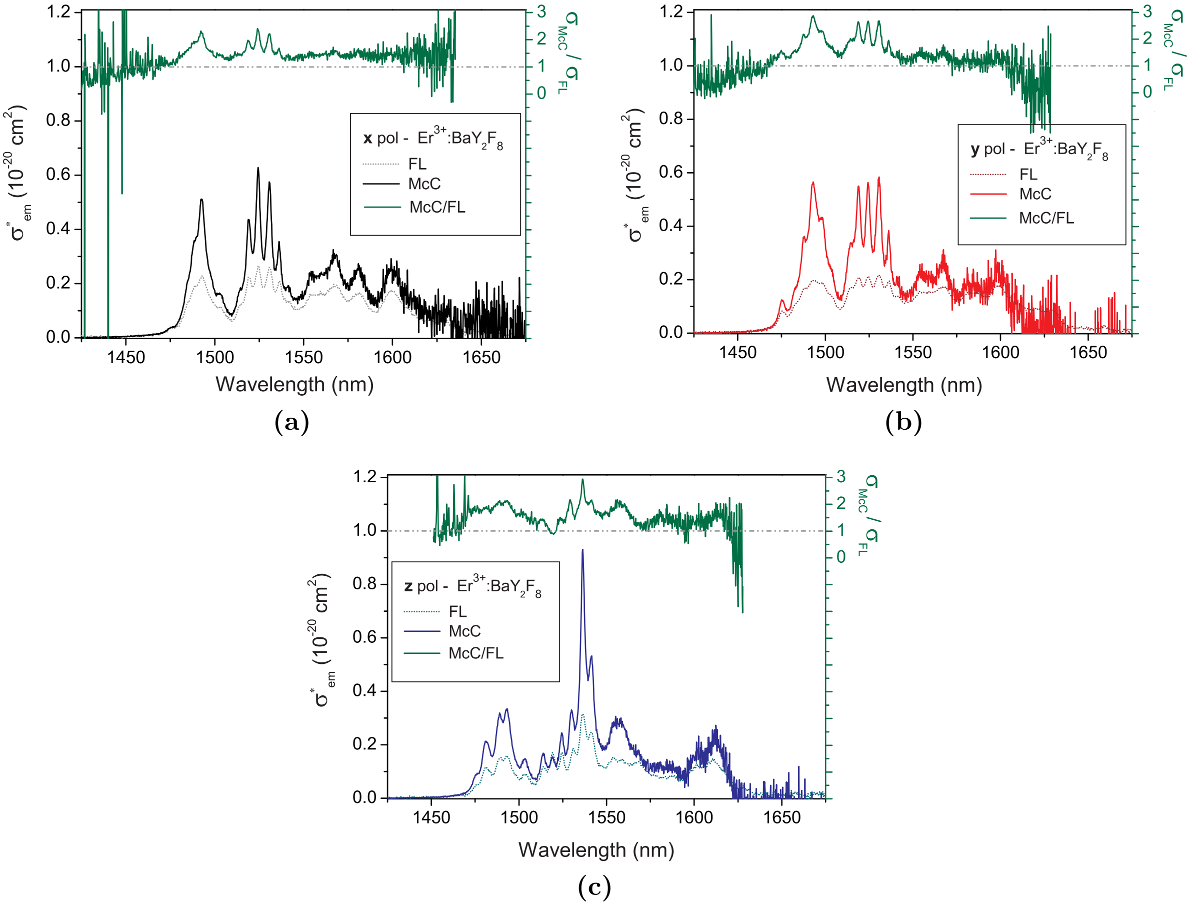

(a)

(b)

(c)

Figure 5.28: Estimated emission cross sections in a 1% Er^{3+}-doped BaY_2F_8 crystal from the $^4I_{13/2}$-multiplet. The cross sections σ^*_{em} are only estimated because of the biaxial nature of the crystal host. A comparison between the results of the FL and McC calculations is shown in the three polarizations, respectively. On the right vertical axis the McC/FL ratio is shown and it has been limited in order to hide the divergence due to the low signal-to-noise of the McC curves. The most accurate estimation, considering the limits in a biaxial crystal, is still given by the McC calculations.

As a conclusion, for Er^{3+}:$BaYLuF_8$ no gain spectrum can be calculated, while for Er^{3+}:BaY_2F_8 the McC curves are to be considered as a reference for the emission cross sections up to 545 nm, because for longer wavelengths the FL spectrum can be easily perfectly rescaled and employed.

The erbium $^4I_{13/2} \rightarrow ^4I_{15/2}$ transition has been studied also in these two host crystals. A comparison between results obtained via the FL and McC methods in Er^{3+}:BaY_2F_8 are represented in Fig. 5.28, separated according to the polarization. Emission cross sections are only estimated because of the biaxial nature of the crystal host.

Similarly to the results obtained in Er^{3+}:LaF_3, on the average the two methods have given comparable results. Nevertheless, on the two groups of peaks around 1490 and 1525 nm extremely strong reabsorption is evident, with peaks of almost 3 in the McC/FL ratio in **y**- and **z**-polarization. Starting from $\lambda = 1550\,\text{nm}$, reabsorption is not detected anymore and the reference McC spectrum can be substituted by the calibrated FL spectrum, in order to hide the low signal-to-noise ratio of the McC curve in this wavelength range. To perform the FL calculations, the radiative decay time measured in Er^{3+}:$BaYLuF_8$ has been adopted, because of the similarity of the two hosts. Considering the average underestimation of the $\sigma^*_{\text{em}}(\text{FL})$, it is expected that a shorter τ_{rad} should be employed in the calculations.

It is worth to remind that the difference in resolution of the spectra in the range of 1.5 µm (0.9 nm for the fluorescence spectrum for the FL method, instead of 0.6 nm for the absorption spectrum for the McC method) are not expected to affect the McC/FL ratio because of the relatively high broadness of the peaks in this spectral region.

Also in the case of the infrared spectral range, the McC method cannot be applied to Er^{3+}:$BaYLuF_8$ because of the missing information about the exact position of the Stark energy levels. Nevertheless, the profile of the spectrum can be determined estimating the $Z_l/Z_u = 1$ ratio of Eq. (5.7) (for simplicity considered equal to one) and the value of E_{ZL}. Similarly to Er^{3+}:BaY_2F_8, the value of E_{ZL} has been considered equal to $6535\,\text{cm}^{-1}$ Therefore, for each FL calculation, based on polarization-dependent fluorescence spectra, an approximated McC spectrum could be deduced and the results are shown in Fig. 5.29. In this case the McC/FL cannot have a quantitative meaning, but only be significant in order to establish the spectral range where reabsorption effects are present and discrepancies between the two methods. None of the two methods can be reliable to determine the emission cross sections in Er^{3+}:$BaYLuF_8$.

Furthermore, the similarity between the estimated absorption cross sections in Er^{3+}:BaY_2F_8 and Er^{3+}:$BaYLuF_8$ is once again high and the average value of the $\sigma^*_{\text{abs}}(Er^{3+}:BaY_2F_8)/\sigma^*_{\text{abs}}(Er^{3+}:BaYLuF_8)$ ratio shows a discrepancy lower than 20%. This is possible because the orientation and the polished faces of the two crystals Pi1 and AC3 (see Tables A.4 and A.6) allow detection of the spectra with the same orientation of both **E** and **B** fields (see Sect. 5.2.1). As a consequence, the McC spectrum calculated for Er^{3+}:BaY_2F_8 is expected to be a reference also for Er^{3+}:$BaYLuF_8$. Nevertheless, this concept is not strictly valid for a comparison between the two FL spectra. The higher erbium doping concentration in the Er^{3+}:$BaYLuF_8$ crystal Pi2 resulted advantageous for increasing the signal-to-noise ratio of the fluorescence and it has been preferred to the lower concentrated Er^{3+}:$BaYLuF_8$ crystal AC3. But, at the same time, the polished faces allow only for a different orientation of the **k**-vector and the magnetic component, when

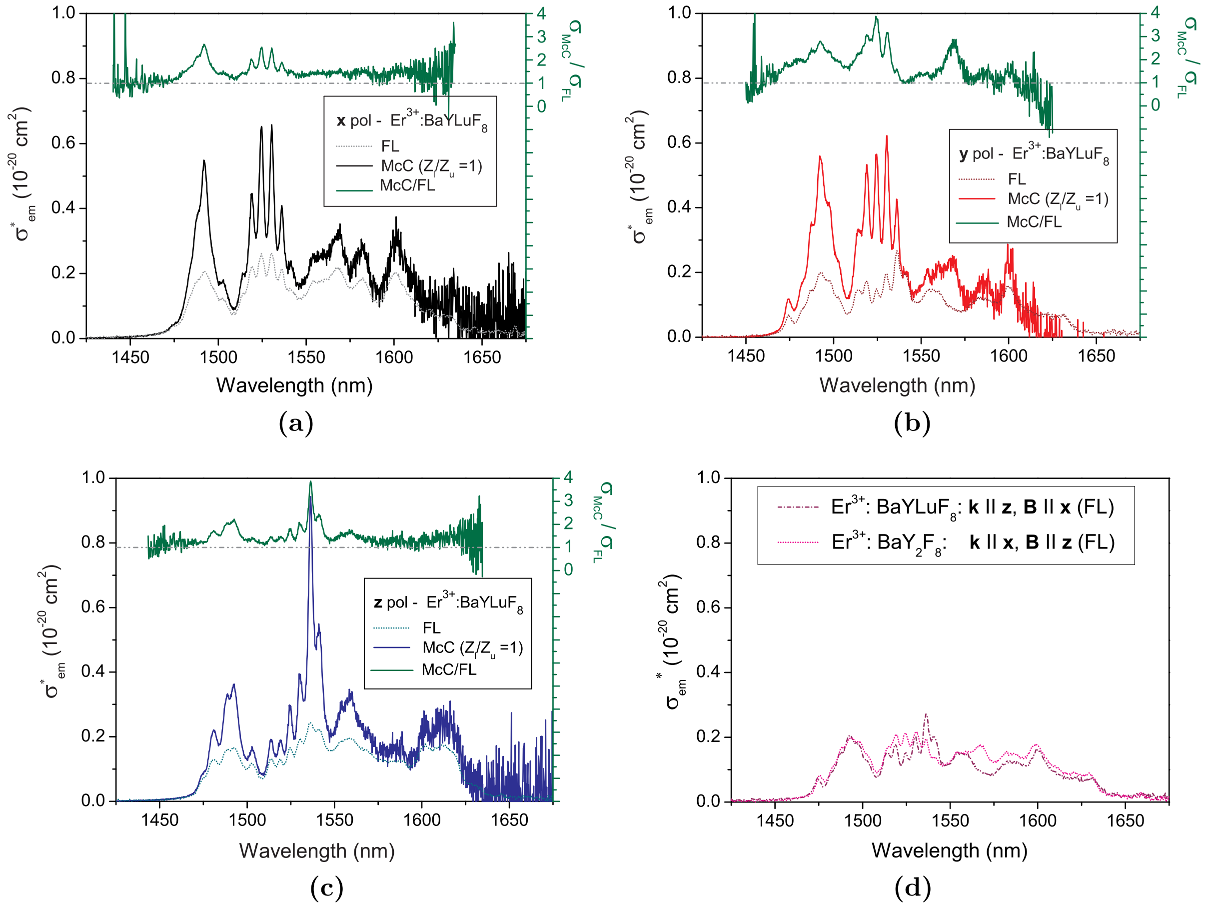

(a) (b) (c) (d)

Figure 5.29: Polarization-dependent FL spectrum of 1.3 at.% Er^{3+}-doped $BaYLuF_8$ and estimated McC spectrum (with $Z_l/Z_u = 1$) and comparison with the results in Er^{3+}:BaY_2F_8. The E_{ZL} has been also estimated. The emission cross sections could be only estimated, because of the biaxial nature of $BaYLuF_8$. In (a)-(c), a comparison between the results of the FL and McC methods is shown in the three polarizations, respectively. On the right vertical axis the ratio of the two curves McC/FL is shown. The McC curves have been limited in order to hide the divergence due to the low signal-to-noise ratio. In this case the McC/FL ratio is only useful to determine the regions where reabsorption is active. In (d), the **y**-polarization curve of Er^{3+}:$BaYLuF_8$ is compared to the the **y**-polarization curve of Er^{3+}:BaY_2F_8 detected with a different orientation of **k**- and **B**-vectors. For Er^{3+}: $BaYLuF_8$ none of the spectra (neither FL nor McC) can be considered reliable in this spectral range.

the measurement in **y**-polarization is performed. Furthermore, the other two polarization couples have been tested with the same orientation of both **k**- and **B**-vectors.

From the comparisons in Figures 5.29a-5.29c, it is evident that there is a correspondence between the spectra in **x**- and **z**-polarization estimated with the two methods and that reabsorption is particularly evident in the region 1480 - 1560 nm. For **y**-polarization the results of the comparison are different: the two spectra calculated with the FL and McC methods do not correspond to each other. As previously mentioned, the fluorescence spectrum in this polarization has been recorded with a different orientation of the **k**- and **B**-vectors if compared to the absorption spectrum and the differences are evident also comparing the two FL spectra in **y**-polarization estimated for Er^{3+}:BaY_2F_8 and Er^{3+}:$BaYLuF_8$ as depicted in Fig. 5.29d

Er^{3+}:KY_3F_{10}

A similar analysis of the dynamics and of the emission spectra to the one performed in previously described erbium-doped crystals, has been carried out also for Er^{3+}:KY_3F_{10}.

Concerning the $^4S_{3/2}$-manifold, lifetime measurements have been performed and emission spectra have been recorded to estimate the emission cross sections. The results are summarized in Fig. 5.30.

To determine the radiative lifetime of the $^4S_{3/2}$-multiplet, the excitation wavelength has been tuned to 520 nm and the fluorescence has been detected at around 550 nm. The nominal doping concentration of the sample was 2 at. % and effects of interionic transitions are evident from the decay curve shape in Fig. 5.30a: it is clearly non-single-exponential. A single-exponential fit can be performed with a relatively long delay of more than 0.5 ms and an average lifetime of 0.30 ms could be measured. A double-exponential fit has been performed on the same curve depicted in the inset on linear scale and the result was a 10% shorter lifetime and a second value of 85 µs which can be related to fast exchange of excitation among pairs of ions. An average lifetime value of the $^4S_{3/2}$-multiplet of 0.29 ms has been considered as a reference in the FL calculations for the estimated emission cross sections in Fig. 5.30b. This value is in good agreement with the lifetime of 295 µs reported in [Dia03].

Considering the not confirmed nominal doping concentration of 2 at.% of Er^{3+}-ions in the available Czochralski-grown boule (also the segregation coefficient of Er^{3+}-ions in KY_3F_{10} is not known), the emission cross sections σ^*_{em} calculated via McC method have to be considered as an underestimation, because they are directly derived from the previously introduced estimated absorption cross sections. The erbium content is expected to be 2 at. % or lower due to the similarity of the lifetime measured with this crystal and the one in literature based on a 1% Er^{3+}-doped sample, and the segregation coefficient being ≤ 1. The positions of the energy Stark levels in this host has been deduced from those published in [Dia03, Bou06]. Furthermore, the branching ratios of the different decay channels starting from $^4S_{3/2}$-multiplet in Er^{3+}:KY_3F_{10} are also unknown and the FL curve displayed in Fig. 5.30b is calculated with $\beta = 1$. This approximation still allows for the localization of the wavelength range where reabsorption is present. Therefore, if the FL curve is compared to the curve resulting from the McC method, reabsorption is visible, mainly at the peaks centered at 522 nm, and moderately at the peaks around 542 and 544 nm. As expected for a branching ratio $\beta = 1$, the FL curve is on the average more intense than the McC curve and the McC/FL ratio can allow for an estimation of a more realistic branching ratio for the decay $^4S_{3/2} \rightarrow {}^4I_{15/2}$. When the two spectra are superimposed and calibrated on the peaks which are not affected by reabsorption at 550 and 552 nm, the β value estimation corresponds to 35%. Compared to other erbium-doped host crystals ($\beta = 65 - 66\%$ in Er^{3+}:$LiLuF_4$ and Er^{3+}:LaF_3), this value results too low to be eligible. In this case, the origin of the discrepancy is most probably due to the underestimated erbium concentration in the sample (consequently lower estimated absorption and then emission cross sections via the McC method) than to a wrong value of the assumed lifetime. Nevertheless, to define the gain spectrum, the McC spectrum is considered valid up to 552 nm. For longer wavelengths, the calibrated FL curve is adopted.

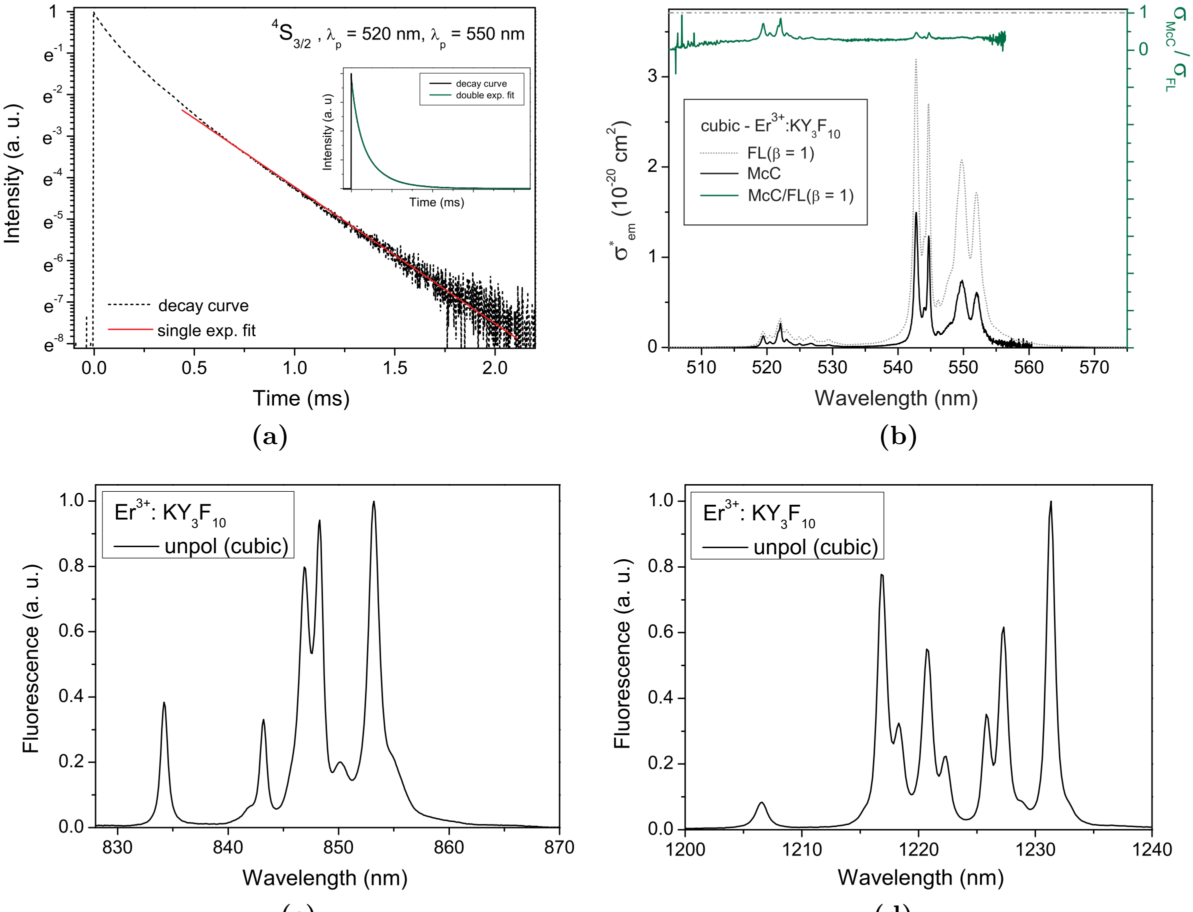

(a) (b)

(c) (d)

Figure 5.30: Dynamics and emission spectra of the $^4S_{3/2}$-multiplet in a nominally 2 at.% Er^{3+}-doped KY$_3$F$_{10}$ crystal. In (a), an example of non-single exponential decay curve at 550 nm, when excited at 520 nm, with a delayed single-exponential fit on semilogarithmic scale is displayed. In the inset, the same curve is plotted on a linear scale together with a double-exponential fit. In (b), a comparison between the results of the FL and McC methods is shown. The emission cross sections σ^*_{em} are only estimated because of the not confirmed nominal Er^{3+}-doping concentration and the missing information about the branching ratio β for the $^4S_{3/2} \rightarrow {}^4I_{15/2}$ decay. In green the McC/FL curve for $\beta = 1$ is plotted. This curve and the McC curve have been limited in order to hide the divergence due to the low signal-to-noise ratio of the McC spectrum. In (c) and (d), the results obtained around 850 nm and 1.2 µm, respectively, are depicted in an arbitrary unit scale of fluorescence because of the missing β value for both the $^4S_{3/2} \rightarrow {}^4I_{13/2}$ and $^4S_{3/2} \rightarrow {}^4I_{11/2}$ transitions. -none of the displayed spectra can be strictly numerically reliable.

In [Hey98], three different sites for Er^{3+}-ions in KY$_3$F$_{10}$ are reported. Nevertheless, the authors assure the different siting does not affect the energy level positions, although the crystal-field parameters which can be calculated belong to three different sets, according to the three sites. Consequently, they influence the form of the crystal-field wavefunctions. Therefore, the application of the McC method could be questionable, but considering the missing influence on the energy level positions, the method has been applied also for this crystal host.

In the Figures 5.30c and 5.30d, the spectra related to the other two main decay channels from the $^4S_{3/2}$-manifold are depicted. Because of the low signal, it was not possible to

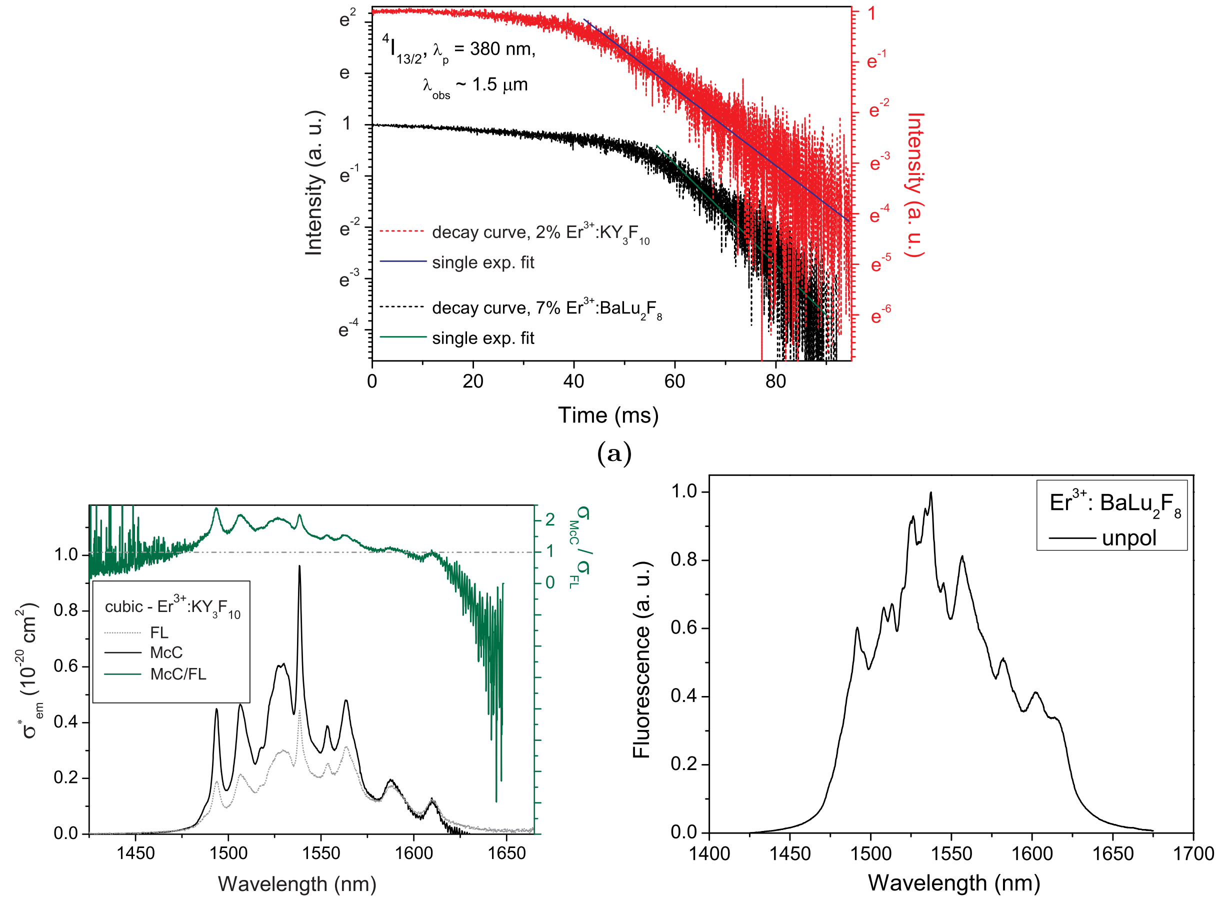

(a)

(b) (c)

Figure 5.31: Dynamics of the $^4I_{13/2}$-multiplet and emission spectra in the 1.5 µm-spectral range in a nominally 2 at.% Er^{3+}-doped KY_3F_{10} and a 7 at.% Er^{3+}-doped $BaLu_2F_8$. In (a), two examples of decay curves in the two different crystals are reported on semilogarithmic scale. The low signal and unusual pre-decay dynamics are due to the different decay processes which determine the population of the $^4I_{13/2}$-manifold occurring when the excitation wavelength is 380 nm. In (b), a comparison between the results of the FL and McC methods for Er^{3+}:KY_3F_{10} is shown. The emission cross sections σ^*_{em} represent only an estimation. On the right vertical axis the ratio of the two curves McC/FL is shown and it has been limited in order to hide the divergence due to the low signal-to-noise ratio of the McC curve.

record the emission centered at 1.7 µm. The missing branching ratio and McC reference calculations force the fluorescence curves to be illustrated in arbitrary units.

For Er^{3+}:KY_3F_{10}, also a study of the dynamics and the emission characteristic of the $^4I_{13/2}$-multiplet has been performed and the results are summarized in Fig. 5.31, together with those obtained for Er^{3+}:$BaLu_2F_8$ in the same spectral range.

In Fig. 5.31a, the decay of the fluorescence around 1.5 µm after excitation at a wavelength of 380 nm is displayed. Due to the numerous transitions involved in the population of the $^4I_{13/2}$-multiplet when such short-wavelength pump pulses are employed, the curve has a low signal-to-noise ratio and the initial portion of the curve has been omitted. Nevertheless, a single-exponential fit on semilogarithmic scale could be performed. The measured average radiative lifetime corresponds to 13.5 ms. This value has been employed to perform a FL study of the fluorescence spectra in order to obtain an estimation of the emission cross sections at around 1.5 µm, as reported in Fig. 5.31b. The spectrum could be compared to the one obtained via the McC method. Considering the not confirmed nominal content of erbium in the crystal, this spectrum has to be considered less reliable than in other host crystals. The McC/FL ratio plotted in green shows major reabsorption effects in the spectral range up to 1540 nm and a reduced effects on the peaks up to 1575 nm. Reabsorption seems to be not effective on the long-wavelength peaks of the spectrum, at around 1588 and 1610 nm, where the McC and FL spectra almost perfectly coincide. From this comparison, it is possible to deduce that, if the reabsorption-free portion of the spectrum is taken as a reference, the two parameters with the highest degree of uncertainty involved in the calculation match to each other: a doping concentration of 2 at. % in the crystal and a radiative lifetime of the manifold of 13.5 ms. This would partially confirm a higher reliability of the lifetime value measured in this work, rather than the 35% shorter one reported in [Dia03]. Nevertheless, if the segregation coefficient of Er^{3+}-ions in KY_3F_{10} is lower than 1, lower absorption cross sections and consequently lower emission cross sections would be estimated. In this case, a shorter lifetime of the $^4I_{13/2}$-multiplet would cause the same McC/FL ratio to be equal to 1. Therefore, if each of the calculation methods relies on a dimension affected by uncertainty, no conclusion can be drawn just observing the behavior of the McC/FL ratio, which can lead to the compensation of the uncertainties.

Nevertheless, the gain spectrum has been calculated and the McC curve has been considered valid up to 1597 nm. For higher wavelengths, the rescaled FL spectrum has been adopted.

Er^{3+}:$BaLu_2F_8$

The last crystal host doped with Er^{3+}-ions whose dynamics and emission spectra were studied is $BaLu_2F_8$.

The results concerning the $^4S_{3/2}$-manifold are reported in Fig. 5.32. The consequence of the extremely high doping concentration of 7 at.%, if compared to the other hosts previously examined, emerges from the dynamic study of the $^4S_{3/2}$-multiplet shown in Fig. 5.32a. The decay curve on semilogarithmic scale is extremely non-single exponential and not even a delayed single-exponential fit could be performed. In the inset of the figure, the same curve is reported on linear scale and fitted by a double-exponential fit. The results of this fit were two values of lifetimes, on average one corresponds to 100 µs and the other one to 40 µs. As most probable radiative lifetime of the manifold the longest value has been adopted, while the shortest has been evaluated as the timescale of the energy transfer processes between different ions, being strongly effective when the density of erbium ions is so high and the average distance among the ions reduced. Nevertheless, this short value of 100 µs could not be adopted as the effective radiative lifetime of Er^{3+}-ions in this host, due to this high concentration-quenching effect. These observations are not in contrast with the results in [Wen99]. It is demonstrated that up to 4.5% of Er^{3+}-ions concentration, the concentration quenching of the $^4S_{3/2}$-multiplet lifetime does not take place. This is a remarkable characteristic of Er^{3+}:$BaLu_2F_8$ compared to most of other fluoride hosts where the concentration quenching starts at much lower Er^{3+}-ions densities. It is worth to remind that the Er^{3+}:$BaLu_2F_8$ sample available for spectroscopy (R, see Tab. A.5) has been extracted as product of a fast cooling-down process in order

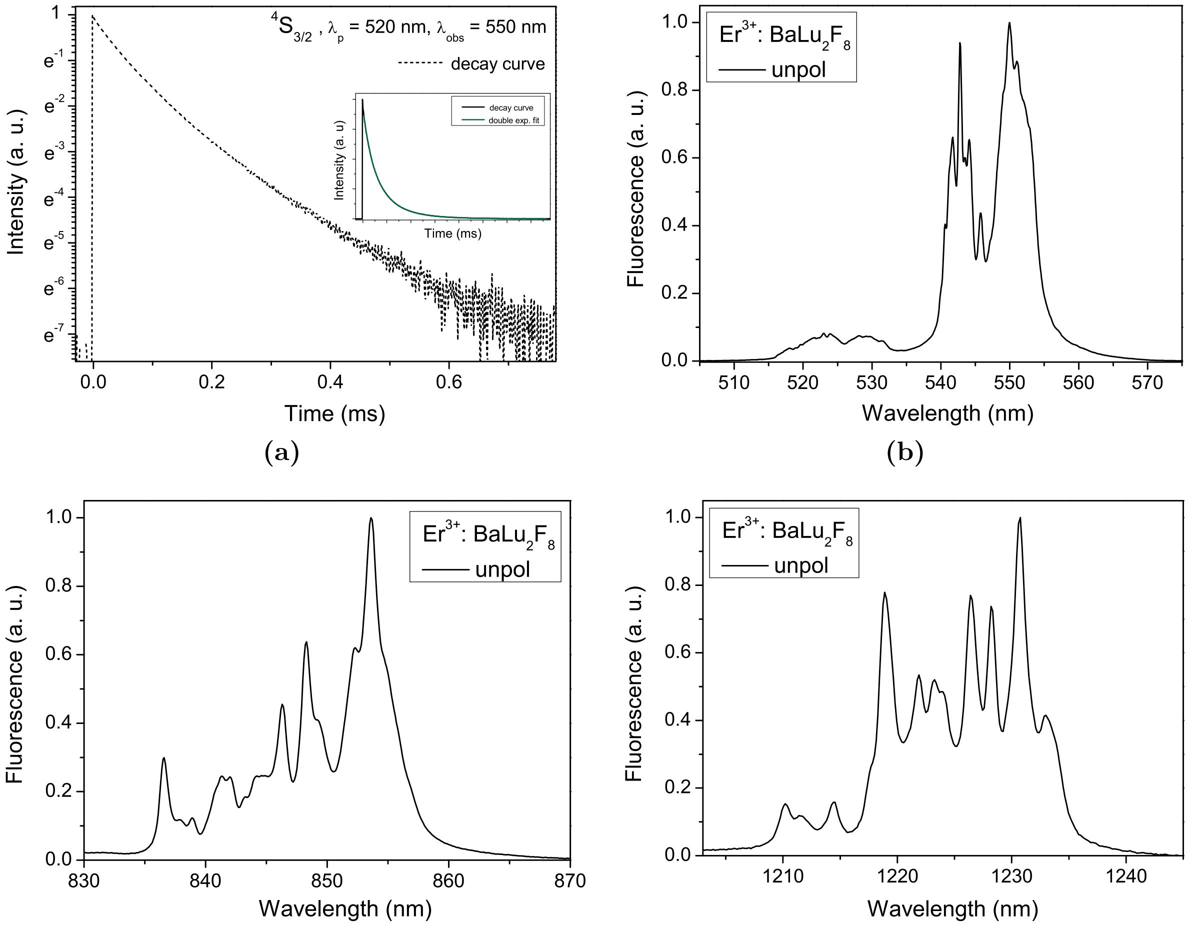

(a) (b) (c) (d)

Figure 5.32: Dynamics and emission spectra from the $^4S_{3/2}$-multiplet in a 7 at. % Er^{3+}-doped BaLu$_2$F$_8$ crystal. In (a), an example of a strongly non-single exponential decay curve of the emission at 550 nm, after an excitation at a wavelength of 520 nm, on semilogarithmic scale is plotted. In the inset, the same curve is represented on a linear scale and a double-exponential fit is reported. In (b), (c) and (d), the fluorescence spectra recorded in the green spectral range, around 850 nm and 1.2 µm, respectively, are depicted in arbitrary unit scale of fluorescence. No emission cross sections could be calculated because of the limited crystal size not allowing for polarization-dependent measurements.

to freeze the α-BaLu$_2$F$_8$-structure and confirmed via EDX technique to be 7 at.% Er^{3+}-doped, although the desired doping concentration in the melt was 5.5 at.%.

Considering the unknown effective radiative lifetime, the difficulties to perform polarization-dependent measurements (small size of the sample) and the missing knowledge of the branching ratios for the transitions starting at the $^4S_{3/2}$-manifold, no emission cross sections could be calculated. The three spectra reported in Fig. 5.32 show the fluorescence expressed in arbitrary units, in the three spectral ranges around 550 nm, 850 nm and 1200 nm. Also for this crystal host, the emission signal around 1.7 µm was too weak to be detected. Furthermore, Er^{3+}:BaLu$_2$F$_8$ presents double-siting [Wen99, Wen00], with different energy Stark levels associated to the two different sites. This would render harder the application of the McC method to estimate emission cross sections.

Although no quantitative comparison can be performed with Er^{3+}:BaY$_2$F$_8$, interesting differences emerge from the positions and relative intensities of the peaks. If the two main groups of peaks centered at 543 and 550 nm in Er^{3+}:$BaLu_2F_8$ are compared to those in Er^{3+}:BaY_2F_8 (see Fig. 5.26), it is clear that they are slightly closer to each other in Er^{3+}:$BaLu_2F_8$ (only 7 nm of distance, instead of 11 nm in the average polarization-dependent spectrum of Er^{3+}:BaY_2F_8). Furthermore, the second group of peaks is much more relatively intense in Er^{3+}:$BaLu_2F_8$ than in Er^{3+}:BaY_2F_8, even higher than the first group, although stronger reabsorption effects are expected on the first group of peaks than on the second (although in Fig. 5.26 for Er^{3+}:BaY_2F_8 there are no dramatic differences). In conclusion, Er^{3+}:$BaLu_2F_8$ is expected to show higher cross sections in the most probable laser emission wavelength in the green spectral range, than Er^{3+}:BaY_2F_8.

Concerning the decay curve of the $^4I_{13/2}$-manifold in Er^{3+}:$BaLu_2F_8$, similar observations to Er^{3+}:KY_3F_{10} (see Fig. 5.31a) can be made. In this case, the average measured value of radiative decay time in the 1.5-µm spectral range corresponds to 9.9 ms. The experience with other erbium-doped fluoride hosts suggests the absence of concentration quenching effects on the lifetime of this manifold, although at this high doping level, an influence could be evident as in other crystal hosts (e. g. Lu_2O_3 [Li12]).

The unpolarized emission spectrum in the 1.5-µm range for Er^{3+}:$BaLu_2F_8$ is depicted in Fig. 5.31c. Also in this case, the missing polarization-dependent emission curves did not allow the estimation of emission cross sections. The comparison with emission spectra in Er^{3+}:BaY_2F_8 (see Fig. 5.28) is less significant than the one in the green spectral range. It is possible to confirm the same wavelength range of the emission (1475-1625 nm), but no further comments on the structure of the peaks are possible because of their broadness in this spectral range.

Excitation-power-dependent upconversion fluorescence measurements

In this section, the behavior of the upconversion fluorescence depending on incident pump power in a few Er^{3+}-doped crystals is presented. The theory has been introduced in Sect. 2.4.

In Fig. 5.33, the results for four different erbium-doped crystals excited by the beam of a Ti:sapphire laser at ∼ 970 nm are summarized: LaF_3, KY_3F_{10}, $LiLuF_4$ and $BaYLuF_8$. The arbitrary unit scale is different for the axes in a single diagram, but the scale on one axis is comparable to the same axis across the four diagrams. Linear fits have been performed and the relative slopes evaluated.

For the spectra regarding Er^{3+}:LaF_3 and Er^{3+}:KY_3F_{10}, the measurement results confirm the theory. If a relatively low incident power is applied, the fluorescence increases linearly in double logarithmic scale and with a slope between one and two, which implies that the process which populates level 2 ($^4S_{3/2}$-manifold) involves two photons. When the incident power reaches a certain amount, the onset of the so-called “high-incident-power regime” is reached and the slope changes, fitting approximately a value of one.

Concerning the plot obtained with Er^{3+}:$LiLuF_4$ the situation is different: all the points on the diagram fit with a low uncertainty a unique slope, such as if the regime of high incident power was not reached, yet. Also in this case, the value of the slope is between one and two, confirming a two-photon process being involved. Therefore, the solution with a single slope, ignoring the high-incident-power regime has been chosen as most

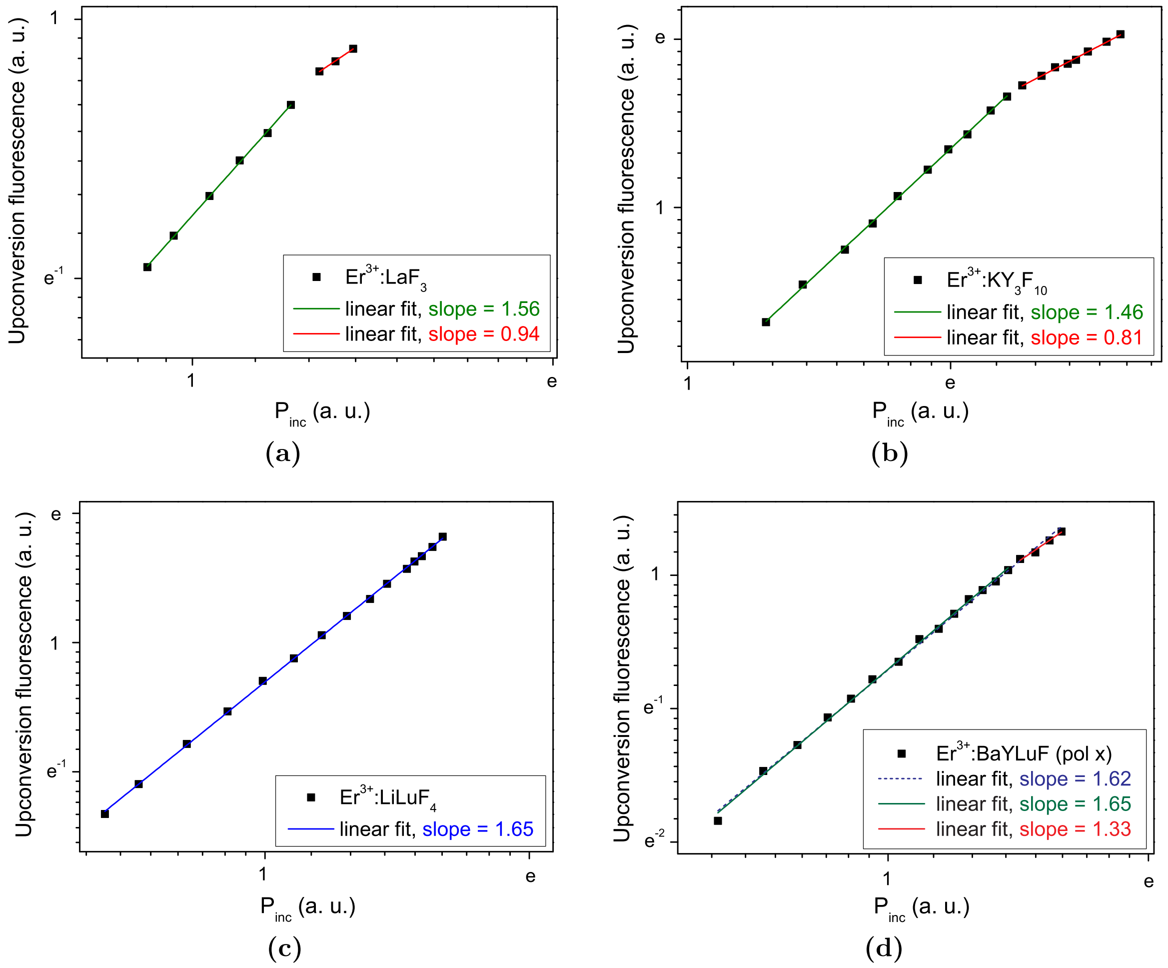

Figure 5.33: Plot on double logarithmic scale of upconversion fluorescence in the green spectral range vs incident pump power ($\lambda \sim 970\,\mathrm{nm}$) in Er^{3+}- doped fluoride crystals. The arbitrary scales of fluorescence and incident power are independent to each other, but for different crystals the scaling on the same axis is the same. In (a) and (b), the results for Er^{3+}:LaF_3 and Er^{3+}:$\mathrm{KY}_3\mathrm{F}_{10}$ for random polarization are reported, together with the results of the linear fits at low and high incident power. In (c) and (d), the same spectra for Er^{3+}:LiLuF_4 (random polarization) and Er^{3+}:BaYLuF_8 (in **x**-polarization) are displayed.

probable.

Also in the plot of the polarization-dependent measurements with Er^{3+}:BaYLuF_8, the onset of the high-incident-power regime is not well identifiable. In this case, the two possible interpretations are both plotted. If it is evaluated that the high-incident-power regime is not yet reached, a single linear fit can be performed (blue dashed line), showing a high degree of uncertainty, although showing a slope between one and two, as expected. On the contrary, it is possible to match a low-incident-power linear fit (green line) to the first fourteen points in the diagram showing a slope slightly higher than in the single slope, still included between one and two. At the same time, a further linear fit (red line) would better match the remaining four points on the diagram, which, nevertheless, would show a lower slope, but still excesses the expected slope of one by more than 30%. It has to be noticed that for the polarization-dependent measurement with Er^{3+}:BaYLuF_8, the detected signal was roughly an e-factor lower than in the other polarization-independent measurements. This has influenced the precision of the estimation of the slope at the low-incident-power regime.

It has to be observed that if a slope does not confirm the expected dependence $N_n \sim P^1$, it can also mean that the level considered is actually not the n-th level of the upconversion process, but the $(n-1)$-th or even lower, admitting the possibility of further upconversion pumping into higher levels. This phenomenon can be tested with ESA measurements with a short-wavelength pump source (equivalent to two times 970 nm, for example the 2ω-OPSL described in Chap. 6) which can excite and probe even higher energy levels.

No saturation of the upconversion fluorescence has been observed at the maximum possible incident pump power of roughly 2 W.

Unfortunately, with a solely two-steps upconversion process ($n = 2$), it is not possible to evaluate a different slope for the high-incident-power regime which would allow for $n > 2$ in distinguishing whether the main pumping process is an intraionic GSA/ESA process or an interionic ETU one [Pol00, Gam01].

5.4 Non-standard analysis of fluorescence decay curves

When single-exponential fits do not properly describe a fluorescence decay curve, it is expected that interionic processes are taking place.

In order to simulate the relationship between transfer rate and luminescence decay, a few models have been proposed, mainly as a development of the Inokuti-Hirayama model (IH) [Ino65].

Theoretically, starting from the description of interaction among ions derived by *Förster and Dexter* [För48, Dex53] (introduced in Chap. 2), a random distribution of donors and acceptors able to interact is assumed, therefore four further assumptions have to be defined:

- it is possible to clearly define a distance donor-acceptor at which the energy transfer can take place (the Brownian motion of the ions is slow enough);
- the transfer rate is independent on the crystal orientation;
- the energy transfer can happen only between donor and acceptor, other combinations, such as donor-donor transfers, are forbidden;
- the nature of the interaction can be electric dipole-dipole ($s = 6$), electric dipole-quadrupole ($s = 8$) or electric quadrupole-quadrupole ($s = 10$).

Consequently, the function which describes the decay of the intensity of luminescence reads:

$$I(t)_{\mathrm{IH}} = I_0 \exp\left(-\frac{t}{\tau_{\mathrm{d}}} - \Gamma\left(1-\frac{3}{s}\right)\frac{N_{\mathrm{a}}}{N_{\mathrm{c}}}\left(\frac{t}{\tau_{\mathrm{d}}}\right)^{\frac{3}{s}}\right), \tag{5.14}$$

where τ_{d} is the lifetime of the donor, Γ is the gamma function, N_{a} is the concentration of the acceptors and N_{c} is the critical transfer concentration. N_{c} can be expressed by

$N_\mathrm{c} = 3/(4\pi R_\mathrm{c}^3)$, where the critical transfer distance R_c represents the distance between donor and acceptor when the energy transfer takes place at the same rate dictated by τ_d.

Considering the much higher probability of incidence for the lowest order of interaction in the multipole expansion, which is confirmed by the experience reported in [Aga13], the study can be limited to the electric dipole-dipole interaction($s = 6$). In this case, Eq. (5.14) becomes:

$$I(t) = I_0 \exp\left(-\frac{t}{\tau_\mathrm{d}} - \gamma\sqrt{t}\right), \qquad \text{with} \qquad \gamma = \frac{4}{3}\pi^{3/2} N_\mathrm{a}\sqrt{C_\mathrm{da}}, \tag{5.15}$$

where C_da is the donor-acceptor parameter already defined by *Förster and Dexter* [För48, Dex53].

Nevertheless, some observations have to be made:

- in systems such as rare-earth-doped crystals, the concentration of ions is typically high enough to allow for donor-donor interactions [Kus73];
- the assumption that the acceptors are homogeneously distributed cannot be consistent with a lattice structure where ions are located in discrete positions [Dor80].

As a consequence, a possible extension of the IH model has been developed by *Burshtein and Zusman* (BZ model) [Bur84, Zus77], including the possibility of donor-donor interactions, in order to be applicable also in rare-earth doped systems. The improved formula reads:

$$I(t)_\mathrm{BZ} = I_0 \exp\left(-\frac{t}{\tau_\mathrm{d}} - \gamma\sqrt{t}\right) \exp(-\bar{W}t), \tag{5.16}$$

where the IH formula is enriched by a second exponential decay factor dependent on the average migration-assisted energy-transfer rate $\bar{W} = \pi(2\pi/3)^{5/2}\sqrt{C_\mathrm{da}C_\mathrm{dd}N_\mathrm{d}N_\mathrm{a}}$ (C_dd is the donor-donor parameter defined by *Förster and Dexter*).

These two models have been applied to selected fluorescence decay curves which are characterized by a non-single-exponential behavior and the results are summarized in Fig.5.34.

The fits have been performed considering the lifetime as a parameter able to vary in a discrete interval around the lifetime values estimated in Sect. 5.3 and with the other factors equal or larger than zero.

In Fig. 5.34a, the evolution of the $^4\mathrm{S}_{3/2}$-multiplet fluorescence in the green spectral range has been investigated after pulsed inband-excitation in three different and differently Er^{3+}-doped crystals. In this case, both the IH as well as the BZ fits match the beginning of the decay curves but none describe the whole temporal range. The fits converge to a lifetime value in the allowed interval of variation but the results are so similar to each other that a difference in the plots of IH and BZ fits cannot be distinguished. The expected higher reliability of the BZ model over the IH model in highly concentrated samples has not been verified.

In Fig. 5.34b, all the samples present a low concentration of Er^{3+}-ions. Two curves are a consequence of pulsed upconversion pumping of the $^4\mathrm{S}_{3/2}$-multiplet and observed in the green spectral range. In these cases, the two fits do not converge and they adapt to one of the two borders of the allowed interval of variation of the lifetime value and mostly do not match the effective profile. Nevertheless, the BZ model seems to be the more appropriate.

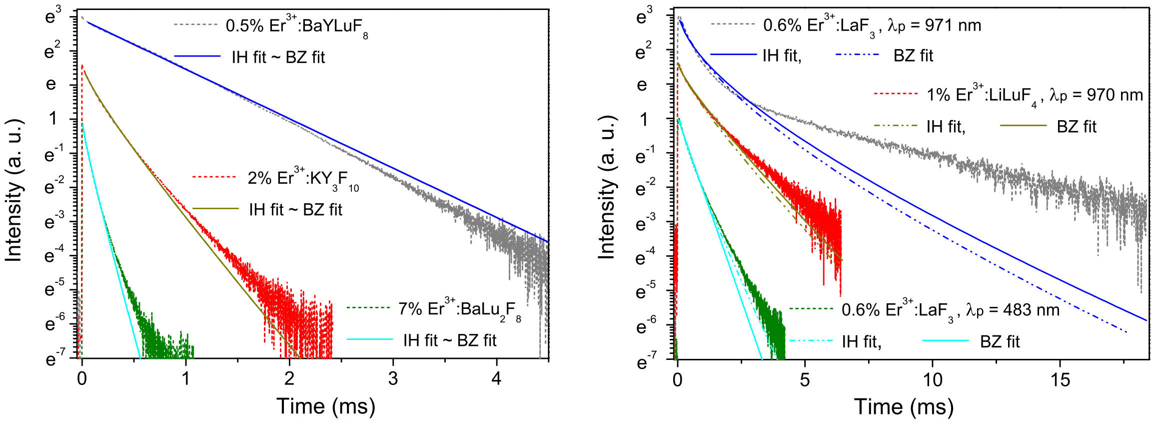

(a) **(b)**

Figure 5.34: Inokuti-Hirayama and Burshtein-Zusman fits of the decay curves, arising from the fluorescence of the $^4S_{3/2}$-multiplet in different Er^{3+}-doped crystals. In (a), three different crystals are inband-pumped at 520 nm and the two fits converge, but give very similar results. In (b), the three fluorescence curves derive from upconversion pumping and the two fits do not converge, always adapting to one of the limits of variation of the lifetime value (given as parameter). In two cases over three, BZ fits more precisely the decay curves than IH, but none of them represents a satisfying method to properly fit the observed fluorescence decays.

In the case of Stokes fluorescence, where the excitation wavelength is in the blue spectral range, both fits do not converge and they adapt to one of the border values of the allowed variation range of the lifetime value and the IH model offers the best interpolation of the effective decay curve.

Finally, a further observation has been argued [Gra71]: IH and BZ model can be both inappropriate for rare-earth-doped materials because they cannot properly take into account the nonlinearity typical for ETU processes which are expected to take place, together with cross relaxation processes. Consequently, IH and BZ models demonstrate to be able to treat interaction between donors and acceptors of different species (for example linear quenching processes due to energy transfer to impurities), rather than interaction between two ions of the same kind.

More structured models have been developed and applied in order to consider the nonlinearity of ETU processes in rare-earth-doped materials and the description of these models and some results can be found in literature (e. g [Gra71, Zub97, Aga13]).

Although for samples with a low Er^{3+}-doping concentration no ETU processes have been considered as active, the missing perfect match of the IH and the BZ model to some decay curves can be a sign of the effective influence of interionic processes.

5.5 Gain spectra

Most of the transitions which are analyzed in this work have the ground level as final level. This implies that GSA cross sections have to be considered in order to evaluate the gain spectra for a certain erbium-doped crystal, at a certain wavelength. If the density of excited ions N_2 introduced in Chap. 2 and the total density of active ions N_{tot} are accounted, the inversion level β corresponds to:

$$\beta = \frac{N_2}{N_{\mathrm{tot}}}. \tag{5.17}$$

The effective polarization-dependent gain spectrum can be calculated as:

$$\sigma^{\kappa}_{\mathrm{gain}}(\lambda) = \beta\sigma^{\kappa}_{\mathrm{em}}(\lambda) - (1-\beta)\sigma^{\kappa}_{\mathrm{GSA}}. \tag{5.18}$$

If the inversion level β varies, also the gain spectrum varies consistently. A plot of $\sigma^{\kappa}_{\mathrm{gain}}(\lambda)$ at different possible values of β is fundamental to establish if and at which inversion level laser oscillation can take place at a certain wavelength. When laser oscillation is obtained, it is possible to estimate, increasing the needed inversion level, at which wavelength the laser will operate at higher outcoupling transmissions.

5.5.1 Results in the visible and in the 1.6-µm spectral range

In every crystal host, the gain cross sections have been calculated or estimated for relatively low levels of inversion. The β values displayed in the diagrams are either allowing laser emission in the laser experiments described in Chap. 6, or those which can determine a change of the emission wavelength with respect to the immediate higher or lower one.

The positive gain cross sections have to be considered eligible only in the spectral region where they are clearly not affected by the random influence of the noise.

The only crystal host in which laser emission in the visible spectral range has been demonstrated is $\mathrm{Er^{3+}{:}LiLuF_4}$. In this case, it is possible to verify at which inversion levels β the obtained laser emission wavelengths are allowed.

In Fig. 5.35, the $\mathrm{Er^{3+}{:}LiLuF_4}$ gain spectra for low inversion levels in π- and σ-polarizations are reported, together with one at high inversion levels exclusively regarding π-polarization. In Fig. 5.35a, the gain spectrum in π-polarization, for low β is reported. Already at an inversion of 0.01, laser emission is possible at 566.6 nm, but it is an unrealistic value. At $\beta = 0.06$, a realistic value for the emission wavelength 553.6 nm emerges, but at $\beta = 0.0645$ the wavelength of 552.6 nm (552.6 nm in the resolution of the wavelength detector) of operation identified in laser experiments in circular waveguiding claddings is possible (see Chap. 6). Starting at an inversion of 0.08, the laser wavelength of 551.6 nm obtained in experiments with bulk crystals and rhombic-cladding waveguides can be reached and only slightly moved to 551.55 nm starting at $\beta = 0.09$. In Fig. 5.35b, the gain spectrum in σ-polarization, for low β is displayed. Considering the uncertainty of the results at wavelengths higher than 554 nm and the particular low gain cross sections, laser emission is considered possible, but unlikely, in this polarization starting at $\beta = 0.01$.

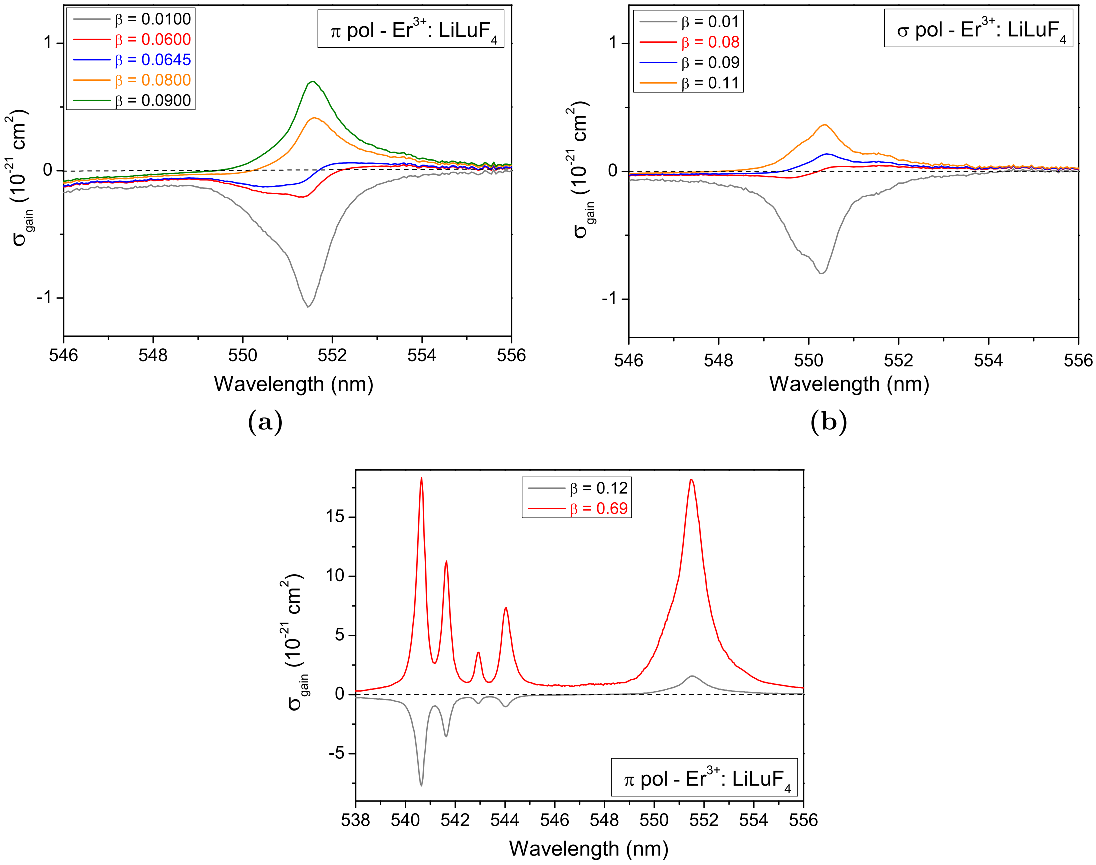

(a) **(b)**

(c)

Figure 5.35: Polarization-dependent gain spectrum of Er^{3+}:$LiLuF_4$ in the green spectral range, at low and high inversion levels β. The inversion levels highlighted with colors in the legend represent either the minimum level which allows laser emission, or significant values concerning specific laser experiments (see text and Chap. 6 for further details). In (a), the gain spectrum in π-polarization, for low β is reported. In (b), the gain spectrum in σ-polarization, for low β is displayed. In (c), the spectrum for high inversion levels is reported concerning π-polarization.

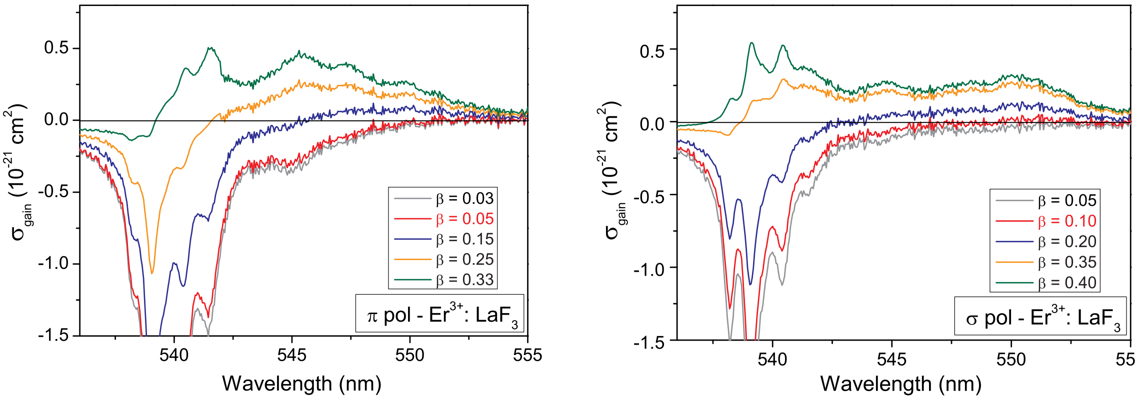

(a) **(b)**

Figure 5.36: Polarization-dependent gain spectrum of Er^{3+}:LaF_3 in the green spectral range. Both the gain spectra for π-polarization (a) and σ-polarization (b) show relatively low gain cross sections and they start to allow laser emission at $\beta = 0.05$ and $\beta = 0.10$, respectively.

Increasing the inversion level causes a shortening of the emission wavelength: at $\beta = 0.08$ the maximum gain cross section is at 551.6 nm, at $\beta = 0.09$ it is moved to 550.4 nm and starting from $\beta = 0.09$ the most probable emission wavelength is slightly moved to 550.35 nm. In Fig. 5.35c, the spectrum for high inversion levels is reported concerning π-polarization in order to show at which β the laser wavelength of 540.6 nm reached in rhombic waveguides is possible. Starting at $\beta = 0.69$, the most probable emission wavelength moves to 540.6 nm, after being for most of the medium-high inversion levels, starting with $\beta = 0.12$, stable at 551.5 nm.

For Er^{3+}:LaF_3 crystals, the calculation of the gain allows to predict which would be the expected emission wavelength during laser experiments. In Fig. 5.36 the spectra for π- and σ-polarization are reported. In comparison to Er^{3+}:$LiLuF_4$, the gain cross sections are lower at the same inversion levels. As a result, the laser emission is harder to realize. Indeed, in Fig. 5.36a, it is possible to notice that at $\beta = 0.05$ the gain cross section is positive at $\lambda = 551.3$ nm, but the cross sections stay relatively low also increasing the inversion level. The most probable emission wavelength is expected to decrease, increasing β. The further three values reported in the diagram are those expected to cause a change to 548.5, 545.3 and 541.6 nm, respectively. For σ-polarization, reported in Fig. 5.36b, the situation is even less favorable for laser emission. Laser emission at 551.2 nm can theoretically be observed at an inversion level as high as 0.10. The three further higher values of β are needed to move the emission wavelength to 550.5, 540.5 and 539.2 nm, respectively.

In Fig. 5.37, the estimation of the gain cross sections in Er^{3+}:BaY_2F_8 and Er^{3+}:KY_3F_{10}, varying the inversion level, is represented. For both crystals, the asterisk reminds the impossibility to determine the cross sections for the biaxial Er^{3+}:BaY_2F_8 and for the not confirmed Er^{3+}-doping concentration in the Er^{3+}:KY_3F_{10} sample. The first three graphs show the estimated gain spectrum of Er^{3+}:BaY_2F_8 for each polarization. The magnitude of the cross sections as a function of the inversion level is on the average lower than in Er^{3+}:$LiLuF_4$, but higher than in Er^{3+}:LaF_3. In the three polarizations, the minimum inversion level which allows the maximum of the gain to be positive is 0.05. Up to an inversion level of 0.20 - 0.25, the eligible maxima of the gain lie in the spectral range included between 551.7 and 553.9 nm.

In Er^{3+}:KY_3F_{10}, whose estimated gain spectrum is depicted in Fig. 5.37d, the magnitude of the estimated gain cross sections resembles the values of Er^{3+}:BaY_2F_8. Nevertheless, for roughly the same range of inversion levels, the estimated maxima of the gain span a broader wavelength range, from 556.0 nm for $\beta = 0.05$, to 549.8 nm for $\beta = 0.25$. The broadness of the corresponding wavelength range is connected to the broadness of the single emission peaks and of the total spectrum associated to the whole decaying multiplet.

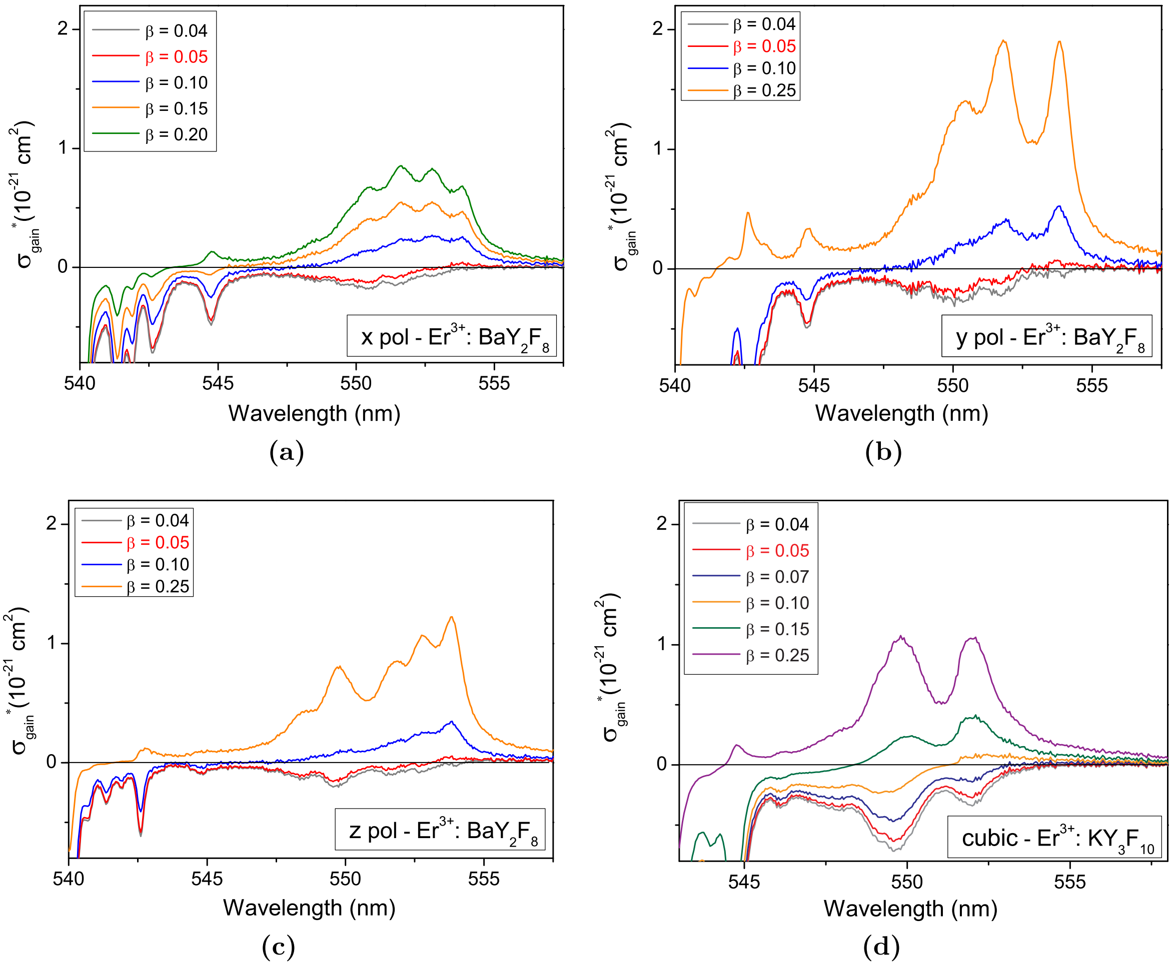

Figure 5.37: Gain spectra of Er^{3+}:BaY_2F_8 and Er^{3+}:KY_3F_{10} in the green spectral range. In (a)-(c), the estimation of the three polarization-dependent gain cross sections for Er^{3+}:BaY_2F_8 are depicted. The $*$ reminds that the cross sections can only be estimated due to the biaxial nature of the crystal. The highlighted β values are those which allows positive estimated gain cross sections, first, at around 553.8 nm for the three polarizations, although the gain cross sections are estimated to be too low to be effective for laser emission. In (d), the estimated gain cross sections for Er^{3+}:KY_3F_{10} are depicted, as if the Er^{3+}-doping concentration were 2 at. %. Also in this case, the first theoretically eligible laser emission wavelength is obtained at $\beta = 0.05$.

Beside the analysis of the gain spectra in the visible spectral range, it is possible to calculate those for the 1.6 µm range, useful to confirm or estimate the possibility of laser emission when Er^{3+}-doped crystals are inband-pumped with the available fiber laser operating at 1535 nm. The typically broader spectra in this spectral range in comparison to the visible spectral range cause a broader discrete tuning of the different gain maxima, when the inversion level is varied.

In Fig. 5.38, the gain spectra at 1.6 µm for Er^{3+}:$LiLuF_4$ and Er^{3+}:LaF_3 are summarized. In Figures 5.38a and 5.38b, the spectra in π- and σ-polarization for Er^{3+}:$LiLuF_4$ are depicted. In π-polarization the gain cross section is positive (although very low) already at an inversion level of 0.01, at 1644.9 nm. At $\beta = 0.16$ the possible emission wavelength moves to 1625.0 nm, while at $\beta = 0.18$ and $\beta = 0.27$ the probable emission wavelengths match those detected during laser experiments (see Chap. 6) of 1619.9 nm and 1619.0 nm

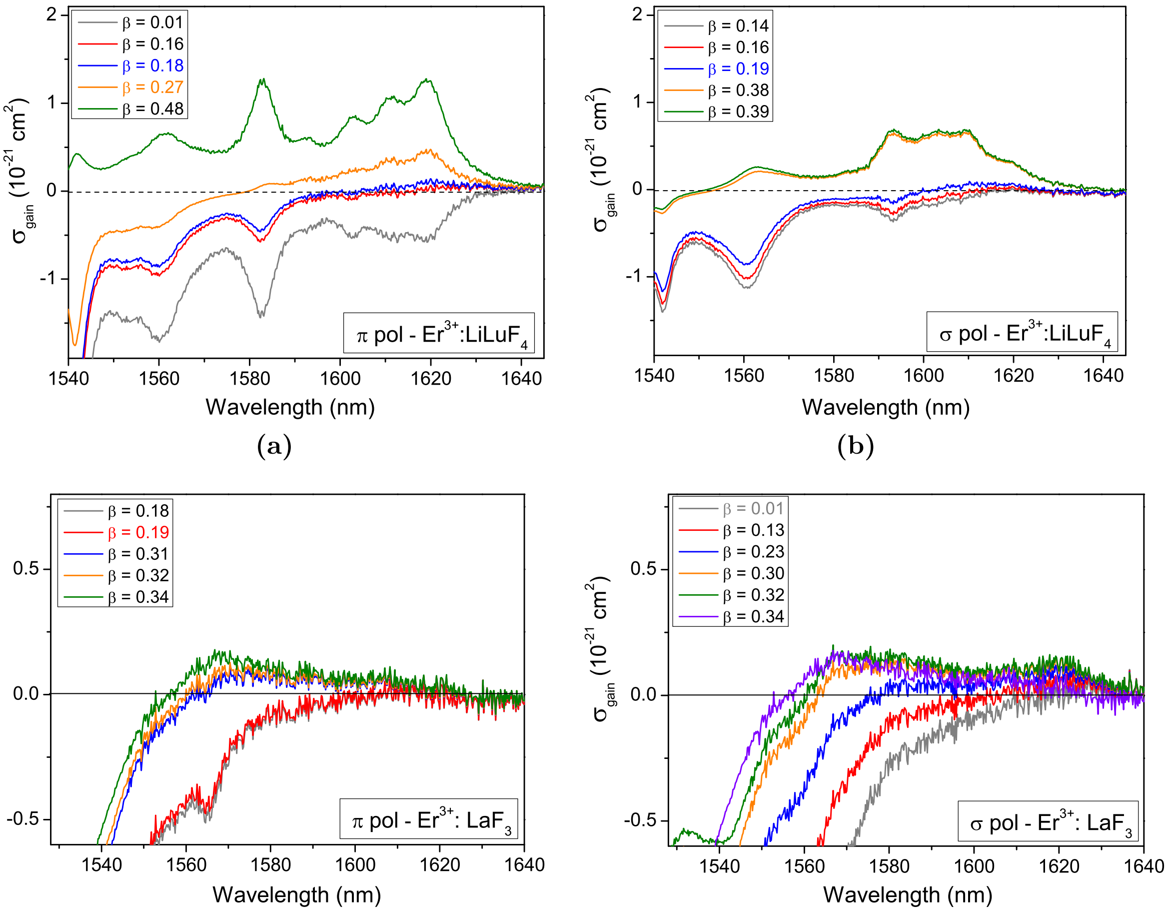

(a) (b)

(c) (d)

Figure 5.38: Polarization-dependent gain spectra of Er^{3+}:$LiLuF_4$ and Er^{3+}:LaF_3 in the infrared spectral range. In (a) and (b), the spectra in π- and σ-polarization for Er^{3+}:$LiLuF_4$ are depicted and the gain cross section is positive (although very low) already at an inversion level of 0.01, in π-polarization, while only at $\beta = 0.14$ in σ-polarization. The laser emission wavelengths recorded during laser experiments (see Chap. 6), have been all identified, together with their interval of inversion level. In (c) and (d), the equivalent spectra are depicted for Er^{3+}:LaF_3. Positive gain maxima are reached at a minimum inversion level of 0.19 and 0.01 for π- and σ-polarization, respectively.

(i. e. 1620 nm and 1619 nm in the resolution of the wavelength detection device during the laser experiments). When an inversion level of 0.48 is reached, the gain maximum moves to 1583.2 nm. In σ-polarization, the minimum required inversion level to have positive gain corresponds to 0.14 at a wavelength of 1619.6 nm, while at $\beta = 0.16$ it is moved to 1616.0 nm. At $\beta = 0.19$ the gain maximum moves to 1610.2 nm, which match the emission wavelength in laser experiments. When the inversion reaches a level of 0.38 the wavelength of the maximum turns to 1603.4 nm, while at $\beta = 0.39$ to 1593.4 nm. The plotted curves in the different polarizations correspond roughly to the same inversion interval, allowing for the comparison of the gain cross sections at certain inversion levels and showing that they are slightly higher in π-polarization.

In Figures 5.38c and 5.38d, the two polarization-dependent gain spectra of Er^{3+}:LaF_3 are depicted. In this case, the signal-to-noise ratio and the gain cross sections are much

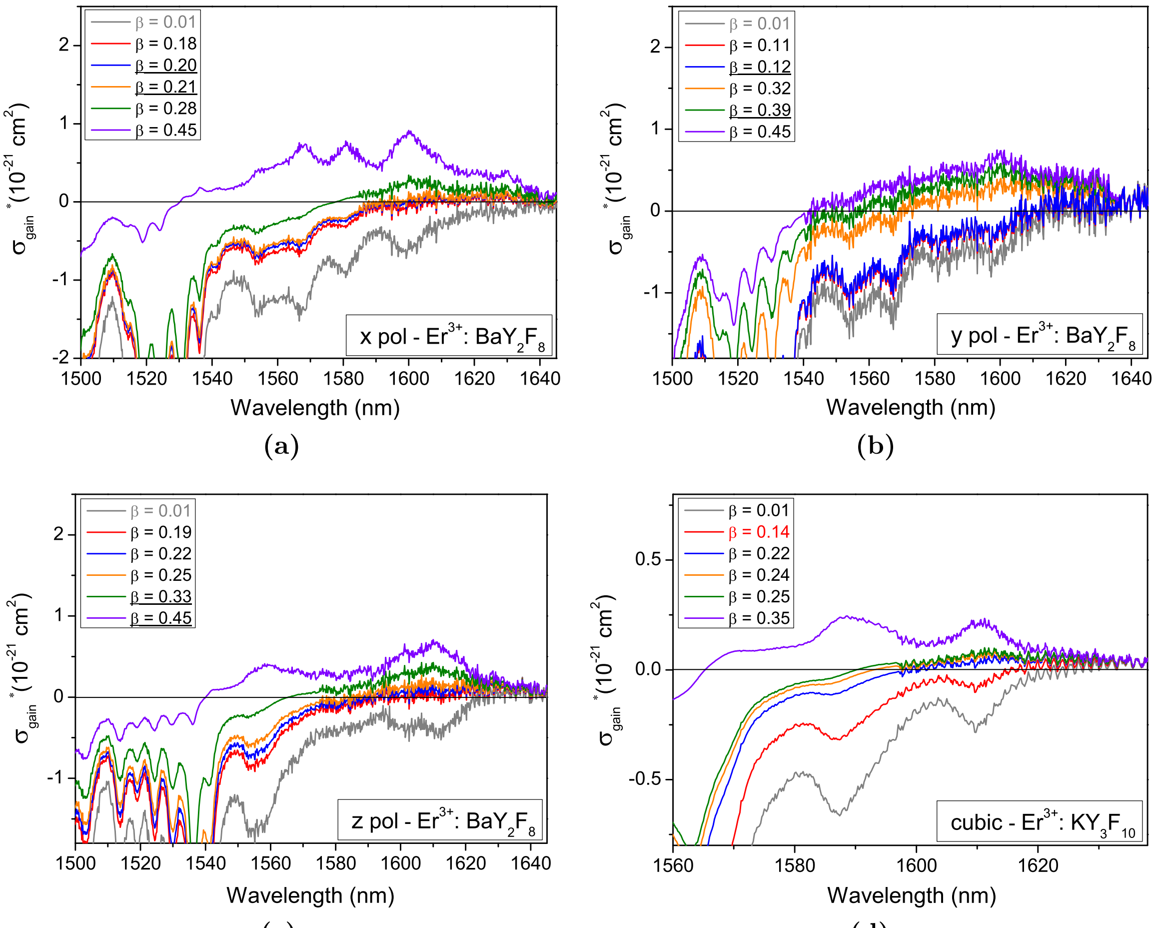

(a) **(b)**

(c) **(d)**

Figure 5.39: Polarization-dependent gain spectra of Er^{3+}:BaY_2F_8 and the gain spectrum for the cubic Er^{3+}:KY_3F_{10} in the infrared spectral range. The gain cross sections represent an estimation ($*$). In (a)-(c), the three polarization-dependent spectra for Er^{3+}:BaY_2F_8 are depicted. Laser experiments have been carried out with Er^{3+}:$BaYLuF_8$ (see Chap. 6), which is expected to have a similar gain spectrum. Indeed, the underlined inversion levels in the diagram are those centering the gain maxima approximately at the emission wavelengths of Er^{3+}:$BaYLuF_8$. In (d), the gain spectrum of Er^{3+}:KY_3F_{10} is depicted. Due to the very low values of estimated cross sections, the signal-to-noise ratio is low and an incorrect zeroing of the curves is evident.

lower than in Er^{3+}:$LiLuF_4$. In π-polarization, the gain is positive starting at the relatively high inversion level of 0.19 at 1608.2 nm, while in σ-polarization already at $\beta = 0.01$ the gain maximum is positive at 1636.6 nm, although the cross sections are very low and the low signal-to-noise ratio makes this value not completely reliable. Nevertheless, the emission cross sections are positive at this wavelength, representing the end of the shoulder of the main peak structure. The further chosen inversion levels are those determining a change in the wavelength of the gain maximum, down to 1566.8 nm for both polarizations, at $\beta = 0.34$ in π-polarization and at $\beta = 0.32$ in σ-polarization.

In Fig. 5.39, the gain spectra of Er^{3+}:BaY_2F_8 and Er^{3+}:KY_3F_{10} in the 1.6-µm spectral range are reported. In both cases the cross sections represent an estimation (asterisk) because of the biaxial nature of Er^{3+}:BaY_2F_8 and for the uncertain erbium doping concentration in the Er^{3+}:KY_3F_{10} sample (see Chap. 4). The first three graphs show the three polarization-dependent gain curves of Er^{3+}:BaY_2F_8. The signal-to-noise ratio is lower than in other hosts, especially in **y**-polarization. Therefore, the positive gain obtained at already 0.01 of inversion level at 1637.0, 1642,0 and 1637.4 nm, respectively has to be considered not reliable to estimate possible laser emission wavelengths, with the only exception of **x**-polarization, which has slightly positive emission cross sections at 1637.0 nm. For higher β values up to 0.45, five different curves for every polarization have been calculated. Considering the similarity with Er^{3+}:$BaYLuF_8$, the underlined values of β approximately correspond to those allowing the gain maxima to be centered at the laser emission wavelengths recorded during laser experiments with this similar crystal (see Chap. 6). Namely, laser oscillation has been reached at 1601 nm and 1631 nm in **y**-polarization for $\beta = 0.39$ and $\beta = 0.11$ (actual values in the gain spectrum: 1601.2 and 1633.0, respectively) and at 1610-1612 nm in **z**-polarization for $\beta \geq 0.33$ (actual value in the gain spectrum: 1610.0 nm)[3]. Laser operation has been also reached at 1611 - 1612 nm in **x**-polarization, but the gain maxima have been not matched in this case, because for $\beta = 0.20$ - 0.21 they are centered at 1614.8 nm and 1606.4 nm, respectively, possibly due to the low signal-to-noise ratio.

In Fig. 5.39d, the gain curve for the cubic Er^{3+}:KY_3F_{10} is reported. This crystal has the lowest estimated cross sections together with Er^{3+}:LaF_3. This causes a higher noise level and additionally in this case the influence of a slightly imprecise zeroing of the gain curves is obvious. As a consequence, a positive shift of all the estimated gain cross sections of $\sim 3 \cdot 10^{23}\,\mathrm{cm}^2$ has to be considered and it causes a positive gain maximum already at $\beta = 0.01$, even less reliable than in other crystals so far analyzed. Therefore, the inversion level highlighted in the graph is the second one, with $\beta = 0.14$, centering the gain maximum at 1629.4 nm, although the emission cross section at this wavelength is almost zero. Imposing higher inversion levels, theoretically the wavelength of the gain maximum can be discretely tuned down to 1588.6 nm, if the inversion level reaches 0.35.

5.6 Excited State Absorption - ESA

In this work, great attention has been devoted to the measurement and elaboration of excited state absorption (ESA) spectra.

As explained in Chap. 2, ESA is typically considered a drawback during laser experiments, in the case it occurs either at the pump or at the emission wavelength. Nevertheless, when crystals are investigated as potential single-wavelength upconversion-laser hosts, a resonance between GSA and ESA peaks is fundamental.

In the framework of this thesis, the applied measurement technique is the one developed in the nineties at the ILP in Hamburg [Pol92, Dan93, Koe95, Küc98]. Erbium-doped crystals have been mostly object of these works.

The technique can be classified as a pump - probe experiment, where pulses from a pump source are used to excite a sample, while a second light source probes it, after a certain delay time. Typically, this kind of measurements are adopted to investigate ultrafast phenomena (in the femtosecond-regime or shorter) with a dependence on the time [Pas13]. In the case of ESA measurements, the shortest pulses are in the millisecond-

---

[3] It has been calculated that this wavelength is addressed by the gain maximum at least up to $\beta = 0.50$

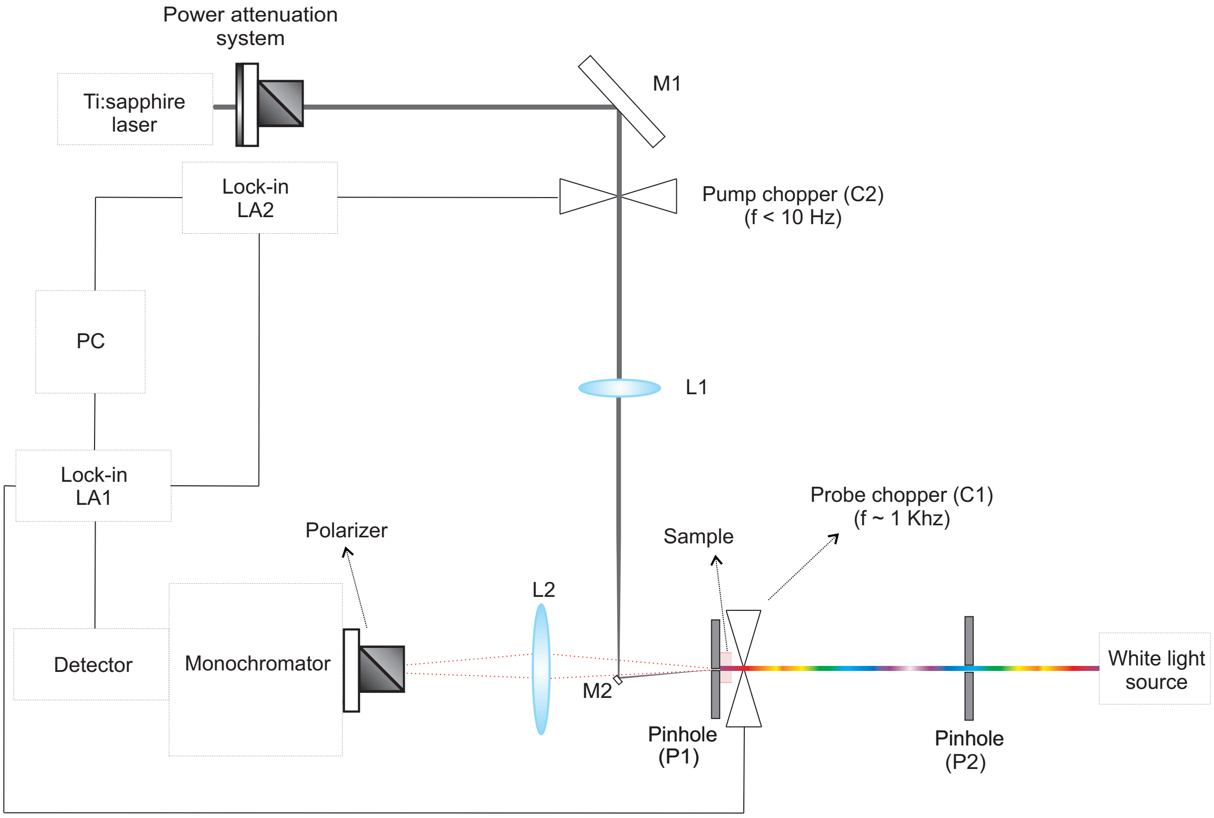

Figure 5.40: Setup for the performance of ESA measurements.

regime and the comparison of the signals transmitted by the crystal when either pumped or unpumped has the aim to determine excited state absorption cross sections.

A detailed description of the technique has been reported by *Koetke and Huber* [Koe95] and a representation of the setup is reported in Fig. 5.40.

The probe beam consisted of a supercontinuum laser source from *Fianium* (FemtoPower 1060) driving a white light generator emitting a broad spectrum of 440 - 1750 nm (SC450-PP-HE) which has been periodically interrupted by the chopper C1, set to a frequency $\nu_{C1} \sim 1\,\mathrm{kHz}$. This is a collimated source which does not need to be focused by a lens onto the sample, as it was previously done with either a halogen or a xenon lamp, because of its higher brightness.

The pump source, a Ti:sapphire laser, has been periodically interrupted by the chopper C2, set at a frequency ν_{C2} in the order of a few Hz, and afterwards focused with a lens L1 with a relatively long focal length ($f = 32\,\mathrm{cm}$) onto the sample. In order to obtain the best overlap between pump and probe beams into the crystal, the focused pump beam is driven almost onto the same optical axis of the probe beam via the mirror M2. The beam overlap volume in the crystal is limited by the presence of the 500 µm-wide pinhole P1. The mirror M2 is recommended to be only as wide as the pump beam diameter and positioned slightly out of the optical axis of the probe beam, in order to blind minimal portions of the transmitted light. This configuration still allows a good overlap between the beams in the crystal and a slight deviation of the non-absorbed pump beam which if coupled into the fiber of the supercontinuum laser source could cause instabilities or even damages. Nevertheless, the $\sim$3 mm-wide pinhole P2 has been mounted as a protection of the supercontinuum laser source. Screens to avoid reflexes of the pump beam to reach the monochromator slits are essential for a noise-free measurement signal.

Consequently, the light transmitted through the crystal is imaged onto the slits of the same 1 m-SPEX monochromator of Sect. 5.3.2. For polarization-dependent measurements, a Glan-Taylor polarizer has been located directly in front of the slits. The investigated spectral range has been always restricted to 440 - 1050 nm, allowing the use of the 500 nm-blazed grating, with 1200 lines per millimeter and a Si-photodiode for the detection of the signal.

To amplify and analyze the measurement signals, two lock-in amplifiers LA1 and LA2 of the same kind of the one described in Sect. 5.3.2 have been employed. LA1 receives the signal from the Si-photodiode (detector) as input, triggered by the fast chopper C1. Its output represents the input of LA2, triggered by the slow chopper C2. Both outputs of the lock-in amplifiers are recorded to be represented and analyzed by a LabView program on a PC.

The output of LA1 represents the amplified transmitted signal I_u when the crystal is unpumped. Via the modulation with the slow-chopper signal, LA2 can measure directly $\Delta I = I_\mathrm{p} - I_\mathrm{u}$, the difference between the signal transmitted through the crystal when it is pumped and unpumped, respectively.

In order to efficiently realize this double modulation, conditions on the frequency of the choppers and the relative integration times set for the lock-in amplifiers have to be imposed. To allow a sharp distinction between the frequencies of the choppers by the lock-in amplifiers, it is recommendable to maintain $\nu_\mathrm{C1}/\nu_\mathrm{C2} \geq 100$. The slow chopper should be slow enough to cause a steady state excitation of the levels. The integration time of LA1 should be short compared to half a period of the slow chopper, in order to have enough data points per resolution to be averaged and increase the signal-to-noise ratio. As a consequence, $\nu_\mathrm{C1} \sim 1\,\mathrm{kHz}$ and $6\,\mathrm{Hz} < \nu_\mathrm{C2} < 9\,\mathrm{Hz}$ fit the requests (time C2 is open is between 63 and 83 ms). Furthermore, LA1 has been working with an integration time of 30 ms and LA2 with a minimum of 3 s, up to 10 s in the case of the presence of a particularly high noise-level. The LabView program has been set to calculate a further average over three times the integration time of LA2, leading the total duration for a single point to either 9 or 30 s.

Nevertheless, in comparison to a halogen or xenon lamp, the application of the supercontinuum laser source had the main advantage of a higher spectral intensity improving the signal-to-noise ratio. Consequently, it allowed for reducing drastically the time needed to record spectra, mainly measured with an integration time of 3 s per point (9 s after the integration of the LabView program).

When the slow chopper is blocking the pump beam, it is possible to define the intensity of the unpumped transmitted signal I_u through the crystal. At this point, all the optical active doping ions with a concentration density n_dop populate the ground level. When the excitation by the probe beam is considered, the Beer-Lambert law can be applied as in the Equations (5.1) and (5.3) as follows:

$$I_\mathrm{u}^\kappa(\lambda) = I_0^\kappa(\lambda)\mathrm{e}^{-\sigma_\mathrm{GSA}^\kappa(\lambda)\, n_\mathrm{dop}\, d}. \tag{5.19}$$

Also in this case, for anisotropic crystals, measurements and calculations have to be repeated for every polarization κ.

When the slow chopper allows the pump beam to reach the crystal, further higher energy levels with a population density n_i can be excited and $\sum_i n_i = n_\mathrm{e}$, where n_e denotes the total excitation density. Consequently, in the pumped case, the intensity of the polarization-dependent transmitted beam I^κ_p, in absence of saturation processes, can be defined as [Koe95]:

$$I^\kappa_\mathrm{p}(\lambda) = I^\kappa_0(\lambda)\mathrm{e}^{\left(-\sigma^\kappa_\mathrm{GSA}(\lambda)\,(n_\mathrm{dop}-n_\mathrm{e})\,d+\sum_i n_i(\sigma^\kappa_{\mathrm{SE},i}(\lambda)-\sigma^\kappa_{\mathrm{ESA},i}(\lambda))\,d\right)}. \tag{5.20}$$

When the pump beam is active, the ground state is depopulated to $(n_\mathrm{dop} - n_\mathrm{e})$ in favor of higher energy states. Consequently, either the population of even higher excited states via ESA (where the ESA coefficient corresponds to $n_i\sigma^\kappa_{\mathrm{ESA},i}$) or stimulated emission to the ground state (where the SE coefficient corresponds to $n_i\sigma^\kappa_{\mathrm{SE},i}$) is allowed. The saturation effects which could invalidate Eq. (5.20) occur when $n_\mathrm{dop} \to n_\mathrm{e}$.

If the Equations (5.19) and (5.20) are combined, it is possible to define:

$$\ln\left(\frac{I^\kappa_\mathrm{p}(\lambda)}{I^\kappa_\mathrm{u}(\lambda)}\right) = n_\mathrm{e}\,d\left(\sigma^\kappa_\mathrm{GSA}(\lambda) + \sum_i \frac{n_i}{n_\mathrm{e}}(\sigma^\kappa_{\mathrm{SE},i}(\lambda) - \sigma^\kappa_{\mathrm{ESA},i}(\lambda))\right). \tag{5.21}$$

At this point, in order to be able to independently address the signals from the two lock-in amplifiers and perform a calibration of the final spectra, an important assumption must be made. The pump source must be considered able to cause only a sufficiently low total excitation density n_e, such as:

$$\Delta I = I_\mathrm{p} - I_\mathrm{u} << I_\mathrm{p}, I_\mathrm{u}. \tag{5.22}$$

In this way, applying the approximation: if $x \to 0 \Longrightarrow \ln(x+1) \approx x$, it is possible to assume:

$$\ln\left(\frac{I_\mathrm{p}}{I_\mathrm{u}}\right) = \ln\left(1 + \frac{I_\mathrm{p} - I_\mathrm{u}}{I_\mathrm{u}}\right) \approx \frac{I_\mathrm{p} - I_\mathrm{u}}{I_\mathrm{u}} = \frac{\Delta I}{I_\mathrm{u}} \approx \frac{\Delta I}{I}. \tag{5.23}$$

The second approximation in Eq. (5.23) is allowed because the transmitted signal I amplified by LA1 is triggered by the slow chopper, causing a modulation between I_p and I_u which is comparable to the noise-level of the spectra. This is also a direct consequence of Eq. (5.22).

Due to the amplification by the lock-in amplifiers, a measurement results in $A'\Delta I = \Delta I^\star$, and the ratio between the spectra recorded via the two lock-in amplifiers reads:

$$\frac{\Delta I^{\kappa\star}(\lambda)}{I^\kappa(\lambda)} = An_\mathrm{e}\,d\left(\sigma^\kappa_\mathrm{GSA}(\lambda) + \sum_i \frac{n_i}{n_\mathrm{e}}(\sigma^\kappa_{\mathrm{SE},i}(\lambda) - \sigma^\kappa_{\mathrm{ESA},i}(\lambda))\right). \tag{5.24}$$

where, A is an amplification factor not easy to be estimated. Nevertheless, it is possible to determine this factor via a calibration with a part of the spectra where stimulated emission SE and ESA phenomena are not present and a known absorption spectrum at the same wavelength range is available. Indeed:

$$\sigma_{\mathrm{SE},i} = \sigma_{\mathrm{ESA},i} = 0 \quad\Longrightarrow\quad \frac{\Delta I^{\kappa\star}(\lambda)}{I^\kappa(\lambda)} = An_\mathrm{e}\,d\sigma^\kappa_\mathrm{GSA}(\lambda). \tag{5.25}$$

Once the calibration has been performed, a known absorption cross section spectrum can be subtracted from Eq. (5.24) to obtain:

$$\left(\frac{\Delta I^{\kappa\star}(\lambda)}{I^{\kappa}(\lambda)}\right)_{\text{SE-ESA}} = \sum_i \frac{n_i}{n_\text{e}}(\sigma^{\kappa}_{\text{SE},i}(\lambda) - \sigma^{\kappa}_{\text{ESA},i}(\lambda)). \tag{5.26}$$

If the emission cross sections are also known, it is possible to extract solely the ESA cross sections from Eq. (5.26), but in the framework of this thesis all the ESA spectra will present a plot of the difference between SE and ESA cross sections. For simplicity, in the following these cross sections will be defined as $(\sigma_\text{SE} - \sigma_\text{ESA})$.

5.6.1 Measurement results

In this section, all the ESA spectra will be summarized and ordered concerning the crystal host. The 440 - 880 nm spectral range will be shown adding two insets focusing on the wavelength of the available pump sources and expected laser emission wavelengths. Here any ESA influence is detrimental for the operation of the laser.

The spectral range around 970 nm will be displayed separately, together with the GSA spectrum, in order to show the most convenient wavelengths for upconversion pumping. In Tab. 5.4 at the end of the chapter, a list of the two distinguished most efficient wavelengths for upconversion pumping in all the investigated erbium-doped crystals is present, together with the products $(\sigma_\text{SE} - \sigma_\text{ESA}) \cdot \sigma_\text{GSA}$ and $\sqrt{|(\sigma_\text{SE} - \sigma_\text{ESA}) \cdot \sigma_\text{GSA}|}$. The two wavelengths have been chosen with at least a distance of 0.6 nm in order to match different combination of peaks, when the narrowness of the peaks allows for such a distinction. In this case, a negative $(\sigma_\text{SE} - \sigma_\text{ESA})$ favors upconversion pumping, even more advantageously if at the same wavelength of a GSA peak.

All the spectra here reported have a resolution of 0.15 nm. Unfortunately, in the range of 970 nm, although the ESA spectra have the same 0.15 nm-resolution, the GSA spectra needed to calculate $(\sigma_\text{SE} - \sigma_\text{ESA})$, cause a decrease of resolution between 0.30 nm and 0.75 nm, depending on the spectrum, although an interpolation to steps of 0.05 nm has been performed.

Every ESA spectrum has been recorded under pumping at the most convenient wavelength around 970 nm. In order to obtain undisturbed spectra also around 970 nm, the possibility to record two spectra pumped at slightly different wavelengths (a few nanometers away from each other) has been tested together with the possibility of calibrating both to each other, isolating the area of saturation or deviation around the pumping wavelength. This is possible only when the slits of the monochromator are set very narrow and they are very efficiently screened towards spurious traces of the pump beam. With the resolution set for these experiments, in all cases only an area narrower than 2 nm was influenced by saturation or deviation effects around the pumping wavelength. In doing so, it could be avoided to record spectra pumping at the second convenient area of overlap between GSA and ESA, between 790 and 810 nm, which typically leads to very low signal-to-noise ratios and consequently to reduced resolutions.

In Fig. 5.41, the three most interesting spectra regarding Er^{3+}:$LiLuF_4$ and Er^{3+}:LaF_3 are reported. The overview on both polarizations in the spectral range between 440 and 880 nm is reported for both crystals in the Figures 5.41a and 5.41b. Here two insets

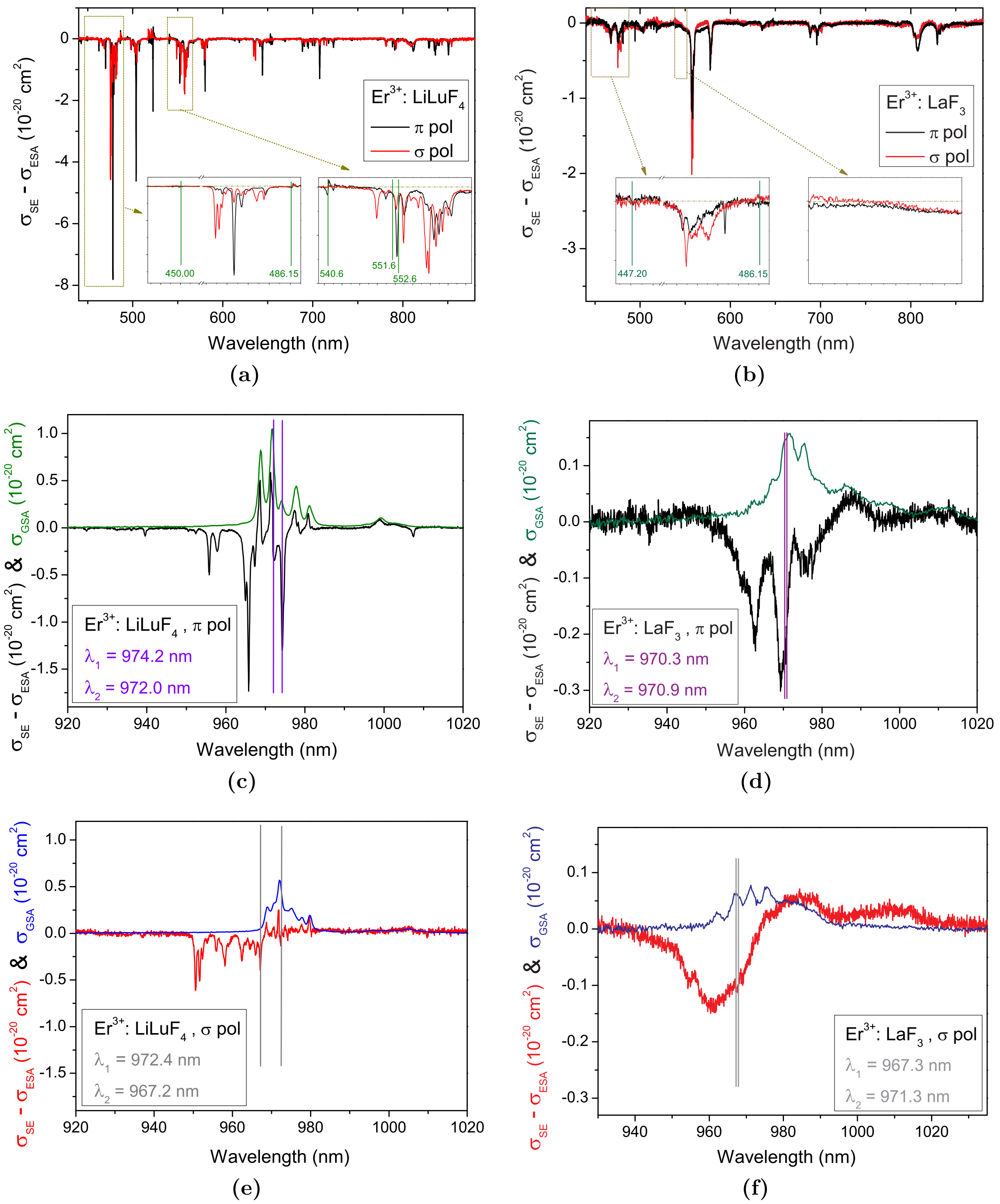

(a) (b) (c) (d) (e) (f)

Figure 5.41: Polarization-dependent ESA spectra of Er^{3+}:$LiLuF_4$ and Er^{3+}:LaF_3 in the visible and near IR spectral range. In (a), (c) and (e) the spectra regarding Er^{3+}:$LiLuF_4$ are displayed, while in (b), (d) and (f) those regarding Er^{3+}:LaF_3 are shown. In (a) and (b), the two polarizations are reported together in the spectral range between 440 and 880 nm and the green lines mark the wavelengths of particular interest in the two insets: wavelengths of the available pumping sources and potential emission wavelengths of the lasers. The right inset in (b) covers the range predicted by the gain spectra, where potential emission wavelengths lie (see Sect.5.5). In (c) and (e) (Er^{3+}:$LiLuF_4$) and in (d) and (f) (Er^{3+}:LaF_3), the two polarizations are split and shown together with the relative absorption spectrum in the 970-nm range. The two most convenient wavelengths for a high overlap of GSA and ESA are marked by lines and defined λ_1 and λ_2.

are displayed, focusing on the two spectral ranges of highest interest, concerning available pumping sources and possible emission wavelengths. In the left inset, the range of emission wavelengths of the InGaN laser diodes and the 2ω-OPSL is shown. For both crystals, the pumping wavelength with blue InGaN diode lasers matching the highest GSA cross section is not affected by detrimental ESA processes, while the 2ω-OPSL-pumping could suffer from moderate ESA in π-polarization. The emission wavelengths recorded with Er^{3+}:LiLuF_4 crystals are highlighted in the right inset in Fig.5.41a. For the short wavelength, detected during waveguide lasers experiments (see Chap. 6), ESA effects are avoided. For the long and most commonly obtained wavelength of 551.5 - 551.6 nm, apparently problems can occur, due to the evidently negative $(\sigma_{\mathrm{SE}} - \sigma_{\mathrm{ESA}})$ signal. Nevertheless, it has to be reminded that the ESA spectra have been recorded at a wavelength ~ 970 nm which can populate both the Er^{3+}-ions $^4\mathrm{I}_{11/2}$- and the $^4\mathrm{S}_{3/2}$-multiplets. As a consequence, the spectra are a convolution of the ESA phenomena which start from both the multiplets. Furthermore, it is expected that the $^4\mathrm{I}_{11/2}$- multiplet decays populating the long-living $^4\mathrm{I}_{13/2}$-multiplet which has been already identified (see Chapters 2 and 6) as possible starting level for excited state reabsorption ESR at the possible green laser wavelength. Additionally, it has already been recognized in [Bär00], that the picture given by spectroscopic measurements does not correspond exactly to the situation during laser operation. In this last case, the involved excitation densities are lower and the determined occupation densities can be different from what is predicted by spectroscopic investigations. A solution to this could be the numerical calculation of the occupation densities in laser operation and consequently the possibility to separate the contribution of the stimulated emission from the ESA contribution. However, performing high-power-ESA measurements is not recommendable, because the approximation in Eq. (5.22) would not be valid anymore and the evaluation of ESA spectra not anymore straightforward.

In Fig. 5.41b, the right inset gives information about the influence of detrimental effects on the possible laser wavelengths predicted by the gain spectra of the previous section for Er^{3+}:LaF_3 (see Fig.5.36). Considering the contribution of both polarizations, it is possible to summarize in the right inset the spectrum between 539 and 552 nm, where all the possible laser emission wavelengths at relatively low inversion densities are included. Due to on the average higher absorption and emission cross sections, the polarization in which laser operation is most probable is π-polarization. Nevertheless, the $(\sigma_{\mathrm{SE}} - \sigma_{\mathrm{ESA}})$ signal is always slightly negative in this spectral range, while the signal in σ-polarization is positive only at comparatively short wavelengths, where high inversion levels are needed to reach gain. Also the ESA spectrum in the visible spectral range is not encouraging regarding the possibility of Er^{3+}:LaF_3 to lase in the green spectral range.

In the Figures 5.41c, 5.41e, 5.41d and 5.41f, the ESA spectrum is analyzed in order to establish the possibility of a single-wavelength upconversion-pumping mechanism in Er^{3+}:LiLuF_4 and Er^{3+}:LaF_3. On this purpose, the most effective range around 970 nm and at the same time, for each polarization, the respective GSA spectrum are shown. The two lines in every graph indicate the two most advantageous wavelengths where either the value of $(\sigma_{\mathrm{SE}} - \sigma_{\mathrm{ESA}}) \cdot \sigma_{\mathrm{GSA}}$ is minimized (i. e. the maximum negative value) or the value $\sqrt{|(\sigma_{\mathrm{SE}} - \sigma_{\mathrm{ESA}}) \cdot \sigma_{\mathrm{GSA}}|}$ is maximized, and labeled by λ_1 and λ_2. The differences between LiLuF_4 and LaF_3 are clear: the first host allows for much higher cross sections and narrower peaks than the second. As a consequence, the signal-to-noise ratio is much

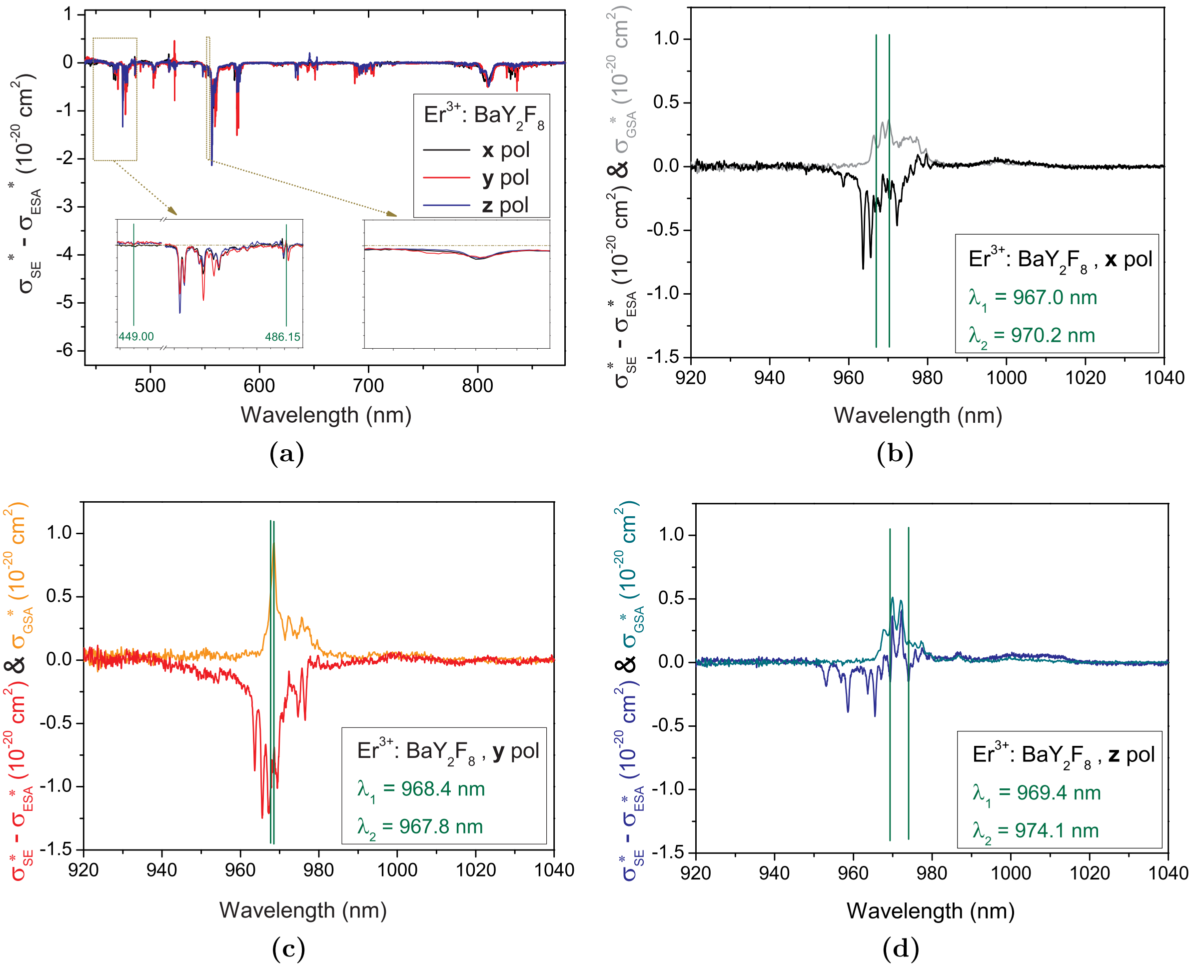

(a) (b) (c) (d)

Figure 5.42: Polarization-dependent ESA spectra of Er^{3+}:BaY_2F_8. In (a), the estimated $\sigma_{\mathrm{SE}} - \sigma_{\mathrm{ESA}}$ for the three polarization in the range 440 - 880 nm are summarized. Due to the biaxial nature of the host, only an estimation of the cross sections was possible ($*$). In the two insets, the estimated cross sections in the wavelength range of available pumping sources and possible laser emission wavelengths (based on the calculation of the gain in Sect. 5.5) are depicted. In (b)-(d), the three polarization-dependent estimated cross sections are separately plotted, together with the respective σ_{GSA} in the 970 nm-spectral range. The two most convenient wavelengths for single-wavelength upconversion-pumping are highlighted and labeled by λ_1 and λ_2.

higher in Er^{3+}:$LiLuF_4$, as already evident in Figures 5.41a and 5.41b concerning the visible spectral range. In Tab.5.4, a factor of almost ten between the squares of the products of the ESA and GSA cross sections in the two hosts is found.

In Fig. 5.42, the polarization-dependent ESA spectra concerning Er^{3+}:BaY_2F_8 are displayed. In Fig. 5.42a, the spectra in the range 440-880 nm for the three polarizations are shown. As for former measurements, also in this case, due to the biaxial nature of BaY_2F_8, the cross sections could only be estimated. The two insets focus on the spectral ranges where available pump sources operate (InGaN laser diodes and 2ω-OPSL in the blue spectral range) and the possible emission wavelengths in the green spectral range, estimated via the gain calculation are expected to be. The pumping wavelengths seem to be not affected in any polarization by the influence of ESA. Nevertheless, the opposite can be observed in the spectral range of possible emission wavelengths, highlighted by the right inset. For the three polarizations, the $(\sigma_{\text{SE}} - \sigma_{\text{ESA}})$ signal is always slightly negative, with the exception of the region around 553 nm, where a deeper negative peak in the three polarizations is present. Despite the negative sign of the signal, in laser regime the situation could be favorable, due to the possibly different occupation densities of the involved energy levels. Nevertheless, the further negative cross sections around 553 nm are expected to prevent laser operation around this wavelength. This implies that it is more probable to observe laser emission when higher inversion levels than 0.10 are reached and the gain maximum is shifted to shorter wavelengths. In the further three spectra, the polarization-dependent curves in the 970 nm region are displayed, each together with the relative GSA spectrum. Due to the narrowness of peaks, such as in LiLuF_4, always two distinct combinations of peaks could be highlighted as two most effective wavelengths for single-wavelength upconversion-pumping. The products $\sqrt{|(\sigma_{\text{SE}} - \sigma_{\text{ESA}}) \cdot \sigma_{\text{GSA}}|}$ show lower values than in Er^{3+}:LiLuF_4, except an exceptionally higher value for **y**-polarization.

Although no gain cross sections could be calculated, an estimation of ESA spectra has been performed also for Er^{3+}:BaYLuF_8 and it is displayed in Fig. 5.43. Despite the similarity between the two crystal hosts, differences can be found if a comparison with the results obtained in BaY_2F_8 is carried out. The signal-to-noise ratio appears slightly higher in the spectra BaYLuF_8, especially in the visible spectral range, plotted in Fig. 5.43a. In the first inset, it is confirmed that for both the pumping sources in the blue spectral range no detrimental ESA effects are expected. In the right inset concerning the expected emission wavelengths of Er^{3+}:BaYLuF_8, no real estimation can be deduced from the gain spectrum which could not be calculated, but it is reasonable to consider the results of the calculation performed for Er^{3+}:BaY_2F_8 as a reliable reference. Indeed, in this spectral range the three polarization-dependent curves resemble those recorded with Er^{3+}:BaY_2F_8 and the conclusion is the same: the estimated cross sections are always slightly negative with a deeper negative peak at 553 nm. Also in this case, the situation is not favorable for laser operation in the green spectral range. Nevertheless, the possibility of different occupation densities in laser regime does not absolutely prevent laser emission to be detected also at room temperature (upconversion green laser emission has been demonstrated in Er^{3+}:BaY_2F_8 at $T = 77\,\text{K}$ [Joh71, Joh72]).

The strongest differences, if compared to Er^{3+}:BaY_2F_8 can be detected in the near infrared spectral range, where the ESA spectra are compared, for every single polarization, to the GSA spectrum. The three spectra are depicted in the figures 5.42b - 5.42d. Slight differences in the calibration if compared to Er^{3+}:BaY_2F_8 have possibly caused some differences in the spectra. Also in this case, the two best wavelengths for single-wavelength upconversion pumping have been highlighted and labeled as λ_1 and λ_2.

In Fig. 5.44, the ESA spectra regarding Er^{3+}:KY_3F_{10} and Er^{3+}:BaLu_2F_8 are summarized. For both crystal hosts the results show an estimation of the cross sections due to the missing information about the real Er^{3+}-concentration in the KY_3F_{10} crystal and the impossibility to perform polarization-dependent measurements for Er^{3+}:BaLu_2F_8.

In Fig. 5.44a, the spectral range included between 440 and 880 nm is depicted, and the two insets focus on the spectral range where available InGaN diode lasers and a 2ω-OPSL operate and on the possible laser emission wavelengths. Differently than for the other examined crystal hosts, Er^{3+}:KY_3F_{10} suffers from ESA on both the pump wavelengths, more severely on the one characteristic for the 2ω-OPSL. In the right inset,

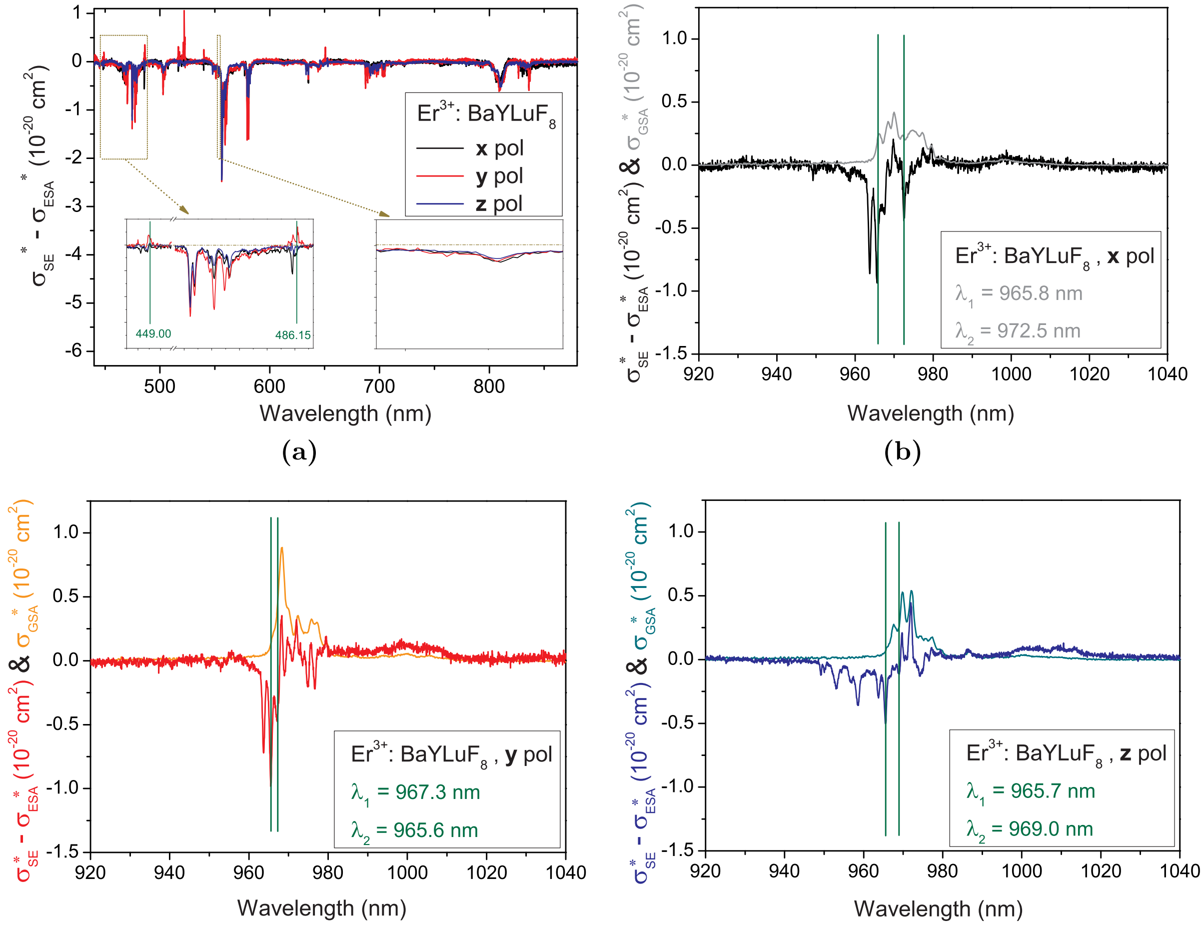

(a) **(b)**

(c) **(d)**

Figure 5.43: Polarization-dependent ESA spectra of Er^{3+}:$BaYLuF_8$. In (a), the estimated $\sigma_{SE} - \sigma_{ESA}$ for the three polarizations in the range 440 - 880 nm are summarized. Due to the biaxial nature of the host, only an estimation of the cross sections was possible (∗). In the two insets, the estimated cross sections of the wavelength range of available pump sources and possible laser emission wavelengths are depicted. In the right inset, due to the missing calculation of the gain spectrum, the expected emission wavelengths are those calculated for Er^{3+}:BaY_2F_8. In (b)-(d), the three polarization-dependent estimated cross sections are separately plotted, together with the respective σ^*_{GSA} in the 970 nm-spectral range. The two most convenient wavelengths for single-wavelength upconversion-pumping are highlighted and labeled as λ_1 and λ_2.

the wavelength interval where Er^{3+}:KY_3F_{10} can possibly lase, at relatively low inversion levels, is reported. In this case, the signal is still mostly slightly negative, but no emission is calculated to be active around 551 nm, where a negative peak is centered. In Fig. 5.44b, the estimated $\sigma^*_{SE} - \sigma^*_{ESA}$ is plotted for the 970-nm range together with the GSA spectrum in the same spectral region, in order to show possible overlaps, effective for single-wavelength upconversion pumping. The two wavelengths being characterized by the highest estimated $\sqrt{|(\sigma^*_{SE} - \sigma^*_{ESA}) \cdot \sigma^*_{GSA}|}$ are both close to 971 nm, because of the dominant GSA peak centered at that wavelength.

In Fig. 5.44c, the ESA spectrum of Er^{3+}:$BaLu_2F_8$ in the 440 - 880 nm range is shown. As already observed for estimated emission and absorption cross sections, also in this case the values are lower than in Er^{3+}:BaY_2F_8 and Er^{3+}:$BaYLuF_8$, the peaks are gener-

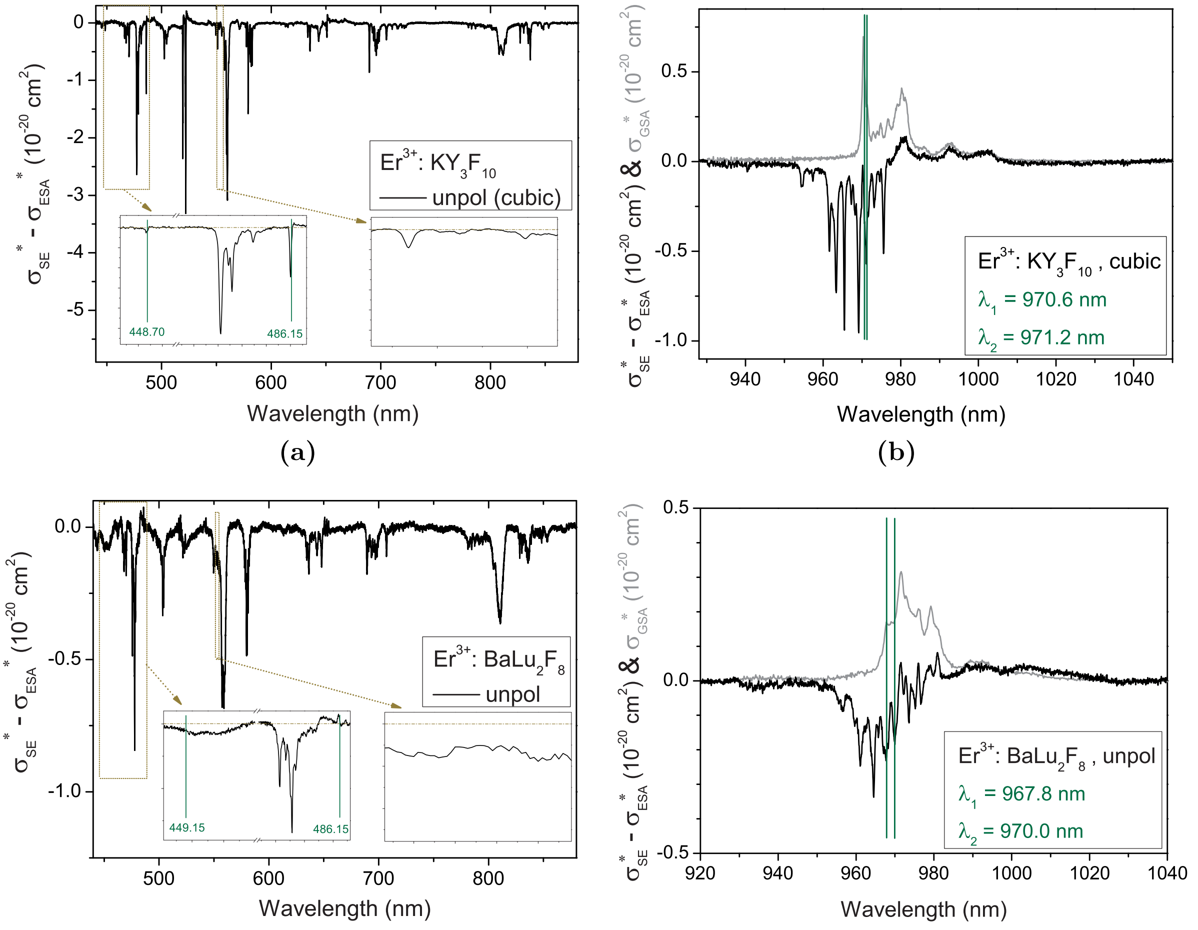

(a) **(b)**

(c) **(d)**

Figure 5.44: ESA spectra of Er^{3+}:KY$_3$F$_{10}$ and Er^{3+}:BaLu$_2$F$_8$. In (a) and (c), the estimated $\sigma_{\mathrm{SE}}^{*} - \sigma_{\mathrm{ESA}}^{*}$ in the range 440 - 880 nm are displayed for both crystal hosts. Due to the missing value of the real Er^{3+}-concentration in KY$_3$F$_{10}$ and of the polarization-dependent measurements of Er^{3+}:BaLu$_2$F$_8$, only an estimation of the cross sections was possible ($*$). In the left inset, the incidence of detrimental ESA at the wavelength of available pump sources can be investigated. In the right inset in (a), for Er^{3+}:KY$_3$F$_{10}$ the range of possible laser emission wavelengths resulting from gain calculations at relatively low inversion levels are highlighted. Considering the impossibility to calculate the gain for Er^{3+}:BaLu$_2$F$_8$, the right inset in (c) shows the same spectral range already shown for Er^{3+}:BaY$_2$F$_8$ and Er^{3+}:BaYLuF$_8$ in Figures 5.42 and 5.43. In (b) and (d), the estimated $\sigma_{\mathrm{SE}}^{*} - \sigma_{\mathrm{ESA}}^{*}$ cross sections are plotted together with the σ_{GSA} in the 970 nm-spectral range. The two most convenient wavelengths for single-wavelength upconversion-pumping in each host are highlighted and labeled as λ_1 and λ_2.

ally broader and the signal-to-noise ratio is lower. In the left inset, it can be noticed that a broad peak structure is located in the range of the available InGaN laser diode wavelength, possibly detrimental for laser pumping. Nevertheless, it is possible that if single polarizations are addressed, not all are affected by this problem. Furthermore, no ESA influence is predicted at the emission wavelength of the 2ω-OPSL. Considering the missing estimation of gain cross sections, the same wavelength region where emission is expected in Er^{3+}:BaY$_2$F$_8$ and Er^{3+}:BaYLuF$_8$ is depicted. The signal is slightly negative, as in the other two crystal hosts, and for polarization-dependent measurements similar results such as in Er^{3+}:BaY$_2$F$_8$ and Er^{3+}:BaYLuF$_8$ could emerge. In Fig. 5.44d, the possibility of overlap between ESA and GSA spectra is shown. Despite the reduced estimated cross section values, the curves could resemble a convolution of the three polarizations shown for Er^{3+}:BaY_2F_8 and Er^{3+}:$BaYLuF_8$, with a tendency of locating the lowest estimated $(\sigma^*_{\mathrm{SE}} - \sigma^*_{\mathrm{ESA}})$ at relatively short wavelengths, where the GSA signal of the multiplet starts (i. e. $\lambda \leq 970\,\mathrm{nm}$).

5.7 Summary of the most important reliable data

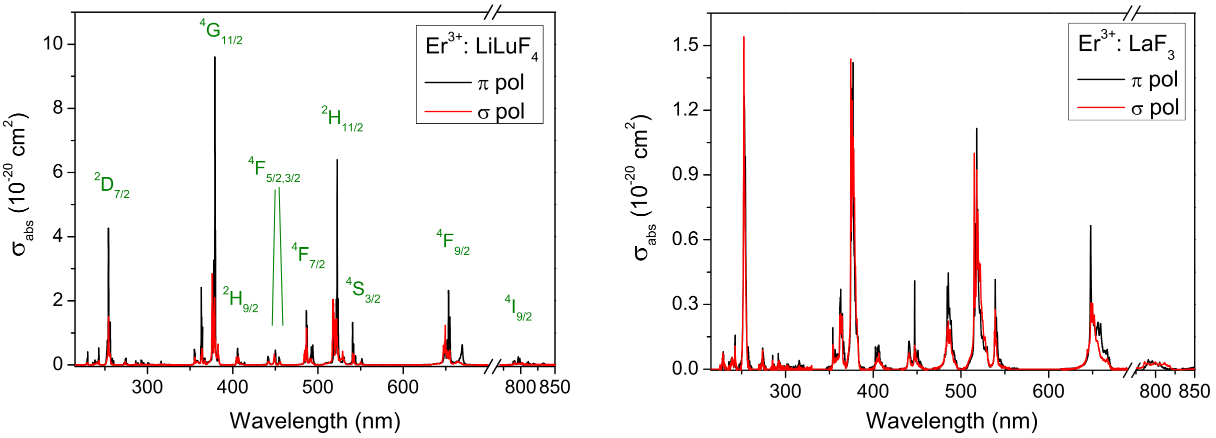

(a) **(b)**

Figure 5.45: Polarization-dependent absorption cross sections at room temperature of 1.25 at.% Er^{3+}:LiLuF$_4$ (a) and 0.6 at.% Er^{3+}:LaF$_3$ (b), in the wavelength range 215 - 850 nm. The absorption lines in this spectral range correspond to the transitions between the Er^{3+}-ion ground state ^{4}I$_{15/2}$ and different excited states. In (a), the final energy levels of the dominant transitions are displayed [Die63, Weg00]. For a complete list of cross sections in both polarizations and involved energy levels, see Tab. D.1.

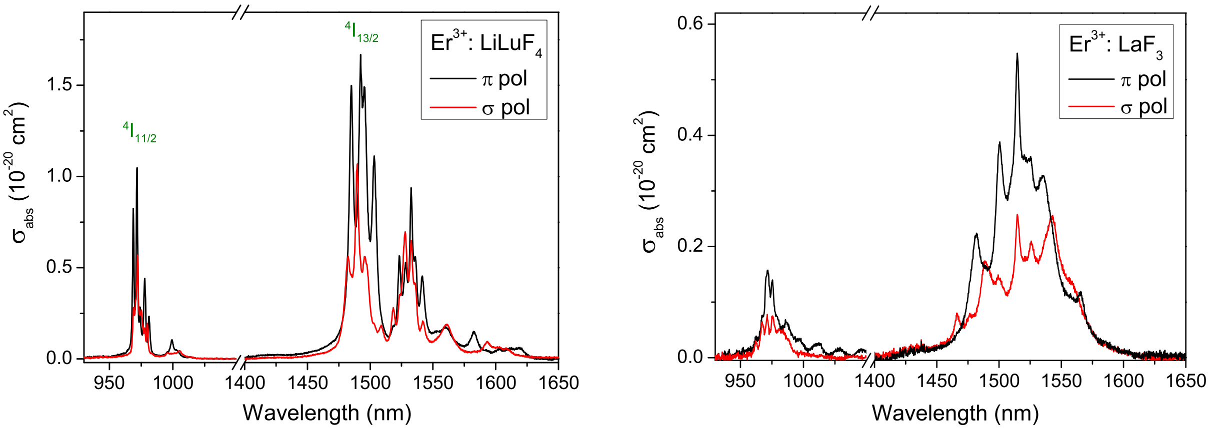

(a) **(b)**

Figure 5.46: Polarization-dependent absorption cross sections at room temperature of Er^{3+}:LiLuF$_4$ (a) and Er^{3+}:LaF$_3$ (b). In (a) the final energy levels of the two transitions from the ground state ^{4}I$_{15/2}$ are labeled.

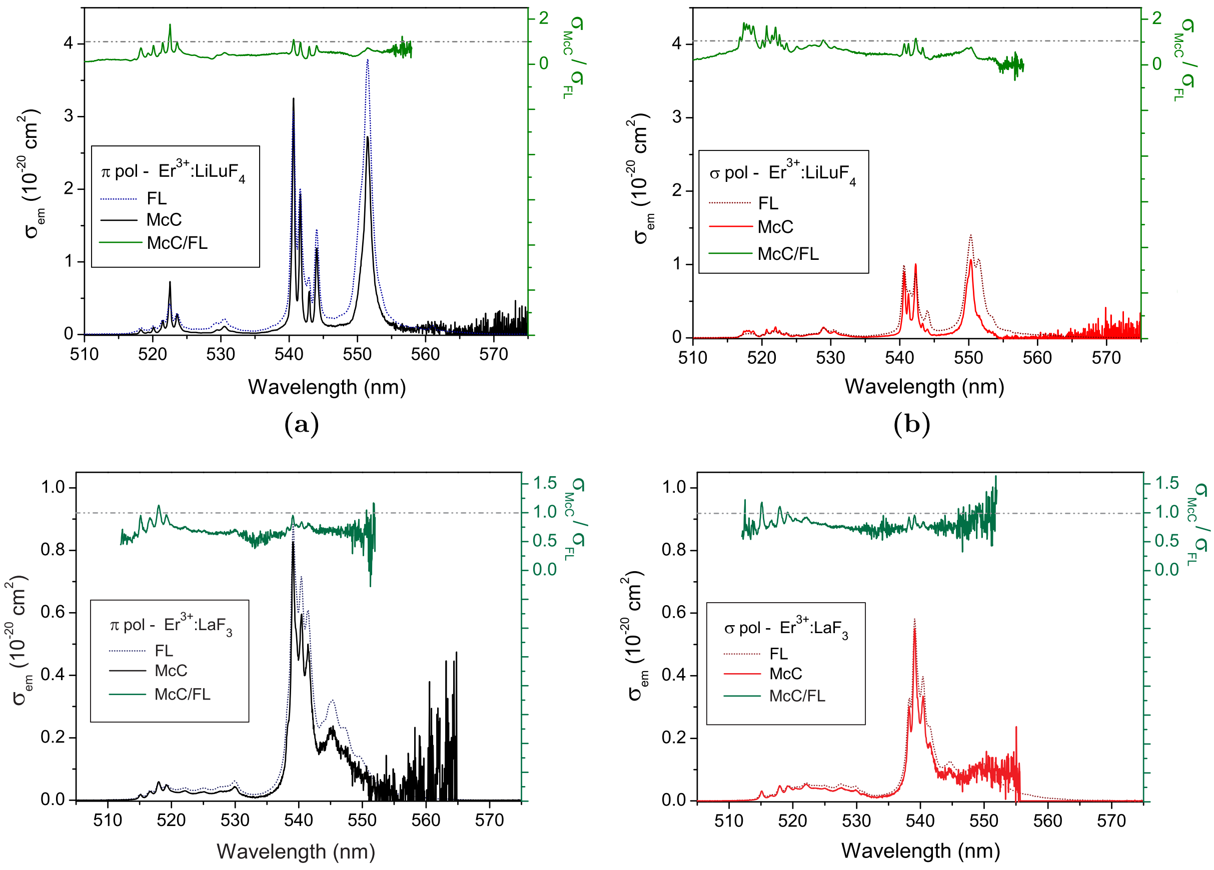

(a) **(b)**

(c) **(d)**

Figure 5.47: Comparison between the results of the FL and McC technique of transitions starting from the $^4S_{3/2}$-multiplet in the green spectral range in Er^{3+}:LiLuF$_4$ and Er^{3+}:LaF$_3$. In (a) and (b), a comparison between the results calculated with the FL (with 1 at.% Er^{3+}:LiLuF$_4$) and McC (with 1.25 at.% Er^{3+}:LiLuF$_4$) methods (energy level scheme based on [Kam86]) is shown in π- and σ-polarization, respectively. On the right vertical axis the ratio of the two curves McC/FL is shown. This curve has been limited to 558 nm in order to hide the divergence due to the low signal-to-noise ratio of the McC curve. In (c) and (d), the same is shown for Er^{3+}:LaF$_3$, based on measurements performed with a 0.6 at.% Er^{3+}-doped and a 0.43 at.% Er^{3+}-doped samples. In both polarizations, the reliable spectra are those derived with the McC method.

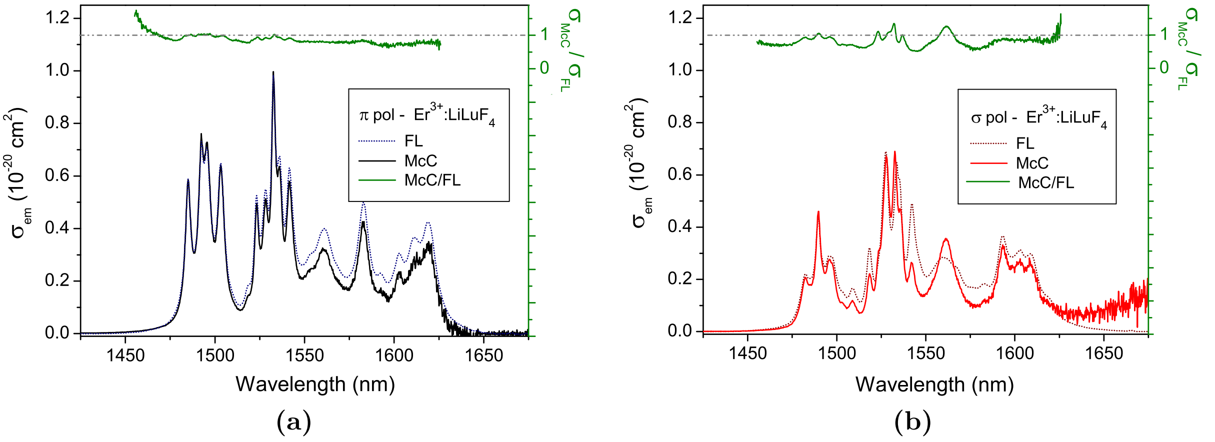

(a) (b)

Figure 5.48: Polarization-dependent emission cross sections of the transition $^4I_{13/2} \rightarrow {}^4I_{15/2}$ in Er^{3+}:$LiLuF_4$. The cross sections have been calculated from the emission spectra of a 1.3 at.% -doped Er^{3+}:$LiLuF_4$ crystal (FL) and the absorption spectra of a 1.25 at.% -doped Er^{3+}:$LiLuF_4$ crystal (McC). On the right vertical axis the ratio of the two curves McC/FL is shown. This curve has been limited to 1645 nm in order to hide the divergence due to the low signal-to-noise ratio of the McC curve. In both polarizations, the reliable spectra are those derived with the McC method.

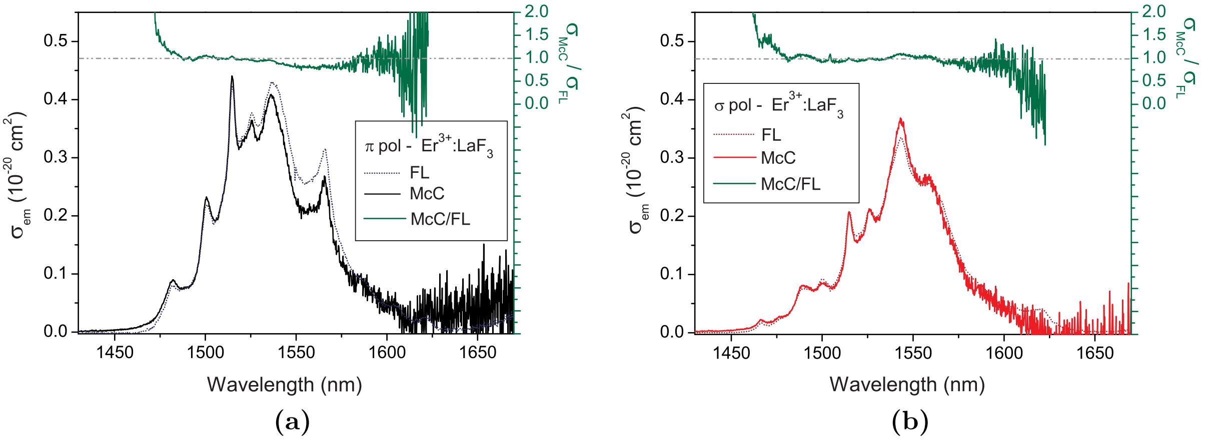

(a) (b)

Figure 5.49: Emission cross sections in a 0.6% - and a 0.43% -doped Er^{3+}:LaF_3 from the $^4I_{11/2}$-multiplet. In (a) and (b), a comparison between the results of the FL (with the higher Er^{3+}-doped sample) and McC (with the lower Er^{3+}-doped sample) methods is shown in π- and σ-polarization, respectively. On the right vertical axis the ratio of the two curves McC/FL is shown. This curve has been limited in order to hide the divergence due to the high signal-to-noise of the McC curve. In both polarizations, the reliable spectra are those derived with the McC method.

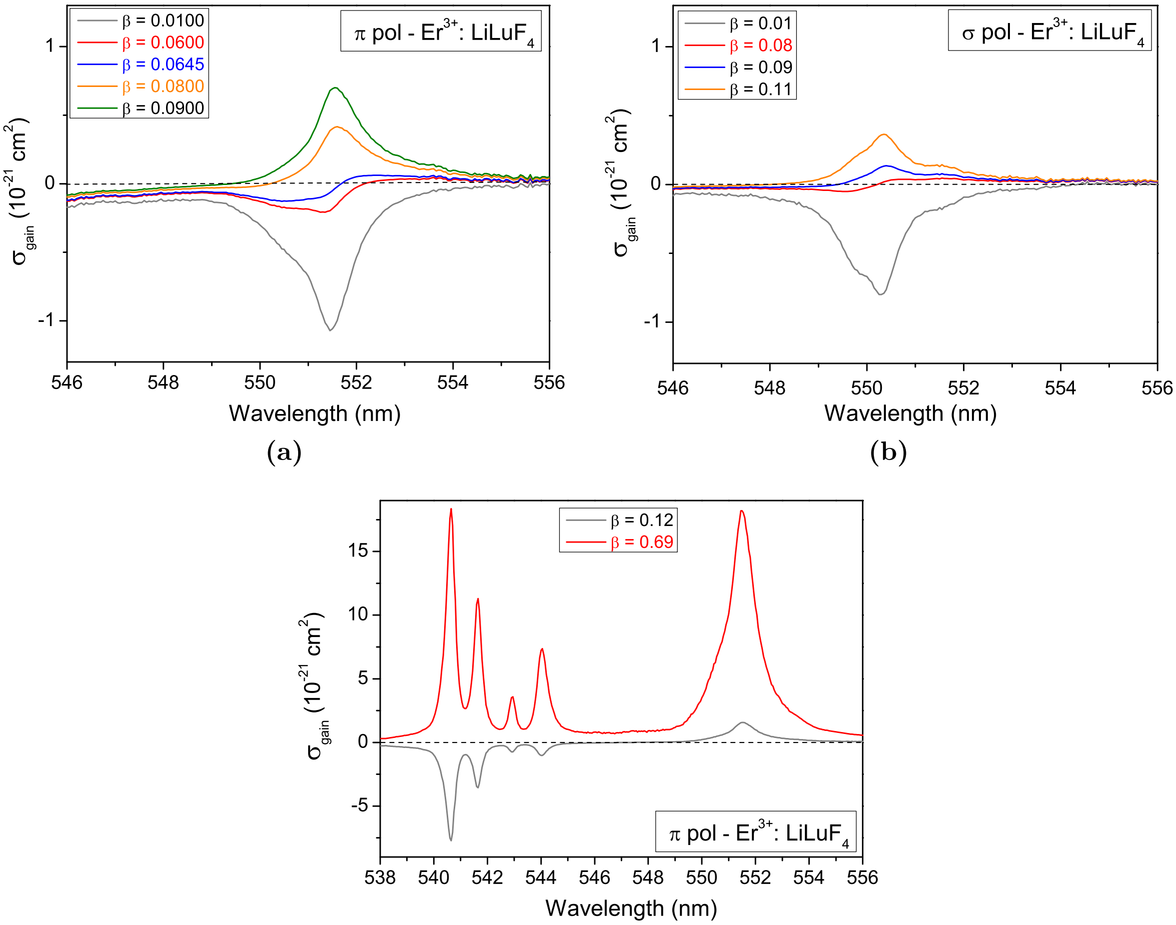

(a)

(b)

(c)

Figure 5.50: Polarization-dependent gain spectrum of Er^{3+}:$LiLuF_4$ in the green spectral range, at low and high inversion levels β. The inversion levels highlighted with colors in the legend represent either the minimum level which allows laser emission, or significant values concerning specific laser experiments (see text and Chap. 6 for further details). In (a), the gain spectrum in π-polarization, for low β is reported. In (b), the gain spectrum in σ-polarization, for low β is displayed. In (c), the spectrum for high inversion levels is reported concerning π-polarization.

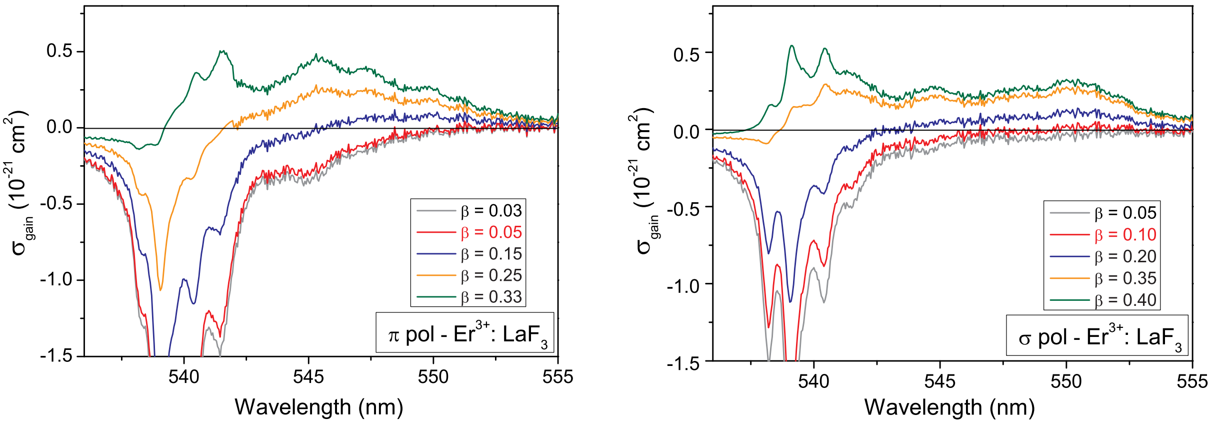

(a) (b)

Figure 5.51: Polarization-dependent gain spectrum of Er^{3+}:LaF_3 in the green spectral range. Both the gain spectra for π-polarization (a) and σ-polarization (b) show relatively low gain cross sections and they start to allow laser emission at $\beta = 0.05$ and $\beta = 0.10$, respectively.

Er^{3+}-doped crystal	Multiplet	Lifetime τ (ms)
$LiLuF_4$	$^4S_{3/2}$	0.40
	$^4I_{11/2}$	3.4
	$^4I_{13/2}$	9.7
LaF_3	$^4F_{7/2}$	0.015
	$^2H_{11/2}$	0.022
	$^4S_{3/2}$	0.67
	$^4I_{11/2}$	12.6
BaY_2F_8	$^4S_{3/2}$	0.58
$BaYLuF_8$	$^4S_{3/2}$	0.62
	$^4I_{13/2}$	12.8
KY_3F_{10}	$^4S_{3/2}$	0.29
	$^4I_{13/2}$	13.5
$BaLu_2F_8$	$^4S_{3/2}$	0.100 ($\star$)
	$^4I_{13/2}$	9.9

Table 5.3: Summary of the measured radiative lifetimes. ($\star$) has been measured in a highly doped sample and it does not correspond to the effective radiative lifetime of the multiplet.

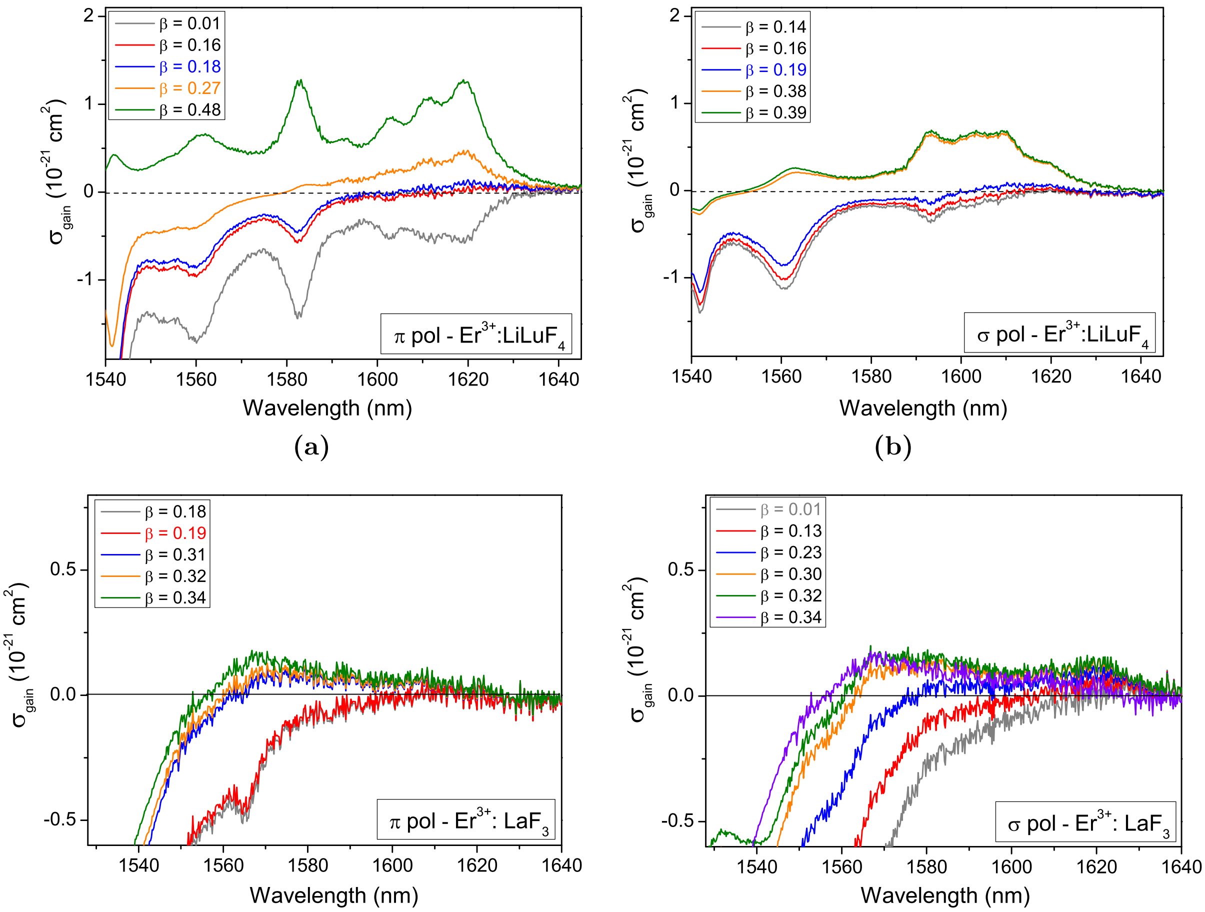

(a) **(b)**

(c) **(d)**

Figure 5.52: Polarization-dependent gain spectra of Er^{3+}:$LiLuF_4$ and Er^{3+}:LaF_3 in the infrared spectral range. In (a) and (b), the spectra in π- and σ-polarization for Er^{3+}:$LiLuF_4$ are depicted and the gain cross section is positive (although very low) already at an inversion level of 0.01, in π-polarization, while only at $\beta = 0.14$ in σ-polarization. The laser emission wavelengths recorded during laser experiments (see Chap. 6), have been all identified, together with their interval of inversion level. In (c) and (d), the equivalent spectra are depicted for Er^{3+}:LaF_3. Positive gain maxima are reached at a minimum inversion level of 0.19 and 0.01 for π- and σ-polarization, respectively.

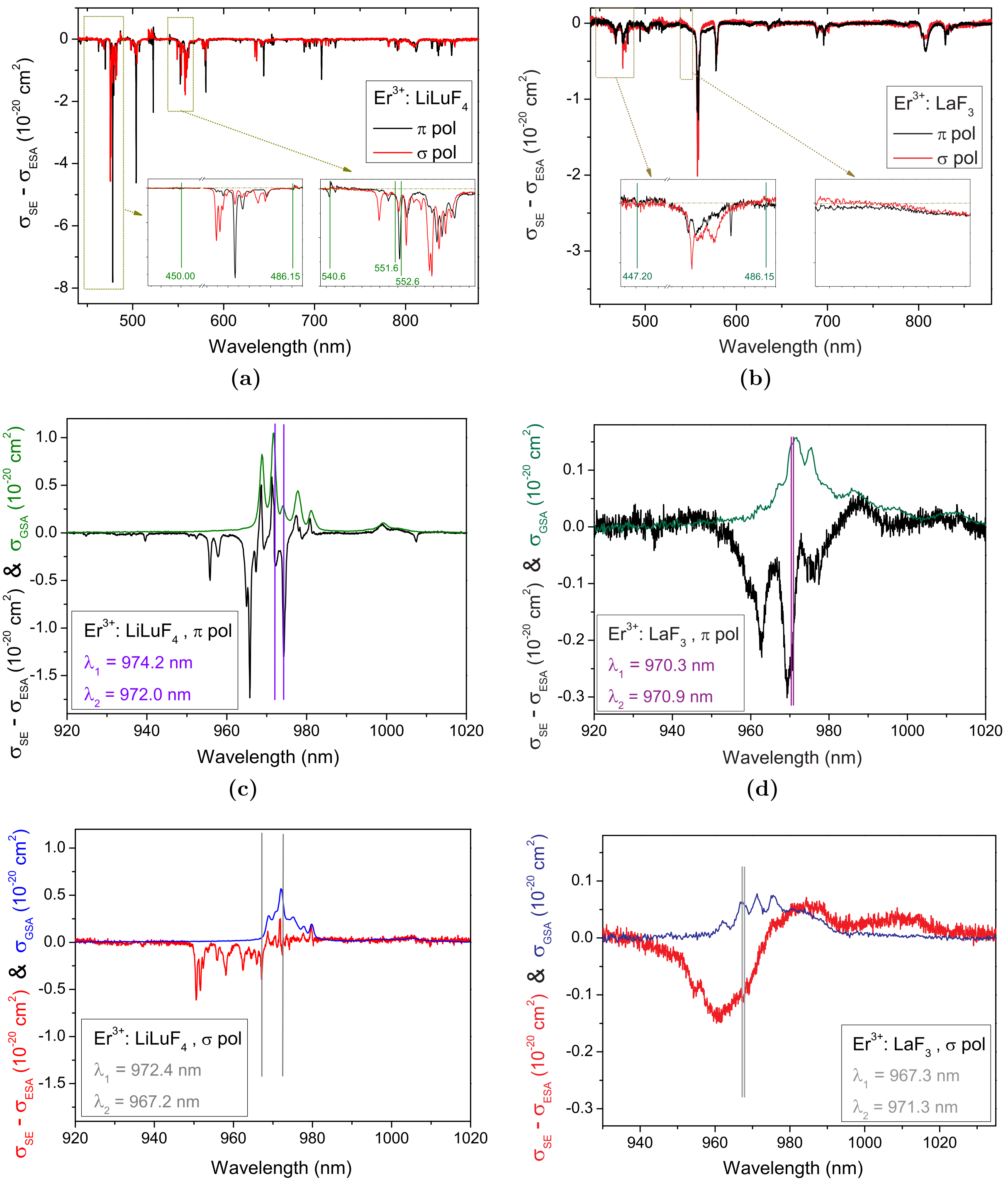

(a) (b) (c) (d) (e) (f)

Figure 5.53: Polarization-dependent ESA spectra of Er^{3+}:$LiLuF_4$ and Er^{3+}:LaF_3 in the visible and near IR spectral range. In (a), (c) and (e) the spectra regarding Er^{3+}:$LiLuF_4$ are displayed, while in (b), (d) and (f) those regarding Er^{3+}:LaF_3 are shown. In (a) and (b), the two polarizations are reported together in the spectral range between 440 and 880 nm and the green lines mark the wavelengths of particular interest in the two insets: wavelengths of the available pumping sources and potential emission wavelengths of the lasers. The right inset in (b) covers the range predicted by the gain spectra, where potential emission wavelengths lie (see Sect.5.5). In (c) and (e) (Er^{3+}:$LiLuF_4$) and in (d) and (f) (Er^{3+}:LaF_3), the two polarizations are split and shown together with the relative absorption spectrum in the 970-nm range. The two most convenient wavelengths for a high overlap of GSA and ESA are marked by lines and defined λ_1 and λ_2.

Er^{3+}-doped crystal	Polarization	$(\sigma_{SE} - \sigma_{ESA}) \cdot \sigma_{GSA}$ (10^{-42} cm^4)	$\sqrt{\lvert(\sigma_{SE} - \sigma_{ESA}) \cdot \sigma_{GSA}\rvert}$ (10^{-21} cm^2)	Wavelength (nm)
$LiLuF_4$	π	-35.7	6.0	974.2
	π	-28.2	5.3	972.0
	σ	-6.9	2.6	972.4
	σ	-2.1	1.5	967.2
LaF_3	π	-3.9	2.0	970.3
	π	-3.0	1.7	970.9
	σ	-0.71	0.84	967.2
	σ	-0.67	0.82	967.8
BaY_2F_8	**x**	-9.6 $\ast$	3.1 $\ast$	967.0
	x	-9.1 $\ast$	3.0 $\ast$	970.2
	y	-73 $\ast$	8.5 $\ast$	968.4
	y	-56 $\ast$	7.5 $\ast$	967.8
	z	-5.0 $\ast$	2.2 $\ast$	969.4
	z	-2.5 $\ast$	1.6 $\ast$	974.1
$BaYLuF_8$	**x**	-18 $\ast$	4.2 $\ast$	965.8
	x	-9.6 $\ast$	3.1 $\ast$	972.5
	y	-19.6 $\ast$	4.4 $\ast$	967.3
	y	-13.8 $\ast$	3.7 $\ast$	965.6
	z	-3.7 $\ast$	1.9 $\ast$	965.7
	z	-2.9 $\ast$	1.7 $\ast$	969.0
KY_3F_{10}	cubic	-19 $\ast$	4.4 $\ast$	970.6
	cubic	-19 $\ast$	4.4 $\ast$	971.2
$BaLu_2F_8$	unpol	-3.8 $\ast$	1.9 $\ast$	967.8
	unpol	-3.3 $\ast$	1.8 $\ast$	970.0

Table 5.4: List of the two distinguished most efficient wavelengths for single-wavelength upconversion pumping in Er^{3+}-doped fluoride crystals, together with the relative product $(\sigma_{SE} - \sigma_{ESA}) \cdot \sigma_{GSA}$ and the square of its absolute value, which has the more valuable unit of a cross section (cm^2). The second most efficient wavelength is spectrally separated from the first by at least 0.6 nm. The $\ast$ is present when the cross sections are only an estimation, due to the approximations explained in the previous sections.

6 Laser experiments

In this chapter, the results and the problems encountered during the laser experiments will be explained.

The major part of the chapter will concern upconversion lasers and the different configurations in which it is possible to operate them, either single-wavelength or dual-wavelength pumped. A straightforward comparison of the results of the single-wavelength pumped system can be done with the results of experiments performed with a pump wavelength in the blue spectral range, delivering photons with an energy which is twice of the one carried by an infrared photon of the single-wavelength pumped system.

In the end, the attention will be moved to the 1.5-µm spectral range, where inband-pumped experiments can be performed in erbium-doped crystals, in order to obtain laser emission at 1.6 µm.

6.1 Upconversion lasers

As explained along the whole thesis, the most fascinating application of erbium-doped fluoride crystals is upconversion lasers.

In Chap. 5, the suitability of the crystals for upconversion laser experiments has been confirmed. In the following, the results concerning lasing in a four-fold cavity, in a thin disk geometry, in waveguides and in a dual-wavelength pump scheme will be introduced, together with a few theoretical aspects.

6.1.1 Rate equations for upconversion lasers

In the case of Er^{3+}-doped media, the possible pumping schemes which allow for single-wavelength upconversion pumping are depicted in Fig. 2.5.

If the upconversion pump takes place as intraionic process, an ESA-pumping scheme describes the excitation with only one involved ion.

In the easiest model, only four energy levels are involved, as depicted in Fig. 6.1a and discussed by *Huber* [Hub99]. Level 3 is considered to fast relax into level 2 and it is not involved further in the process and not included in the rate equations. Level M is the intermediate level which is populated by the GSA process and then depopulated by the ESA process. This model is considered with a single-wavelength pump source and without distinguishing the branching ratios in the decay of level 2, supposed to decay exclusively to the ground level 1. In this way, with population densities of the three energy levels N_1, N_M and N_2, the rate equations for the system are:

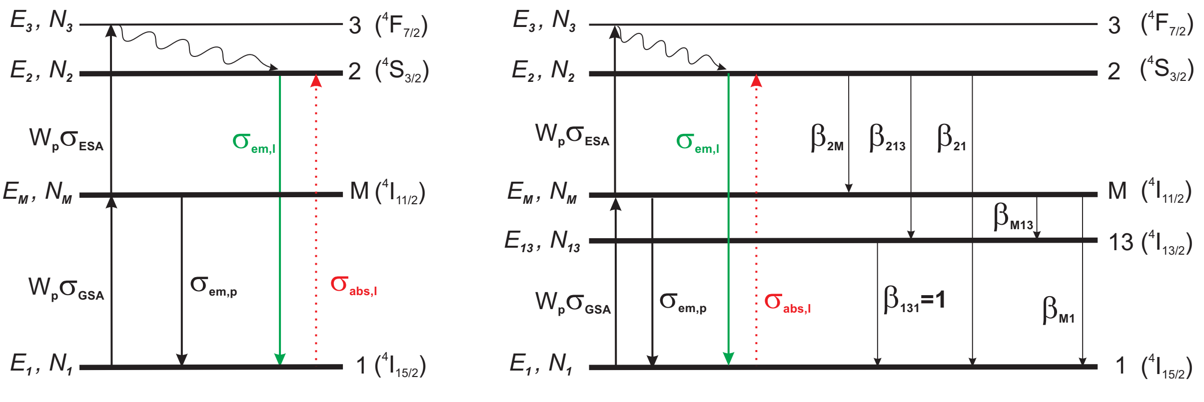

(a) (b)

Figure 6.1: Energy level schemes for the rate equation in upconversion lasers in Er^{3+}:$LiLuF_4$. If the third pumping scheme of Fig. 2.5 is adapted to the three-level laser scheme in Fig. 2.4b, the ESA-pumping scheme with a fourth intermediate level M is obtained, like in (a). The different branching ratios of level 2 are neglected and it supposed to decay exclusively into the ground state 1. The energy level names in brackets refer to the Er^{3+}-ion. If a more complete model is developed, a fifth energy level has to be involved: level 13 ($^4I_{13/2}$-multiplet for Er^{3+}-ions) and it is added in (b). In this model, all the different decaying channels are labeled with a branching ratio β_{ij}, indicating the starting i-th and the final j-th levels.

$$\begin{aligned}
\frac{\mathrm{d}N_2}{\mathrm{d}t} &= W_\mathrm{p}\sigma_\mathrm{ESA}N_\mathrm{M} - \frac{N_2}{\tau_2} - l\sigma_\mathrm{em,l}qN_2 + l\sigma_\mathrm{abs,l}qN_1 && (6.1)\\
\frac{\mathrm{d}N_\mathrm{M}}{\mathrm{d}t} &= W_\mathrm{p}\sigma_\mathrm{GSA}N_1 - W_\mathrm{p}\sigma_\mathrm{ESA}N_\mathrm{M} - \frac{N_\mathrm{M}}{\tau_\mathrm{M}} - W_\mathrm{p}\sigma_\mathrm{em,p}N_\mathrm{M} && (6.2)\\
\frac{\mathrm{d}N_1}{\mathrm{d}t} &= -W_\mathrm{p}\sigma_\mathrm{GSA}N_1 + \frac{N_2}{\tau_2} + \frac{N_\mathrm{M}}{\tau_\mathrm{M}} + l\sigma_\mathrm{em,l}qN_2 + W_\mathrm{p}\sigma_\mathrm{em,p}N_\mathrm{M} + \\
&- l\sigma_\mathrm{abs,l}qN_1 && (6.3)\\
N_\mathrm{tot} &= N_1 + N_\mathrm{M} + N_2 && (6.4)\\
\frac{\mathrm{d}q}{\mathrm{d}t} &= \Big((N_2\sigma_\mathrm{em,l} - N_1\sigma_\mathrm{abs,l})l - \gamma\Big)\frac{cq}{L'}. && (6.5)
\end{aligned}$$

Apart from the dimensions defined in Sect. 2.3.1, τ_i represents the fluorescence lifetime of the i-th level, N_tot the total density of active ions and “p” and “l” define either the absorption or the emission cross sections at the pump wavelength ad at the laser wavelength, respectively.

In the steady state, all the temporal derivatives are equal to zero and the solutions for the population densities N_1 and N_2 from the Equations (6.2) and (6.1), respectively are:

$$\begin{aligned}
N_1 &= \frac{W_\mathrm{p}\sigma_\mathrm{ESA} + 1/\tau_\mathrm{M} + W_\mathrm{p}\sigma_\mathrm{em,p}}{W_\mathrm{p}\sigma_\mathrm{GSA}}N_\mathrm{M} && (6.6)\\
N_2 &= \left(W_\mathrm{p}\sigma_\mathrm{ESA} + \frac{l\sigma_\mathrm{abs,l}q}{W_\mathrm{p}\sigma_\mathrm{GSA}}(W_\mathrm{p}\sigma_\mathrm{ESA} + 1/\tau_\mathrm{M} + W_\mathrm{p}\sigma_\mathrm{em,p})\right)\frac{N_\mathrm{M}}{1/\tau_2 + l\sigma_\mathrm{em,l}q} && (6.7)
\end{aligned}$$

From Eq. (6.4), N_{M} can be expressed as a function of N_{tot} and it reads:

$$N_{\mathrm{M}} = \frac{N_{\mathrm{tot}}}{1 + \frac{W_{\mathrm{p}}\sigma_{\mathrm{ESA}}}{1/\tau_2 + l\sigma_{\mathrm{em,l}}q} + \frac{W_{\mathrm{p}}\sigma_{\mathrm{ESA}} + 1/\tau_{\mathrm{M}} + W_{\mathrm{p}}\sigma_{\mathrm{em,p}}}{W_{\mathrm{p}}\sigma_{\mathrm{GSA}}}\left(1 + \frac{l\sigma_{\mathrm{abs,l}}q}{W_{\mathrm{p}}\sigma_{\mathrm{GSA}}(1/\tau_2 + l\sigma_{\mathrm{em,l}}q)}\right)}. \tag{6.8}$$

Consequently, the other two population densities N_1 and N_2 can be written as well as functions of N_{tot}.

If it is considered that the $^4\mathrm{I}_{13/2}$-manifold of Er^{3+}-ions has a particularly long lifetime (9.7 ms in Er^{3+}:LiLuF_4 see Chap. 5), it is expected that it will be partially populated influencing the occupation of the other three multiplets (see Fig. 6.1b). Therefore, the system of rate equations can be extended to a fifth level 13. The Equations (6.1) - (6.4) can be substituted by:

$$\begin{aligned}
\frac{\mathrm{d}N_2}{\mathrm{d}t} &= W_{\mathrm{p}}\sigma_{\mathrm{ESA}}N_{\mathrm{M}} - \frac{N_2}{\tau_2} - l\sigma_{\mathrm{em,l}}qN_2 + l\sigma_{\mathrm{abs,l}}qN_1 && (6.9)\\
\frac{\mathrm{d}N_{\mathrm{M}}}{\mathrm{d}t} &= W_{\mathrm{p}}\sigma_{\mathrm{GSA}}N_1 - W_{\mathrm{p}}\sigma_{\mathrm{ESA}}N_{\mathrm{M}} - \frac{N_{\mathrm{M}}}{\tau_{\mathrm{M}}} - W_{\mathrm{p}}\sigma_{\mathrm{em,p}}N_{\mathrm{M}} + \frac{\beta_{2\mathrm{M}}}{\tau_2}N_2 && (6.10)\\
\frac{\mathrm{d}N_{13}}{\mathrm{d}t} &= \frac{\beta_{\mathrm{M}13}}{\tau_{\mathrm{M}}}N_{\mathrm{M}} + \frac{\beta_{213}}{\tau_2}N_2 - \frac{N_{13}}{\tau_{13}} && (6.11)\\
\frac{\mathrm{d}N_1}{\mathrm{d}t} &= -W_{\mathrm{p}}\sigma_{\mathrm{GSA}}N_1 + \frac{\beta_{21}}{\tau_2}N_2 + \frac{\beta_{\mathrm{M}1}}{\tau_{\mathrm{M}}}N_{\mathrm{M}} + \frac{N_{13}}{\tau_{13}} + l\sigma_{\mathrm{em,l}}qN_2 + \\
&+ W_{\mathrm{p}}\sigma_{\mathrm{em,p}}N_{\mathrm{M}} - l\sigma_{\mathrm{abs,l}}qN_1 && (6.12)\\
N_{\mathrm{tot}} &= N_1 + N_{\mathrm{M}} + N_{13} + N_2. && (6.13)
\end{aligned}$$

In this 5-level-scheme, at the steady state, the Eq. (6.11) leads to:

$$N_{13} = \left(\frac{\beta_{\mathrm{M}13}}{\tau_{\mathrm{M}}}N_{\mathrm{M}} + \frac{\beta_{213}}{\tau_2}N_2\right)\tau_{13}, \tag{6.14}$$

while Equations (6.9) and (6.10) lead to two definitions of N_2, which read:

$$\begin{aligned}
N_2 &= \frac{W_{\mathrm{p}}\sigma_{\mathrm{ESA}}N_{\mathrm{M}} + l\sigma_{\mathrm{abs,l}}qN_1}{1/\tau_2 + l\sigma_{\mathrm{em,l}}q} && (6.15)\\
N_2 &= \Big(-W_{\mathrm{p}}\sigma_{\mathrm{GSA}}N_1 + (W_{\mathrm{p}}\sigma_{\mathrm{ESA}} + 1/\tau_{\mathrm{M}} + W_{\mathrm{p}}\sigma_{\mathrm{em,p}})N_{\mathrm{M}}\Big)\frac{\tau_2}{\beta_{2\mathrm{M}}} && (6.16)
\end{aligned}$$

From Equations (6.15) and (6.16), it is possible to write N_1 as a function of N_{M}, resulting in:

$$N_1 = \frac{(W_{\mathrm{p}}\sigma_{\mathrm{ESA}} + 1/\tau_{\mathrm{M}} + W_{\mathrm{p}}\sigma_{\mathrm{em,p}})\frac{\tau_2}{\beta_{2\mathrm{M}}} - \frac{W_{\mathrm{p}}\sigma_{\mathrm{ESA}}}{1/\tau_2 + l\sigma_{\mathrm{em,l}}q}}{\frac{l\sigma_{\mathrm{abs,l}}q}{1/\tau_2 + l\sigma_{\mathrm{em,l}}q} + \frac{\tau_2 W_{\mathrm{p}}\sigma_{\mathrm{GSA}}}{\beta_{2\mathrm{M}}}}N_{\mathrm{M}} = A\,N_{\mathrm{M}}, \tag{6.17}$$

where for simplicity the factor A has been introduced.

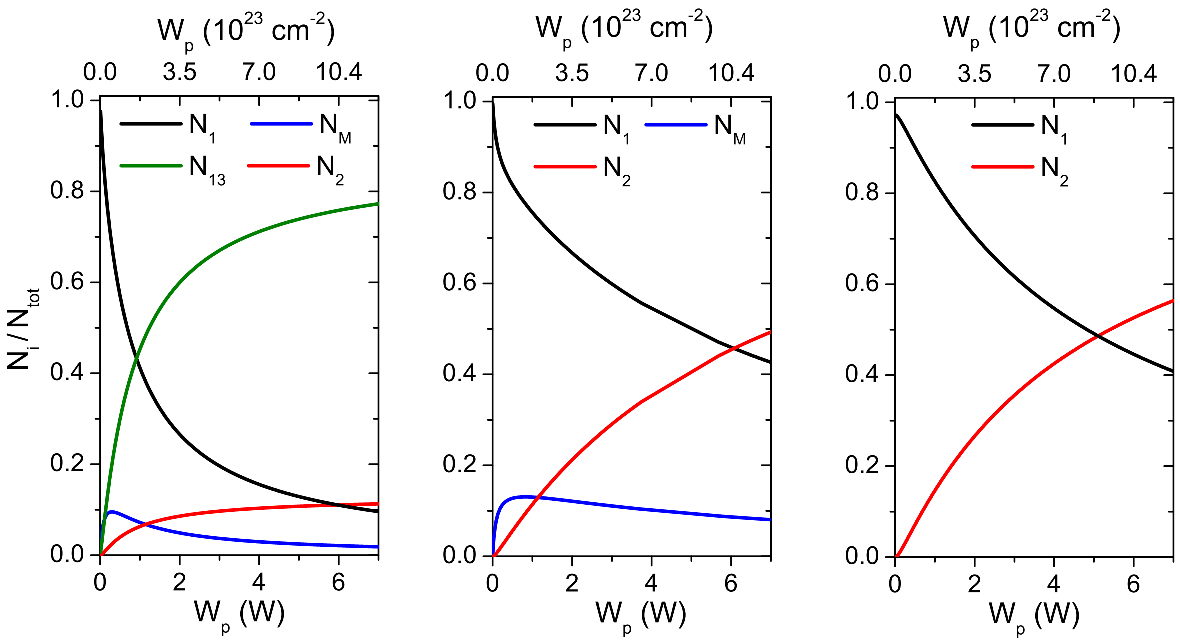

Figure 6.2: Simulations of the population densities of the energy levels of Er^{3+}-ions as a function of W_p, in three different laser schemes: a five-level, a four-level, and a three-level scheme. The possible losses are not taken into account and the laser threshold condition is imposed with $q = 0$. W_p is expressed in units of ($\mathrm{cm}^{-2}\,\mathrm{s}^{-1}$) on the upper scale and in units of W imposing a beam waist diameter of 60 µm in the lower scale.

Finally, if the Eq. (6.13) is used, N_M can be written as a function of N_tot as:

$$N_\mathrm{M} = \frac{N_\mathrm{tot}}{1 + A + \frac{\tau_{13}\beta_{\mathrm{M}13}}{\tau_\mathrm{M}} + \frac{1}{1/\tau_2 + l\sigma_{\mathrm{em,l}}q}\left(\frac{\beta_{213}\tau_{13}W_\mathrm{p}\sigma_\mathrm{ESA}}{\tau_2} + Al\sigma_{\mathrm{abs,l}}q\left(1 + \frac{\beta_{213}\tau_{13}}{\tau_2}\right) + W_\mathrm{p}\sigma_\mathrm{ESA}\right)} \tag{6.18}$$

and all the other population densities can be consequently calculated.

Additionally, the Er^{3+}-level scheme can be simplified to the easiest three-level model, where only level 1 and 2 are involved. In the laser process, level 3 is still assumed to fast relax in level 2 and it does not appear in the equations.

In this model, the rate-equation system, without the laser threshold condition, is represented by:

$$\frac{\mathrm{d}N_2}{\mathrm{d}t} = W_\mathrm{p}\sigma_{\mathrm{abs,p}}N_1 - \frac{N_2}{\tau_2} - l\sigma_{\mathrm{em,l}}qN_2 + l\sigma_{\mathrm{abs,l}}qN_1 \tag{6.19}$$

$$\frac{\mathrm{d}N_1}{\mathrm{d}t} = -W_\mathrm{p}\sigma_{\mathrm{abs,p}}N_1 + \frac{N_2}{\tau_2} + l\sigma_{\mathrm{em,l}}qN_2 - l\sigma_{\mathrm{abs,l}}qN_1 \tag{6.20}$$

$$N_\mathrm{tot} = N_1 + N_2. \tag{6.21}$$

If a simulation for each of the three different systems is performed, a qualitative behavior of the different population densities in dependence of W_p in absence of losses, and imposing the laser threshold condition, can be determined. The results of the simulations are plotted in Fig. 6.2, using the parameters summarized in Tab. F.1. W_p is expressed in two units: as a pump rate in $\mathrm{cm}^{-2}\,\mathrm{s}^{-1}$ and in units of W imposing a diameter of the beam waist of 60 µm, such as in the four-fold-resonator-based experiments described in the following section. The dependency on time is not significant because of the imposed threshold conditions.

Despite the approximations mentioned above, the possibility of reaching the inversion of populations allowing for laser operation ($N_2 > N_1$) is shown. The laser threshold can be reached at the same pump rate for the four-level and the five-level models (almost 6 W in the case of a 60-µm pump spot) but at a lower one for the three-level model, where the bleaching of the pump of level M is not influential. In the figure, the highlighted needed pump power to reach the laser threshold is the minimum needed because in the simulations the losses are not considered. At the same level of losses, the laser threshold is expected will increase more in models with a higher number of levels, than in models with a lower number of involved levels. Moreover, when the number of involved energy levels increases, the population density is distributed decreasing progressively the population density in the original two energy levels N_1 and N_2, in favor of N_M and N_{13}. As expected, a relatively low population density of level M is calculated, because it efficiently allows for the population of the higher level 2 in the upconversion scheme. Furthermore, the relatively high population density of level 13, due to its long decay lifetime, is shown.

If instead of an ESA-pumping an ETU-pumping is considered, donor and acceptor ions are involved. In this case, in the equations describing $\mathrm{d}N_2/\mathrm{d}t$ and $\mathrm{d}N_\mathrm{M}/\mathrm{d}t$ the contribution of $W_\mathrm{p}\sigma_\mathrm{ESA}N_\mathrm{M}$ would be substituted by two factors $\propto \delta N_\mathrm{M}^2$, where δ is the ETU-parameter [Sch96]. This would lead to a second-order equation with two possible solutions for N_M, under certain conditions.

Nevertheless, this concept is neglected here as the usual Er^{3+}-doping concentration are relatively low, reducing the probability of such processes (see Chap. 2).

6.1.2 Preliminary measurements

Once suitable materials providing low effective phonon energies are recognized, a second fundamental requirement for upconversion lasers is to apply a resonator geometry which allows for high pump and laser intensities in cw operation.

Considering the favorable absorption and emission cross sections of Er^{3+}:LiLuF_4 (see Chap. 5), it has been successfully employed in a linear resonator with a Ti:sapphire laser as pumping source ([Möb98] and see Sect. 6.1.5). In order to improve the results with this crystal, different approaches are possible.

A higher doping concentration in the crystal to increase the absorption of the incident power cannot be an option in Er^{3+}-doped crystals, because of quenching of the lifetime of the $^4\mathrm{S}_{3/2}$-manifold, caused by detrimental upconversion and cross-relaxation processes. Using longer crystals would increase the gain and adopting a pump source able to deliver higher pump power can be possible. Furthermore, decreasing the size of the pump beam spot inside the crystal and applying a multi-pass geometry can determine an overall higher pump intensity in the crystal, thus lowering the laser threshold. However, these approaches are limited by the spatial overlap of pump and laser modes.

Heumann et. al performed experiments with a more powerful pump source, in asso-

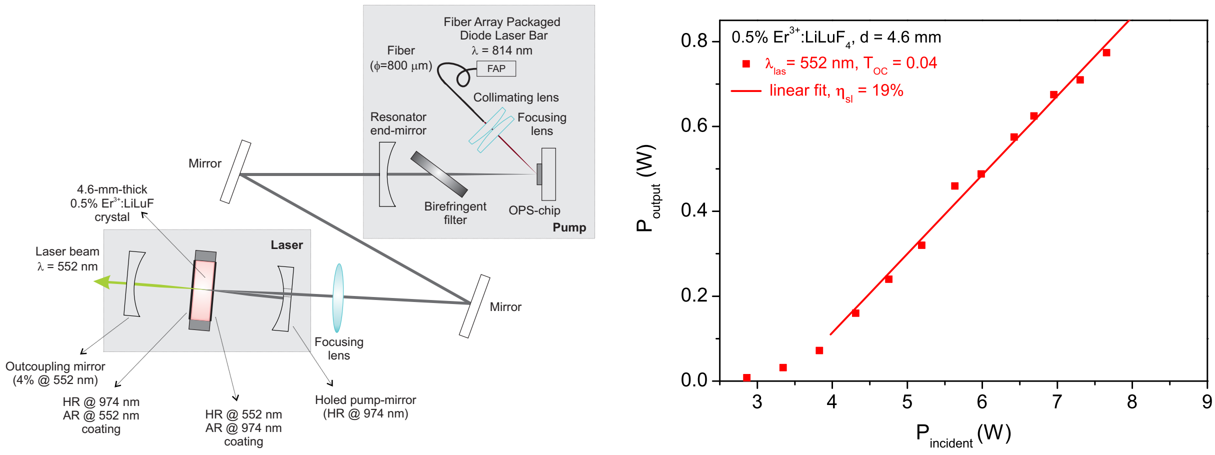

(a) **(b)**

Figure 6.3: Laser experiment with an OPSL-pumped 0.5 Er^{3+}:LiLuF_4 in a four-fold resonator. In (a), the four-fold resonator with the description of the OPSL source is depicted. The characteristics of the needed specific coatings are also shown. In (b), the best laser curve is represented, where the outputcoupling transmission $T_{\mathrm{OC}} = 0.04$, the threshold incident power was 2.9 W, the maximum output power 0.774 W and a slope efficiency $\eta = 19\%$.

ciation to a multi-pass geometry and a relatively tight focusing of the pump beam in the crystal [Heu02a, Sch04, Heu06]. The requirement of a high-brightness pump source has always defined Ti:sapphire lasers as an optimal choice, although the output power is lower, if compared to diode lasers. In order to offer a low spectral width and ensure the possibility of tight focusing, OPSLs are one of the best alternatives, as they combine a relatively high power with a good beam quality. Furthermore, a beam waist diameter $< 50\,\mu\mathrm{m}$, proportioned to the output power of the adopted pump source, ensures the sufficient intensity to reach the laser threshold and obtain relatively high output power.

Nevertheless, together with the use of an OPSL as pump source, the real improvement in terms of output power has been due to the four-fold resonator.

In Fig. 6.3a, the setup is depicted, together with a description of the pumping source. The OPSL is pumped by a fiber-array-packaged laser diode bar (FAP) at 810 nm with a maximum power around 35 W. It is coupled into a fiber of 800 µm of core diameter and collimated and focused on the OPSL chip. It provides the gain medium (quantum wells of InGaAs alternated with GaAs layers) and a high-reflective layer on the rear side, constituted by further alternated high- and low-refractive-index layers acting as a low-loss distributed-Bragg-reflector mirror optimized for the output wavelength of the OPSL. Thus, the chip represents also the flat side of a hemispherical resonator with an end-mirror with a radius of curvature *ROC* of 100 mm. The chip is cooled by a Peltier-element. In the resonator, a birefringent plate is placed in order to tune the emission wavelength of the OPSL. The maximum output power is 10.5 W at a wavelength of 972 nm, while in order to have a minimum output power of 6 W, the tuning range is between 960 and 980 nm [Heu12]. The advantage given by the optical pumping is in the beam quality: the OPSL has a spectral bandwidth of about 1 nm and a slightly elliptical shape of the beam which at maximum power determines $M_x^2 = 2.5$ and $M_y^2 = 2.4$ [Heu06].

The four-fold cavity is based on two curved mirrors with $ROC = 50\,\mathrm{mm}$ and two different optical coatings on the two faces of the crystal. The outputcoupling mirror has 0.04 transmission at the emission wavelength of 552 nm, and the input coupling mirror is highly reflective (HR) for the pumping wavelength of 974 nm. The pump cavity allows for four pump passes through the crystal. Therefore, an off-axis 5-mm-diameter hole has been drilled into the input coupling mirror. The crystal for the best results is a 4.6-mm long 0.5% Er^{3+}-doped $LiLuF_4$ crystal (crystal HEU in Tab. A.2), mounted onto a copper heat-sink cooled by a Peltier-element. The coating which faces the input coupling mirror is HR for the emission wavelength and anti-reflective (AR) for the pump wavelength, while the second side is HR for the pump wavelength and AR for the emission wavelength. In this way, the pump can enter the cavity after being focused typically by a 70-mm lens, through the hole with a slight tilt with respect to the resonator axis. The beam is focused into the crystal, then reflected by the HR coating of the mirror and sent back the same way by the input coupling mirror. In this way, the pump beam overlaps with itself four times. The green fluorescence light cannot cross the first coating but it is confined in the second half of the setup, resembling a hemispherical resonator. When the threshold is reached, the coherent green beam can escape from the outputcoupling mirror as laser emission.

In Fig. 6.3b, the laser characteristic with $T_{\mathrm{OC}} = 0.04$ is depicted. When the incident pump power reaches the value of 2.9 W, the laser threshold is reached and the maximum output power, showing no thermal roll-over problems, in true cw-operation, is 0.774 W. The slope efficiency with respect to the incident pump power can be determined to be $\eta_{\mathrm{sl}} = 19\%$.

In a previous work [Heu06], the absorbed pump power has been measured for the two-fold geometry and consequently estimated for the four-fold geometry, obtaining an absorption fraction of roughly 30%. With this value, a slope efficiency $\eta_{\mathrm{sl,abs}}$, with respect to the absorbed pump power, can be estimated, corresponding to $\eta_{\mathrm{sl,abs}} \sim 59\%$. In this case the pump beam focus, due to the tilting angle, is slightly broader then in two-fold resonators, and the pump beam waist diameter measures roughly 60 µm.

A second problem which has been overcome, but has to be taken into account for further experiments, is the thermal management inside the crystal during laser operation. In previous experiments [Heu06], a similar output power could be reached only with a pump duty cycle of 50%. Starting roughly at 1 W of absorbed pump power, roll over issues started to appear, limiting the output power of the pure cw regime to roughly 500 mW. The solution of the problem was to substitute the ordinary water-cooling of the crystal with room-temperature water, by a Peltier-element, which could be kept at a temperature below 20 °C (usual working temperature ~15 °C). The reason for this sensitivity of the system to the temperature is the increased reabsorption due to the Boltzmann population of the Stark sublevels of the $^4I_{15/2}$ final laser level (see Chap. 2).

From the results of the experiments obtained in true cw-operation in [Heu06], the threshold incident pump intensity has been estimated as roughly 15 - 20 kW/cm^2.

6.1.3 Thin-disk-laser geometry

When the strategy of the multipass-pumping is extended, a straightforward option is to move to a thin-disk-laser (TDL) geometry.

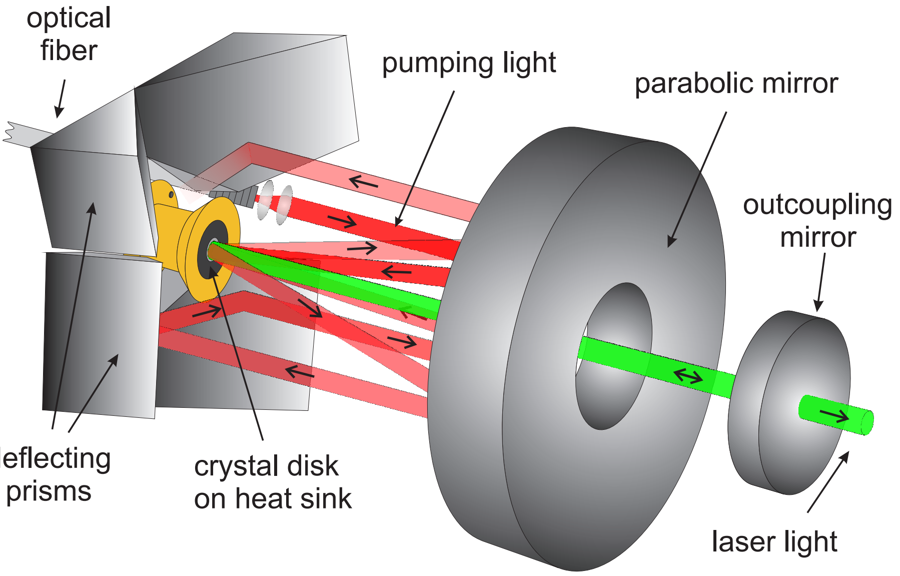

Figure 6.4: Representation of a TDL module (modified version of [Krä07]).

Normally, the thin-disk-laser model is devoted to the extraction of high output power, because of the ability of suppressing thermal problems encountered in rod-based lasers. Typically, in a rod the heat can be transmitted in three directions inside the volume: one coincident to the axis of the laser beam and two in the plane perpendicular to this axis, or radially, if the cross section of the crystal is circular. In this case, even if the rod is cooled, the heat can be dissipated only in a direction perpendicular to the axis of the laser and thermal lensing effects, due to the change in refractive index induced by the different temperature in different regions of the crystal, cannot be avoided. Therefore, together with the Boltzmann population in quasi-three-level lasers, thermal issues can decrease the quality of the beam via the lensing effect.

The solution to this problem is given by the thin-disk geometry because of the low thickness of the active medium and the cooling along the laser axis. Typically, disks with a thickness of a few hundreds of micrometers are coated with a double HR coating (HR at both pumping and emission wavelengths) on the rear side, in the simplest case constituting the flat side of a hemispherical resonator, and they can be mounted on a heat sink. In this way, the heat deposited by the high pump power incident on the AR coated front side is easily removed by the heat sink in a direction correspondent to the laser beam axis. Together with the principle of a high surface-to-volume ratio, the thermal lens issues are drastically reduced, also at incident power in the kilowatt-regime.

Nevertheless, a drawback due to the reduction of the thickness of the medium, is the reduction of the gain and of the absorbed pump power. To overcome these problems, there are two ways: increasing the doping concentration in the crystal and adopting a multipass pumping scheme.

The possibility of using highly doped crystals was already discussed and it is no option for Er^{3+}:$LiLuF_4$ upconversion lasers (see Chap. 4).

The possibility of multiple passes of the same pumping beam in the crystal is allowed by a resonator such as the one depicted in Fig. 6.4. The disk mounted on the heat-sink, as previously described, is surrounded by a system of deflecting prisms which faces a holed parabolic mirror, both HR coated for the wavelength of the pumping source. The pumping light is incoupled with a system of two incoupling lenses which collimate the beam after emerging from a fiber. The pump laser is then sent onto the parabolic mirror which reflects and focuses it onto the disk, with an incident angle of about 35°. The pump light which is not absorbed can be reflected by the HR coating on the rear side of the disk, back onto the parabolic mirror. With the help then of further deflections also onto the prisms, the beam can cross, depending on the module, sixteen, twenty-four, thirty-two, up to forty-eight times the disk, such as in the most common, commercially-available thin-disk modules. The system of prisms and parabolic mirrors assures the continuous collimation and focusing of the beam during the different passes. The size of the pump spot on the disk depends on the incoupling lenses. For thin-disk-laser experiments in the framework of this thesis, a twenty-four-fold module with a 1:2 incoupling system has been employed, which means the diameter of the spot on the disk is two times larger than the diameter of the fiber where the pump source is incoupled.

The resonator for laser emission is completed by a curved mirror located behind the parabolic mirror, in correspondence of the hole, functioning as output coupling mirror.

To increase the gain, multiple passes are possible adding further mirrors outside the module, but they are typically very difficult to align.

Theoretical aspects

The application of the thin-disk-laser geometry to Er^{3+}-doped fluoride crystals for the realization of an upconversion laser in the green spectral range is characterized by specific requirements.

With Yb^{3+}-doped crystals, the original material for thin disk lasers [Gie94], to compensate for the reduced gain due to the low thickness of the medium, it is possible to increase the doping concentration up to a certain amount. Unfortunately, in Er^{3+}-doped fluorides this is not possible. The most effective compromise between the quenching of the lifetime of the upper emitting level and the net amount of absorbed pump power referring to the absorption cross sections, establish for $LiLuF_4$ an ideal Er^{3+}-doping concentration around 1 at. %.

In order to compensate for this low maximum doping concentration, the only possibility is to increase the thickness of the disks, without altering the Er^{3+}-doping concentration.

To estimate which are the possible effective thicknesses of the disks, it is necessary to impose a condition on the amount of absorbed pump power in the crystal after the twenty-four passes. This condition has to both allow for laser operation and for a sufficient absorption of the pump, which can otherwise be back-reflected by the HR coating on the rear side of the disk and possibly cause damage either of the fiber or of the pumping source.

A way to estimate the fraction of absorbed pump power in the disk is applying the Lambert-Beer law assuming the disk to be twenty-four times thicker and neglecting the two dimensions perpendicular to the laser axis. Furthermore, a homogeneous power distribution in the crystal is considered.

These fundamental principles applied to the theory of laser can be summarized as follows.

Considering the limited thickness of the disks and consequently the low gain-per-roundtrip, the gain can be neglected in the calculation of the effective internal power density $E_{\mathrm{r,eff}}$. Therefore, if the number of passes through the crystal per roundtrip is called M_{r} (equal to two in this work) and E_{r} the internal power density, $E_{\mathrm{r,eff}}$ reads:

$$E_{\mathrm{r,eff}} \approx M_{\mathrm{r}} E_{\mathrm{r}}. \tag{6.22}$$

When a thin-disk-laser module is used, the multipass scheme improves the efficiency of the pump in a way such that the portion of the beam which is not absorbed in the first passes, can be recycled by the parabolic mirrors and the prisms and different times re-focused on the crystal. Therefore, considering a homogeneous distribution of the pump power, the effective pump power density $E_{\mathrm{p,eff}}$ can be defined as [Voß02]:

$$E_{\mathrm{p,eff}} = E_{\mathrm{p}} \frac{\eta_{\mathrm{abs}}}{\alpha l}, \tag{6.23}$$

where E_{p} is the incident pump power density, η_{abs} the absorption efficiency, α the absorption coefficient and l the crystal length.

With the application of the Beer-Lambert law in Eq. (5.19), in a system where the crystal is crossed by the beam for M_{p} times (in this work $M_{\mathrm{p}} = 24$), the absorption efficiency η_{abs} reads:

$$\eta_{\mathrm{abs}} = 1 - \exp(-M_{\mathrm{p}} \alpha l). \tag{6.24}$$

When an experimental result is available, it is possible to estimate the behavior of η_{abs}. If in a four-fold resonator a 0.5% -doped, 4.6 mm-thick $\mathrm{Er^{3+}}$:$\mathrm{LiLuF_4}$ crystal absorbs roughly 30% of the incident pump power, as mentioned in Sect. 6.1.2, it is possible to assume that a 1.3% -doped crystal, twenty-four-times passed by the pump beam, should absorb the same amount of incident pump power if it were 290 µm long. With this single value, it is possible to estimate α reversing Eq. (6.24) and then extrapolate the results of the same formula when l is varied, in order to increase the absorption efficiency. The result of the extrapolation is reported in Fig. 6.5 named "empirical curve". This approximation assumes similar bleaching of the pumped energy levels (in the case of $\mathrm{Er^{3+}}$-based upconversion lasers pumped at $\sim$ 970 nm the intermediate laser level) in the twenty-four-fold as in the four-fold resonator, and it is expected to be optimistic, if the bleaching is stronger in the twenty-four-fold resonator. Nevertheless, the approximation has been considered trustworthy and the best compromise between limited thickness and sufficient absorbed incident pump power has been shown in the range of 500 - 800 µm of thickness, where the absorption efficiency varies between 48 and 65%. However, in $\mathrm{Yb^{3+}}$-doped crystals, much higher absorption efficiencies can be reached with much shorter crystals ($\eta_{\mathrm{abs}} > 99\%$ for thicknesses < 200 µm [Pet09a]). This difficulty with $\mathrm{Er^{3+}}$-doped disks is the main source of the problems encountered during the performance of laser experiments.

The results of this estimation can be compared to the theoretical predictions if the model is applied to the upconversion-laser scheme. If α in Eq. (6.24) is substituted with the following:

$$\alpha = \sigma_{\mathrm{GSA}} N_1 - \sigma_{\mathrm{em,p}} N_{\mathrm{M}} + \sigma_{\mathrm{ESA}} N_{\mathrm{M}}, \tag{6.25}$$

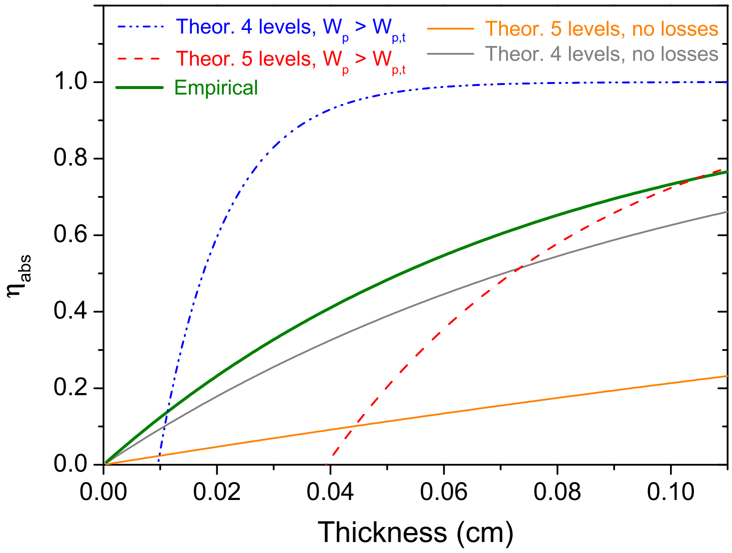

Figure 6.5: Theoretically and experimentally derived absorption efficiency values in dependence of the thickness of Er^{3+}:LiLuF$_4$ disks. The absorption efficiency of Er^{3+}:LiLuF$_4$ disks for upconversion-thin-disk-laser experiments is calculated in different approximations to be compared to the curve derived from experimental data obtained in the four-fold resonator (empirical curve).

the Beer-Lambert law becomes:

$$I(l) = I_0 \exp(-(\sigma_{\mathrm{GSA}} N_1 - \sigma_{\mathrm{em,p}} N_{\mathrm{M}} + \sigma_{\mathrm{ESA}} N_{\mathrm{M}})\, M_{\mathrm{p}} l), \tag{6.26}$$

where $\sigma_{\mathrm{em,p}} N_{\mathrm{M}}$ represents the bleaching on the GSA absorption. A possible bleaching on the ESA absorption $\sigma_{\mathrm{em,p}} N_2$ is omitted, if it is considered that the complete pumping scheme resembles a three-level scheme where level 3 rapidly and non-radiatively decays populating level 2.

In order to estimate dimensions regarding the laser system, it is possible to impose the condition of steady state $\mathrm{d}q/\mathrm{d}t = 0$ and the Eq. (6.5) (corresponding to Eq. (2.18)) becomes:

$$\gamma = L_{\mathrm{int}} + T_{\mathrm{i}} = \left(N_2 \sigma_{\mathrm{em,l}} - N_1 \sigma_{\mathrm{abs,l}}\right) M_{\mathrm{r}}\, l, \tag{6.27}$$

with $\gamma = L_{\mathrm{int}} + T_{\mathrm{i}}$.

In any model assuming the role of more than two energy levels, one variable more than in the one applicable to the quasi-three-level laser scheme is present. Therefore, some approximations have to be performed.

If losses are not considered and the values at the minimum threshold of N_1 and N_{M} are extracted from the Fig. 6.2 (where $N_1 = N_2$), an equation for η_{abs} in dependence of the thickness of the disks can be deduced as in Eq. (6.24) and it is plotted in Fig. 6.5 for the four-level and the five-level models (named as theoretical curves for no losses). It can be noticed that the curve in the four-level model is slightly more pessimistic than the empirical one, which means the absorption efficiency is estimated lower for the same thickness of the disks, despite the missing effects of the losses in the rate equations. As expected, in the five-level model the curve is even more pessimistic, because of the low population density of the level 1 and level M at the presumed laser threshold.

Furthermore, if the losses are taken into account, it is possible to use the solutions of the rate equations of the desired system, applying the conditions at the steady state and expressing one of the population densities inverting Eq. (6.27) and then once more calculate η_{abs}. Two curves of this kind, based on the four-level and the five-level model, are depicted in Fig. 6.5. A further condition concerns W_{p}, which has been imposed slightly higher than the minimum threshold value estimated in Fig. 6.2 because a higher inversion is needed. The number of photons q has been set to zero (or anyway a very small number) as at the laser threshold. The sum of internal losses and outputcoupling rate have been imposed to $T_i + L_{\text{int}} = 0.045$: 0.04 of outputcoupling as in the experiments from which the empirical value is taken [Heu06] and $L_{\text{int}} = 0.005$ as internal losses due to scattering of the light inside the crystal, which is a reasonable value compared to other thin-disk-laser materials [Bei13].

It has to be noticed that the curves in Fig. 6.5 which do not include the possible losses cross the origin unrealistically. Therefore, the curves are not valid for very thin disks.

If the quasi-three-level model developed by *Voß* [Voß02] for thin disk lasers is applied, it is possible to obtain an expression, without unresolved variables, for the population density $N_{2,\text{t}}$ at the laser threshold and consequently of the pump power P_{s} at the laser threshold. In this case, $N_{2,\text{t}}$ reads:

$$N_{2,\text{t}} = N_{\text{dot}} \frac{\sigma_{\text{abs, l}}}{\sigma_{\text{em,l}} + \sigma_{\text{abs,l}}} + \frac{L_{\text{int}} + T_i}{M_{\text{r}} l (\sigma_{\text{em,l}} + \sigma_{\text{abs,l}})}. \tag{6.28}$$

At the laser threshold, the internal resonator power density is equal to zero and the expression for the pump power density at the threshold $E_{\text{p,t}}$ corresponds to:

$$E_{\text{p, t}} = \frac{h\nu_{\text{p}}}{\tau_2 \eta_{\text{abs}}} l N_{2,\text{t}}. \tag{6.29}$$

If the area of the pump spot A_{p} is known, the P_{t} can be written in dependence either of the losses $L_{\text{int}} + T_i$ or of the thickness l of the disks. The complete formula reads:

$$P_{\text{t}} = A_{\text{p}} \cdot E_{\text{p,t}} = \frac{A_{\text{p}} h\nu_{\text{p}}}{\tau_2 \eta_{\text{abs}}} \left(\frac{\sigma_{\text{abs, l}}}{\sigma_{\text{abs,l}} + \sigma_{\text{em, l}}} N_{\text{dot}} l + \frac{L_{\text{int}} + T_i}{M_{\text{r}} (\sigma_{\text{em,l}} + \sigma_{\text{abs,l}})} \right). \tag{6.30}$$

In Fig. 6.6a, the behavior of $N_{2,\text{t}}$ in function of the losses is depicted for the four thicknesses of thin disks which have been part of the experimental work about upconversion thin disk lasers (500, 600, 700, and 800 µm). The results are probably affected by an over-simplified quasi-three-level-model. Furthermore, ν_{p} had to be approximated as twice of the frequency of the pump source used in upconversion experiments. $N_{2,\text{t}}$ is plotted up to $0.564\,N_{\text{tot}}$ defined as maximum inversion level possible to reach. This value has been estimated imagining the double-pump scheme as divided into two single steps where the maximum inversion level of the first step is given by:

$$\beta_{\text{max, M1}} = \frac{\sigma_{\text{GSA}}}{\sigma_{\text{GSA}} + \sigma_{\text{em, p}}} = 0.564 \tag{6.31}$$

and the maximum inversion level of the second step is given by one, because, such as in Eq. (6.26), bleaching of the ESA absorption is considered to be not possible.

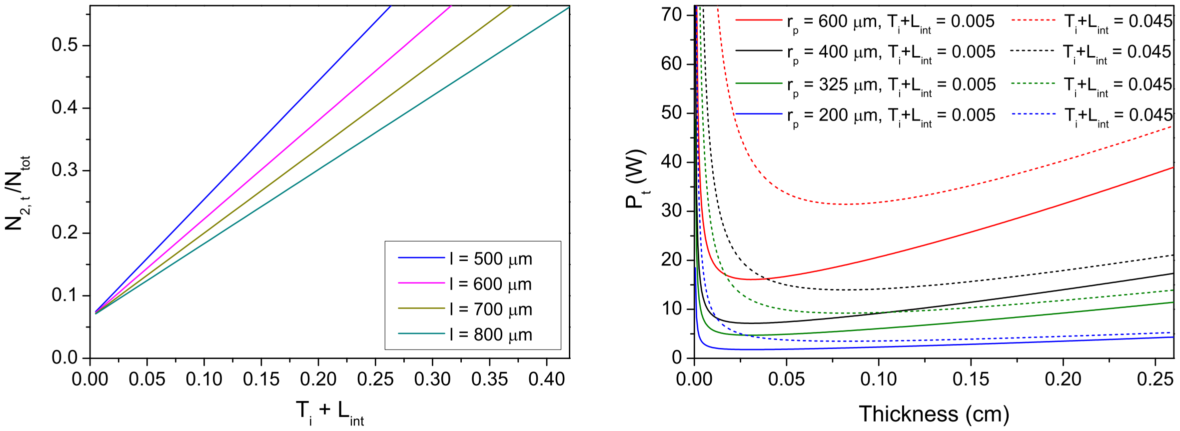

(a) **(b)**

Figure 6.6: Estimated values of $N_{2,\mathrm{t}}$ and $P_{2,\mathrm{t}}$ in the quasi-three-level model for Er^{3+}:LiLuF$_4$ disks. In (a), $N_{2,\mathrm{t}}$ is considered up to the maximum inversion level of 0.564 N_{tot} and the behavior in dependence of the losses $T_i + L_{\mathrm{int}}$ for four different thicknesses is represented. In (b), P_{t} is calculated for different radii r_{p} of the pump spot on the disks, for both, HR mirrors and an outputcoupling transmission of 0.04 for the laser wavelength.

The relationship between $N_{2,\,\mathrm{t}}$ and the outputcoupling rate T_i seems to unrealistically allow T_i to be higher than 0.70, apart from the short thickness of 500 µm. Nevertheless, considering $L_{\mathrm{int}} = 0.005$, the equivalent of the optimum $T_{\mathrm{i}} = 0.04$ for the empiric case would imply a population density of $N_{2,\,\mathrm{t}} \leq 0.10 N_{\mathrm{tot}}$ for all the four possible thicknesses of the disk, which is very similar to the one estimated by the loss-free five-level model ($\sim 0.11\,N_{\mathrm{tot}}$).

In Fig. 6.6b, P_{t} is plotted in function of the thickness of the disks for four different radii of the pump spot. For each radius of the spot, the losses are either limited to $L_{\mathrm{int}} = 0.005$, as an HR mirror were used as outputcoupling mirror, or set to 0.045 with an output coupling rate of 0.04, as in the reference experiment in four-fold geometry. The η_{abs} is set with the empirical parameters.

These approximations to the quasi-three-level system demonstrate the possibility to reach the laser threshold also at relatively low pump intensity, if compared to the empirical value of 15 kW/cm^2 deduced by experiments with the four-fold cavity.

From this theoretical analysis, it emerges that none of the three models fits the empirical estimation and all the aspects of the laser experiments described in the following. The five-level model predicts a very low population density of N_2 at the inversion (Fig. 6.2), which matches the prediction of the population threshold depending on the losses in Fig. 6.6a, based on the quasi-three-level model. The estimated η_{abs} values are in most of the cases too pessimistic than the empirical value and changing the free parameters does not allow for matching the curve, if not at longer thicknesses than the interesting ones. A curve which particularly underestimates the absorption efficiency of the crystal is the five-level model without including the losses. This value is extremely low because it is based on the very low $N_{2,\mathrm{t}}$ predicted by the model. Nevertheless, considering that the empirical value is also a possibly optimistic extrapolation and that a low population density of level 2 is predicted also in Fig. 6.6a, an extremely low absorption efficiency preventing laser emission for very short crystals is plausible.

The estimation of incident pump power at the laser threshold in Fig. 6.6b defines the possibility of lasing also at relatively low pump power. This result is not completely unrealistic. In the following, it will be explained how for certain small sizes of the pump spot is problematic to reach a good overlap on the disk. These difficulties are not accounted in the simulations. However, the general underestimation of the predictions shows the inefficiency of the quasi three-level model in describing all the aspects of an upconversion thin disk laser based on Er^{3+}-ions.

Nevertheless, if the Fig. 6.6a is limited to the $N_{2,\mathrm{t}} = 0.11\,N_{\mathrm{tot}}$ deduced by the five-level model in Fig. 6.2, no total losses higher than 0.03 would be allowed, making the estimation more realistic.

It is possible to improve the theoretical model also involving further processes possibly depopulating the emitting level 2 and the intermediate level M, either of an intraionic (such as ESA at the laser wavelength, as predicted in the spectroscopic measurements in Chap. 5 which is a contribution concerning both energy levels) or interionic nature. This model would then need to be applied to the TDL theory, extending the quasi-three-level model.

Furthermore, another detrimental effect for laser operation which has been suggested to be particularly active in Er^{3+}:$LiYF_4$ [Pol95] is another reabsorption process. It can be defined, as for the reabsorption from level M, an Excited State Reabsorption (ESR) which matches the transition $^4I_{13/2} \rightarrow {}^2H_{9/2}$ depicted in Fig. 2.6 at the laser wavelength. Considering the relatively high population of the $^4I_{13/2}$-level (level 13 in the simulations) estimated by the five-level model, it is expected that this transition is an efficient loss channel to be included in optimized simulations.

Furthermore, in literature also more complex simulations can be found involving more energy levels and more possible transitions [Tom07, Tom11]. One consideration which is missing in the simulations here reported is the possible competition of the laser emission in the green with others at a different wavelength (e. g. at 850 nm or at 1.5 µm).

Another improvement would also be to involve the dynamics in the simulations. Most of the cases give results valid at the laser threshold, without representing the actual situation in steady state conditions.

Nevertheless, simulations which involve a relative high number of parameters base their validity on the precision of these values. Typically, they are either deduced via approximated calculations or resulting from experiments which can suffer from a high degree of uncertainty.

Preliminary experiments

In order to test the possibility of using the OPSL with the TDL module, a few preliminary experiments have been carried out with Yb^{3+}-doped disks previously already successfully employed for diode-pumped thin-disk-laser experiments.

Relatively high-power diode lasers are typically fiber-coupled and a thin-disk-laser module can be equipped with incoupling systems of lenses. Nevertheless, coupling into the fiber causes losses and the first experiments had the aim of testing the possibility of pumping with a collimated beam, not previously coupled into a fiber, such as the one of the available OPSL. The slight divergence of the beam has been corrected via a telescope

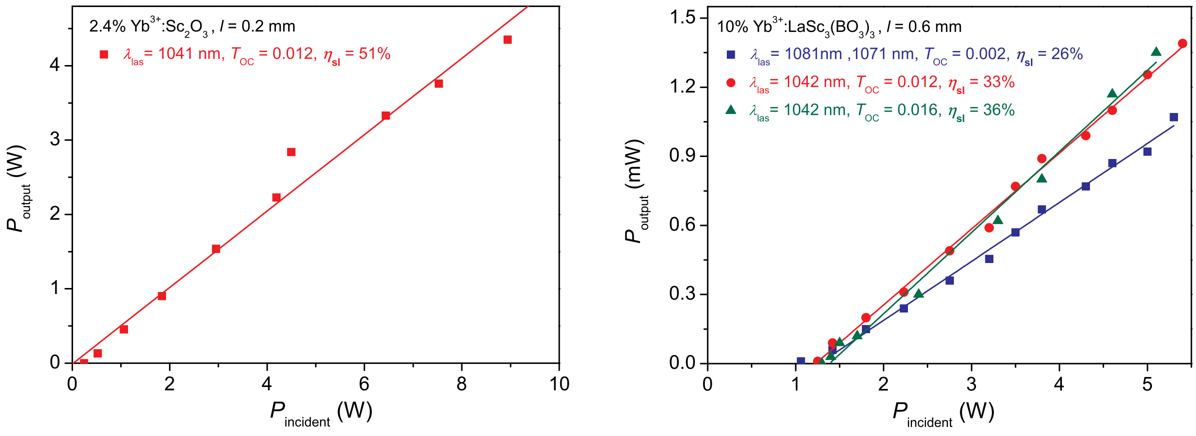

(a) **(b)**

Figure 6.7: OPSL-pumped thin-disk-laser experiments with Yb^{3+}-doped disks. In (a), an input-output curve for a 200-µm-thick Yb^{3+}:Sc$_2$O$_3$ disk, with an outputcoupling transmission of 0.012 are shown. The pump beam was not fiber-coupled but the estimated beam spot had a diameter of roughly 120 µm. In (b), three different outputcoupling mirrors have been employed in experiments with a 600-µm-thick Yb^{3+}:LaSc$_3$(BO$_3$)$_3$ disk. In this case the OPSL beam was coupled into a fiber with a core of 600 µm. Both experiments can be compared to results obtained in diode-pumped experiments [Pet09b, Krä07].

system of lenses. Nevertheless, the twenty-four-fold cavity is extremely sensitive to the collimation of the beam due to the relatively long optical path which twenty-four-passes imply and to the small spot size estimated to be roughly 120 µm of diameter. Therefore, the module fails in focusing on one single spot on the disk in the case the beam is not perfectly collimated. In Fig. 6.7a, the results with a 200-µm-thick Yb^{3+}:Sc$_2$O$_3$ disk with an outputcoupling mirror with 0.012 transmission at the laser wavelength are shown. The slope efficiency of 51% has to be compared with the 82% obtained via diode-pumping [Pet09b]. The almost 40% decrease in slope efficiency is mostly caused by the difficulties of a perfect collimation of the beam.

The experiments shown in Fig. 6.7b have been performed in order to test the resonator with a relatively thick disk of 600 µm of thickness, such as those planned for upconversion TDL experiments (500 - 800 µm of thickness). The gain material was Yb^{3+}:LaSc$_3$(BO$_3$)$_3$. In this case, the OPSL was incoupled in a 600-µm-core fiber and collimated with a 1:2 collimating system and the alignment of the twenty-four spots was more easily achievable than in the free-beam experiments. The results show a lower incident pump power at the laser threshold, but also a 25% lower slope efficiency, if compared to results in [Krä07]. A reason for this can be an inhomogeneity of the beam spot on the disk, due to a non-gaussian mode of the pump laser guided in the fiber.

Upconversion thin-disk-laser experiments

As previously specified, a high pump intensity is needed in order to reach the laser threshold for upconversion lasers. A way to reach 15 - 20 kW/cm^2 estimated as needed intensity to reach the threshold in Er^{3+}:LiLuF$_4$-based laser experiments, is to reduce the pump spot on the disk, which can compensate for the limited incident power that the available OPSL can deliver.

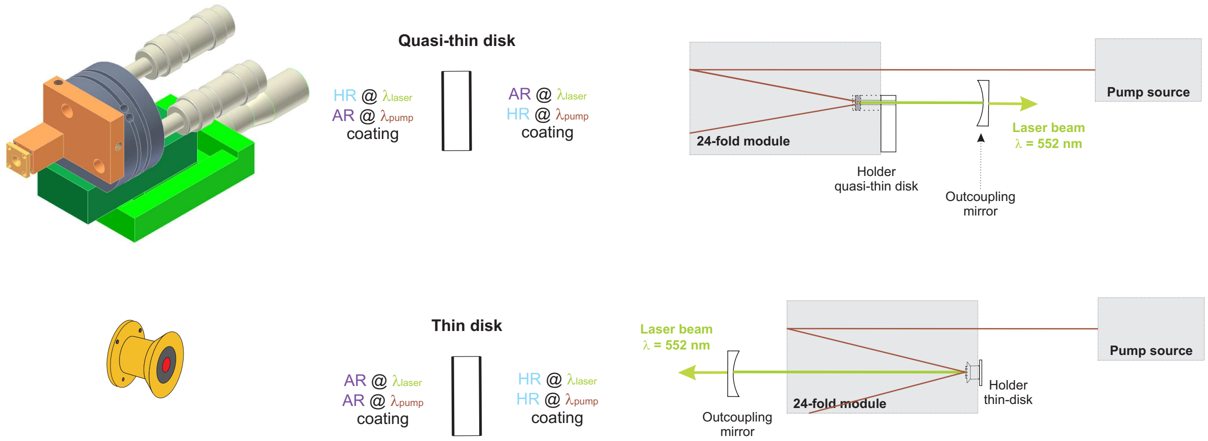

Figure 6.8: Comparison between quasi-thin-disk-laser setup and thin-disk-laser setup. In the upper part, the heat-sink-holder designed to hold crystals with a specific coating for the four-fold resonator and the scheme of the setup are depicted. In the lower part, the copper holder for thin disks is depicted, together with the arrangements of the coatings on a thin disk and the relative schematic setup.

On this purpose, the beam of the OPSL has been coupled via an AR coated lens of 20 mm of focusing length into either a 50-µm- or a 100-µm-core fiber, and via the same 1:2 incoupling system used in the preliminary experiments, collimated and focused by the twenty-four-fold module onto the samples. In this way, a maximum pump intensity of either roughly 100 kW/cm^2 or 25 kW/cm^2 can be reached with the maximum output power of the OPSL of roughly 8 W, if the losses due to the fiber-incoupling are evaluated.

With the twenty-four-passes module and these two fibers, two sets of experiments have been performed.

Considering the availability of crystals with a specific coating for the four-fold cavity previously described, a series of experiments has been performed with relatively thin crystals coated in this way (BÄR2, HEU2 and HEU3 in Tab.A.2) and mounted on a special water-cooled heat-sink-holder. In Fig. 6.8, a comparison between the holder, the coatings and the setup in a twenty-four cavity designed either for the so-called “quasi-thin-disks” or ordinary thin disks is shown. In the upper part it is possible to notice how the resonator for quasi-thin disks is built: the crystals are mechanically fixed with a holed copper plate onto a copper heat-sink, also with a hole on the rear side. When placed in the twenty-four-passes module, the hole on the copper plate allows the pump for being focused on the crystal and being imaged back by the rear HR coating for the pump wavelength of the quasi-thin disk. The green fluorescence and the possible laser emission cannot cross the HR coating for the laser wavelength on the front, but they can emerge from the rear side, where an AR coating and a hole in the copper are provided. In this way, the same twenty-four-fold cavity can be used for both kinds of coated crystals, only changing the direction of the output beam.

The available thin disks for laser experiments are divided into two series by the different coating: D1 - D5 and E2 - E5. They have been commercially polished by *FEE* and coated by *Tafelmaier* as represented in the lower part of Fig. 6.8. The disks are listed in Tab. A.2, but in Tab. 6.1 the simulated transmission of the coatings are summarized. The thickness has been chosen as optimum compromise between thickness and absorption efficiency

Series	HR coating	AR coating	Thickness	Metallization
D series D1 - D5	T<0.0002 @ λ_{laser} T<0.0007 @λ_{pump}	R<0.001 @ λ_{laser} R<0.002 @ λ_{pump}	2× 0.8 mm, 0.7 mm, 0.6 mm, 0.5 mm	0.2 µm NiCr + + 0.3 µm Au (1×0.8 mm, 0.6 mm no metallization)
E series E1 - E5	T<0.013 @ λ_{laser} T<0.041 @λ_{pump}	R<0.001 @ λ_{laser} R<0.002 @ λ_{pump}	2× 0.8 mm, 0.7 mm, 0.6 mm, 0.5 mm	0.2 µm NiCr + + 0.3 µm Au
Jenoptik ability ⋆	T<0.001 @ λ_{laser} T<0.001 @λ_{pump}	R<0.0003 @ λ_{laser} R<0.0015 @ λ_{pump}		0.15 µm Cu + + 0.09 µm Al_2O_3 + + 0.3 µm Ni + + 0.3 µm Au

Table 6.1: Characteristics of the disks and possible alternative by *Jenoptik*. The values of transmission and reflection are at 0° for λ_{laser} and at 35° for λ_{pump}. ⋆ taken from [Krä08].

estimated by the empirical curve in Fig. 6.5.

Starting with these experiments, the twenty-four-fold module has been equipped with a special holder for the fiber, able to fine adjust the position and the inclination of the end-facet of the fiber in the three directions of the space. Nowadays, most of the commercially available modules for TDLs are equipped with this kind of fiber holder.

Unfortunately, no laser experiment performed in these two geometries has been successful, mainly due to the too small pump spot. In the available twenty-four-fold module, if not extremely thin disks are employed, it is not recommendable to implement fibers with too narrow core for two reasons: the pump spots have no circular shape and the overlap of twenty-four of them is hardly reachable.

The volume overlap of the pump beams compared to the total volume occupied by the beams has been estimated for a few combinations of fiber-diameters and thicknesses of the disks. In Fig. 6.9 a visualization of the cross section of the overlapping pump regions in a TDL is depicted. It is scaled to match the characteristics of Er^{3+}-doped $LiLuF_4$ disks ($n \sim 1.48$) and for an incident pump beam at 35°. The side view shows a maximum thickness of the disks of 1.0 mm and a maximum pump spot diameter of 1.0 mm. The red lines indicate the direction of the incident and the consequently emerging beams. It can be clearly seen that the diameter of the pump beam should be of the order of the thickness of the gain material to avoid overlap of the laser mode with completely unpumped regions in the upper part of the disk. The overturned yellow dashed triangle represents the section of the unpumped region in the case of the smallest pump spot diameter. Unpumped material crossed by the laser mode means that losses are added to the system, especially for ground-state-lasers, which suffer from reabsorption at the laser wavelength. From this representation, it is clear that the pumped volume overlap realized by either a 50-µm- or a 100-µm-diameter core fiber with 1:2 incoupling system causes the presence of unpumped volume above the pump focus at thicknesses of 0.4 mm, which means at all the thicknesses of the available thin disks for experiments. This leads to an inefficient pump of the gain medium.

If the same estimation is applied to the case of the Yb^{3+}:$LaSc_3(BO_3)_3$ disk of the preliminary experiments, the estimated volume overlap in a 600-µm-thick disk pumped

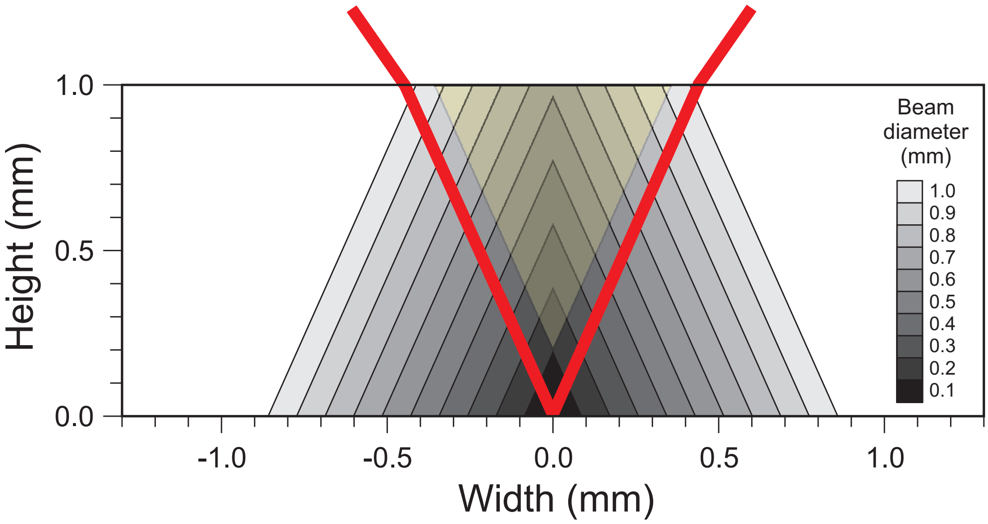

Figure 6.9: Pump overlap in Er^{3+}:$LiLuF_4$ thin disks for TDL. Side view of height and width of the cross section of the overlapping pump regions in a TDL in dependence of the pump beam diameter. This representation is valid for Er^{3+}:$LiLuF_4$ ($n \sim 1.48$) and for an incident angle of the pump beam of 35°. The red lines indicate the direction of the incident and the consequently emerging beams. The overturned yellow dashed triangle represents the completely unpumped region in the case of the smallest pump spot diameter.

by a 600-µm-core fiber inducing a beam spot diameter of 1.2 mm is much higher, especially if it is considered that the average refractive index of $LaSc_3(BO_3)_3$ (~ 1.8) is higher than in $LiLuF_4$ and the overlap is enhanced. Nevertheless, border volume where unpumped material is crossed by the laser mode is still present and for the improvement of the laser performances an optimization of the laser and pump mode overlap could be realized.

In certain cases, the damage threshold of the crystal has been reached, due to the high amount of deposited heat in a small volume. A picture of two different cracks suffered by a 800-µm-thick disk is shown in Fig. 6.10. The laser threshold has never been reached.

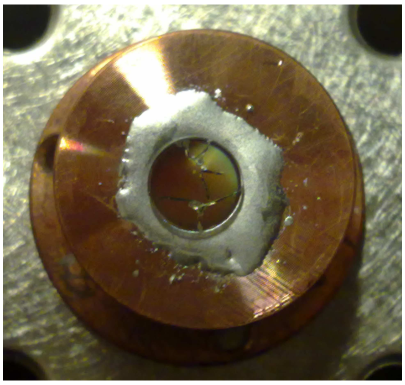

Figure 6.10: Cracks on a 800-µm-thick disk. The two cracks are the consequence of too high deposited heat on the disk by the OPSL incoupled in a 50-µm-core fiber.

Furthermore, the alignment of the prisms and the parabolic mirror in the module does not allow for an overlap of spots obtained with very thin fibers, which in these cases do not appear as circular. Moreover, with such small volume overlap, every thin-disk approximation fails.

In the following, only thin disks have been employed with larger fibers and consequently more powerful pump sources. In order to maintain a relatively high incident intensity, the OPSL had to be substituted with a VBG diode laser (Bright-Lock Ultra 50 by *QPC Lasers*), able to deliver a power of 25 W at 976 nm and coupled into a 200-µm-core fiber. This laser presents a Volume Bragg Grating directly inscribed into the gain structure which can lock the emission wavelength, determining a spectral width

< 0.5 nm. The drift with the temperature, which diode lasers usually suffer, is in this case exceptionally low (0.07 nm/ °C). Unfortunately, the difference to the ideal pumping wavelength of 1.8 nm has been the major issue causing a failure of the experiments with this pump source. Although the ideal maximum allowed incident pump intensity would be roughly 16 kW/cm^2, the imposed cooling via Peltier-element to lower the emission wavelength lowered also the emitted power drastically and, below a certain temperature, even shorter emission wavelengths ($\lambda \sim 960$ nm) were emitted. This caused a detrimental dual-wavelength emission of the pump source, increasing the amount of heat deposited on the disks. Also in this configuration, no laser emission has been obtained. Additionally, although the pumped volume overlap was increased, from the estimation of Fig. 6.9 it is clear that, for the thicknesses of the disk included between 0.5 and 0.8 mm, still large volume of unpumped material was distributed laterally and above the pump focus, introducing still too high losses for reaching the laser threshold.

The pumping source able to deliver the highest amount of power at the correct absorption wavelength for Er^{3+}:$LiLuF_4$ was the laser diode JOLD-45-CPXF-1L by *Jenoptik*, able to deliver 45 W at 980 nm coupled into a 600-µm-core fiber. The difference of more than 5 nm between the room-temperature emission of the pump source and the absorption wavelength of Er^{3+}:$LiLuF_4$ can be easily bridged via cooling of the device. With a system of two Peltier-elements, the temperature could be driven down to 2 - 3 °C and still obtaining an output power of almost 45 W. Unfortunately, the highest deliverable pump intensity is only roughly 4 kW/cm^2.

Although the experiments performed with this diode laser as pump source have also not been successful, further information about the problems of the system could be investigated.

The possibility of high-power pumping up to the kW-regime typical of Yb^{3+}-materials is due to the optimized absorption of the incident power, usually kept higher than 90%, adapting the thickness to the absorption efficiency of the material [Pet09a]. In the case of the disks D1 - D5, the empirical data of absorption efficiency are included between 0.48 and 0.65 depending on the thickness. The lower absorption efficiency does not only increase the minimum incident power required to reach the laser threshold, but also limits the maximum incident pump power that the module can sustain. The major issue is caused by the non-absorbed incident power. The amount that is not absorbed can be back-reflected and back-coupled into the fiber. These back reflection can cause major damages of the fiber.

A fiber has been damaged using a 800-µm-thick disk with 43 W incident pump power. Considering that this is the highest thickness available, therefore the highest expected absorption efficiency, the non-absorbed pump power has to be considered beyond the damage threshold of the system. Furthermore, this power is similar to the one applied when also a disk of 600 µm of thickness has been damaged, which means also that this level of incident pump power deposited on the disk can cause damages, if the laser threshold is not reached.

A reason why the laser threshold cannot be reached can be connected to the temperature of the disk. The temperature of the disk in function of incident pump power has been measured with two disks of the E series (see Tables A.2 and 6.1) having the same thickness of 800 µm. One had been soldered on the heat-sink (indium as soldering sub-

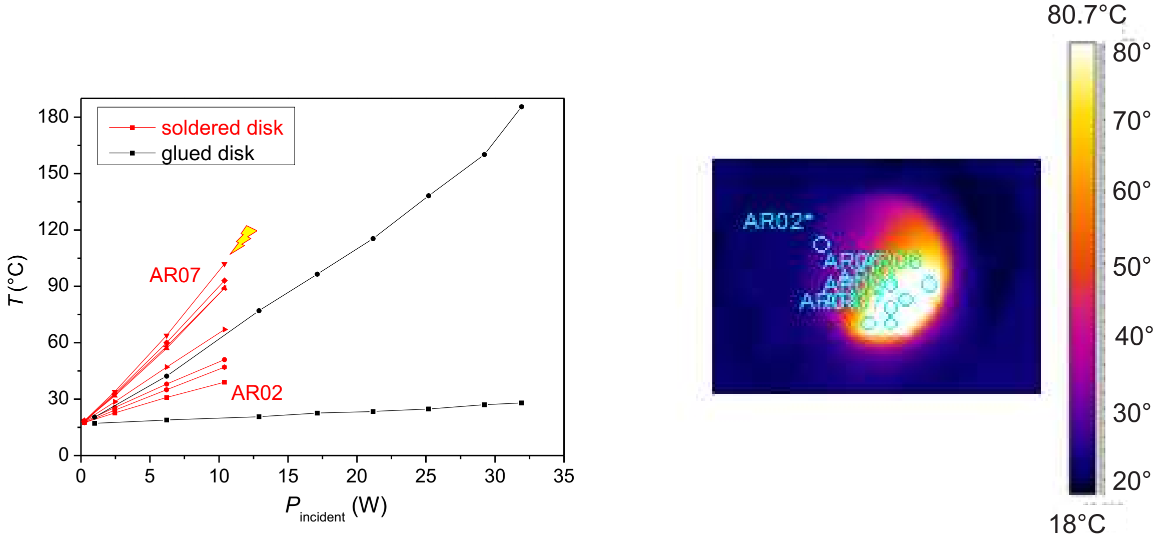

(a)

(b)

Figure 6.11: Temperature behavior in thin disks. In (a), the temperature in function of the incident pump power is depicted for different spots located on two disks of the same thickness (800 µm) but differently contacted on the heat-sink. The soldered disk incurred in damage at the relatively low temperature of 100 °C. In (b), an image detected with a thermal camera at about 6 W of incident pump power on the soldered disk is reported. The different positions on the disk where the temperature has been measured are highlighted, in particular the minimum temperature AR02 and the maximum temperature AR07.

stance between copper of the holder and the metallic coating on the rear side of the disk), while the second had been glued (contacting of the rear side coated with a dielectric HR layer with the copper of the holder via a two-component glue UHU Endfest 300 by *UHU*, increased in strength via heating up to 180 °C [Lar09]). The transmission of the coatings is different than in the D series, so numerical comparisons cannot be performed among the two series of disks, but the general behavior verified in one series can be extended to the other one.

The test of the temperature behavior has been performed in four different situations and the results have been not always unambiguous. The common deductions which can be made will be pointed out in the following.

In Fig. 6.11, an example of study of the behavior of the temperature in the disk while it is laser pumped is depicted. A comparison between a soldered disk and a glued one of the same thickness is directly shown in Fig.6.11a. At low incident power the first difference emerges. The temperature on the disk is more homogeneously distributed on the soldered disk, but not in a round shape resembling the shape of the spot, than on the glued disk, where two spots where predominantly warmer. For this reason, the temperature on the soldered disk has been measured for different areas, while for the glued disk only in the two areas of increased temperature have been evaluated. When the incident pump power was increased, it was common in all the experiments a faster increase of the temperature on soldered disks compared to glued ones. In the case depicted in Fig. 6.11a, the incident pump power led only to a temperature up to 100 °C before reaching the damage threshold. On the contrary, the glued disk could reach the temperature of almost 190 °C without incurring in damages. The presence of a second area at higher temperature on this disk was probably due to air bubbles in the glue or to an inhomogeneous contact to the heat-sink which did not affect the distribution of the heat at higher incident pump power (the temperature did not strongly increase such as in the area of the pump spot).

Nevertheless, other experiments show that at slightly higher pump power and consequently temperature (less than 200 °C) a glued disk can be damaged, while a soldered one can even reach a temperature up to 220 °C without being damaged, but already at less than 15 W of incident pump power.

With Yb^{3+}:YAG, a typical material for thin disk lasers, it has been demonstrated that without laser operation disks can reach up to almost 300 °C without suffering damages. In laser operation, the maximum reached temperatures are slightly higher than 100 °C when outputcoupling rates are either very low or particularly high [Wol13].

In Fig. 6.11b an image detected with a thermal camera by *FLIR* at roughly 6 W of incident pump power on the soldered disk is represented. As previously mentioned, the temperature distributes homogeneously but not in a round shape around the beam spot. This is evidence of the tendency of the heat to be distributed in the crystal rather than flowing to the heat-sink. Considering the relatively low thermal conductivity of the crystal, this is evidence of a bad contacting of the disk to the heat-sink on the right side of the disk

A reason for the inefficient contacting via soldering has been found in the characteristics of the metallic coating provided by *Tafelmaier* (see Tab. 6.1).

Considering the previous experience with another kind of metallic coating (provided by *Jenoptik*), highly efficient contacting via soldering has been performed when the metallic coating is composed such as described in the same Table 6.1. The last layer of gold is supposed to melt together with indium and create the contact between the copper of the heat-sink and the disk. The *Tafelmaier* coating which could be deposited on the Er^{3+}:$LiLuF_4$ disks is in contrast composed of only: 200 nm of NiCr and 300 nm of gold. Although the thickness of the last layer of gold is the same of the *Jenoptik* coating, the total thickness of the metallic coating is lower and considerable problems have been encountered during the contacting procedure: most of the disks have been tried to be contacted two times because the first attempt had failed. This procedure leads to a clear reduction of the thickness of the metallic coating and to a consequent mix of indium with NiCr, not directly suitable for soldering.

As a consequence, the main reason for thermal issues encountered during thin disk lasers experiments has been recognized as the inhomogeneous contact between the heat-sink and the disks. These problems have seriously compromised the possibility to reach the laser threshold and they have been amplified by the low thermal conductivity of $LiLuF_4$ (on the average $< 6\,\mathrm{W/(m\,K)}$), if compared to the one of typical TDL materials, e. g. YAG ($\sim 10\,\mathrm{W/(m\,K)}$) and Lu_2O_3 ($12.6\,\mathrm{W/(m\,K)}$) [Pet11].

Normally, the experiments have been performed with a linear resonator, with an outputcoupling mirror with $ROC = 100\,\mathrm{mm}$ and a limited transmission at the laser wavelength, in order to have transmission higher than the presumed internal losses, but not too high, to not increase the laser threshold (namely $T \sim 0.01$). These attempts have been further improved applying a folded resonator. Two external mirrors with a certain *ROC* (depending on the results of simulations about the stability of the resonator) have been placed symmetrically in front of the module (maximum angle between the axes of the mirrors, with the focus on the disk, ∼ 18°) in order to cause a further double pass through the crystal, increasing the total gain and decreasing the laser threshold.

Unfortunately, also these attempts did not lead to laser operation.

The attempts to reach a high incident pump intensity on the disks have set the lower limit in terms of the diameter of the fiber core to a diameter larger than 200 µm. In this case, the pump spot, relatively to the thickness of the available disks, approaches the circular shape but the pumped volume does not reach a sufficient overlap in the crystal, causing the presence of residual unpumped regions crossed by the laser mode, as shown by Fig. 6.9.

The upper incident intensity limit is driven by the power of the pump source and can be set at roughly 40 W of incident power, at least if the threshold is not reached.

6.1.4 Waveguide lasers

As mentioned before, a way to increase the gain without increasing the doping concentration of the crystal, is to use longer samples. In waveguides such as rare-earth-doped fibers, the gain medium is extended for all the length of the fiber and a very efficient overlap between the pump mode and the laser mode is ensured inside the core. Waveguiding is possible when a change of refractive index is present between the core, with a higher refractive index, and the external cladding, with a lower refractive index.

It is well known since more than fifteen years that intense laser radiation can induce changes of refractive index in dielectric materials due to non-linear absorption processes [Dav96, Stu96].

In crystalline structures, it is expected that the high intensity of the radiation can locally melt the crystal and consequently create an isolated polycrystalline structure after a fast disordered solidification or micro-explosions. This modification can perturb the surrounding area inducing birefringence.

Intense ultra-short pulses can be focused below the surface of a dielectric medium and tracks of modified materials can be directly written. These modifications exhibit refractive index change and also the surrounding is affected by the modification due to stress. In oxide materials, for example, the variation of refractive index is typically -10^{-4}, with respect to the surrounding area [Cal13].

To increase the material modification and the symmetry of the waveguide, two tracks parallel to each other can be written, at a distance in the order of a few tens of micrometers to each other. In this case, laser light can be guided between the two tracks with a high quality. In this configuration, waveguiding and laser emission have been successfully obtained in crystalline media with high output power and slope efficiencies (e. g. [Nej05, Sie10, Cal10]).

Nevertheless, in fluoride crystals the most efficient approach to obtain waveguiding and waveguide lasers is slightly different. If the number of parallel written tracks is increased and they are distributed in a way that a volume is included by the tracks, the structure resembles an inscribed fiber inside the crystal. The tracks with a lower refractive index constitute the cladding and the enclosed volume with a higher refractive index the core. From this concept the name *depressed cladding* waveguides, or simply *cladding* waveguides, is derived. Also this approach in waveguide structuring has been successfully employed for the realization of waveguide lasers [Okh05, Lan11, Mül12].

Fabrication and characterization of the waveguides

Similarly to the optimal parameters for laser operation in the bulk, two different 1.3%-doped Er^{3+}:$LiLuF_4$ crystals from the crystal AC1 (see Tab. A.2), have been cut and polished on the six faces. The length of the crystals is of 10.4 and 11.9 mm, respectively and it is measured along the direction the parallel tracks have been written and represents the length of the gain medium.

To inscribe the tracks, a CPA (Chirped-Pulse Amplification) femtosecond-laser system (*Clark-MXR CPA-2010*) has been employed. The center wavelength is 775 nm, the pulses have a duration of 160 fs, an energy up to 1 mJ and a repetition rate of 1 kHz.

The crystal sample is mounted on a motorized high-precision translation stage (ABL1000 by *Aerotech*) which can be programmed to perform translation in the three dimensions with a resolution of 2 nm. The laser beam from the CPA can be focused via an aspheric lens ($NA = 0.55$ and $f = 4.51\,\mathrm{mm}$) approximately 150 µm below the surface of the crystal while the translation stage moves the crystal and allows for the creation of tracks of modified material.

In the framework of this thesis, two different geometries of claddings have been employed.

It has to be noticed that to match the higher absorption and emission cross sections of Er^{3+}-doped $LiLuF_4$ and at the same time optimizing the waveguiding efficiency, the crystals have been inscribed with an orientation of the **c**-axis perpendicular to both the axis of the laser beam and the translation direction.

In the first approach, eight parallel tracks have been inscribed into the volume of the crystal, giving the cladding a rhombic structure (see Fig. 6.12a). The most effective set of parameters for waveguiding and laser experiments has been 0.6 µJ of fs-pulse energy and a translation velocity of 25 µm/s, according to the set of parameters investigated by *Müller* with claddings inscribed in Pr^{3+}:$LiYF_4$ [Mül12]. The final size of the cladding structure is roughly 30 µm in height (axis of the fs-laser beam) and 20 µm in width (along the **c**-axis) of the rhomboid.

A second approach is based on the inscription with a lower energy of the fs-pulses and a higher number of tracks which are located closer to each other than in the rhombic structure, inscribing a circular cladding of roughly the same external dimensions. In Fig. 6.12b, a reduced track size can be identified. A core with a diameter of $\phi \sim 20\,\mu\mathrm{m}$ has been inscribed. Two technical advantages of this approach are the possibility to use in the best case an energy of only 0.3 µJ of the fs-pulses at a ten times faster velocity of writing of 250 µm/s. The losses are expected to be lower and the mode circular.

The elongation of the tracks is elliptically shaped. Especially in the circular cladding, it is evident how the elongation in the direction of the beam is also suffered by the form of the cladding. The elliptical cross section of every track is partly responsible for this, together with a non-perfect reproducibility of the translation of the stage in the plane

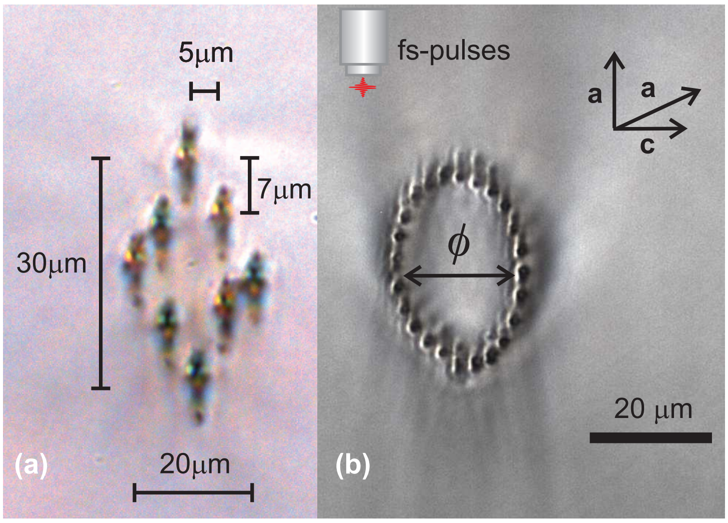

Figure 6.12: Microscope image of two different fs-written waveguide claddings. In (a), the rhombic cladding inscribed by eight tracks is presented, while in (b), the circular cladding of diameter ϕ inscribed by twenty-four tracks is shown on the same scale. For all the claddings, the writing direction has been kept parallel to one of the **a**-axis to improve the waveguiding properties and access the π -polarization typically allowing for higher cross sections in Er^{3+}-doped fluorides.

perpendicular to the writing direction.

To investigate the waveguiding properties of such structures, it is possible to couple the beam of a laser source into the core of the waveguide and perform a transmission measurement.

In the present cases, the beam of a polarized HeNe laser at 633 nm has been coupled into the waveguides via different aspheric lenses or microscope objectives and the transmitted mode has been imaged via a 50× microscope objective on the chip of a CCD camera (DAT-WinCamD-UCD15).

When the transmission of the single mode is analyzed in the rhombic waveguide, a polarization-dependent transmission is detected. As depicted in Fig. 6.13a, the mode can be either transmitted in the core (left), if the beam of the HeNe laser is π-polarized, or transmitted in the single tracks (right), if the beam is σ-polarized. The mode size has been measured to be $\sim 12\,\mu\mathrm{m} \times 14\,\mu\mathrm{m}$.

When the circular waveguide is tested in the same setup, the mode has a size of $\sim 10\,\mu\mathrm{m}\times 10\,\mu\mathrm{m}$, as depicted in Fig. 6.13b, despite the relatively broader available core than in the rhombic cladding. The dependency on the polarization of the incoupled HeNe laser beam is limited to be a high transmission, if the beam is π-polarized, and a low transmission if the beam is σ-polarized.

The strongest difference which underlines the higher efficiency of the circular waveguides with respect to the rhombic one, is given by the calculation of the internal losses.

To calculate the damping D which a beam suffers along the waveguide, the following formula can be applied:

$$D = \frac{1}{l} 10 \log \left(\frac{1}{T_{\mathrm{wg}}} \right) , \tag{6.32}$$

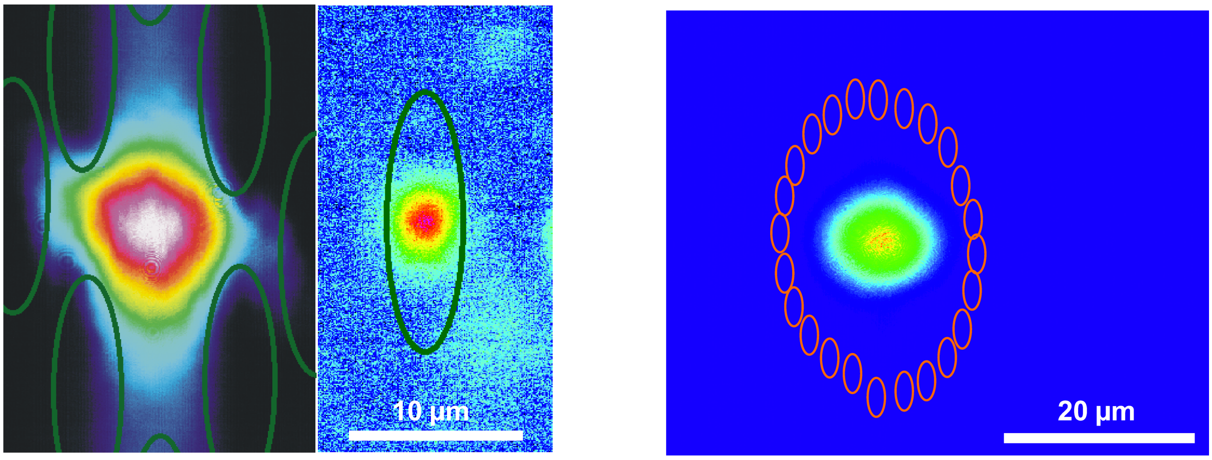

(a) (b)

Figure 6.13: Images from a CCD camera of waveguide modes. Green and orange ellipses remind the position and shape of the tracks in the two different configurations, respectively. In (a), on the left the mode is guided in the core of the rhombic cladding, when the beam is π-polarized, while on the right it is guided in the track, when the beam is σ-polarized. In (b), on roughly a double scale, an image of the guided beam in the core of the circular cladding, when the beam is π-polarized, is depicted.

where l is the length of the waveguide and T_{wg} is its transmission, which is defined as:

$$T_{\mathrm{wg}} = \frac{P_{\mathrm{out}}}{P_{\mathrm{in}}} \frac{1}{\eta_{\mathrm{i}}(1 - R_{\mathrm{F}})^2}, \tag{6.33}$$

where P_{out} and P_{in} are the output and the input power of the waveguide, R_{F} is the Fresnel reflection and η_{i} the incoupling efficiency, considered here to be one.

When D is estimated for the two different claddings, using the beam of the HeNe laser as a reference, the losses caused by the rhombic waveguide determine $D_{\mathrm{rhomb}} < 5.3\,\mathrm{dB/cm}$. Nevertheless, when the same measurement is performed in the circular cladding, losses as low as $D_{\mathrm{circ}} < 0.50\,\mathrm{dB/cm}$ emerge, less than e. g. in Yb^{3+}:YAG waveguides [Cal13].

It has to be noticed that the damping for these cladding waveguides is a maximum value considering $\eta_{\mathrm{i}} = 1$.

The superiority of the circular over rhombic waveguides is confirmed in the following by laser experiments.

Laser experiments in fluoride waveguides

As pump source for cw laser experiments, the Ti:sapphire has been chosen because of its diffraction limited beam quality and consequent ability in being tight focused, optimizing the incoupling procedure.

The setup for the experiments is depicted in Fig. 6.14. The Ti:sapphire laser is set at the GSA-ESA pumping wavelength of 974.2 nm, emitting at a maximum power of 3 W. A power attenuation system composed by a polarizer and a $\lambda/2$ plate is inserted. The laser cavity is composed by two flat mirrors M_1 and M_2 with an intracavity microscope objective (10×, $NA = 0.22$). The crystal is put in contact with M_2. A third mirror M_3,

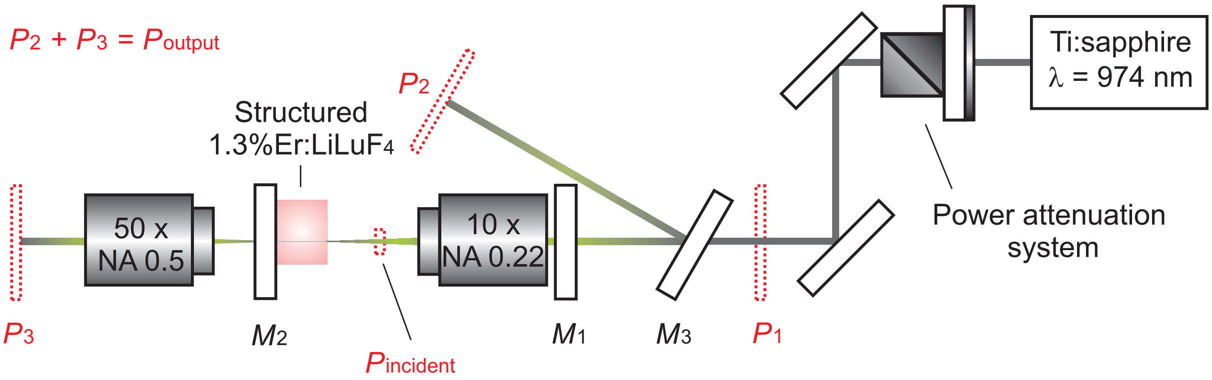

Figure 6.14: Setup for laser experiments with waveguides. The cavity is composed by the flat mirrors M_1 and M_2 and one intracavity microscope objective (10×, $NA = 0.22$). The second microscope objective (50×, $NA = 0.5$) helps during the alignment procedure and in the detection of laser emission.

with an AR coating for the pump wavelength and HR coating for the laser wavelength, is positioned in order to separate the emitted laser beam from the pumped beam. The total power emission corresponds to the sum of P_2, deflected by M_3, and P_3, which is imaged by a second microscope objective (50×, $NA = 0.5$) outside the cavity. This second objective lens helps in the detection of the transmitted light during the alignment procedure and consequently of the laser emission. The incident power has to be calculated after the measurement of P_1 and the consideration of the transmission of M_1 (ideally HR at 974.2 nm) and the intracavity objective. Furthermore, the outputcoupling transmission associated to every laser curve is constituted by the contribution of the transmission of M_1 and M_2. The intracavity objective represents a considerable loss in the resonator. The reflectivity of the other optical elements outside the cavity represents only an attenuation of the output power.

Compared to experiments with bulk laser media, the losses to be considered are much higher but also the gain is higher. Consequently, it is expected that laser emission takes place at higher inversion levels than in bulk experiments.

When laser experiments have been performed with the rhombic waveguides, emission in the green wavelength range and at around 850 nm has been obtained. A representation of the results is depicted in Fig. 6.15. Laser operation was possible only in π-polarization and only inside the core of the waveguide.

The laser results can be summarized as follows:

- green laser emission has been obtained at $\lambda = 540.6$ nm, with a total outputcoupling transmission of 0.675, with a maximum output power of 1 mW. The signal was extremely unstable and no input-output curve could be recorded.
- Green true-cw laser emission has been obtained at $\lambda = 551.6$ nm for a total output coupling transmission of 0.01. The signal was more stable and the maximum output power was 200 µW at 2.75 W incident pump power (see Fig. 6.15a).
- Infrared emission in quasi-cw regime has been obtained at $\lambda = 849.8$ nm, with a maximum average output power of 3.2 mW at 2 W of incident pump power. The two input-output curves for a total outputcoupling transmission of 0.23 and 0.98,

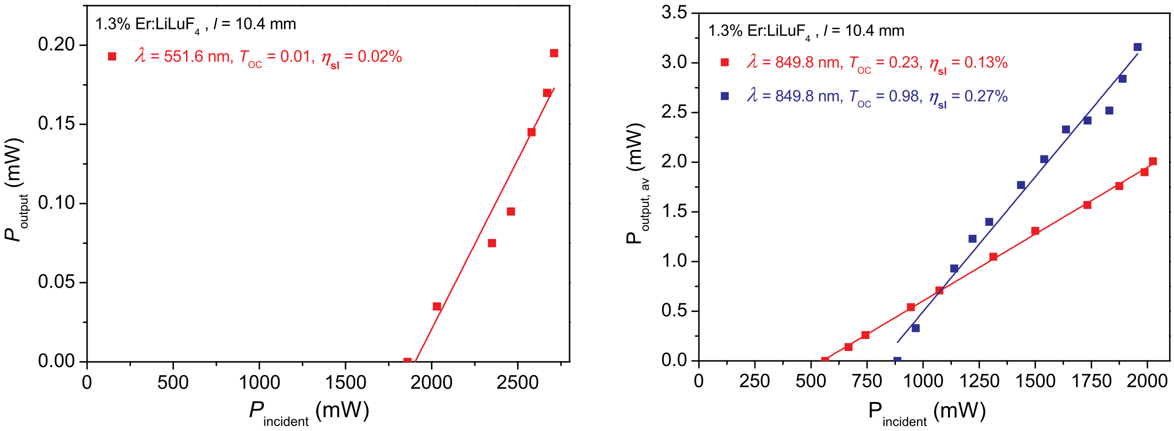

(a) **(b)**

Figure 6.15: Laser input-output curves in rhombic waveguides. In (a), the only input-output curve in the green spectral range which could be measured with sufficient stability of the signal is depicted. In (b), two examples of input-output curve at around 850 nm are shown. The laser at this wavelength can operate also without one of the resonator mirrors, but in a very unstable way. The power is averaged because of the intrinsic quasi-cw nature of the operation.

respectively, are depicted in Fig. 6.15b. Laser emission without one of the two resonator mirrors was also possible, with the only contribution of the Fresnel reflection from the surface, but in a very unstable regime.

The same kind of experiments could be performed with the circular waveguides as well. Also with this structure, laser operation has been obtained only in π-polarization and inside the core. Laser emission was detected in the same two different spectral ranges. The results are plotted in Fig. 6.16 and summarized to:

- green true-cw laser emission has been obtained only at $\lambda = 552.6$ nm, with a maximum output power of 10 mW. Two input-output curves are reported in Fig. 6.16a for a total outputcoupling transmission of 0.044 and 0.32, respectively.

- Infrared quasi-cw laser emission has been obtained with a maximum average output power of roughly 10 mW with almost reflection-free resonator mirrors (T_{OC}=0.996). Fresnel reflection from the crystal surface decreases the transmission more than the nominal transmission of the mirror. Therefore, it has to be assumed a total lower outputcoupling transmission. Furthermore, considering the difficulties in obtaining laser operation without employing mirrors, it is probable that the mirrors were providing an even lower transmission due to damages of the optical coating.

Obtaining green laser emission from the waveguides was the main aim of this part of the work. The laser operation in the infrared has been detected in competition with it. Nevertheless, the application of AR mirrors for 850 nm in the cavity has not been always successful in the forced termination of this laser emission.

Moreover, in the pumping configuration of GSA-ESA pumping at around 970 nm, laser emission at around 850 nm should be forbidden. The lifetime of the final laser level $^4\mathrm{I}_{13/2}$, is much longer than the emitting level $^4\mathrm{S}_{3/2}$ (9.7 ms vs 0.400 ms) and the laser

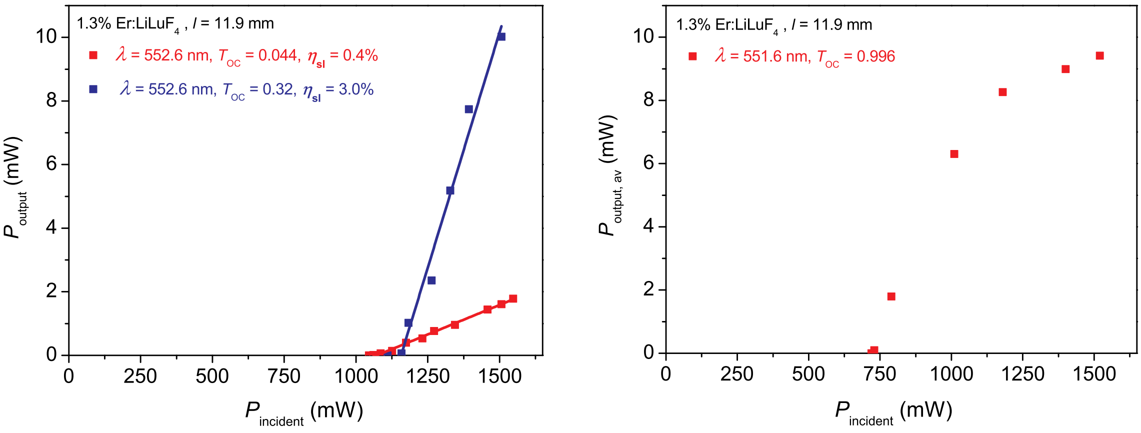

(a)

(b)

Figure 6.16: Laser input-output curves in circular waveguides. In (a), two input-output curves in the green spectral range are reported. In (b), an input-output curve at around 850 nm is depicted. The laser presents a saturation at high incident pump power with roughly 10 mW of output power.

emission is expected to be self-terminating, as also confirmed by different theoretical and experimental works about Er^{3+}:LiYF$_4$ (e. g. [Qui91]). Efficient laser operation at this wavelength can be obtained with the other two schemes of upconversion pumping depicted in Fig. 2.3.1, which means pumping at a wavelength of either 790 or 810 nm, in a way that an upconversion-pumped laser can be realized, because $\lambda_{\mathrm{pump}} < \lambda_{\mathrm{laser}}$ (in Er^{3+}:LiYF$_4$ [Möb98]). These two pumping processes have ^{4}I$_{13/2}$ as intermediate level, which can be efficiently depopulated during the pumping process, allowing for an efficient inversion between emitting and final laser level.

Consequently, further investigations about the nature of the laser emission have been performed and with the use of a digital oscilloscope, the actual quasi-cw nature of the laser operation at around 850 nm has been detected.

In Fig. 6.17, a comparison between the signal detected by the digital oscilloscope in the case of the laser operation in the green, is compared to the one at around 850 nm in the circular claddings. The pump signal has been modulated by means of a chopper, whose signal has been adopted as reference by the oscilloscope. The frame reported in Fig. 6.17a, shows the relaxation oscillations which characterize the beginning of the laser emission in the green spectral range and the following stabilization of the signal in a pure cw-regime, also highlighted in the enlargement in the inset. In Fig. 6.17b, the oscillation relaxations are periodically present and in the inset, plotted on the same scale as in Fig. 6.17a, it is possible to compare the amplitude of the oscillations, which is extremely high for the infrared laser and at a frequency of roughly 300 kHz.

An explanation for the partially allowed laser oscillation around 850 nm could be found in the high gain and high losses which characterize the lasing process in these crystalline waveguides. If compared to experiments in bulk media, the inversion is higher in the waveguide laser, so a higher difference of population densities between the ^{4}S$_{3/2}$-multiplet and the ground state is present. But this can be valid also between the ^{4}S$_{3/2}$- and the ^{4}I$_{13/2}$-multiplet . This could be enough to generate a competition between the natural self-termination of the laser emission and the cw-operation, resulting in a quasi-cw operation.

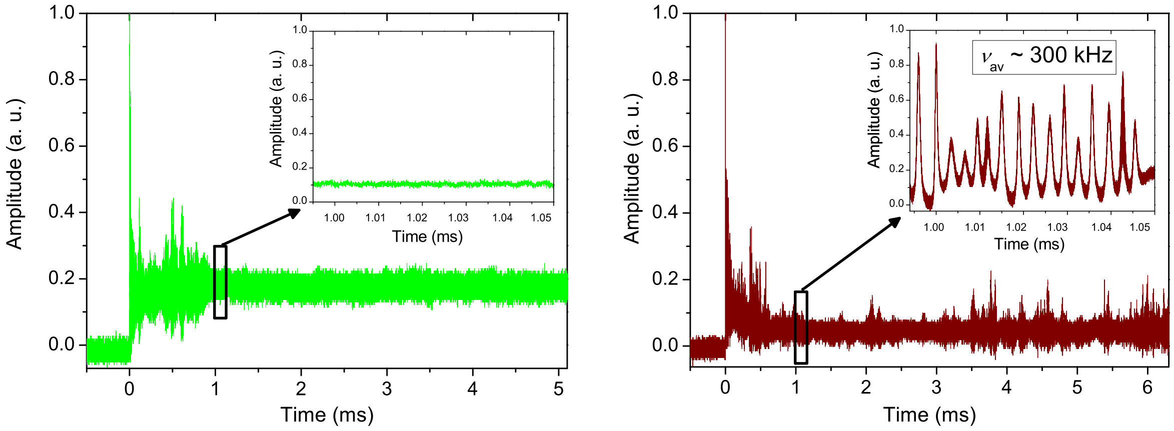

(a) **(b)**

Figure 6.17: Comparison between relaxation oscillations and laser operation of the green and the 850-nm emission in a circular cladding. In (a), the green emission is considered. At the onset of the laser emission, relaxation oscillations can be detected and then true-cw operation is established and confirmed by the enlargement in the inset. In (b), the relaxation oscillations are periodically present for the infrared emission and in the inset a portion is depicted showing a frequency of oscillation of roughly 300 kHz, at the same arbitrary unit of amplitude as in the inset in (a).

This has been theoretically demonstrated by *Toma* [Tom11].

Furthermore, in Er^{3+}:$LiLuF_4$ crystals, the expected laser wavelength in the green spectral range in π-polarization is around 552 nm, as established by the gain spectrum in Chap. 5 and by experiments with bulk media. As pointed out in Chap. 5, the shorter wavelength 540.65 nm for laser emission is nevertheless allowed at extremely high levels of inversion (starting at $\beta = 0.69$). As estimated in Sect. 6.1.3, the highest possible inversion in this system is $\beta_{\max} = 0.564$. Nevertheless, if a miscalibration of the emission cross section spectrum is admitted, an explanation for this second emission wavelength could be found once again directly in the high-gain and high-losses nature of the waveguide laser. Moreover, no detailed analysis of the relaxation oscillation has been carried out at this wavelength, due to the high instability of the signal. A quasi-cw behavior could have also affected this laser operation.

The low slope efficiency and high threshold incident pump power which characterize the green laser emission in circular waveguides have to be improved. The absorbed pump power of roughly 80% calculated in bulk experiments with Er^{3+}:$LiLuF_4$ (see next Section) would determine an improvement of the slope efficiency if calculated with respect to the absorbed pump power. Moreover, the determination of the incoupling efficiency η_{i} and of a possible bleaching factor would further contribute in showing the effective efficiency of the system. Nevertheless, improving the results obtained in bulk experiments where the best slope efficiency is more than 5% with respect to the incident pump power at much lower outputcoupling rates, is still a challenge.

A fundamental optimization of the setup would be to perform laser experiments without the intracavity microscope objective which causes the most of the losses and the high laser threshold. This would allow for taking advantage of the extremely low damping observed during transmission measurements. Nevertheless, reducing the losses for green emission leads to the reduction also for the emission at 850 nm and it is possible no improvement concerning the suppression of the infrared emission would be obtained. The optimization of the mirror coatings or the direct deposition of optical coatings onto the surfaces of the crystal would reduce the competition with the 850-nm radiation to the minimum and increase the stability of the green laser, because wavelength-dependent losses would be introduced. Moreover, maintaining the circular form of the waveguide, but reducing the number of tracks, the internal diameter of the core and the pulse energy, could improve the performances of the laser, although the present parameters are optimal to reduce the damping. Finally, the available effective incident pump power from the Ti:sapphire laser has been less than the standard $\sim 2.8\,W$ for the laser experiments with the circular claddings. If 2.5 W of incident pump power such as in the experiments with the rhombic waveguides were available, and the slope efficiency of 3% could be maintained, an output power of roughly 75 mW is potentially obtainable. In bulk experiments, this output power is reached at around 2 W of incident pump power.

6.1.5 Dual-wavelength upconversion lasers

An upconversion laser is convenient when it can be single-wavelength pumped. This means that the laser medium offers a high $\sqrt{|(\sigma_{\mathrm{SE}} - \sigma_{\mathrm{ESA}}) \cdot \sigma_{\mathrm{GSA}}|}$ for a certain wavelength, at which efficient pump laser sources are available (see Sect. 5.6).

Nevertheless, when two different pumping wavelengths are employed, one can address the highest σ_{GSA}, while the other one the lowest $(\sigma_{\mathrm{SE}} - \sigma_{\mathrm{ESA}})$. In this way, the efficiency of the pump process can be further improved and the dynamics of the population of the energy levels can be modified in favor of the laser emission process.

For Er^{3+}-doped fluorides, the pumping mechanisms to obtain laser emission in the green spectral range are depicted in Fig. 2.5. An interesting option could be to combine two different pumping schemes. For example, one absorbed photon could be at $\lambda \sim 970\,\mathrm{nm}$ (GSA), such as in the third pumping scheme, and the second at $\lambda \sim 790\,\mathrm{nm}$ (ESA). The advantage of mixing two schemes which can independently work for single-wavelength upconversion would be an expected overall improved pumping efficiency. Furthermore, this would be combined in this case with an efficient depopulation of the $^4\mathrm{I}_{13/2}$-multiplet, due to its long decay time of almost 10 ms tends to be highly populated.

The alternative pumping scheme which is introduced in the following is slightly different. It is still based on the most efficient pumping mechanism at $\sim 970\,\mathrm{nm}$, but instead of addressing a single wavelength where GSA and ESA are in resonance, it has the aim of tuning the two different pump sources to the highest GSA peak and to the highest ESA peak, respectively.

If the experiment is carried out with Er^{3+}:LiLuF_4 and the highest absorption cross sections are addressed (π-polarization) the two most efficient pumping wavelengths follow from Fig. 5.41c: 971.8 nm for GSA and 966.8 nm for ESA. Nevertheless, considering that the second most favorable peak for ESA is located at 974.3 nm, basically matching the optimal wavelength for single-wavelength pumping (974.20 nm), the chosen wavelengths for dual-wavelength upconversion pumping are 971.8 nm and 974.3 nm.

In order to efficiently pump the crystal and to address the narrow absorption peaks, it is necessary to employ high-brightness pump sources. Together with a Ti:sapphire laser, two Distributed Bragg Reflector tapered diode lasers (DBR-TDLs) have been used. This

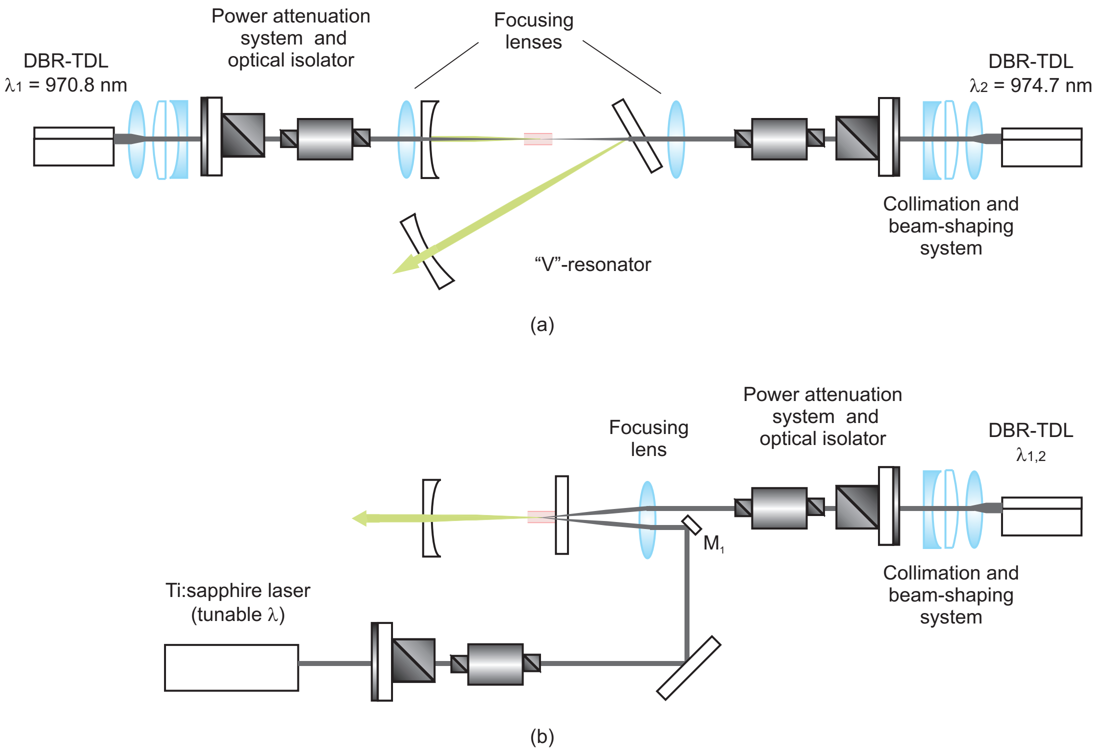

Figure 6.18: First and second setups for laser experiments with tapered diode lasers. In (a), the first setup for the simultaneous use of the two tapered diode lasers in a double-side pumped "V"-resonator is depicted. In (b), the second setup with the employment of a tunable Ti:sapphire laser and one DBR-TDL in a hemispherical resonator pumped from one side is shown.

part of the work was conducted in collaboration with the *Ferdinand-Braun-Institut* in Berlin, Germany [Fie11].

The DBR-TDLs emit radiation in a single longitudinal mode at a certain wavelength in the range of 970 nm which can be chosen during the fabrication of the device. The emitted beam is nearly diffraction limited and the maximum output power is 7 W. The laser is driven by increasing the applied current which causes a drift in the wavelength of up to 0.4 nm. For more information about DBR-TDLs see [Fie08].

The two DBR-TDLs available for experiments have a central wavelength at the output power of roughly 6 W of 970.8 and 974.7 nm. Due to the difficulties in addressing the target wavelengths during the fabrication of the DBR-TDLs, unfortunately the GSA and ESA cross sections are lower than expected. Nevertheless, the most difficulties have been encountered in the preparation of the laser setup.

Initially, the setup was the one depicted in Fig. 6.18a). The DBR-TDLs were supposed to be employed simultaneously and symmetrically from the two sides, in order to obtain a homogeneous pumping of the crystal. Unfortunately, the extremely high sensitivity of the amplifier built into the DBR-TDLs, did not allow this pumping geometry. Despite the presence of high-performance optical isolators, spurious either back-reflections or transmissions from the opposite laser caused damages of the amplifiers.

The final solution to avoid transmission and back reflections is the one depicted in Fig. 6.18b). The resonator has been exchanged with a hemispherical design, pumped

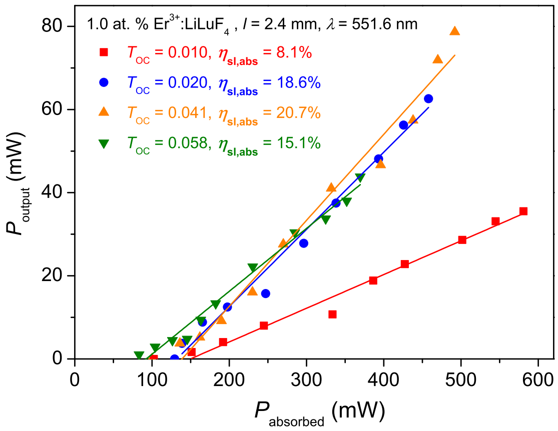

Figure 6.19: Bulk, Ti:sapphire-pumped laser experiment at 551.6 nm of a 1 at.% Er^{3+}:LiLuF$_4$. The green laser output is plotted against the absorbed pump power, calculated at the laser threshold.

from one side. Unfortunately, this geometry suffers from an inhomogeneous distribution of the pump radiation in the crystal due to a slight dislocation of the two beam waists in the focus. The mirror M$_1$ is made of a thin substrate with a diameter of 8 mm coated to be HR for the wavelength around 970 nm and supplied by *Barlösious* [Bar12]. The small size is required in order to allow the two beams for being brought together, as close as possible, thus to obtain an efficient focusing by the lens and a good overlap in the crystal. In this geometry detrimental back reflections from the output coupling mirror, which is HR coated for the pump wavelengths, are avoided.

In order to optimize the setup, preliminary experiments with the hemispherical resonator with only the Ti:sapphire laser as pump source have been performed. The laser was tuned at the single-frequency pumping wavelength of 974.2 nm and focused with a lens of 40 mm of focal length into a 1 at.%-doped Er^{3+}:LiLuF$_4$ crystal (from crystal AL in Tab.A.2). The sample was 2.4 mm long, cut along the **a**-axis and mounted on a heat-sink which could be water-cooled. The curvature of the outputcoupling mirrors was 50 mm and four different input-output curves have been recorded. The output power with respect to the absorbed pump power is depicted in Fig. 6.19. Four different output coupling mirrors have been employed and the best results have been obtained with an output coupling transmission of 0.041 giving almost 80 mW of output power for less than 500 mW of absorbed pump power and with a slope efficiency of $\eta_{\mathrm{sl,abs}} = 20.7\%$. These results show an improvements if compared to very similar experiments performed with Er^{3+}:LiYF$_4$ reported in [Möb98]. The absorbed pump power was about 24% of the incident power and has been measured at the laser threshold for an almost pure double pass, due to the relatively high reflectivity at the pump wavelength of the output coupling mirrors.

Once the resonator has been optimized for lasing, the beam of the Ti:sapphire laser could be shifted as long as the laser emission was still possible. The second pump source was then added along the same optical path, starting from the focusing lens, as depicted in Fig. 6.18b.

Once the alignment of the second pump source has been optimized, the wavelength of the Ti:sapphire laser was tuned in order to show the gain in green output power due to the second pump source, as depicted in Fig. 6.20. A diagram of the green output power in

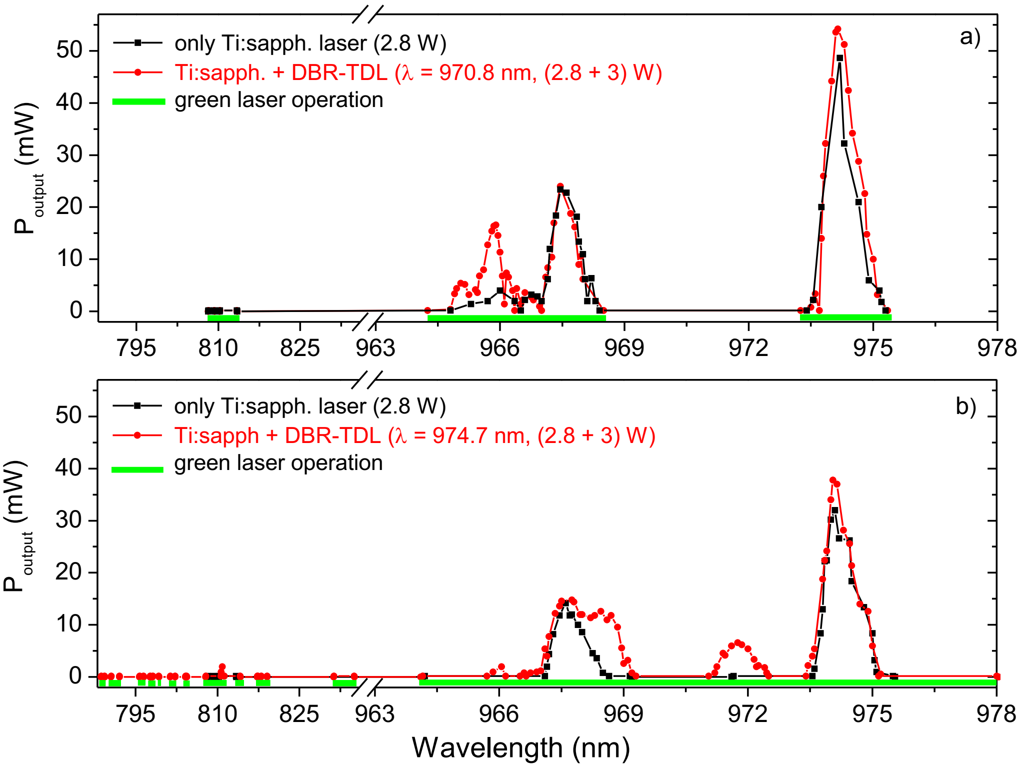

Figure 6.20: Comparison between the influences on the green laser emission of two DBR-TDLs operating at slightly different wavelengths. The black curves represent the results when pumped only by the Ti:sapphire laser. The two curves are not exactly comparable to each other, but they are a reference for the red curves obtained with the added contribution of the DBR-TDL at 970.8 nm in a) and of the DBR-TDL at 974.7 nm in b). The green band indicates when the green emission was above the lasing threshold. The emission wavelength was always 551.6 nm.

function of the tuning range of the Ti:sapphire laser is plotted for both the DBR-TDLs. In each diagram, the same curve for the same setup but with only the Ti:sapphire laser is depicted. This curve has been recorded when the beam of the Ti:sapphire laser was shifted, in order to be directly comparable with the curves in presence of the DBR-TDLs. This means that a certain fraction of the possible tunability of the pump allowing for green laser emission and of the maximum obtainable output power have been quenched by the misalignment. Furthermore, the two black curves are not directly comparable to each other, and the shift can be quantified in roughly 35% more output power in a). It has been chosen to lose the reproducibility in favor of a renewed maximization of the laser performance before substituting one DBR-TDL with the other one. Both the DBR-TDLs have been set to the maximum incident pump power on the crystal of roughly 3 W because for further higher incident power the effects on the green laser emission were either not improving or negatively affecting the output power, due to thermal problems. For this reason, the experiment has been carried out with the contribution of a chopper at roughly 30 Hz of frequency placed after the focusing lens, in order to decrease the heat load of the crystal, extend the tunability range of the Ti:sapphire laser allowing for the green laser operation, and increasing the total output power. The Ti:sapphire laser was operating at an output power that in the range of tunability varies between 2.75 and 2.95 W.

From this study, it is possible to understand how a difference of less than 4 nm can perturb the laser emission of the system in terms of output power and operation of the laser with different pumping schemes.

Considering that the better alignment of the Ti:sapphire in a) obviously determines an advantage compared to b), it is evident that the closeness of the wavelength of the DBR-TDL in b) to the optimum wavelength for single-wavelength upconversion laser allows this laser for determining the broadest range of tunability of the Ti:sapphire maintaining green laser operation. Furthermore, it is possible to recognize which range of wavelengths of the Ti:sapphire laser are more effective for simultaneous pumping with the two different DBR-TDLs. In the spectral range around 974.2 nm, the optimal wavelength for single-wavelength pumping, both the DBR-TDLs are contributing, but not significantly, because the load of heat limits the advantage of higher incident pump power. The same is valid between 967 and 968 nm where the second highest GSA peak and a bleaching of the ESA peak are present. The DBR-TDL in a) in this setup would not be able to pump the green emission in a single-wavelength scheme, but it causes higher power emission when coupled to the wavelength range between 965 - 966.5 nm. This spectral range is exactly where the deepest ($\sigma_{\mathrm{SE}} - \sigma_{\mathrm{ESA}}$) peak in Fig. 5.41c is located. Nevertheless, this wavelength would not be recommendable to be employed with a second wavelength in the range of 790 or 810 nm because no advantage compared to the green laser operation due only to the Ti:sapphire is recorded. On the other hand, the small cross sections associated to these two spectral ranges when pumping in single-wavelength, are amplified by the contribution of the DBR-TDL in b), which, despite the misalignment of both the pump sources, allows for green laser operation in different spectral ranges between 788 and 835 nm. Furthermore, this DBR-TDL increases the green output power when coupled to another pump wavelength between 971 and 972.4 nm, which means the exact range of the highest GSA peak in Fig. 5.41c.

In conclusion, the technical difficulties in setting up an efficient pumping scheme of the Er^{3+}:LiLuF_4 crystal did not allow for showing the possible positive effects of pumping separately at the two wavelengths where the highest GSA and ESA cross sections are located for the pumping scheme based on the 970-nm-wavelength range. Probably due to thermal management issues combined with the inefficient pump beam overlap in the crystal, no significant increase of the output power in the green spectral range has been obtained. Nevertheless, information about which pair of wavelengths would be interesting to investigate in an efficient resonator could be deduced.

An interesting outlook for this work would be the performance of further laser experiments with the DBR-TDL in b) and the Ti:sapphire laser tuned to the 790 nm and the 810 nm range. The setup should allow for efficient pumping by both the pump sources, focusing on the importance of the depopulation of the ${}^4\mathrm{I}_{13/2}$-multiplet. It is expected to be efficient with the 790 nm/974 nm scheme but not with the 810 nm/974 nm scheme.

It has to be considered that when the wavelengths are so well separated, the application of a dichroic mirror to merge the two beam is an option because of the possibility of depositing AR/HR coatings for the two wavelengths, improving the overlap of the beams.

The combination of different wavelengths can also be extended (e. g. the combination 790 nm - 1.54 µm from a Ti:sapphire laser and an erbium-based fiber laser, respectively),

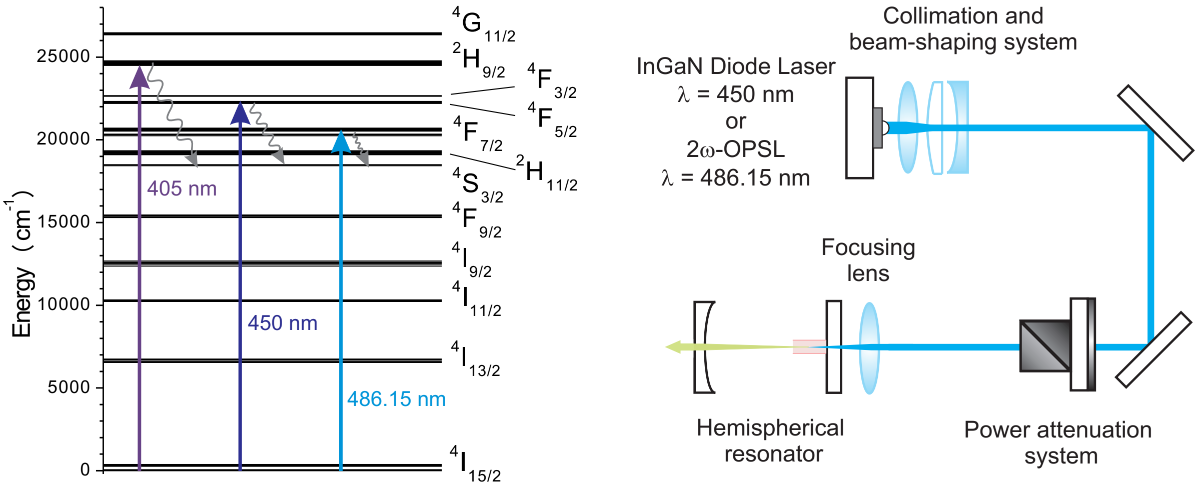

(a) (b)

Figure 6.21: Possible excitations of Er^{3+}: $LiLuF_4$ and setup for laser experiments with pump sources in the blue spectral range. In (a), the energy level scheme of Er^{3+}:$LiLuF_4$ is shown [Kam86], with highlighted three possible pumping wavelengths in the blue spectral range. In (b), the standard hemispherical resonator adopted for laser experiment with pump sources in the blue spectral range is depicted. The output coupling mirror had $ROC = 50\,\mathrm{mm}$ and the focusing lens typically 40 mm of focal length. In the case of experiments with the 2ω-OPSL, an optical isolator has to be added in order to protect the pump laser from back reflections

with the only requirement of similarity of the two beams, to obtain an efficient overlap in the crystal.

A more efficient cooling of the crystal (Peltier-element) would be also recommended in order to fully take advantage of the maximum output power of the pump sources, while suppressing the detrimental effects of the heat in a ground state laser.

6.2 Green laser pumped in the blue spectral region

Considering that the efficiency of upconversion lasers is still relatively low, the possibility of either directly or indirectly pump with short-wavelength photons the laser emitting level could offer a new prospective for highly efficient, visible Er^{3+}-based lasers.

Er^{3+}:$LiLuF_4$ has three multiplets which can absorb in the blue-violet spectral range, which are represented in Fig. 6.21a). In π-polarization, the maximum peak of absorption into the $^2H_{9/2}$-multiplet is centered at 405.7 nm, with an absorption cross section of $1.27 \cdot 10^{-20}\,\mathrm{cm}^2$. This wavelength is usually supported by GaN diode lasers, emitting a few hundreds of milliwatts. The $^4F_{5/2}$-multiplet exhibits an absorption cross section peak of $1.50 \cdot 10^{-20}\,\mathrm{cm}^2$ at 450.0 nm, in the spectral region covered by InGaN diode lasers, which recently have reached the possibility to achieve output powers in the watt regime, for low production costs. Finally, the highest absorption cross sections characterize the

$^4F_{7/2}$-multiplet with a peak of $4.2 \cdot 10^{-20}\,\mathrm{cm}^2$ at 486.4 nm. This spectral region is covered by frequency-doubled optically-pumped semiconductor lasers (2ω-OPSLs) based on InGaS-GaAs semiconductor chips. 2ω-OPSLs are the newest among these products and they can deliver a few watts of output power, with a nearly diffraction-limited beam centered at a wavelength that can be tailored during the fabrication. 2ω-OPSLs are the most promising pump sources, but production costs are still high for a broad commercial spread.

Therefore, if gas and dye lasers or frequency-doubled solid state lasers are not considered, frequency-doubled semiconductor-based pump sources are those which can cover part of the blue spectral range.

In the framework of this thesis, the first experiments with a pump source in the blue spectral range have been performed with an OPO (described in Chap. 5). The setup was composed by a hemispherical resonator as the one depicted in Fig. 6.21b, with an outputcoupling mirror with $ROC = 50\,\mathrm{mm}$ and a focusing lens with 40 mm of focal length. An optical parametric oscillator is a pulsed source and the one available for experiments delivers roughly 3 mJ in the blue spectral range, with pulses of a duration of 10 - 20 ns, at a repetition rate of 10 Hz.

Independently from the multiplet addressed by the freely tunable pump source in this spectral range, laser emission has never been reached due to the limited duration of the pulses and the low repetition rate of the OPO, if it is considered that the lifetime of the $^4S_{3/2}$-multiplet (400 µs) is 20000 times longer than every pulse.

For a four-level laser it is possible to define the time before the onset of laser relaxation oscillations t_c as :

$$t_c = \tau_{\mathrm{eff}} \ln \left(1 - \frac{P_{\mathrm{thresh}}}{P_{\mathrm{abs}}}\right)^{-1}, \tag{6.34}$$

where τ_{eff} is the lifetime of the upper laser level, P_{thresh} is the absorbed pump power at the laser threshold the absorbed power in the active medium.

In the present case, to have the possibility to obtain the onset of the relaxation oscillations before the pump pulse is extinguished, it has to be imposed $t_c < 20\,\mathrm{ns}$ and $\tau_{\mathrm{eff}} = 400\,\mu\mathrm{s}$. This condition inserted into Eq. (6.34) would lead to:

$$\left(\frac{P_{\mathrm{abs}}}{P_{\mathrm{thresh}}}\right)_{\mathrm{min}} = 20000. \tag{6.35}$$

This is clearly an unrealistic value.

A second attempt has been performed using an InGaN diode laser as a pump source. It operates at the wavelength of 447 nm but it is still tunable with increasing current to $\lambda = 450\,\mathrm{nm}$. The maximum output power was 1 W at an applied current of roughly 1 A. When the diode has been operated in cw mode, the green laser threshold has not been reached. For this reason, a further attempt has been performed imposing a pulsed operation to the diode which could cause a higher peak output power than 1 W. The limit of damage threshold of the diode laser allowed for the operation at 1.37 A, with a pulse duration of 6.0 ms, a duty-cycle of 42% and a repetition rate of 70 Hz. In this case, the excitation and the consequent possible laser operation have to be considered quasi-cw because $6\,\mathrm{ms} \sim 15\,\tau_{\mathrm{eff}}$. Therefore, the peak-power of roughly 1.4 W at $\lambda = 450\,\mathrm{nm}$ can be

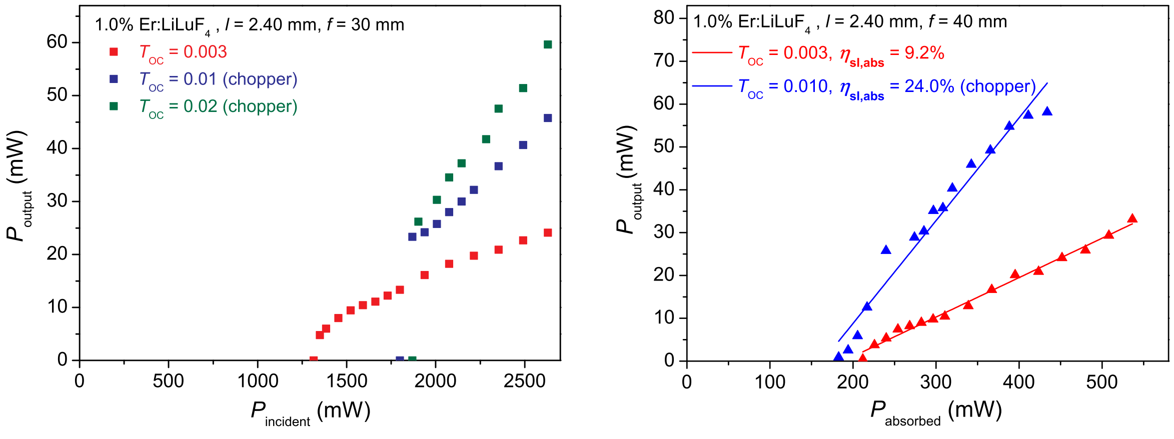

(a) **(b)**

Figure 6.22: Laser input-output curves obtained pumping with the 2ω-OPSL a 1 at.% Er^{3+}-doped LiLuF$_4$ crystal, at $\lambda = 551.6$ nm. In (a), serious thermal problems affect the result obtained with a lens with focal length of 30 mm and in two cases a chopper had to be used to favor the cooling of the crystal. In (b), more stable results are obtained with a lens with focal length of 40 mm. Here the slope efficiency could be calculated with respect to the absorbed pump power, calculated at the laser threshold. Thermal issues are still present.

evaluated as 1.4 W in cw regime and as not enough to reach the laser oscillation threshold in Er^{3+}:LiLuF$_4$.

The only successful way to reach the laser threshold has been to increase the incident cw pump power using a 2ω-OPSLs. The one available for laser experiments has a non-tunable emission wavelength of 486.15 nm with a nearly diffraction limited beam, and a maximum output power of 4 W. Unfortunately, the shift of only 0.25 nm from the highest absorption peak causes a loss in absorption efficiency of a factor of four ($\sigma_{abs} = 4.0 \cdot 10^{-21}\,\text{cm}^2$). Nevertheless, experiments to obtain green laser emission have been successful and the results are reported in Fig. 6.22.

The emission wavelength of the 2ω-OPSL corresponds to a half of the wavelength adopted for upconversion experiments. This means that every photon emitted by the 2ω-OPSL has twice the energy of one photon from the Ti:sapphire laser in the experiments in the previous section. Thus, a direct comparison between the two schemes can be performed.

The experiments have been carried out in the same a hemispherical resonator, such as the one depicted in Fig. 6.21b, with an optical isolator in order to protect the pump laser from back reflections. Three different lenses have been adopted to focus the excitation beam into the crystal. The results obtained with the lens with 30 mm of focal length are summarized in Fig. 6.22a, while those obtained with the lens with focal length of 40 mm are depicted in Fig. 6.22b. The lens with a focal length of 50 mm led to particular instability of the laser and the results are thus not reported here.

In order to compare these results with those obtained in the upconversion experiments, the same 1 at% Er^{3+}-doped, 2.40-mm long sample has been employed. It was mounted on a copper heat-sink and water-cooled.

The results of the experiments show a clear problem of heat management in the crystal. 2 W of incident pump power can be enough to destabilize the laser emission and in all the cases where it is mentioned in Fig. 6.22, a chopper operating at roughly 50 Hz of frequency has been employed to reduce the load of heat and the output power has been averaged. The effects of the chopper are visible in Fig. 6.22a, if the two curves at high outputcoupling transmissions are compared to the one based on an almost HR mirror at the laser wavelength. In the first two cases, the laser threshold is reached at high incident pump power and the chopper causes an almost vertical step in output power when the incident pump power is slightly increased. The laser characteristics can be then recorded with approximately a linear behavior. In order to be able to compare the results with those obtained in upconversion experiments, the system for cooling the crystal has not been modified, but in order to perform further experiments, the use of a Peltier-element is recommended.

Such as in the upconversion experiments, a focal length of 40 mm resulted in the best performance. The longer focal length causes a less tight focus which causes a lower excitation density for laser pumping and heating up of a broader volume of the crystal. The shorter focal length has given lower output power results at the same outputcoupling rates, and also slightly less stability in facing thermal issues. Simulations of the modes in the resonator show a worse overlap between the pump mode and the laser mode, if compared to the overlap induced by the intermediate focal length.

Considering the difficulties in calculating the absorbed pump power because of the too high instability, the results in Fig. 6.22a are plotted vs incident pump power. On the contrary, in Fig. 6.22b the input output curves are plotted vs absorbed pump power which on the average was about 18% of the incident power, calculated at the laser threshold for an almost pure double pass, due to the relatively high reflectivity at the pump wavelength of the output coupling mirrors.

Compared to the upconversion laser results in Fig. 6.19, the laser threshold is reached if almost double of the pump power is absorbed. Nevertheless, the maximum output powers are similar or even better in the direct-pumped experiments, if a comparison between the laser characteristics at 0.01 of transmission is performed. Furthermore, on the average, the Er^{3+}-doped $LiLuF_4$ crystal absorbed a few per-cents more pump power of the 2ω-OPSL compared to the Ti:sapphire laser. The absorption efficiency of the blue laser has to be considered even more positively, if it is reminded that the 2ω-OPSL does not perfectly address the absorption peak of Er^{3+}:$LiLuF_4$.

This result can be compared to the excimer/dye-laser-pumped experiments reported in [Bre93a] performed with a 1% Er^{3+}:$LiYF_4$ and described as the first room temperature green erbium-doped crystal laser. The pump wavelength and the sample characteristics are very similar to the experiments performed in the framework of this thesis but 75% of the incident pump power has been absorbed. Furthermore, the recorded slope efficiency is lower to the one here reported and for a higher output coupling rate. This shows the potential of the cw system after the stabilization of the temperature and an optimization of the pump wavelength have been realized.

Despite the attempts to keep the setups equivalent for comparison, most of the results obtained with the upconversion laser are not comparable with those obtained via blue pumping because of the need of a chopper for reducing the heat load in the crystal. The only comparison possible is between the two red laser characteristics in Figures 6.19 and 6.22a. Both have been recorded without the support of the chopper and although the outputcoupling transmission is lower in the blue-pumped experiments, the obtained maximum output power is similar and at the same time the laser threshold tremendously higher (more than three times with respect to the incident pump power). The worse mode overlap can also play a role in the excessive needed incident pump power to reach the threshold, but the contemporary relatively high extracted output powers does not find an explanation.

In conclusion, despite the emerged problems, these experiments led to the demonstration of the first cw direct-pumped in the blue spectral range erbium-based laser.

New experiments can be performed after a definition of the optimal length and doping concentration in the crystal, probably with longer and lower doped samples. The cooling system of the crystal needs also to be optimized and if possible the emission wavelength of the pump source centered to the absorption peak of Er^{3+}:$LiLuF_4$, avoiding to match the detrimental ESA peak at slightly longer wavelength which is shown in Fig. 5.41a.

6.3 Laser experiments in the 1.6-µm spectral range

As specified in Sect. 4.2, Er^{3+}-doped materials are interesting for the possibility of laser emission in the eye-safe spectral region of 1.5 - 1.6 µm, based on the $^4I_{13/2} \rightarrow {}^4I_{15/2}$ transition.

New fiber lasers based on Er^{3+}-doped materials provide currently relatively high output power and good beam quality allowing for inband-pumping at 1.5 µm.

With the advent of these new powerful pump laser sources, the conventional pumping scheme can be abandoned. It is based on pump sources emitting at around 970 nm to excite directly the upper $^4I_{11/2}$-multiplet and after non-radiative decay populate the $^4I_{13/2}$-manifold.

In this way, also Er^{3+}-doped fluorides, particularly efficient in converting the photons at 970 nm of wavelength more into emission in the green spectral range than at 1.6 µm, can be evaluated as possible host materials.

In the framework of this thesis, Er^{3+}-doped $LiLuF_4$ and $BaYLuF_8$ crystals have been employed for polarization-dependent laser experiments in the 1.5 - 1.6-µm spectral range.

Two kinds of resonators have been employed: a Z-shaped one, feasible to reduce thermal lens effects, and a linear hemispherical one. Both allowed for almost pure double pass of the pump, due to a relatively high reflectivity of the outputcoupling mirrors at the pump source. The Z-shaped resonator is displayed in Fig. 6.23a. Each collimated arm of the resonator had a length of 90 mm, while the two curved folding mirrors were separated by a distance of 110 mm. The hemispherical resonator was similar to the one depicted in Fig. 6.21b but it was characterized by a curved outputcoupling mirror with $ROC = 200$ mm, and a focusing lens with a focal length of 100 mm. A linearly polarized erbium fiber laser ELR-10-1535-LP by *IPG*, emitting a maximum output power of about 8 W (after the optical isolator) at 1535 nm, with a nearly diffraction-limited beam, has been employed as pump source.

This work is partly the result of a collaboration with *Brandt* [Bra11b]. Two of the crystals involved in this work have been provided by *Schellhorn* [Sch12] and one supplied by *Parisi* [Par12].

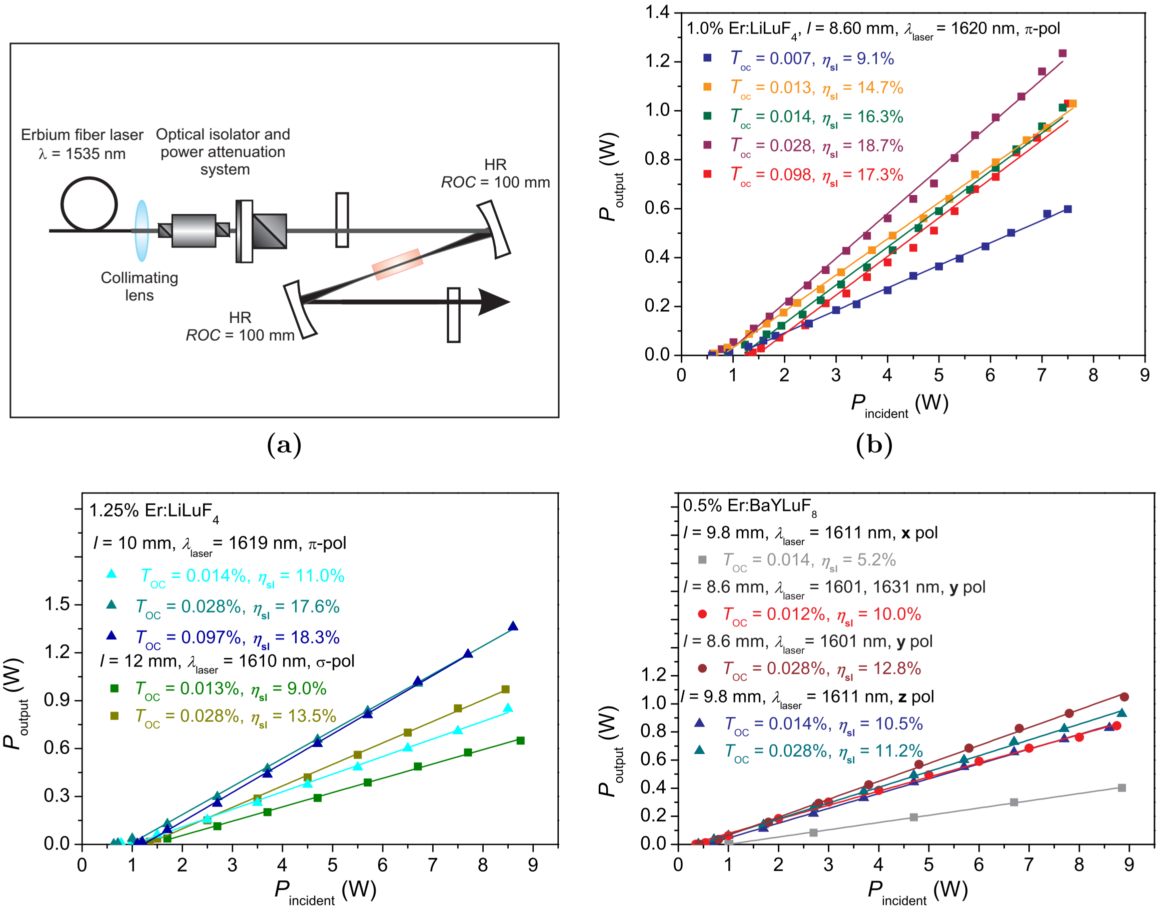

(a) **(b)**

(c) **(d)**

Figure 6.23: Illustration of the Z-shaped resonator and laser input-output curves obtained with inband-pumped Er^{3+}-doped fluorides at 1.6 µm. In (a), the Z-shaped resonator is illustrated. In (b), the results obtained with a 1.0 % Er^{3+}-doped $LiLuF_4$ crystal in the Z-shaped resonator are shown. In (c) and (d) the input-output curves recorded in a hemispherical resonator with a 1.25% Er^{3+}-doped $LiLuF_4$ and a 0.5% Er^{3+}-doped $BaYLuF_8$ crystals, respectively are reported.

A summary of the results is displayed in Fig. 6.23b-d and listed in Tab. 6.2.

The most promising laser crystal of the two which have been investigated in terms of maximum output power and slope efficiency is Er^{3+}:$LiLuF_4$.

In both resonators with different Er^{3+}-doping concentrations the results are similar. They show a maximum output power of 1.40 W in the linear resonator, for a slope efficiency higher than 18%. In the Z-shaped resonator, the results present slightly less output power and incident power at the threshold and a slightly higher slope efficiency. But this is possible only because in the experiments in the hemispherical resonator roughly 1 W more incident pump power was available than in the Z-shaped resonator experiments.

As previously mentioned, one of the benefits of an inband-pumping mechanism is to abandon pump sources emitting at 970 nm where ESA/ETU to higher energy levels is particularly strong. Nevertheless, ESA/ETU processes are active also at 1.5 µm and this is demonstrated by the strong green fluorescence which is evident in all the Er^{3+}-doped fluoride crystals during these experiments and higher than in oxides such as Er^{3+}:YVO_4.

In order to reduce the losses at the pump wavelength, it is therefore convenient to work with crystals with a low Er^{3+}-doping concentration and compensate for the decreased absorption efficiency by increasing the length of the samples.

Considering the absorption spectra depicted in Fig. 5.6a, the absorption cross sections of Er^{3+}:$LiLuF_4$ in the 1.5 µm are higher in π-polarization than in σ-polarization. For Er^{3+}:$LiLuF_4$ crystals the length of the samples in the experiments in the Z-shaped resonator corresponds to 0.66 absorption lengths in π-polarization, but it corresponds to almost one in the highly doped crystal, yielding almost the same performances.

Considering that the results in the highly Er^{3+}- doped sample for the addressed σ-polarization have been recorded with a crystal length implying less than 0.9 absorption lengths, further experiments are expected to improve the results if longer crystals with an even lower Er^{3+}-doping concentration are employed for both the polarizations. Reducing the concentration would decrease the effects of ETU. Nevertheless, ESA is not concentration-dependent and its detrimental effects would not be lowered.

With Er^{3+}:$BaYLuF_8$ samples the best laser performance has been obtained with the low-Er^{3+}-doped sample, addressing **y**-polarization, using an output coupling of 0.028, for an output power of 1 W, at a slope efficiency of 12.8% and with an incident pump power at the threshold corresponding to 0.42 W. Comments on these results are not straightforward, because of the missing definition of the real absorption cross sections for the crystal at the wavelength of the pump source, as explained in Chap. 5 and shown in Figures 5.7b and 5.8. Nevertheless, approximations can be defined which clearly show that the length of the sample was insufficient for efficient absorption. For all the orientations, in the most optimistic case, the length corresponds to less than a half absorption length. The dramatic drop of the performances in the higher Er^{3+}-doped sample (see Tab. 6.2) can be as well found on the stronger ESA/ETU at the pump wavelength. Therefore, also in this case, it would be recommendable to perform new experiments with longer and lower Er^{3+}-doped crystals. Nevertheless, a limit could be represented by a loss in homogeneity of the pump volume and in efficiency of the absorption over the whole length, when the samples are excessively long. If a high-brightness source such as the erbium-based fiber laser is used, a high depth of focus can be reached and also in relatively long samples a tight focus of the pump beam can be obtained. If low-brightness sources such as diodes are available, a solution for compensation of the high beam divergence, is to barrel-polish the rods and using waveguiding in the crystal in order to have an homogeneous distribution of the pump [Bra11a, Koo12], although the pumped volume is larger than when high-brightness sources are employed.

As outlook of this work, spectroscopic measurements to determine the cross sections of detrimental ESA/ETU at the laser wavelength would clarify which polarization should be addressed to obtain the best laser performance with the same crystals and pump source. Alternatively, the possibility to find most suitable crystal hosts and pump wavelengths could be determined, with a more detailed study of the absorption pump power.

It has to be noticed that not always the incident laser power at the laser threshold was increasing for increasing output coupling and therefore losses. This leads to the conclusion that the coatings of the available mirrors were of different quality, leading to unexpected lower or higher losses.

In one of the experiments performed with the low Er^{3+}-doped $BaYLuF_8$ crystal, one wavelength was characterizing the laser emission at low incident pump powers (1631 nm) and a lower one (1601 nm) at higher incident pump power. This was probably due to thermal effects which can change the population of the upper and lower laser levels. This would induce a modification in the gain cross sections (see Fig. 5.39b relatively to Er^{3+}:BaY_2F_8 spectra, which are expected to be very similar to those for Er^{3+}:$BaYLuF_8$) which for this setup are expected to be at the border between the two different maxima centered at the two different wavelengths, for a change of the inversion levels β from 0.11 to 0.39. Alternatively, a non-flat mirror transmission profile can induce this phenomenon.

Moreover, further investigations concerning Er^{3+}-doped $LiLuF_4$ crystals lasing with addressed σ-polarization can be particularly interesting for LIDAR applications. The wavelengths in the range included in $\lambda = 1609 - 1610$ nm allows for the detection of CO_2 [Bra11a].

The results reported here are the first demonstration of laser operation of Er^{3+}:$BaYLuF_8$ and the first inband-pumped laser operation at 1.6 µm for Er^{3+}:$LiLuF_4$.

Nevertheless, other crystal hosts doped with Er^{3+}-ions can deliver in the same inband-pumped scheme higher output powers and slope efficiencies. With a maximum output power of 2.3 W and a slope efficiency of almost 50% with respect to the absorbed pump power, Er^{3+}:YVO_4 represents an efficient system emitting in the 1.6 µm region, mainly because of much less detrimental ESA/ETU effects [Bra11b]. Er^{3+}:YAG can also deliver efficiently high output power in this spectral range when inband-pumped (43% of optical efficiency has been reached in Q-switched operation with 7 W of maximum output power [You04]). Finally, at cryogenic temperature, a record in slope efficiency of 84% has been established by an Er^{3+}:$GdVO_4$ in cw operation for a maximum output power of 10.3 W [Ter12].

Crystal	Length (mm)	Pol.	λ_{las} (nm)	Resonator	T_{OC}	η_{sl}	$P_{\mathrm{inc,thresh.}}$ (W)	$P_{max,out}$ (W)
1.0% Er^{3+}:$LiLuF_4$ from AL	8.60	π	1620	Z-shaped	0.007	9.1%	0.59	0.60
	8.60	π	1620	Z-shaped	0.013	14.7%	0.60	1.0
	8.60	π	1620	Z-shaped	0.014	16.3%	0.60	1.0
	8.60	π	1620	Z-shaped	0.028	18.7%	0.61	1.24
	8.60	π	1620	Z-shaped	0.098	17.3%	1.30	1.0
	8.60	π	1620	hemisph.	0.013	12.2%	0.75	1.24
	8.60	π	1620	hemisph.	0.028	18.5%	0.80	1.24
1.25% Er^{3+}:$LiLuF_4$ from AC1	12.00	σ	1610	hemisph.	0.013	9.0%	1.00	0.66
	12.00	σ	1610	hemisph.	0.028	13.5%	1.16	0.97
	10.00	π	1619	hemisph.	0.014	11.0%	0.71	0.85
	10.00	π	1619	hemisph.	0.028	17.6%	0.65	1.40
	10.00	π	1619	hemisph.	0.097	18.3%	1.10	1.40
0.5% Er^{3+}:$BaYLuF_8$ AC3	9.80	**x**	1611	hemisph.	0.014	5.2%	1.00	0.41
	8.60	**y**	1631, 1601	hemisph.	0.012	10.0%	0.35	0.84
	8.60	**y**	1601	hemisph.	0.028	12.8%	0.42	1.0
	9.80	**z**	1611	hemisph.	0.014	10.5%	0.50	0.83
	9.80	**z**	1611	hemisph.	0.028	11.2%	0.40	0.93
1.3% Er^{3+}:$BaYLuF_8$ Pi2	13.40	**x**	1612	hemisph.	0.014	4%	1.50	0.30
	13.40	**x**	1612	hemisph.	0.028	4%	1.60	0.46
	13.40	**z**	1612	hemisph.	0.014	6%	1.28	0.46
	13.40	**z**	1612	hemisph.	0.028	8%	2.05	0.54

Table 6.2: Summary of the results of laser experiments at 1.6 µm of wavelength. The results are distinguished by material, dimensions and orientation (polarization) of the crystal, as well as by the emission wavelength, the resonator kind, the total output coupling, the obtained slope efficiency, the incident pump power at the threshold and the maximum output power. The detailed description of every crystal can be found in the Tables A.2 and A.6.

7 Conclusions

7.1 Summary

In the framework of this thesis, Er^{3+}-doped fluoride materials have been grown and spectroscopically investigated to show their potential as upconversion-laser and as lasers in the 1.6-µm spectral range.

The Czochralski crystal growth technique has been successfully applied for three of the host crystals which have been investigated (Er^{3+}:$LiLuF_4$, Er^{3+}:BaY_2F_8, Er^{3+}:KY_3F_{10}). The crystal growth of β-$BaLu_2F_8$ has the fundamental issue of being based on a high-temperature phase transition ensuring the orthorombic structure, preventing the growth of large boules. Concerning Er^{3+}:LaF_3, it has been demonstrated that the seedless cooling down method is efficient in the growth of large high quality samples if the evaporation of the material is impeded and a particularly slow cooling ramp is set over the crystallization range. Nevertheless, the large difference in ionic radii between Er^{3+}- and La^{3+}-ions limits the segregation coefficient of the doping ion in the lattice and the size of the obtainable crystals.

The spectroscopic investigations were mainly focused on the determination of absorption, emission, gain and ESA cross sections. The dynamics of important multiplets has been studied, together with the behavior of the green fluorescence dependence on the incident pump power.

All crystals show the possibility to be excited for single-wavelength upconversion lasers. The dynamic study of the lifetime of the involved multiplets shows the suitability for upconversion lasers, with the exception of the 7% at Er^{3+}-doped $BaLu_2F_8$ which at this doping level suffers from lifetime quenching of the laser emitting $^4S_{3/2}$-multiplet. Er^{3+}:$BaYLuF_8$ has been for the first time spectroscopically investigated.

Er^{3+}:$LiLuF_4$ was determined to be the most suitable material for upconversion lasers. It offers the highest cross sections when π-polarization is addressed, and high $(\sigma_{\mathrm{SE}} - \sigma_{\mathrm{ESA}}) \cdot \sigma_{\mathrm{GSA}}$ and $\sqrt{|(\sigma_{\mathrm{SE}} - \sigma_{\mathrm{ESA}}) \cdot \sigma_{\mathrm{GSA}}|}$ parameters. A very promising crystal is Er^{3+}:BaY_2F_8 in **y**-polarization, which shows very beneficial spectroscopic features for both upconversion pumping and in the 1.6 -µm spectral range.

A study of the decay curve of the important multiplets for the realization of the lasers has been performed. An effective model for the simulation of non-single exponential behaviors has not been found. It has been presumed that weak effects of the interaction between ions of the same kind are present and they could not be correctly treated by the two IH and BZ models. Nevertheless, the inaccuracy of the estimates of the lifetime values has not exceeded the usual 15 - 20% error which this kind of measurements.

None of the proposed theoretical models can thoroughly describe the various aspects of the dynamics of upconversion lasers. For upconversion thin disk lasers, the extreme approximation implemented by the three-level model (the one which can be analytically solved, being based on the quasi-three-level model valid for Yb^{3+}-doped crystals) leads to underestimations of the requirements for reaching the laser threshold for different thicknesses of the disks and diameter of the pump beam.

The need for a high pump intensity in the crystal to reach upconversion laser operation has been demonstrated by experiments with bulk crystals in a four-fold geometry.

Thin disk lasers, with a multi-pass pumping geometry, offer the possibility to increase the amount of effective pump power incident on the crystal. Considering the relatively low estimated absorption efficiency of Er^{3+}:$LiLuF_4$, compared to standard materials for thin disk lasers (e. g. Yb^{3+}-doped materials), thick disks have been used for laser experiments. Decreasing the pump spot diameter on the disks can contribute to the increase of the overall incident intensity. However, the results of the experiments establish a lower limit for the diameter of the spot relative to the thickness of the disks, if a sufficiently homogeneous pumped volume is desired. An upper limit for the pump power which can be applied during the experiments is given by the limited absorption efficiency of the disks. Damage either of the fiber or of the pump source can occur if back-reflections from the HR coating of the disk are coupled back into the fiber. Unfortunately, even if the parameters are within these intervals of applicability, thermal problems mostly due to the ineffective contacting of the disks to the heat sink and the lower thermo-mechanical properties of the fluoride hosts compared to oxides, typical media for thin disk lasers, prevented lasing.

On the other hand, the application of the waveguide geometry, which also allows for high pump intensity in the crystal, gave successful results. The first crystalline green upconversion waveguide laser could be realized in rhombic claddings. With a circular waveguide structure the maximum output power could be increased up to 10 mW, with a slope efficiency of 3% and the internal losses have been drastically reduced to less than 0.5 dB/cm.

Infrared-pumped upconversion laser experiments with bulk crystals have been carried out successfully and compared to a direct-pumping scheme with a pump source emitting in the blue spectral range. Severe problems due to the heat deposited by the blue 2ω-OPSL pump source have affected the results, mostly increasing the incident pump power required to reach the laser threshold. Nevertheless, higher output powers have been achieved with comparable outputcoupling rates than in upconversion experiments. The experiments are not completely comparable because of the employment of a chopper to reduce the heat load in the direct-pumped experiments. However, these preliminary results represent the first demonstration of a visible cw erbium-based directly pumped laser, pumped in the blue spectral range.

Bulk dual-wavelength-pumped upconversion experiments have shown the consequences of different pumping schemes on the output in the green spectral range and have given guidelines for the best pairs of wavelengths to adopt in further investigations for the determination of efficient dual-wavelength upconversion lasers.

Finally, successful inband-pumped laser experiments at 1.6 µm have been carried out with Er^{3+}:$LiLuF_4$ and Er^{3+}:$BaYLuF_8$ samples. Er^{3+}:$LiLuF_4$ has been recognized as the most efficient material in terms of obtained maximum output power (1.40 W) and slope efficiency (19%) at 1620 nm, in π-polarization. Furthermore, laser operation addressing σ-polarization is centered in the range of 1609 - 1610 nm, where LIDAR techniques allow for the detection of CO_2. The first laser operation in Er^{3+}:$BaYLuF_8$ has been demonstrated ($P_{\mathrm{out,max}}$=1 W, η_{sl}= 13%, in **y**-polarization, at 1601 nm) and the first inband-pumped laser operation at 1.6 µm in Er^{3+}:$LiLuF_4$ has been realized.

7.2 Outlook

The research of new fluoride materials for upconversion lasers is still ongoing. Often, the spectroscopic features of these materials are favorable, but not all can allow for laser operation. Therefore, efforts in the improvement of the problematic crystal growth of Er^{3+}:LaF_3 could be redirected towards new crystal hosts, considering the relatively poor spectroscopic features which it has shown.

If room-temperature laser operation is the aim, further laser experiments in bulk samples are meaningful if the spectroscopic features of the crystal are promising enough, compared to the brightness of the available pump sources. For this reason, laser experiments with Er^{3+}:BaY_2F_8 pumped by the infrared OPSL could be the first step.

Concerning the theoretical part of this work, improvements in the interpretation of the dynamics of the non-exponential behavior of the decay of the multiplets can be obtained extending the IH and BZ models so far adopted. The future study should consider the possibility of interionic transitions and be able to distinguish the strength of the interaction.

For a realistic description of the upconversion process, more energy levels and a wider variety of parameters should be involved in the simulations. In particular, more mechanisms which could cause losses should be considered, such as the ESR (Excited State Reabsorption) from the $^4I_{13/2}$-multiplet. Adding the possibility of interionic transitions could be fundamental for the description of the upconversion process also when the Er^{3+}-doping concentration is low. The model describing the upconversion thin disk laser would also benefit from these improvements.

Considering the difficulties encountered in thin-disk-laser experiments, a next possible attempt could be imposing a higher brightness, limiting the spot diameter (e. g. to 800 µm). Furthermore, constant monitoring of the temperature of the disks should be applied. If a suitable metallization process of the disks is not possible, glueing instead of soldering to the heat sink can be an option. The loss in thermal conductivity should not be detrimental at the power regime which the experimental setup allows.

The results of the waveguide-laser experiments represent a proof of principle and a systematic investigation of the structuring parameters for the fs-writing of the tracks has still to be performed. Furthermore, improvements of the resonator can be applied, most of all removing the internal microscope objective, in order to reduce losses. Nevertheless, attention must be paid in the variation of the losses in order to avoid any regime involving laser operation at 850 nm.

Also in the case of the experiments with the 2ω-OPSL operating in the blue spectral range, the reported results represent only a preliminary study. Further improvements can be applied, independent of the comparison study with the corresponding upconversion laser. For example, an efficient cooling system for the crystal is the first requirement which could not be performed. Furthermore, the laser emission wavelength does not correspond to the absorption peak in Er^{3+}:$LiLuF_4$. If the pump wavelength were optimized, the doping concentration could be reduced and, if needed, the length of the crystal increased. Main aims of new experiments would be to reach the laser threshold at lower incident pump power.

Further experiments in dual-wavelength pumping should also set up an appropriate system of cooling of the sample. The most interesting pairs of wavelengths which could be considered are 970 / 790 nm and 1.5 µm / 790 nm. In both cases, dichroic mirrors could be mounted in order to combine the beams and pump the crystal only from one side, for better homogeneity of the pumped volume.

In the 1.6 -µm spectral range, fluoride hosts do not show extremely promising properties, if the interest is power scaling and higher efficiency. Nevertheless, if the aim is to match certain wavelengths e. g. for the detection of gases, the whole variety of crystals involved in this work offers a potential laser host for Er^{3+}-ions in this spectral range and experiments are expected to be successful in terms of obtained laser oscillation.

A Crystals involved in this work

In this appendix chapter all the crystal boules and growth attempts which are involved in this work are summarized, sorted by the kind of host material.

some abbreviations which have been employed are explainable as follows:

- Er^{3+} cont. or Er^{3+} dop. conc. ⇒ content of Er^{3+}-ions in the melt;
- HF/Ar ⇒ amount of HF compared to argon, estimated from a certain amount of H_2 pumped in the chamber with CF_4;
- $t_{cooling}$ or cooling rate ⇒ duration of the cooling time or imposed ramp for cooling indicating a temperature per time;
- $P_{residual}$ ⇒ residual pressure in the chamber before refilling with the chosen gas;
- flow ⇒ flow of gases, indicated in volume per time, as fluorination at high temperature ($T > 500\,^{\circ}C$);
- over-P valve ⇒ valve which ensures a variable overpressure between the inside and the outside of the chamber.

A.1 $LiLuF_4$ crystals

Name - Er^{3+} cont.	Date	Extra LiF	Atmosphere			$t_{cooling}$	Crystal quality and condition	$P_{residual}$ (mbar)	Comment
			CF_4/Ar	HF/Ar	Flow				
A - 1%	02/06/09	No	10%	No	No	$\sim$27 h	Excellent upper part, light scattering lower part	-	Old ErF_3 and LiF, no seed
B - 1%	06/29/09	No	10%	No	No	$\sim$24 h	Half milky, half good clear parts	$7\,\mathrm{x}\,10^{-3}$	Old ErF_3, new LiF, seed
C - 1.3%	11/11/09	No	10%	No	5 l/h	$\sim$50 h	Bottom+center: light scattering, Upper part: excellent	$< 5\,\mathrm{x}\,10^{-4}$	Seed, no over-P valve
D - 1.3%	01/27/10	No	100%	No	9 l/h	Failure[1]	Opaque crystal, Bottom: almost excellent	$< 5\,\mathrm{x}\,10^{-4}$	No seed, no over-P valve
E - 1.3%	02/10/10	+ 4%	100%	No	9 l/h	$\sim$33 h	Opaque crystal, scattering possible	$< 5\,\mathrm{x}\,10^{-4}$	Seed, no over-P valve
F - undoped	02/24/10	+ 4%	100%	No	No	$\sim$48 h	Upper part: excellent Bottom: evident scattering	$< 5\,\mathrm{x}\,10^{-4}$	No seed
G - 1.3%	04/22/10	+ 4%	100%	No	No	$\sim$37 h	Perfect	$2.4\,\mathrm{x}\,10^{-4}$	No seed, new ErF_3
H - 1.3%	05/05/10	+ 4%	15%	No	No	$\sim$25 h	Isolated scattering centers, especially in the upper part	Good	No seed
I - 1.3%	06/01/10	+ 4%	15%	No	No	$\sim$50 h	Isolated scattering centers especially in the upper part	$2.2\,\mathrm{x}\,10^{-4}$	No seed
J - 1.3%	06/17/10	+ 4%	15%	No	10 l/h 3h melting	$\sim$48 h	Fractures but good quality	Good	No seed
K - 1.3%	07/29/10	+ 4%	7%	4%	6 l/h 3h melting	$\sim$7 h	Fractures, half milky, half good clear part	$1.36\,\mathrm{x}\,10^{-4}$	No seed

Table A.1: List of $LiLuF_4$ crystal boules grown by Czochralski method at the ILP facility.

---

[1] An unexpected failure at the generator occured; it was impossible to establish the correct cooling ramp over the set 48 h.

Name	Er^{3+} dop. conc.	Origin	Description
AC1	1.3%	*AC Materials* - USA facility	35 mm-long cylindric boule, $\phi = 20$ mm, c-axis perpendicular to the rotation axis
AC2	1.25%	*AC Materials* - USA facility	$10 \times 10 \times 12\,\mathrm{mm}^3$ oriented sample, 6 laser-quality polished faces
AL	1%	*Altechna* - Lithuania	51 mm-long cylindric boule, $\phi = 10$ mm, c-axis perpendicular to the rotation axis
BÄR	1%	unknown	2.8-mm-thick, oriented, laser quality sample
BÄR2	1%	unknown	1.6-mm-thick, oriented and coated for four-fold resonator
HEU	0.5%	unknown	4.5-mm-thick, oriented and coated for four-fold resonator
HEU2	1%	unknown	0.6-mm-thick, oriented and coated for four-fold resonator
HEU3	0.2%	unknown	0.7-mm-thick, oriented and coated for four-fold resonator
Disk series D1-D5	1.3%	from AC1	2× 800 µm, 700 µm, 600 µm, 500 µm oriented and optically coated for thin-disk-laser experiments, three have a metallization coating on the rear side
Disk series E1-E5	1.3%	from AC1	2× 800 µm, 700 µm, 600 µm, 500 µm similar to D1-D5, but different optical coatings and all have a metallization coating on the rear side

Table A.2: List of $LiLuF_4$ crystals which were not grown at the ILP facility, but nevertheless are involved in this work .

A.2 Other host materials

Name - Er^{3+} cont.	Date	Atmosphere CF_4/N_2	Flow	$t_{cooling}$	Strategy - crystal quality
L - 1.3%	09/03/10	15% (in Ar)	No	~ 82 h 1 ramp	Crucible closed with a lid with a slit, only cooling down - samples for spectroscopy and laser experiments
M - 1.3% failure	10/15/10	100%	No	-	Pulling attempt in closed volume - fallen wire, no samples
N - 2% failure	11/24/10	40%	3 l/h 3 h	-	Pulling attempt in closed volume - impossible contact keeping, no samples
O - 2%	12/06/10	40%	3 l/h 3 h	~ 84 h 1 ramp	Pulling attempt in closed volume - lost contact, slow cooling but many carbon inclusions, bad quality
P - 2.7%	01/11/12	40%	3 l/h 3 h	1st: 1-2 °C/h (48 h) 2nd: to RT in ~ 40 h	Nacken-Kyropoulos growth - many inclusions due to long time growth - poor quality samples

Table A.3: List of Er^{3+}:LaF_3 crystal growth attempts at the ILP facility. The residual pressure before the growth was always the lowest allowed by the setup ($\sim 10^{-4}$ mbar). The insulation to reach high temperatures described in Chapt. 3 has been adopted.

Name - Er^{3+} cont.	Date	Atmosphere CF_4/N_2	HF	Flow	Origin	Crystal description
Q - 1%	02/17/11	8%	5%	15 l/h 4 h	ILP facility	Unoriented boule, diminishing inclusions concentration from neck to bottom
Pi1 - 1%	03/12	Argon			Pisa facility	High-quality oriented sample, 9 mm-long (y-dir.), base = 4×4 mm^2

Table A.4: List of Er^{3+}:BaY_2F_8 crystals in use in the framework of this thesis.

		Atmosphere				
Name - Er^{3+} cont.	Date	CF_4/N_2	HF	Flow	Cooling rate	Description
R - 5.5%	03/02/11	40%	No	No	10 °C/min→ $t_{cooling}$∼ 100 min	Failed Czochralski-growth + fast cooling → small, highly-doped spectroscopic samples

Table A.5: List of the chosen parameters to grow an Er^{3+}:α-$BaLu_2F_8$ crystal.

Name - Er^{3+} cont.	Atmosphere	Origin	Sample description
AC3 - 0.5%	Argon	*AC Materials* - USA facility	High quality crystal, but isolated inclusions - very high quality refractive-index- orientation and polishing on 6 faces - 9.4 × 9.8 × 8.6 mm^3
Pi2 - 1.3%	Argon	Pisa facility	High-quality oriented sample - laser polished on 4 faces - ∼ 4 × 5 × 16 mm^3

Table A.6: List of Er^{3+}:$BaYLuF_8$ samples in use in the framework of this thesis.

		Atmosphere				
Name - Er^{3+} cont.	Date	CF_4/N_2	HF	Flow	Cooling rate	Description
S - 2%	04/19/11	33%	7%	12 l/h ∼ 6 h	∼ 20 °C/h	stress-induced fracture - moderate quality

Table A.7: List of the chosen parameters to grow an Er^{3+}:KY_3F_{10} crystal.

B Characteristics of the host materials

	$LiLuF_4$	LaF_3	BaY_2F_8	α-$BaLu_2F_8$	$BaYLuF_8$	KY_3F_{10}	$LiYF_4$
Lattice	tetr.	hex./trig.	monocl.	orth.	monocl.	cub.	tetr.
Space group	$I4_1/a$	$P\bar{3}c1$	$C2/m$	Pnma		$Fm\bar{3}m$	$I4_1/a$
a [Å]	5.130(1)	7.1907	6.9829(5)	6.904	6.931	11.553(1)	5.164(1)
b [Å]			10.519(1)	8.024	10.452		
c [Å]	10.550(3)	7.3531	4.2644(4)	21.900	4.239		10.741(2)
non stand. β[°]			99.676(8)		99.676(8)		
Coordination number	8	9	8	8	8	8	8
Cation density [$10^{22}\,cm^{-3}$]	1.44	1.83	1.30	1.31	1.32	1.56	1.40
Site Symm.	S_4	C_2	C_2	C_1	C_2	C_{4v}	S_4
Molecules per unit cell	4	6^{**}	2	8	2	8	4
T_{melt} [$°C$]	850	1490	960	940	$\lesssim$1000	1030	819
Melting charact.	congr.	congr.	congr.	high T phase	congr.	congr.	incongr.
Density [$g\,cm^{-3}$]	6.15	5.94	5.01	6.94		4.312	3.98
$E_{Phonon\text{-}cut\text{-}off}$ [cm^{-1}]	< 430	340	415	400	<415 >400	495	458
Refr. index @ 633 nm	1.468 $\parallel \mathbf{c}$ 1.494 $\perp$ $\mathbf{c}$	1.595 $\parallel \mathbf{c}$ 1.602 $\perp$ $\mathbf{c}$	1.5142 $\parallel \mathbf{x}$ 1.5232 $\parallel \mathbf{y}$ 1.5353 $\parallel \mathbf{z}$			1.490	1.476 $\parallel \mathbf{c}$ 1.454 $\perp$ $\mathbf{c}$
Transparency range [µm]	0.13 - 7	0.18 - 12	0.2 - 9.5	0.15 - 11		0.2 - 8.5	0.12 - 8
Mohs hardness	3.5	3.5	4 - 5	4.5		4.5	4 - 5
Thermal conductivity [$W\,m^{-1}\,K^{-1}$]	5.0 $\parallel \mathbf{a}$ 6.3 $\parallel \mathbf{c}$	2.06 $\parallel \mathbf{a}$ 2.56 $\parallel \mathbf{c}$	3.5 $\parallel \mathbf{b}$ 6^{***}	7^{***}		3.5	5.3 $\parallel \mathbf{a}$ 7.2 $\parallel \mathbf{c}$

Table B.1: List of the relevant crystallographic and general intrinsic properties of every kind of host material investigated in this work and compared to the characteristics of $LiYF_4$. Thermal conductivities are given for room temperature. * at 250 K.** in the trigonal cell. *** average value. All references can be found in the following table B.2.

	$LiLuF_4$	LaF_3	BaY_2F_8	α-$BaLu_2F_8$	$BaYLuF_8$	KY_3F_{10}	$LiYF_4$
Lattice	[Gar93]	[Udo08]	[Gui93]	[Tka73]	$\star$	[Grz02]	[Web03]
Space group	[Web03]	[Udo08]	[Gui93]	[Kam98b]	$\star$	[Grz02]	[Web03]
Latt. const. and β	[Ran02b]	[Udo08]	[Gui93]	[Kam98b]	this work	[Grz02]	[Gar93]
Coord. numb.	[Ran02b]	[Udo08]	[Kam90b]	[Wen99]	$\star$	[Hey98]	[Gar93]
Cation density	this work	this work	this work	this work	this work	this work	this work
Site Symm.	[Ran02b]	[Dor00]	[Kam90b]	[Kam96a]	$\star$	[Por76]	[Gar93]
Molecules per unit cell	[Ran02b]	[Udo08]	[Gui93]	[Bli91]	$\star$	[Grz02]	[Gar93]
T_{melt} [$^\circ C$]	[Har83]	[Por62]	[McF94]	[Sob82]	[Ver13]	[Cha93]	[Sha69]
Melting charact.	[Har83]	[Por62]	[McF94]	[Kam96a]	$\star$	[Cha93]	[Tho61]
Density	[Agg05]	[Kle67]	[Agg05]	[Kam96a]		[Web03]	[Agg05]
$E_{\text{Phonon-cut-off}}$	[Sal97]	[Yen64]	[Kam90b]	[Kam96a]	expected	[Mor91]	[Sal97]
Refr. index @ 633 nm	[Web03]	[Web75]	[Web03]			[Por78a]	[Cas75]
Transparency range	[Ran02b]	[Moo66]	[Web03]	[Kam96a]		[Tig01]	[Web03]
Mohs hardness	[Web03]	[Rei13a]	[Kam90b]	[Kam96a]		[Web03]	[Kam93b]
Thermal cond.	[Agg05]	[Rei13b]	[Agg05] [Kam90b]	[Kam96a]		[Pop09]	[Agg05]

Table B.2: List of references regarding Tab. B.1. $\star$ considered as in BaY_2F_8.

C Orientation systems of crystals

This chapter is intended to be a collection of fundamental information about how the optical classification of crystals is comparable to the crystallographic classification. Further notions and interpretations can be found in [McA63, McC09, Nel11, Gun13].

A major part of optics studies the modifications which light undergoes when it enters and then emerges from a body. On this purpose, depending on the variations of the refractive index inside a crystal, it can be classified into two different groups. If the refractive index does not depend on the direction of propagation of light, the crystal is defined isotropic. If there is a dependency of refractive index on the propagation direction, the crystal is anisotropic.

Anisotropic crystals can be subsequently divided in further two groups: uniaxial and biaxial. This definition is referred to the number of optic axes belonging to the crystal: one for uniaxial crystals and two for biaxial crystals. An optic axis is the direction in the crystal in which a ray of transmitted light does not suffer birefringence. If a light beam is not propagating parallel to an optic axis, then it is split into two rays, the ordinary and the extraordinary ray. These two beams are mutually orthogonally polarized.

The crystals which are involved in the framework of this thesis have been classified also following crystallographic rules. In this case, the crystal as periodic structure is described by an infinitely repeatable fundamental cell, which is generated by a set of vectors $\mathbf{a}$, $\mathbf{b}$, $\mathbf{c}$, of length a, b, c.

All the edges a, b and c of the fundamental cell have the same length and the three angles α, β and γ between every pair of them is equal to 90°, it is defined as a cubic crystal. If the fundamental cell has $a = b \neq c$ and $\alpha = \beta = \gamma = 90°$ the crystal belongs to the tetragonal system. If the fundamental cell is characterized by: $a = b \neq c$ and $\alpha = \beta = 90°$; $\gamma = 120°$, the crystal is either hexagonal or trigonal. If the fundamental cell has $a \neq b \neq c$ and $\alpha = \beta = \gamma = 90°$, the crystal is orthorhombic. If the fundamental cell respects: $a \neq b \neq c$ and $\alpha = \beta = 90° \neq \gamma$, the structure belongs to the monoclinic system. Finally, if in the fundamental cell the edge lenghts and the angles are all different, the crystal is defined as triclinic.

For these two classifications, it is possible to find a connection as follows:

- Cubic systems are at the same time the only isotropic structures.
- Hexagonal, trigonal and tetragonal systems possess the **c**-axis as source of anisotropy and it represents also their optic axis, defining them uniaxial crystals.
- Crystal systems with higher levels of anisotropy, such as orthorhombic, monoclinic and triclinic systems, have two optic axes and they are then called biaxial.

In order to understand in a visual way how the refractive index can change in an uniaxial or biaxial structure, the concept of *optical indicatrix* has been introduced. The refractive-index system **x**-**y**-**z** can be interpreted as a tensor because it can generate a three-dimensional space where the vectors are proportional to the refractive-indices x, y, z for light propagating from the central point and vibrating parallel to the vector direction. When the ends of all the possible vectors are connected, a three-dimensional object is defined and it is the optical indicatrix.

In the easiest case of a cubic system (e. g. KY_3F_{10}, see Sect. 4.3.6), the refractive index is homogeneously the same and the indicatrix is a sphere.

For uniaxial crystals (e. g. the tetragonal $LiLuF_4$ or the tysonite structure of LaF_3, see sections 4.3.1 and 4.3.2), the indicatrix is an ellipsoid of rotation because of the variation of the refractive index between a maximum and a minimum. This spheroid can be either oblate, if the largest refractive index is in **a**-direction, or prolate, if the largest refractive index is in **c**-direction. In the case of an orthorhombic structure (e. g. α-$BaLu_2F_8$, see Sect. 4.3.4), the ellipsoid is generated by the tensor **x**-**y**-**z**, where every vector corresponds to the crystallographic vectors **a**-**b**-**c**, respectively.

When the ellipsoid of a monoclinic crystal is analyzed (e. g. BaY_2F_8, see Sect. 4.3.3), the crystallographic **b**-axis coincides with the refractive-index-**y**-axis. The perpendicular planes **x**-**z** and **a**-**c** are also in overlap, but they are mutually rotated of a certain angle along the **y**- (or **b**-) axis.

Finally, for triclinic structures there is no correspondence between any of the axes of the two systems, if not occasionally.

For all the biaxial crystals the optic axes lie in the **x**-**z**-plane (called optic plane) and they are separated by an angle named $2V$ characteristic of every crystal. If V_x and V_z are the angles between one optic axis an the **x**- and **z**-axis, respectively, $2V_x + 2V_z = 180°$ and using the three different refractive indices such as $x < y < z$:

$$\cos(V_z) = \frac{x}{y}\sqrt{\frac{(z+y)(z-y)}{(z+x)(z-x)}}. \tag{C.1}$$

The directions of the optic axes are defined as those perpendicular to the only two circular sections of the indicatrix, with a radius equal to y.

D Main absorption peaks of Er^{3+}:$LiLuF_4$ in the visible spectral range

λ (nm)	σ_{abs} (10^{-21} cm^2)	Polarization	Final energy level $^4I_{15/2} \rightarrow \ldots$
229.9	4.0	π	$^2I_{13/2}$
229.9	0.63	σ	$^2I_{13/2}$
242.9	5.3	π	$^2I_{11/2}$
243.2	1.2	σ	$^2I_{11/2}$
254.2	42.6	π	$^2D_{7/2}$
254.3	15.0	σ	$^2D_{7/2}$
274.9	2.1	π	$^4G_{9/2}$
273.9	1.0	σ	$^4G_{9/2}$
286.3	1.2	π	$^2D_{5/2}$
286.5	0.47	σ	$^2D_{5/2}$
292.5	1.5	π	$^4G_{7/2}$
293.0	0.47	σ	$^4G_{7/2}$
300.7	0.70	π	$^2K_{13/2}$
300.7	0.20	σ	$^2K_{13/2}$
316.0	1.2	π	$^2P_{3/2}$
316.6	0.31	σ	$^2P_{3/2}$
355.1	4.9	π	$^2G_{7/2}$
355.8	2.4	σ	$^2G_{7/2}$
363.2	24.1	π	$^2G_{9/2}$
364.1	5.2	σ	$^2G_{9/2}$
379.2	96.0	π	$^4G_{11/2}$
375.9	28.4	σ	$^4G_{11/2}$
405.7	5.1	π	$^2H_{9/2}$
406.6	2.6	σ	$^2H_{9/2}$
441.4	2.7	π	$^4F_{3/2}$
442.00	1.1	σ	$^4F_{3/2}$
450.0	4.6	π	$^4F_{5/2}$
448.8	3.4	σ	$^4F_{5/2}$
486.4	17.0	π	$^4F_{7/2}$
486.7	11.5	σ	$^4F_{7/2}$
522.6	63.9	π	$^2H_{11/2}$
517.8	20.4	σ	$^2H_{11/2}$
540.7	13.2	π	$^4S_{3/2}$
540.7	3.7	σ	$^4S_{3/2}$
653.2	23.2	π	$^4F_{9/2}$
649.3	12.3	σ	$^4F_{9/2}$
796.3	2.4	π	$^4I_{9/2}$
790.5	0.72	σ	$^4I_{9/2}$

Table D.1: List of cross sections of the main absorption peaks in Er^{3+}:$LiLuF_4$ at room temperature, classified considering the polarization and the recognized transition, starting from the ground level $^4I_{15/2}$.

E Pumping schemes

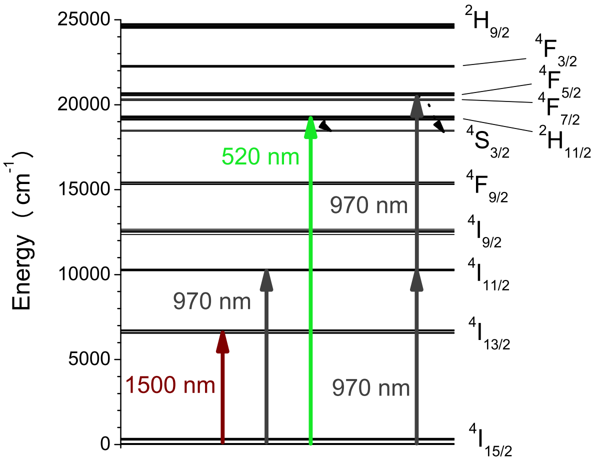

(a) Pumping schemes for the measurements of decay lifetimes in Er^{3+}:$LiLuF_4$ [Kam86] summarized in Chapter 5.

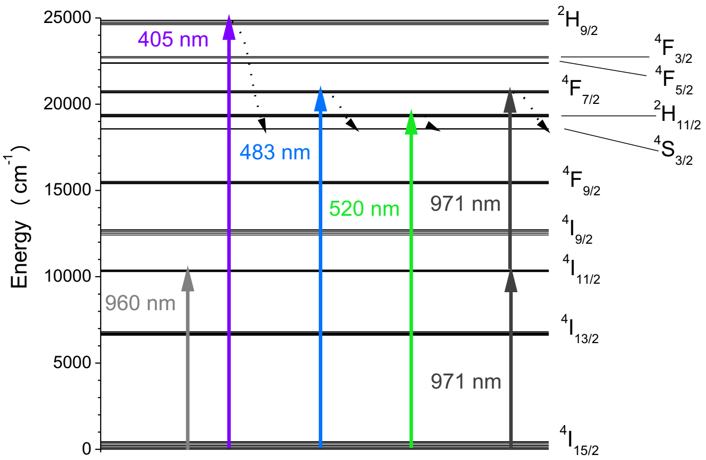

(b) Pumping schemes for the measurements of decay lifetimes in Er^{3+}:LaF_3 [Kru64, Car72, Car86] summarized in Chapter 5.

Figure E.1

F Data for simulations and calculations in Chap. 6

Name	Value	Unit	Wavelength (nm)
σ_{GSA}	2.84	$10^{-21}\mathrm{cm}^2$	974.2
σ_{ESA}	12.6	$10^{-21}\mathrm{cm}^2$	974.2
$\sigma_{\mathrm{em,\ p}}$	2.19	$10^{-21}\mathrm{cm}^2$	974.2
$\sigma_{\mathrm{abs,\ l}}$	1.84	$10^{-21}\mathrm{cm}^2$	551.6
$\sigma_{\mathrm{em,\ l}}$	26.4	$10^{-21}\mathrm{cm}^2$	551.6
τ_{M}	3.4	ms	-
τ_2	0.400	ms	-
τ_{13}	9.7	ms	-
β_{M13}	0.12(*)	-	-
β_{213}	0.28(*)	-	-
β_{2M}	0.02(*)	-	-
$N_{\mathrm{tot}} = N_{\mathrm{doping}}$	1.872	$10^{20}\mathrm{cm}^{-3}$	-
L_{int}	0.005	-	-
T_i	0	-	-

Table F.1: Data for simulation and calculations for upconversion thin disk lasers in Chap. 6. (*) Values taken from [Bär00].

Bibliography

[Abd87a] R. Y. Abdulsabirov, M. A. Dubinskii, N. M. Kazakov, N. I. Silkin, and S. I. Yagudin. Sov. Phys. Crystallogr. **32**, 559 (1987).

[Abd87b] R. Y. Abdulsabirov, A. V. Vinokurov, V. A. Ivanshin, I. N. Kurin, E. A. Pudovik, A. L. Stolov, and S. I. Yagudin. *Optical-spectra and spin-lattice relaxation of rare-earth ions in the* KY_3F_{10} *crystal*. Opt. Spekrosk+ **63**, 97 (1987).

[Abd97] F. Abdoun, A. T. Gaune-Escard, and G. Hatem. *Calorimetric and thermal analysis investigations of the MF-*LaF_3 *mixtures (M = alkali metal)*. J. Phase Equilib. **18**, 6 (1997).

[Abe76] J. S. Abell, I. R. Harris, B. Cockayne, and J. G. Plant. *A DTA study of zone-refined* $LiRF_4$ *(R=Y, Er)*. J. Mater. Sci. **11**, 1807 (1976).

[AF85] E. Antic-Fidancev, M. Lemaitre-Blaise, and P. Porcher. *Energy levels of* Er^{3+} *in* KY_3F_{10}. In: B. Jezowska-Trzebiatowska, J. Lagendzewicz, and W. Strek (editors), *Rare earth spectroscopy - Proc. Int. Symp. Meeting 1984*, 134 (1985).

[Aga13] L. Agazzi, K. Wörhoff, and M. Pollnau. *Energy-Transfer-Upconversion models, their applicability and breakdown in the presence of spectroscopically distinct ion classes: a case study in amorphous* Al_2O_3:Er^{3+}. J. Phys. Chem. C **117**, 6759 (2013).

[Agg05] R. L. Aggarwal, D. J. Ripin, J. R. Ochoa, and T. Y. Fan. *Measurement of thermo-optic properties of* $Y_3Al_5O_{12}$, $Lu_3Al_5O_{12}$, $YAlO_3$, $LiYF_4$, $LiLuF_4$, BaY_2F_8, $KGd(WO_4)_2$, *and* $KY(WO_4)_2$ *laser crystals in the 80-300 K temperature range*. J. Appl. Phys. **98**, 103514 (2005).

[Agn04] A. Agnesi, A. Guandalini, A. Tomaselli, E. Sani, A. Toncelli, and M. Tonelli. *Diode-pumped passively mode-locked and passively stabilized* Nd^{3+}:BaY_2F_8 *laser*. Opt. Lett. **29**, 1638 (2004).

[Ahm12] S. Ahmad, G. V. Prakash, and R. Nagarajan. *Hexagonally ordered* $KLaF_4$ *host: phase-controlled synthesis and luminescence studies*. Inorg. Chem. **51**, 12748 (2012).

[All90] J. Y. Allain, M. Monerie, and H. Poignant. *Room temperature CW tunable green upconversion holmium fibre laser*. Electron. Lett. **26**, 261 (1990).

[Asa66] C. K. Asawa and M. Robinson. *Temperature−dependent concentration quenching of fluorescence by cross relaxation of* Nd^{3+} *in* LaF_3. Phys. Rev. **141**, 251 (1966).

[Ash76] N. W. Ashcroft and N. D. Mermin. *Solid state physics* (Saunders College Publishing, Ithaca, USA, 1976).

[Aul82] B. F. Aull and H. Jenssen. *Vibronic interactions in Nd:YAG resulting in nonreciprocity of absorption and stimulated emission cross sections.* IEEE J. Quantum Elect. **18**, 925 (1982).

[Auz66] F. Auzel and M. A. Kastler. *Electronique quantique - Compteur quantique per transfert d'energie de* Yb^{3+} *a* Tm^{3+} *dans un tungstate mixte et dans un verre germanate.* Cr. Acad. Sci. II B **263**, 819 (1966).

[Auz73] F. Auzel. *Materials and devices using double-pumped-phosphors with energy transfer.* Proc. IEEE **61**, 758 (1973).

[Auz82] F. Auzel, J. Dexpert-Ghys, and C. Gautier. *Minimum ion-ion distance, cross relaxation and excitonic behaviour in* Ln^{3+} *stoichiometric materials.* J. Lumin. **27**, 1 (1982).

[Auz94] F. Auzel, Y. Chen, and D. Meichenin. *Room temperature photon avalanche up-conversion in Er-doped ZBLAN glass.* J. Lumin. **60-61**, 692 (1994).

[Auz95] F. Auzel and Y. Chen. *Photon avalanche luminescence of* Er^{3+} *ions in* $LiYF_4$ *crystal.* J. Lumin. **65**, 45 (1995).

[Auz04] F. Auzel. *Upconversion and anti-Stokes processes with f and d ions in solids.* Chem. Rev. **104**, 139 (2004).

[Bae09] C. R. E. Baer, C. Kränkel, O. H. Heckl, M. Golling, T. Südmeyer, R. Peters, K. Petermann, G. Huber, and U. Keller. *227-fs pulses from a mode-locked* $Yb:LuScO_3$ *thin disk laser.* Opt. Express **17**, 10725 (2009).

[Bai11] Y. Bai, J. Yu, B. Walsh, S. Chen, M. Petros, N. Barnes, U. Singh, A. Cassanho, and H. Jessen. *Spectroscopic properties and 2 micron laser operation of* $Ho:BaYLuF_8$ *crystal.* In: *Advanced Solid-State Photonics*, ATuB4 (Optical Society of America, 2011).

[Bal99] S. L. Baldochi, K. Shimamura, K. Nakano, N. Mujilatu, and T. Fukuda. *Ce-doped* $LiYF_4$ *growth under* CF_4 *atmosphere.* J. Cryst. Growth **205**, 537 (1999).

[Bar86] N. P. Barnes, R. Allen, L. Esterowitz, E. Chicklis, M. Knights, and H. Jenssen. *Operation of an Er:YLF laser at 1.73 μm.* IEEE J. Quantum Elect. **22**, 337 (1986).

[Bar91] N. Barnes and R. E. Allen. *Room temperature Dy:YLF laser operation at 4.34 μm.* IEEE J. Quantum Elect. **27**, 277 (1991).

[Bar93] N. P. Barnes, K. E. Murray, A. Cassanho, K. M. Dinndorf, and H. P. Jenssen. *Flashlamp pumped* $Nd:BaY_2F_8$. In: *Advanced Solid State Lasers (Optical society of America)*, volume 15, 24 (1993).

[Bar98] N. P. Barnes, B. M. Walsh, K. E. Murray, G. J. Quarles, and V. K. Castillo. *Nd:LuLiF operating on the $^4F_{3/2} \rightarrow {}^4I_{11/2}$ and $^4F_{3/2} \rightarrow {}^4I_{13/2}$ transitions.* J. Opt. Soc. Am. B **15**, 2788 (1998).

[Bar05] A. Baraldi, R. Capelletti, M. Mazzera, A. Ponzoni, G. Amoretti, N. Magnani, A. Toncelli, and M. Tonelli. *Role of Er^{3+} concentration in high-resolution spectra of BaY_2F_8 single crystals.* Phys. Rev. B **72**, 075132 (2005).

[Bar12] D. Barlösius (2012). HR coating at ~970 nm of a small substrate for experiments with tapered diode lasers. Institut für Laser Physik -Universität Hamburg, Germany.

[Bei13] K. Beil and F. Moglia. *Estimation of internal losses in Er^{3+}:$LiLuF_4$ in upconversion thin-disk laser experiments as $L_{int} = 0.05$.* (2013). Internal communication - Institut für Laser-Physik - Universität Hamburg, Germany.

[Bel91] R. F. Belt and R. Uhrin. *Top seeded solution growth of Cr^{3+}: $LiCaAlF_6$ in HF atmosphere.* J. Cryst. Growth **109**, 334 (1991).

[Ben01] A. Bensalah, K. Shimamura, V. Sudesh, H. Sato, K. Ito, and T. Fukuda. *Growth of Tm, Ho-codoped $LiYF_4$ and $LiLuF_4$ single crystals for eye-safe lasers.* J. Cryst. Growth **223**, 539 (2001).

[Ben04] A. Bensalah, Y. Guyot, A. Brenier, H. Sato, T. Fukuda, and G. Boulon. *Spectroscopic properties of Yb^{3+}:$LiLuF_4$ crystal grown by the Czochralski method for laser applications and evaluation of quenching processes: a comparison with Yb^{3+}:$LiYF_4$.* J. Alloy. Compd. **380**, 15 (2004).

[Bli91] N. A. Bliznyuk and S. V. Borisov. *Calculation of the similarity index of crystal structures: algorithm, program, and examples.* J. Struct. Chem. **32**, 84 (1991).

[Blo59] N. Bloembergen. *Solid state infrared quantum counters.* Phys. Rev. Lett. **2**, 84 (1959).

[Bor71] M. P. Borzenkova, G. N. Kuznetsova, and A. V. Novoselova. Inorg. Mater+ **7**, 214 (1971).

[Bou99] M. Bouffard, T. Duvaut, J. P. Jouart, N. M. Khaidukov, and M. F. Joubert. *Site-selective upconversion excitation of Er^{3+}:KYF_4.* J. Phys.- Condens. Mat. **11**, 4775 (1999).

[Bou06] E. Boulma, M. Diaf, J. P. Jouart, M. Bouffard, J. L. Doualan, and R. Moncorgé. *Anti-Stokes emissions and determination of Stark sub-level diagram of Er^{3+} ions in KY_3F_{10}.* J. Phys. Condens. Mat. **18**, 6721 (2006).

[Bär00] S. Bär. *Upconversion-Laser und epitaktische Schichten aus Er:$LiLuF_4$.* Diploma thesis, Universität Hamburg (2000).

[Bra00] A. Braud, S. Girard, J. L. Doualan, M. Thuau, R. Moncorgé, and A. M. Tkachuk. *Energy-transfer processes in Yb:Tm-doped KY_3F_{10}, $LiYF_4$ and BaY_2F_8 single crystals for laser operation at 1.5 and 2.3 µm*. Phys. Rev. B **61**, 5280 (2000).

[Bra01] A. Braud, P. Y. Tigreat, J. L. Doualan, and R. Moncorgé. *Spectroscopy and cw operation of a 1.85 µm Tm:KY_3F_{10} laser*. Appl. Phys. B-Lasers O. **72**, 909 (2001).

[Bra11a] C. Brandt. *Charackterrisierung Erbium-dotierter Laserkristalle in Hinblick auf LIDAR-Anwendungen bei 1,6 µm*. Ph.D. thesis, Universität Hamburg - Institut für Laser-Physik, Hamburg (2011).

[Bra11b] C. Brandt, V. Matrosov, K. Petermann, and G. Huber. *In-band fiber-laser-pumped Er:YVO_4 laser emitting around 1.6 µm*. Opt. Lett. **36**, 1188 (2011).

[Bre93a] R. Brede, T. Danger, E. Heumann, G. Huber, and B. Chai. *Room-temperature green laser emission of Er:$LiYF_4$*. Appl. Phys. Lett. **63**, 729 (1993).

[Bre93b] R. Brede, E. Heumann, J. Koetke, T. Danger, G. Huber, and B. Chai. *Green up-conversion laser emission in Er-doped crystals at room temperature*. Appl. Phys. Lett. **63**, 2030 (1993).

[Bri73] J. C. Brice. *The growth of crystals from liquids* (North-Holland Publishing, Amsterdam, 1973).

[Buc96] C. Buchal, T. Siegrist, D. C. Jacobson, and J. M. Poate. *1.5 µm photoluminescence of Er^{3+} in YF_3, LuF_3, and LaF_3 thin films*. Appl. Phys. Lett. **68**, 438 (1996).

[Buk65] G. A. Bukhalova, E. P. Babaeva, and T. M. Khliyan. Russ. J. Inorg. Chem+ **10**, 1158 (1965).

[Bur84] A. I. Burshtein. *Concentration quenching of noncoherent excitation in solutions*. Sov. Phys. Uspekhi **27**, 579 (1984).

[Cac10] D. G. Cacuci. *Handbook of nuclear engineering - nuclear engineering fundamentals* (Springer, 2010).

[Cal10] T. Calmano, J. Siebenmorgen, O. Hellmig, K. Petermann, and G. Huber. *Nd:YAG waveguide laser with 1.3 W output power, fabricated by direct femtosecond laser writing*. Appl. Phys. B-Lasers O. **100**, 131 (2010).

[Cal13] T. Calmano. *Femtosekundenlaser-geschriebene kristalline Wellenleiterlaser im sichtbaren und nahen infraroten Spektralbereich*. Ph.D. thesis, Universität Hamburg - Institut für Laser-Physik (2013).

[Cam04] P. Camy, J. Doualan, S. Renard, A. Braud, V. Ménard, and R. Moncorgé. *Tm^{3+}:CaF_2 for 1.9 µm laser operation*. Opt. Commun. **236**, 395 (2004).

[Cam07] P. Camy, J. L. Doualan, R. Moncorgé, J. Bengoechea, and U. Weichmann. *Diode-pumped* Pr^{3+}*:*KY_3F_{10} *red laser*. Opt. Lett. **32**, 1462 (2007).

[Car72] W. T. Carnall, P. R. Fields, and R. Sarup. *Optical absorption spectra of* Er^{3+}*:*LaF_3 *and* $ErCl_3 \cdot 6H_2O$. J. Chem. Phys. **57**, 43 (1972).

[Car74] W. Carl. AB_2F_7 *phases in the systems AF-*BF_7 *(A = K, Rb, Cs, Tl; B = In, Tl, Ln)*. Mater. Res. Bull. **9**, 1337 (1974).

[Car79] P. Caro and P. Porcher. *Infra-red excitation of visible luminescence in upconverters rare earth materials.* J. Lumin. **18–19**, 257 (1979).

[Car86] W. Carnall, G. Goodman, R. Rana, P. Vandevelde, L. Fluyt, and C. Görller-Walrand. *Crystal-field analysis of* Ho^{3+}*:*LaF_3 *and* Er^{3+}*:*LaF_3 *in* C_{2v} *site symmetry.* J. Less-Common Met. **116**, 17 (1986).

[Cas64] H. H. Caspers, R. A. Buchanan, and H. R. Marlin. *Lattice Vibrations of* LaF_3. J. Chem. Phys. **41**, 94 (1964).

[Cas75] D. E. Castleberry and A. Linz. *Measurement of the refractive indices of* $LiYF_4$. Appl. Opt. **14**, 2056 (1975).

[Cha93] B. H. T. Chai, J. Lefaucheur, A.-T.Pham, G. B. Loutts, and J. F. Nicholls. *Growth of high-quality single crystals of* KYF_4 *by TSSG method.* Proc. SPIE **1863**, 131 (1993).

[Chi71] E. P. Chicklis, C. S. Naiman, R. C. Folweiler, D. R. Gabbe, H. P. Jenssen, and A. Linz. *High-efficiency room-temperature 2.06-µm laser using sensitized* Ho^{3+}*:YLF*. Appl. Phys. Lett. **19**, 119 (1971).

[Chi72] E. Chicklis, C. Naiman, R. Folweiler, and J. Doherty. *Stimulated emission in multiply doped* Ho^{3+}*:YLF and YAG - A comparison.* IEEE J. Quantum Elect. **8**, 225 (1972).

[Chi79] J. S. Chivian, W. E. Case, and D. D. Eden. *The photon avalanche: A new phenomenon in* Pr^{3+}*-based infrared quantum counters.* Appl. Phys. Lett. **35** (2), 124 (1979).

[Coc81] B. Cockayne, J. Plant, and R. Clay. *The Czochralski growth and laser characteristics of Li(Y, Er, Tm, Ho)* F_4 *and Li(Lu, Er, Tm, Ho)* F_4 *scheelite single crystals.* J. Cryst. Growth **54**, 407 (1981).

[Coh68] E. Cohen, L. A. Riseberg, and H. W. Moos. *Effective density of phonon states for* $NdCl_3$ *from vibronic spectra and applications to ion-lattice interactions.* Phys. Rev. **175**, 521 (1968).

[Coh11] Coherent. *Evolution - q-switched Nd:YLF green pump lasers.* Data sheet, Coherent, Inc. (2011).

[Col06a] N. Coluccelli, G. Galzerano, P. Laporta, D. Parisi, A. Toncelli, and M. Tonelli. *Room-temperature Q-switched Tm:Ba*Y_2F_8 *laser pumped by CW diode laser*. Opt. Express **14**, 1518 (2006).

[Col06b] N. Coluccelli, D. Gatti, G. Galzerano, F. Cornacchia, D. Parisi, A. Toncelli, M. Tonelli, and P. Laporta. *Tunability range of 245 nm in a diode-pumped Tm:Ba*Y_2F_8 *laser at 1.9 μm: a theoretical and experimental investigation*. Appl. Phys. B-Lasers O. **85**, 553 (2006).

[Cor02] F. Cornacchia, E. Sani, A. Toncelli, M. Tonelli, M. Marano, S. Taccheo, G. Galzerano, and P. Laporta. *Optical spectroscopy and diode-pumped laser characteristics of codoped Tm-Ho:YLF and Tm-Ho:BaYF - a comparative analysis*. Appl. Phys. B-Lasers O. **75**, 817 (2002).

[Cor09] F. Cornacchia, A. Toncelli, and M. Tonelli. *Lasers with fluoride crystals: research and development*. Prog. Quant. Electron. **33**, 61 (2009).

[Cou04] D. W. Coutts and A. J. S. McGonigle. *Cerium-doped fluoride lasers*. IEEE J. Quantum Elect. **40**, 1430 (2004).

[Czo18] J. Czochralski. *Ein neues Verfahren zur Messung der Kristallisationsgeschwindigkeit der Metalle*. Z. Phys. Chem. **92**, 219 (1918).

[Dan93] T. Danger, K. Petermann, and G. Huber. *Polarized and time-resolved measurements of excited-state absorption and stimulated emission in Ti:*$YAlO_3$ *and Ti:*Al_2O_3. Appl. Phys. A-Mater **57**, 309 (1993).

[Das11] S. Das, A. A. Reddy, S. Ahmad, R. Nagarajan, and G. V. Prakash. *Synthesis and optical characterization of strong red light emitting* $KLaF_4$*:*Eu^{3+} *nanophosphors*. Chem. Phys. Lett. **508**, 117 (2011).

[Dav96] K. M. Davis, K. Miura, N. Sugimoto, and K. Hirao. *Writing waveguides in glass with a femtosecond laser*. Opt. Lett. **21**, 1729 (1996).

[Den91] A. R. Denton and N. W. Ashcroft. *Vegard's law*. Phys. Rev. A **43**, 3161 (1991).

[Der48] E. P. Dergunov. Doklady Akad. Nauk. SSSR **60**, 1185 (1948).

[deR66] C. deRango, G. Tsoucaris, and C. Zelwer. *Determination de la structure du fluorure de Lanthane* LaF_3. C.R. Acad. Sci. II C **263**, 64 (1966).

[Dex53] D. L. Dexter. *A theory of sensitized luminescence in solids*. J. Chem. Phys. **21**, 836 (1953).

[Di 74] B. Di Bortolo (editor). *Optical properties of ions in solids* (Plenum Press, Erice, 1974).

[Dia03] M. Diaf, E. Boulma, and Z. Chouahda. *Synthesis and optical properties of* KY_3F_{10} *laser material doped with rare earth ions (erbium:* Er^{3+}*)*. In: *SPIE Porceedings -Photonic crystals and photonic bandgap structures*, volume 5036 of *Photonics, devices, and systems II*, 419 (2003).

[Die63] G. H. Dieke and H. M. Crosswhite. *The spectra of the doubly and triply ionized rare earths*. Appl. Opt. **2**, 675 (1963).

[Die98] A. Diening, P. E.-A. Möbert, E. Heumann, G. Huber, and B. H. T. Chai. *Diode-pumped cw lasing of Yb, Ho:KYF$_4$ in the 3 µm spectral range in comparison to Er:KYF$_4$*. Laser Phys. **8**, 214 (1998).

[Din92] K. M. Dinndorf, D. S. Knowles, M. Gojer, C. J. Taylor, and H. P. Jenssen. *Principal axes for transitions in monoclinic crystals*. In: *OSA Proceedings on Advanced solid-State Lasers*, volume 13, 270 (1992).

[Don12] Y. Dong, S. T. Li, and X. H. Zhang. *All-solid-state blue laser pumped Pr:KY$_3$F$_{10}$-BBO ultraviolet laser at 305 nm*. Laser Phys. Lett. **9**, 116 (2012).

[Dor80] H. Dornauf and J. Heber. *Concentration-dependent fluorescence-quenching in La$_{1\text{-}x}$Pr$_x$P$_5$O$_{14}$*. J. Lumin. **22** (1), 1 (1980).

[Dor90] P. Dorenbos, C. W. E. van Eijk, R. W. Hollander, and P. Schotanus. *Scintillation properties of Nd^{3+} doped LaF$_3$ crystals*. IEEE T. Nucl. Sci. **37**, 119 (1990).

[Dor00] P. Dorenbos. *5d-level energies of Ce^{3+} and the crystalline environment. I. Fluoride compounds*. Phys. Rev. B **62**, 15640 (2000).

[Dou98] T. J. Dougherty, C. J. Gomer, B. W. Henderson, G. Jori, D. Kessel, M. Korbelik, J. Moan, and Q. Peng. *Photodynamic Therapy*. J. Natl. Cancer I. **90**, 889 (1998).

[Dou03] J.-L. Doualan and R. Moncorge. *Laser crystals with low phonon frequencies*. Ann. Chim. Sci. Mat. **28**, 5 (2003).

[Dub90] M. A. Dubinskii, N. M. Khaidukov, I. G. Garipov, L. N. Dem'Yanets, A. K. Naumov, V. V. Semashko, and V. A. Malyusov. *Spectral-kinetic and lasing characteristics of new Nd^{3+}-activated laser hosts of the KF-YF$_3$ system*. J. Mod. Optic. **37**, 1355 (1990).

[Dub93] M. A. Dubinskii, V. V. Semashko, A. K. Naumov, R. Y. Abdulsabirov, and S. L. Korableva. *Ce^{3+}-doped colquiriite*. J. Mod. Optic. **40**, 1 (1993).

[Dub94] M. A. Dubinskii, V. V. Semashko, A. K. Naumov, R. Y. Abdulsabirov, and S. L. Korableva. *A new active medium for a tunable solid-state UV laser with an excimer pump*. Laser Phys. **4**, 480 (1994).

[Ehr80] D. J. Ehrlich, P. F. Moulton, and J. R. M. Osgood. *Optically pumped Ce:LaF$_3$ laser at 286 nm*. Opt. Lett. **5**, 339 (1980).

[Ein16] A. Einstein. *Zur Quantentheorie der Strahlung*. Physikalische Gesellschaft Zürich **18**, 47 (1916).

[Eli73] L. R. Elias, W. S. Heaps, and W. M. Yen. *Excitation of uv fluorescence in* LaF_3 *doped with trivalent cerium and praseodymium.* Phys. Rev. B **8**, 4989 (1973).

[Est77] L. Esterowitz, R. Allen, M. Kruer, F. Bartoli, L. S. Goldberg, H. P. Jenssen, A. Linz, and V. O. Nicolai. *Blue light emission by a Pr:*$LiYF_4$*-laser operated at room temperature.* J. Appl. Phys. **48**, 650 (1977).

[Est90] L. Esterowitz, R. C. Stoneman, and R. F. Bonner. *Trivalent thulium laser at 1.95 μm for enhanced laser-tissue interactions.* SPIE Proc. Ser. **1202**, 175 (1990).

[Fan88] T. Y. Fan, G. Huber, R. L. Byer, and P. Mitzscherlich. *Spectroscopy and diode laser-pumped operation of Tm,Ho:YAG.* IEEE J. Quantum Elect. **24**, 924 (1988).

[Fan89] T. Y. Fan and M. R. Kokta. *End-pumped Nd:*LaF_3 *and Nd:*$LaMgAl_{11}O_{19}$ *lasers.* IEEE J. Quantum Elect. **25**, 1845 (1989).

[Fie08] C. Fiebig, G. Blume, C. Kaspari, D. Feise, J. Fricke, M. Matalla, W. John, H. Wenzel, K. Paschke, and G. Erbert. *12 W high-brightness single-frequency DBR tapered diode laser.* Electron. Lett. **44**, 1253 (2008).

[Fie11] C. Fiebig, K. Paschke, and G. Erbert (2011). Collaboration in the framework of experiments with DBR tapered diode lasers - Ferdinand-Braun-Institut, Berlin, Germany.

[Fil94] E. D. Filer, C. A. Morrison, N. P. Barnes, and B. M. Walsh. *YLF isomorphs for Ho and Tm laser applications.* In: *Advanced Solid State Lasers (ASSL)*, HL7 (Optical Society of America, 1994).

[Fon76] C. Y. Fong, W. Weber, and J. C. Phillips. *Violation of Vegard's law in covalent semiconductor alloys.* Phys. Rev. B **14**, 5387 (1976).

[För48] T. Förster. *Zwischenmolekulare Energiewanderung und Fluoreszenz.* Ann. Phys-Berlin **437**, 55 (1948).

[För49] T. Förster. *Experimentelle und theoretische Untersuchung den zwischenmolekularen Übergangs von Elektronenanregungsenergie.* Z. Naturforsch. **4**, 321 (1949).

[Fre11] S. T. Fredrich-Thornton, K. Beil, C. Kränkel, K. Petermann, D. Parisi, M. Tonelli, and G. Huber. *Yb:YLF as active medium in the thin disk laser.* In: *CLEO:2011 - Laser Applications to Photonic Applications*, CWP7 (Optical Society of America, 2011).

[Fuk10] K. Fukuda, N. Kawaguchi, S. Ishizu, T. Yanagida, T. Suyama, M. Nikl, and A. Yoshikawa. *Crystal growth and scintillation characteristics of the* Nd^{3+}*-doped* LaF_3 *single crystal.* Opt. Mater. **32**, 1142 (2010).

[Gab68] D. Gabbe and A. Harmer. *Scheelite structure fluorides: the growth of pure and rare earth doped* $LiYF_4$. J. Cryst. Growth **3-4**, 544 (1968).

[Gal04a] G. Galzerano, E. Sani, A. Toncelli, S. Taccheo, M. Tonelli, and P. Laporta. *Experimental investigation of the 2.1-µm single-mode Tm-Ho:KYF laser*. Appl. Phys. B-Lasers O. **78**, 733 (2004).

[Gal04b] G. Galzerano, E. Sani, A. Toncelli, G. D. Valle, S. Taccheo, M. Tonelli, and P. Laporta. *Widely tunable continuous-wave diode-pumped 2-µm Tm-Ho:KYF$_4$ laser*. Opt. Lett. **29**, 715 (2004).

[Gam01] D. R. Gamelin and H. U. Gudel. *Upconversion processes in transition metal and rare earth metal systems*. In: H. Yersin (editor), *Transition Metal and Rare Earth Compounds*, volume 214 of *Topics in Current Chemistry*, 1–56 (Springer Berlin Heidelberg, 2001).

[Gar93] E. Garcia and R. R. Ryan. *Structure of the laser host material LiYF$_4$*. Acta Crystallogr. C **49**, 2053 (1993).

[Gar05] D. Garbuzov, I. Kudryashov, and M. Dubinskii. *110 W (0.9 J) pulsed power from resonantly diode-laser-pumped 1.6-µm Er:YAG laser*. Appl. Phys. Lett. **87**, 121101 (2005).

[Gat07] D. Gatti, G. Galzerano, A. Toncelli, M. Tonelli, and P. Laporta. *Actively mode-locked Tm-Ho:LiYF$_4$ and Tm-Ho:BaY$_2$F$_8$ lasers*. Appl. Phys. B-Lasers O. **86**, 269 (2007).

[Gäb98] K. M. Gäbel, P. Rußbüldt, R. Lebert, and A. Valster. *Diode pumped Cr^{3+}:LiCaF fs-laser*. P. Soc. Photo-Opt. Ins. **157**, 327 (1998).

[Gie94] A. Giesen, H. Hügel, A. Voss, K. Wittig, U. Brauch, and H. Opower. *Scalable concept for diode-pumped high-power solid-state lasers*. Appl. Phys. B-Lasers O. **58**, 365 (1994).

[Gil91] S. L. Gilbert. *Frequency stabilization of a tunable erbium-doped fiber laser*. Opt. Lett. **16**, 150 (1991).

[Gün11a] T. Gün, P. Metz, and G. Huber. *Efficient continuous wave deep ultraviolet Pr^{3+}:LiYF$_4$ laser at 261.3 nm*. Appl. Phys. Lett. **99**, 181103 (2011).

[Gün11b] T. Gün, P. Metz, and G. Huber. *Power scaling of laser diode pumped Pr^{3+}:LiYF$_4$ cw lasers: efficient laser operation at 522.6 nm, 545.9 nm, 607.2 nm, and 639.5 nm*. Opt. Lett. **36**, 1002 (2011).

[Gos00] T. R. Gosnell (editor). *Selected papers on upconversion lasers*, SPIE Milestone Series (B. J. Thompson, 2000).

[Gra71] W. J. C. Grant. *Role of rate equations in the theory of luminescent energy transfer*. Phys. Rev. B **4**, 648 (1971).

[Gre81] O. Greis, P. Stede, and M. Kieser. *Darstellung und Eigenschaften der Ternären Verbindungen BaSE$_2$F$_2$ mit SE = Dy - Lu und Y*. Z. Anorg. Allg. Chem. **477**, 133 (1981).

[Gre83] D. Gregson, C. R. A. Catlow, A. V. Chadwick, G. H. Lander, A. N. Cormack, and B. E. F. Fender. *The structure of* LaF_3*- a single-crystal neutron diffraction study at room temperature.* Acta Crystallogr. B **39**, 687 (1983).

[Gro03] C. P. Groen, A. Oskam, and A. Kovács. *Theoretical study of mixed* $MLaX_4$ *(M = Na, K, Cs; X = F, Cl, Br, I) rare earth/alkali metal halide complexes.* Inorg. Chem. **42**, 851 (2003).

[Grz02] A. Grzechnik, J. Nuss, K. Friese, J. Y. Gesland, and M. Jansen. *Refinement of the crystal structure of potassium tryittrium decafluoride,* KY_3F_{10}. Z. Crystallogr. **217**, 460 (2002).

[Gue01] K. Guedes, K. Krambrock, and J. Gesland. *Gadolinium in lutetium fluoride - an electron paramagnetic resonance study.* J. Phys. Chem. Solids **62**, 485 (2001).

[Gug61] H. Guggenheim. *Growth of single-crystal calcium fluoride with rare-earth impurities.* J. Appl. Phys. **32**, 1337 (1961).

[Gug63] H. Guggenheim. *Growth of highly perfect fluoride single crystals for optical masers.* J. Appl. Phys. **34**, 2482 (1963).

[Gug69] H. J. Guggenheim and L. F. Johnson. *New fluoride compounds for efficient infrared-to-visible conversion.* Appl. Phys. Lett. **15**, 51 (1969).

[Gui93] L. Guilbert, J. Gesland, A. Bulou, and R. Retoux. *Structure and raman spectroscopy of Czochralski-grown barium yttrium and barium ytterbium fluorides crystals.* Mater. Res. Bull. **28**, 923 (1993).

[Gun13] M. E. Gunter. *Optical mineralogy.* online published (2013). Http://www.webpages.uidaho.edu/mgunter/opt_min/article.pdf.

[Gus06] M. A. Gusowski, A. Gagor, M. Trzebiatowska-Gusowska, and W. Ryba-Romanowski. *Crystal structure and vibrational properties of new luminescent hosts* K_3YF_6 *and* K_3GdF_6. J. Solid State Chem. **179**, 3145 (2006).

[Guy97] S. Guy, M. F. Joubert, and B. Jacquier. *Photon avalanche and the mean-field approximation.* Phys. Rev. B **55**, 8240 (1997).

[Han88] D. C. Hanna, I. M. Jauncey, R. M. Percival, I. R. Perry, R. G. Smart, P. J. Suni, J. E. Townsend, and A. C. Tropper. *Continuous-wave oscillation of a monomode thulium-doped fibre laser.* Electron. Lett. **24**, 1222 (1988).

[Har83] I. R. Harris, H. Safi, N. A. Smith, M. Altunbas, B. Cockayne, and J. G. Plant. *The relationship between crystal growth behaviour and constitution in the systems LiF-*LuF_3*, LiF-*ErF_3 *and LiF-*YF_3. J. Mater. Sci. **18**, 1235 (1983).

[Hea76] W. S. Heaps, L. R. Elias, and W. M. Yen. *Vacuum-ultraviolet absorption bands of trivalent lanthanides in* LaF_3. Phys. Rev. B **13**, 94 (1976).

[Heb73] C. Hebecker. *Neue ternäre Fluoride der Lanthaniden vom Typ KMeF$_4$*. Naturwissenschaften **60**, 518 (1973).

[Heb90] T. Hebert, R. Wannemacher, W. Lenth, and R. M. McFarlane. *Blue and green cw upconversion lasing in Er:LiYF$_4$*. Appl. Phys. Lett. **57**, 1727 (1990).

[Heb92] T. Hebert, R. Wannemacher, R. M. MacFarlane, and W. Lenth. *Blue continuously pumped upconversion lasing in Tm:LiYF$_4$*. Appl. Phys. Lett. **60**, 2592 (1992).

[Hei94] F. Heine, E. Heumann, T. Danger, T. Schweizer, G. Huber, and B. Chai. *Green upconversion continuous wave Er^{3+}:LiYF$_4$ laser at room temperature*. Appl. Phys. Lett. **65**, 383 (1994).

[Heu96] E. Heumann, P. Möbert, and G. Huber. *Intracavity frequency doubled Yb, Er:LiYF$_4$ upconversion pumped laser at 617 nm*. Exp. Tech. Phys. **42**, 33 (1996).

[Heu02a] E. Heumann, S. Bär, H. Kretschmann, and G. Huber. *Diode-pumped continuous-wave green upconversion lasing of Er^{3+}:LiLuF$_4$ using multipass pumping*. Opt. Lett. **27**, 1699 (2002).

[Heu02b] E. Heumann, S. Bär, H. Kretschmann, and G. Huber. *Diode pumped cw green upconversion lasing of Er^{3+}: LiLuF$_4$ at room temperature under multipass pumping*. In: *Lasers and Electro-Optics, 2002.Techincal Digest. (CLEO 2002)* (2002).

[Heu06] E. Heumann, S. Bär, K. Rademaker, G. Huber, S. Butterworth, A. Diening, and W. Seelert. *Semiconductor-laser-pumped high-power upconversion laser*. Appl. Phys. Lett. **88**, 061108 (2006).

[Heu12] A. Heuer. *OPS pumping of ytterbium-doped laser crystals*. Bachelor thesis, Universität Hamburg - Institut für Laser-Physik (2012).

[Hey98] K. Heyde, K. Binnemans, and C. Gorller-Walrand. *Spectroscopic properties of KY$_3$F$_{10}$:Er^{3+}*. J. Chem. Soc. Faraday T. **94**, 1671 (1998).

[Hüf78] S. Hüfner. *Optical spectra of transparent rare earth compounds* (Academic Press, New York, 1978).

[Hän99] T. W. Hänsch and H. Walther. *Laser spectroscopy and quantum optics*. Rev. Mod. Phys. **71**, S242 (1999).

[HTW06] HTW Hochtemperatur-Werkstoffe GmbH. *High temperature applications*. Data sheet, HTW Hochtemperatur-Werkstoffe GmbH for glassy carbon SIGRADUR, http://www.htw-germany.com/applications.php5?lang=en&nav0=4&nav1=1 (2006).

[Hua50] K. Huang and A. Rhys. *Theory of light absorption and non-radiative transitions in F-centres.* Proceedings of the Royal Society of London. Series A. Mathematical and Physical Sciences **204**, 406 (1950).

[Hub75] G. Huber, W. W. Kruhler, W. Bludau, and H. G. Danielmeyer. *Anisotropy in the laser performance of* NdP_5O_{14}. J. Appl. Phys. **46**, 3580 (1975).

[Hub99] G. Huber. *Advances in lasers and applications*, chapter Visible cw solid-state lasers, 19–38 (Scottish Universities Summer School in Physics and Institute of physics publishing, Bristol, 1999).

[Hub10] G. Huber, C. Kränkel, and K. Petermann. *Solid-state lasers: status and future (Invited).* J. Opt. Soc. Am. B **27**, B93 (2010).

[Ino65] M. Inokuti and F. Hirayama. *Influence of energy transfer by the exchange mechanism on donor luminescence.* J. Chem. Phys. **43**, 1978 (1965).

[Jac07] K. T. Jacob, S. Raj, and L. Rannesh. *Vegard's law: a fundamental relation or an approximation?.* Int J. Mater. Res. **9**, 776 (2007).

[Jan97] M. G. Jani, N. P. Barnes, K. E. Murray, D. W. Hart, G. J. Quarles, and V. K. Castillo. *Diode-pumped Ho:Tm:*$LiLuF_4$ *laser at room temperature.* IEEE J.Quantum Elect. **33**, 112 (1997).

[Jen96] T. Jensen, A. Diening, G. Huber, and B. H. T. Chai. *Investigation of diode-pumped 2.8-μm Er:*$LiYF_4$ *lasers with various doping levels.* Opt. Lett. **21**, 585 (1996).

[Jen06] H. P. Jenssen and A. Cassanho. *Fluroide laser crystals: old and new.* In: *Proc. SPIE 6100, Solid State Lasers XV: Technology and Devices.* (2006).

[Joh71] L. F. Johnson and H. J. Guggenheim. *Infrared-pumped visible laser.* Appl. Phys. Lett. **19**, 44 (1971).

[Joh72] L. F. Johnson and H. J. Guggenheim. *New laser lines in the visible from* Er^{3+} *ions in* BaY_2F_8. Appl. Phys. L **20**, 474 (1972).

[Jon68] D. Jones and W. Shand. *Crystal growth of flourides in the lanthanide series.* J. Cryst. Growth **2**, 361 (1968).

[Jon75] D. Jones, B. Cockayne, R. Clay, and P. Forrester. *Stockbarger crystal growth, optical assessment and laser performance of holmium-doped yttrium erbium lithium fluoride.* J. Cryst. Growth **30**, 21 (1975).

[Jou99] M. F. Joubert. *Photon avalanche upconversion in rare earth laser materials.* Opt. Mater. **11**, 181 (1999).

[Jou01] M. Joubert, Y. Guyot, B. Jacquier, J. Chaminade, and A. Garcia. *Fluoride crystals and high lying excited states of rare earth ions.* J. Fluorine Chem. **107**, 235 (2001).

[Jou03] M. Joubert and R. Moncorgé. *Rare-earth doped crystals for UV tunable solid state lasers.* Opt. Mater. **22**, 95 (2003).

[Jud62] B. R. Judd. *Optical absorption intensities of rare-earth ions.* Phys. Rev. **127**, 750 (1962).

[Kam83] A. A. Kaminskii and B. N. Sobolev. Inorg. Mater+ **19**, 1947 (1983).

[Kam86] A. A. Kaminskii. *Stimulated emission spectroscopy of* Ln^{3+} *ions in tetragonal* $LiLuF_4$ *fluoride.* Phys. Status Solidi A **97**, K53 (1986).

[Kam90a] A. A. Kaminskii. *Laser crystals* (Springer Verlag Berlin, Heidelberg, New York, 1990).

[Kam90b] A. A. Kaminskii, S. E. Sarkisov, F. Below, and H.-J. Eichler. *Spectroscopic and laser properties of* Er^{3+}*-doped monoclinic* BaY_2F_8 *single crystals.* Opt. Quant. Electron. **22**, S95 (1990).

[Kam93a] A. A. Kaminskii. *New room-temperature diode-laser-pumped efficient quasi-CW and CW single-mode laser based on monoclinic* BaY_2F_8:Nd^{3+} *crystal.* Phys. Status Solidi A **137**, K61 (1993).

[Kam93b] A. A. Kaminskii, H. J. Eichler, B. Liu, and P. Meindl. $LiYF_4$:Pr^{3+} *laser at 639.5 nm with 30 J flashlamp pumping and 87 mJ output energy.* Phys. Status Solidi A **138**, K45 (1993).

[Kam96a] A. A. Kaminskii and A. V. Butashin. $BaLu_2F_8$*- A new crystal-host for lasing* Ln^{3+} *ions.* Phys. Status Solidi A **157**, K29 (1996).

[Kam96b] A. A. Kaminskii, A. V. Butashin, H. J. Eichler, A. Grebe, and R. Macdonald. *New fluoride crystal* $BaLu_2F_8$:Nd^{3+} *for diode pumped lasers.* Phys. Status Solidi A **158**, K31 (1996).

[Kam98a] A. Kaminskii, A. Butashin, J. Hulliger, P. Egger, S. Bagayev, H. Eichler, J. Findeisen, B. Liu, U. Täuber, P. Peuser, and S. Sulyanov. *New anisotropic rare earth fluorides* BaR_2F_8 *(R=Y, Dy-Lu): growth and characterization.* J. Alloy. Compd. **275-277**, 442 (1998).

[Kam98b] A. A. Kaminskii, A. V. Butashin, S. N. Bagaev, H. Eichler, J. Findeisen, U. Tauber, and B. Liu. *Three-micron cw stimulated emission from a new* Er^{3+}:$BaLu_2F_8$ *laser crystal subjected to laser-diode pumping.* Quantum Electron. **28**, 93 (1998).

[Kaw01] J. Kawanaka, H. Nishioka, N. Inoue, and K. Ueda. *Tunable continuous-wave Yb:YLF laser operation with a diode-pumped chirped-pulse amplification system.* Appl. Optics **40**, 3542 (2001).

[Küc98] S. Kück, L. Fornasiero, E. Mix, and G. Huber. *Excited state absorption and stimulated emission of* Nd^{3+} *in crystals. Part I:* $Y_3Al_5O_{12}$*,* $YAlO_3$*, and* Y_2O_3*.* Appl. Phys. B-Lasers O. **67**, 151 (1998).

[Ken02] A. J. Kenyon. *Recent developments in rare-earth doped materials for optoelectronics.* Prog. Quant. Electron. **26**, 225 (2002).

[Küh07] H. Kühn, S. T. Fredrich-Thornton, C. Kränkel, R. Peters, and K. Petermann. *Model for the calculation of radiation trapping and description of the pinhole method.* Opt. Lett. **32**, 143 (2007).

[Kim07] K. J. Kim, A. Jouini, A. Yoshikawa, R. Simura, G. Boulon, and T. Fukuda. *Growth and optical properties of Pr,Yb-codoped* KY_3F_{10} *fluoride single crystals for up-conversion visible luminescence.* J. Cryst. Growth **299**, 171 (2007).

[Kin87] G. J. Kintz, R. Allen, and L. Esterowitz. *cw and pulsed 2.8* μm *laser emission from diode-pumped* Er^{3+}*:*$LiYF_4$ *at room temperature.* Appl. Phys. Lett. **50**, 1553 (1987).

[Kis06] V. E. Kisel, N. A. Tolstik, A. E. Troshin, N. V. Kuleshov, V. N. Matrosov, T. A. Matrosova, M. I. Kupchenko, F. Brunner, R. Paschotta, F. Morier-Genoud, and U. Keller. *Spectroscopy and femtosecond laser performance of* Yb^{3+}*:*$Gd_{0.64}Y_{0.36}VO_4$ *crystal.* Appl. Phys. B-Lasers O. **85**, 581 (2006).

[Kle67] P. H. Klein and W. J. Croft. *Thermal conductivity, diffusivity and expansion of* Y_2O_3*,* $Y_3Al_5O_{12}$*, and* LaF_3 *in the range 77-300 K.* J. Appl. Phys. **38**, 1603 (1967).

[Kli12] D. Klimm. Simulation of a predominance (Ellingham) diagram (2012). IKZ - Leibniz Institute of Crystal Growth, Berlin, Germany - private communication.

[Kna04] V. Knappe, F. Frank, and E. Rohde. *Principles of lasers and biophotonic effects.* Photomed. Laser Surg. **22**, 411 (2004).

[Kno92] D. S. Knowles and H. P. Jenssen. *Upconversion versus Pr-deactivation for efficient 3* μm *laser operation in Er.* IEEE J. Quantum Elect. **28**, 1197 (1992).

[Koc90] M. E. Koch, A. W. Kueny, and W. E. Case. *Photon avalanche upconversion laser at 644 nm.* Appl. Phys. Lett. **56**, 1083 (1990).

[Kod98] N. Kodama, T. Takahashi, and K. Hirao. *Room-temperature persistent spectral hole burning in Sm-doped* $KLaF_4$ *crystals.* Appl. Phys. Lett. **72**, 1548 (1998).

[Koe95] J. Koetke and G. Huber. *Infrared excited-state absorption and stimulated-emission cross sections of* Er^{3+}*-doped crystals.* Appl. Phys. B-Lasers O. **61**, 151 (1995).

[Koo11] P. Koopmann, R. Peters, K. Petermann, and G. Huber. *Crystal growth, spectroscopy, and highly efficient laser operation of thulium-doped* Lu_2O_3 *around 2* μm*.* Appl. Phys. B-Lasers O. **102**, 19 (2011).

[Koo12] P. Koopmann. *Thulium- and Holmium-doped sesquioxides for 2* μm *lasers.* Ph.D. thesis, Universität Hamburg - Institut für Laser-Physik (2012).

[Krä07] C. Kränkel, J. Johannsen, R. Peters, K. Petermann, and G. Huber. *Continuous-wave high power laser operation and tunability of Yb:LaSc$_3$(BO$_3$)$_4$ in thin disk configuration.* Appl. Phys. B-Lasers O. **87**, 217 (2007).

[Krä08] C. Kränkel. *Ytterbium-dotierte Borate und Vanadate mit großer Verstärkungsbandbreite als aktive Materialien im Scheibenlaser*. Ph.D. thesis, Universität Hamburg - Institut für Laser-Physik (2008).

[Kru63] W. F. Krupke and J. B. Gruber. *Absorption and fluorescence spectra of Er^{3+} (4f^{11}) in LaF$_3$.* J. Chem. Phys. **39**, 1024 (1963).

[Kru64] W. F. Krupke and J. B. Gruber. *Energy levels of Er^{3+} in LaF$_3$ and coherent emission at 1.61 µm.* J. Chem. Phys. **41**, 1225 (1964).

[Kum04] G. A. Kumar, R. Riman, E. Snitzer, and J. Ballato. *Solution synthesis and spectroscopic characterization of high Er^{3+} content LaF$_3$ for broadband 1.5 µm amplification.* J. Appl. Phys. **95**, 40 (2004).

[Kus73] T. Kushida. *Energy transfer and cooperative optical transitions in rare-earth doped inorganic materials. III. Dominant transfer mechanism.* J. Phys. Soc. Jpn. **34**, 1334 (1973).

[Kyr26] S. Kyropoulos. *Ein Verfahren zur Herstellung großer Kristalle.* Z. Anorg. Allg. Chem. **154**, 308 (1926).

[Lag04] M. M. Lage, A. Righi, F. M. Matinaga, J.-Y. Gesland, and R. L. Moreira. *Raman-spectroscopic study of lanthanide trifluorides with the β-YF$_3$ structure.* J. Phys.- Condens. Mat. **16**, 3207 (2004).

[Lan59] L. D. Landau and I. M. Lifshitz. *Course of theoretical Physics*, volume 5 (Pergamon Press, London-Paris, 1959).

[Lan11] D. G. Lancaster, S. Gross, H. Ebendorff-Heidepriem, K. Kuan, T. M. Monro, M. Ams, A. Fuerbach, and M. J. Withford. *Fifty percent internal slope efficiency femtosecond direct-written Tm^{3+}:ZBLAN waveguide laser*. Opt. Lett. **36**, 1587 (2011).

[Lap25] O. Laporte and W. F. Meggers. *Some rules of spectral structure.* J. Opt. Soc. Am. **11**, 459 (1925).

[Lap11] D. Lapotko. *Plasmonic nanobubbles as tunable cellular probes for cancer theranostics.* Cancers **3**, 802 (2011).

[Lar03] M. Laroche, S. Girard, R. Moncorgé, M. Bettinelli, R. Abdulsabirov, and V. Semashko. *Beneficial effect of Lu^{3+} and Yb^{3+} ions in UV laser materials.* Opt. Mater. **22**, 147 (2003).

[Lar09] M. Larionov. *Kontaktierung und Charackterisierung von Kristallen für Scheibenlaser*. Ph.D. thesis, Universität Stuttgart - IFSW (2009).

[Lau70] R. A. Laudise. *The growth of single crystals* (Prentice-Hall, Englewood Cliffs, NJ, 1970).

[Lee12] Lee. *Nd:YLF as an alternative to Nd:YAG*. Data sheet, Lee Laser Inc. (2012).

[LeF92] Y. LeFur, N. M. Khaidukov, and S. Aléonard. *Structure of* KYF_4. Acta Crystallogr. C **48**, 978 (1992).

[Len88] W. Lenth, J. Silversmith, and R. M. McFarlane. *Green infrared-pumped erbium upconversion lasers.* In: A. C. Tam, J. L. Gole, and W. C. Stwalley (editors), *Advances in laser science III: proceedings of the third international laser science conference*, volume 172, 8 (1988).

[Li12] T. Li, K. Beil, C. Kränkel, and G. Huber. *Efficient high-power continuous wave* $Er{:}Lu_2O_3$ *laser at 2.85 µm.* Opt. Lett. **37**, 2568 (2012).

[Lim88] K.-S. Lim and D. Hamilton. *UV-induced loss mechanisms in a* $Ce^{3+}{:}LiYF_4$ *laser*. J. Lumin. **40–41**, 319 (1988).

[Lin87] W. Lin and K. E. Benson. *The science and engineering of large- diameter Czochralski silicon crystal growth.* Annu. Rev. Mater. Sci. **17**, 273 (1987).

[Liu08] H. Liu, D. J. Spence, D. W. Coutts, H. Sato, and T. Fukuda. *Broadly tunable ultraviolet miniature cerium-doped LiLuF lasers.* Opt. Express **16**, 2226 (2008).

[Liu12] R. Liu, D. Tu, Y. Liu, H. Zhu, R. Li, W. Zheng, E. Ma, and X. Chen. *Controlled synthesis and optical spectroscopy of lanthanide-doped* $KLaF_4$ *nanocrystals.* Nanos. **4**, 4485 (2012).

[Mai07] H.-X. Mai, Y.-W. Zhang, L.-D. Sun, and C.-H. Yan. *Highly efficient multicolor up-conversion emissions and their mechanisms of monodisperse* $NaYF_4{:}Yb,Er$ *core and core/shell-structured nanocrystals.* J. Phys. Chem. C **111**, 13721 (2007).

[Mai09] D. Maier, R. Bertram, D. Klimm, and R. Fornari. *Influence of the atmosphere on the growth of* $LiYF_4$ *single crystal fibers by the micro-pulling-down method.* Crys. Res. Technol. **44**, 137 (2009).

[Man64] M. Mansmann. *Zur Kristallstruktur von Lanthantrifluorid*. Z. Anorg. Allg. Chem. **331**, 98 (1964).

[Mar01] I. Martin, Y. Guyot, M. Joubert, R. Abdulsabirov, S. Korableva, and V. Semashko. *Stark level structure and oscillator strengths of* Nd^{3+} *ion in different fluoride single crystals.* J. Alloy. Compd. **323-324**, 763 (2001).

[Mar03] M. Marano, G. Galzerano, S. Taccheo, P. Laporta, E. Sani, A. Toncelli, and M. Tonelli. *High efficiency and tunability of holmium-doped fluoride crystals.* Opt. Mater. **24**, 327 (2003).

[Max85] B. Maximov and H. Schulz. *Space group, crystal structure and twinning of lanthanum trifluoride.* Acta Crystallogr. B **41**, 88 (1985).

[Möb98] P. E. A. Möbert. *Er^{3+}:$LiYF_4$ Upconversion lasers.* Ph.D. thesis, Universität Hamburg (1998).

[McA63] J. McAndrew. *Relationship of optical axial angle with the three principal refractive indices.* Am. Mineral. **48**, 1277 (1963).

[McC64] D. E. McCumber. *Einstein relations connecting broadband emission and absorption spectra.* Phys. Rev. A **136**, A954 (1964).

[McC09] S. McCallum. *Optical mineralogy lectures.* Online published (2009). Http://courses.washington.edu/ess439/Lab%204%20lecture%20slides.pdf.

[McF88] R. M. McFarlane, F. Tong, A. J. Silversmith, and W. Lenth. *Violet cw neodymium upconversion laser.* Appl. Phys. Lett. **52**, 1300 (1988).

[McF91] R. A. McFarlane. *High-power visible upconversion laser.* Opt. Lett. **16**, 1397 (1991).

[McF94] R. A. McFarlane. *Upconversion laser in BaY_2F_8:Er 5% pumped by ground-state and excited-state absorption.* J. Opt. Soc. Am. B **11**, 871 (1994).

[Men72] N. Menyuk, K. Dwight, and J. W. Pierce. *$NaYF_4$: Yb,Er - an efficient upconversion phosphor.* Appl. Phys. Lett. **21**, 159 (1972).

[Mül07] G. Müller. *The Czochralski method – where we are 90 years after Jan Czochralski's invention.* Cryst. Res. Technol. **42**, 1150 (2007).

[Mül12] S. Müller, T. Calmano, P. Metz, N.-O. Hansen, C. Kränkel, and G. Huber. *Femtosecond-laser-written diode-pumped Pr:$LiYF_4$ waveguide laser.* Opt. Lett. **37**, 5223 (2012).

[Mog08] F. Moglia. *Crescita ed analisi spettroscopica di cristalli isolanti fotoluminescenti nel visibile e ultravioletto.* Diploma thesis, University of Pisa (2008).

[Moo66] J. Mooney. *Some properties of single crystal lanthanum trifluoride.* Infrared Phys. **6**, 153 (1966).

[Moo70] H. W. Moos. *Spectroscopic relaxation processes of rare earth ions in crystals.* J. Lumin. **1–2**, 106 (1970).

[Mor91] M. Mortier, J. Y. Gesland, M. Rousseau, M. A. Pimenta, L. O. Ladeira, J. C. D. S. Machado, and G. A. Barbosa. *Raman scattering investigations of KY_3F_{10}.* J. Raman Spectrosc. **22**, 393 (1991).

[Mou86] P. F. Moulton. *Spectroscopic and laser characteristics of Ti:Al_2O_3.* J. Opt. Soc. Am. B **3**, 125 (1986).

[Nac15] R. Nacken. *Über das Wachsen von Kristallpolyedern in ihrem Schmelzfluß*. Neues Jahrb. Geol. P. **2**, 133 (1915).

[Naf73] R. Nafziger, R. Lincoln, and N. Riazance. *High-temperature thermal analysis of the systems LaF_3- YF_3 , SrF_2 - YF_3 and MgF_2 - YF_3.* J. Inorg. Nucl. Chem. **35**, 421 (1973).

[Nej05] A. H. Nejadmalayeri, P. R. Herman, J. Burghoff, M. Will, S. Nolte, and A. Tünnermann. *Inscription of optical waveguides in crystalline silicon by mid-infrared femtosecond laser pulses.* Opt. Lett. **30**, 964 (2005).

[Nel11] S. A. Nelson. *Mineralogy lectures - University of Tulane.* Online published (2011). Http://www.tulane.edu/ sanelson/eens211/index.html.

[Neo85] D. Neogy and T. Purohit. *The behavior of active centers in a laser host. A crystal field investigation on Nd^{3+} and Er^{3+} in LaF_3 single crystals.* Phys. Status Solidi B **131**, 329 (1985).

[Neu01] M. Neubert and P. Rudolph. *Growth of semi-insulating GaAs crystals in low temperature gradients by using the Vapour Pressure Controlled Czochralski Method (VCz).* Prog. Cryst. Growth Ch. **43**, 119 (2001).

[Ngu89] D. C. Nguyen, G. E. Faulkner, and M. Dulick. *Blue-green (450-nm) upconversion Tm^{3+}:YLF laser.* Appl. Opt. **28**, 3553 (1989).

[Niz07] A. Nizamutdinov, V. Semashko, A. Naumov, S. Korableva, R. Abdulsabirov, A. Polivin, and M. Marisov. *Optical and gain properties of series of crystals LiF-YF_3 -LuF_3 doped with Ce^{3+} and Yb^{3+} ions.* J. Lumin. **127**, 71 (2007).

[Ofe62] G. S. Ofelt. *Intensities of crystal spectra of rare-earth ions.* J. Chem. Phys. **37**, 511 (1962).

[Oft29] I. Oftedal. *Über die Kristallstruktur von Tysonit und einigen künstlich dargestellten Lanthanidenfluoriden.* Z. Phys. Chem. B-Chem E **5**, 272 (1929).

[Okh05] A. G. Okhrimchuk, A. V. Shestakov, I. Khrushchev, and J. Mitchell. *Depressed cladding, buried waveguide laser formed in a YAG:Nd^{3+} crystal by femtosecond laser writing.* Opt. Lett. **30**, 2248 (2005).

[Osi03a] E. Osiac, E. Heumann, G. Huber, S. Kuck, E. Sani, A. Toncelli, and M. Tonelli. *Orange and red upconversion laser pumped by an avalanche mechanism in Pr^{3+}, Yb^{3+}:BaY_2F_8.* Appl. Phys. Lett. **82**, 3832 (2003).

[Osi03b] E. Osiac, S. Kück, E. Heumann, G. Huber, E. Sani, A. Toncelli, and M. Tonelli. *Spectroscopic characterization of the upconversion avalanche mechanism in Pr^{3+}, Yb^{3+}:BaY_2F_8.* Opt. Mater. **24**, 537 (2003).

[Ovs66] V. V. Ovsyakin and P. P. Feofilov. *Cooperative sensitization of luminescence in crystals activated with rare earth ions.* Sov. Phys. JETP-USSR **4**, 317 (1966).

[Pam75] B. R. Pamplin. *Crystal growth* (Pergamon Press, Oxford, 1975).

[Par10] T.-R. Park. *Phonon-assisted energy up-conversion process of Er^{3+} ions doped in KYF_4 crystal.* Solid State Commun. **150**, 1378 (2010).

[Par12] D. Parisi, S. Veronesi, and M. Tonelli. *Crystal growth of 1 at.% Er^{3+}:BaY_2F_8 and 1.3 at.% Er^{3+}:$BaYLuF_8$ crystals* (2012). Collaboration with the University of Pisa, Italy.

[Par13] D. Parisi. *Decay lifetime measurements of the $^4I_{13/2}$-multiplet in Er^{3+}: $BaYLuF_8$* (2013). Private communication.

[Pas74] R. Pastor, M. Robinson, and K. Miller. *Solid solution single crystals: (1-x)$HoF_3 \cdot xErF_3$.* Mater. Res. Bull. **9**, 449 (1974).

[Pas75a] R. Pastor and K. Arita. *Crystal growth of alkaline earth fluorides in a reactive atmosphere.* Mater. Res. Bull. **10**, 493 (1975).

[Pas75b] R. Pastor, M. Robinson, and W. Akutagawa. *Congruent melting and crystal growth of $LiRF_4$.* Mater. Res. Bull. **10**, 501 (1975).

[Pas76a] R. Pastor and K. Arita. *Crystal growth of alkaline earth fluorides in a reactive atmosphere. Part II.* Mater. Res. Bull. **11**, 1037 (1976).

[Pas76b] R. Pastor and M. Robinson. *Crystal growth of alkaline earth fluorides in a reactive atmosphere: Part III.* Mater. Res. Bull. **11**, 1327 (1976).

[Pas76c] R. C. Pastor, K. Arita, and M. Robinson. *Preparation of alkaline earth metal halide crystals for laser windows* (1976).

[Pas80] R. Pastor, M. Robinson, and M. Braunstain. *Crystal growth of alkaline earth fluorides in a reactive atmosphere. Part IV.* Mater. Res. Bull. **15**, 469 (1980).

[Pas13] R. Paschotta. *RP Photonics Encyclopedia* (2013).

[Pay88] S. A. Payne, L. L. Chase, H. W. Newkirk, L. K. Smith, and W. F. Krupke. *$LiCaAlF_6$:Cr^{3+}: a promising new solid-state laser material.* IEEE J. Quantum Elect. **24** (11), 2243 (1988).

[Pay89] S. A. Payne, L. L. Chase, L. K. Smith, W. L. Kway, and H. W. Newkirk. *Laser performance of $LiSrAlF_6$:Cr^{3+}.* J. Appl. Phys. **66**, 1051 (1989).

[Pay92] S. A. Payne, L. K. Smith, W. L. Kway, J. B. Tassano, and W. F. Krupke. *The mechanism of Tm to Ho energy transfer in $LiYF_4$.* J.Phys.-Condens Mat. **4**, 8525 (1992).

[Pej12] J. Pejchal, K. Fukuda, M. Nikl, N. Kawaguchi, Y. Yokota, T. Yanagida, and A. Yoshikawa. *Luminescence and scintillation properties of VUV scintillation crystals based on Lu-admixed BaY_2F_8.* IEEE T. Nucl. Sci. **59**, 2177 (2012).

[Pet02] K. Petermann, L. Fornasiero, E. Mix, and V. Peters. *High melting sesquioxides: crystal growth, spectroscopy, and laser experiments*. Opt. Mater. **19**, 67 (2002).

[Pet07] R. Peters, C. Kränkel, K. Petermann, and G. Huber. *Broadly tunable high-power Yb:Lu_2O_3 thin disk laser with 80% slope efficiency*. Opt. Express **15**, 7075 (2007).

[Pet09a] R. Peters. *Ytterbium-dotierte Sesquioxide als hocheffiziente Lasermaterialien*. Ph.D. thesis, Universität Hamburg - Institut für Laser-Physik (2009).

[Pet09b] R. Peters, K.Petermann, and G. Huber. *A new mixed sesquioxide Yb:$LuScO_3$: spectroscopic properties and highly efficient thin-disk laser operation*. In: *Advanced Solid-State Photonics*, MC4 (Optical Society of America, 2009).

[Pet11] R. Peters, C. Kränkel, S. T. Fredrich-Thornton, K. Beil, K. Petermann, G. Huber, O. H. Heckl, C. R. E. Baer, C. J. Saraceno, T. Südmeyer, and U. Keller. *Thermal analysis and efficient high power continuous-wave and mode-locked thin disk laser operation of Yb-doped sesquioxides*. Appl. Phys. B-Lasers O. **102**, 509 (2011).

[Pin94] J. F. Pinto., G. H. Rosenblatt, L. Esterowitz., V. Castillo, and G. J. Quarles. *Tunable solid-state laser action in Ce^{3+}:$LiSrAlF_6$*. Electron. Lett. **30**, 240 (1994).

[Pol80] T. Pollak, R. C. Folweiler, E. P. Chicklis, J. W. Baer, A. Linz, and D. Gabbe. *Properties and fabrication of crystalline fluoride materials for high power laser applications*. NBS Spec. Publ. **568**, 127 (1980).

[Pol82] T. M. Pollak, W. Wing, R. Grasso, E. Chicklis, and H. Jenssen. *CW laser operation of Nd:YLF*. IEEE J. Quantum Elect. **18**, 159 (1982).

[Pol86] S. A. Pollack, D. B. Chang, and N. L. Moise. *Upconversion-pumped infrared erbium laser*. J. Appl. Phys. **60**, 4077 (1986).

[Pol89] S. A. Pollack, D. B. Chang, and M. Birnbaum. *Threefold upconversion laser at 0.85, 1.23, and 1.73 µm in Er:YLF pumped with a 1.53 µm Er glass laser*. Appl. Phys. Lett. **54**, 869 (1989).

[Pol90a] S. A. Pollack and D. B. Chang. *Upconversion-pumped population kinetics for $^4I_{13/2}$ and $^4I_{11/2}$ laser states of Er^{3+} ion in several host crystals*. Opt. Quant. Electron. **22**, S75 (1990).

[Pol90b] S. A. Pollack, D. B. Chang, R. A. McFarlane, and H. Jenssen. *Infrared (Er)BaY_2F_8 laser pumped through di- and tri-ionic upconversion processes*. J. Appl. Phys. **67**, 648 (1990).

[Pol92] M. Pollnau, E. Heumann, and G. Huber. *Time-resolved spectra of excited-state absorption in Er^{3+}-doped $YAlO_3$*. Appl. Phys. A-Mater **54**, 404 (1992).

[Pol95] M. Pollnau, W. Luthy, and H. P. Weber. *Population mechanisms of the green Er^{3+}:$LiYF_4$ laser.* J. Appl. Phys. **77**, 6128 (1995).

[Pol96a] M. Pollnau. *Population mechanisms in erbium-doped solid-state lasers.* Ph.D. thesis, Universität Hamburg (1996).

[Pol96b] M. Pollnau, W. Lüthy, H. P. Weber, T. Jensen, G. Huber, A. Cassanho, H. P. Jenssen, and R. A. McFarlane. *Investigation of diode-pumped 2.8-µm laser performance in Er:BaY_2F_8.* Opt. Lett. **21**, 48 (1996).

[Pol97] M. Pollnau, C. Ghisler, W. Lüthy, H. P. Weber, J. Schneider, and U. B. Unrau. *Three-transition cascade erbium laser at 1.7, 2.7, and 1.6 µm.* Opt. Lett. **22**, 612 (1997).

[Pol00] M. Pollnau, D. R. Gamelin, S. R. Lüthi, H. U. Güdel, and M. P. Hehlen. *Power dependence of upconversion luminescence in lanthanide and transition-metal-ion systems.* Phys. Rev. B **61**, 3337 (2000).

[Pop09] P. A. Popov, P. P. Fedorov, V. V. Semashko, S. L. Korableva, M. A. Marisov, E. Y. Gordeev, V. M. Reiterov, and V. V. Osiko. *Thermal conductivity of crystals formed by fluoritelike phases in MF-RF3 systems (M = Li, Na, and K, R = Rare Earth).* Dokl. Phys. **54**, 221 (2009).

[Por62] B. Porter and E. A. Brown. *Melting points of inorganic fluorides.* J. Am. Ceram. Soc. **45**, 49 (1962).

[Por76] P. Porcher and P. Caro. *Crystal field parameters for Eu^{3+} in KY_3F_{10}.* J. Chem. Phys. **65**, 89 (1976).

[Por78a] P. Porcher and P. Caro. *Crystal field parameters for Eu^{3+} in KY_3F_{10}. II. Intensity parameters.* J. Chem. Phys. **68**, 4176 (1978).

[Por78b] P. Porcher and P. Caro. *Crystal field parameters for Eu^{3+} in KY_3F_{10}. III. Radiative and nonradiative transition probabilities.* J. Chem. Phys. **68**, 4183 (1978).

[Qin03] L. Qin, X. Meng, L. Zhu, J. Liu, B. Xu, H. Xu, F. Jiang, C. Du, X. Wang, and Z. Shao. *Influence of the different Gd/Y ratio on the properties of Nd:$Y_xGd1_{1\text{-}x}VO_4$ mixed crystals.* Chem. Phys. Lett. **380**, 273 (2003).

[Qui91] R. S. Quimby. *Output saturation in a 980-nm pumped erbium-doped fiber amplifier.* Appl. Optics **30**, 2546 (1991).

[Ran96] I. Ranieri, S. Baldochi, A. Santo, L. Gomes, L. Courrol, L. Tarelho, W. de Rossi, J. Berretta, F. Costa, G. Nogueira, N. Wetter, D. Zezell, N. V. Jr., and S. Morato. *Growth of $LiYF_4$ crystals doped with holmium, erbium and thulium.* J. Cryst. Growth **166**, 423 (1996).

[Ran02a] I. M. Ranieri, S. P. Morato, A. H. A. Bressiani, L. C. Courrol, E. P. Maldonado, N. U. Wetter, S. L. Baldochi, N. D. V. Jr., K. Shimamura, and T. Fukuda. *Growth of* $LiYO_{1-x}Lu_xF_4$ *crystals under* CF_4 *atmosphere.* J. Alloy. Compd. **344**, 203 (2002). Proceedings of the Rare Earths 2001.

[Ran02b] I. M. Ranieri, S. P. Morato, A. H. A. Bressiani, L. C. Courrol, E. P. Maldonado, N. U. Wetter, S. L. Baldochi, N. D. V. Jr., K. Shimamura, and T. Fukuda. *Growth of* $LiY_{1-x}Lu_xF_4$ *crystals under* CF_4 *atmosphere.* J. Alloy. Compd. **344**, 203 (2002).

[Rei12a] F. Reichert and F. Moglia. *Single crystal growth of rare-earth-doped* LaF_3 *via seedless cooling down method.* (2012). Internal communication.

[Rei12b] F. Reichert, F. Moglia, D.-T. Marzahl, P. Metz, M. Fechner, N.-O. Hansen, and G. Huber. *Diode pumped laser operation and spectroscopy of* $Pr^{3+}:LaF_3$. Opt. Express **20**, 20387 (2012).

[Rei13a] F. Reichert. *Measurement of Mohs hardness of* LaF_3*.* (2013). Internal communication.

[Rei13b] F. Reichert. *Measurement of thermal conductivity of* LaF_3 (2013). Institut für Laser-Physik - Universität Hamburg - private communication.

[Rei13c] F. Reichert and F. Moglia. *Single crystal growth of rare-earth-doped* LaF_3 *via seedless cooling down method at high pressure* (2013). Internal communication.

[Ric04] A. Richter, E. Heumann, E. Osiac, G. Huber, W. Seelert, and A. Diening. *Diode pumping of a continuous-wave* Pr^{3+}*-doped* $LiYF_4$ *laser*. Opt. Lett. **29**, 2638 (2004).

[Ric08] A. Richter. *Laser parameters and performance of* Pr^{3+}*-doped fluorides operating in the visible spectral range.* Ph.D. thesis, University of Hamburg (2008).

[Ris67] L. A. Riseberg., W. B. Gandrud, and H. W. Moos. *Multiphonon relaxation of near-infrared excited states of* $LaCl_3:Dy^{3+}$. Phys. Rev. **159**, 262 (1967).

[Ris68] L. A. Riseberg and H. W. Moos. *Multiphonon orbit-lattice relaxation of excited states of rare-earth ions in crystals.* Phys. Rev. **174**, 429 (1968).

[Rog97] P. Rogin and J. Hulliger. *Growth of* $LiYF_4$ *by the seeded vertical gradient freezing technique.* J. Cryst. Growth **172**, 200 (1997).

[Rot93] K. Rotereau, J. Gesland, P. Daniel, and A. Bulou. *Raman scattering study of Czochralski-grown yttrium fluoride single crystals.* Mater. Res. Bull. **28**, 813 (1993).

[Rub86] J. Rubin, A. Brenier, R. Moncorge, and C. Pedrini. *Excited-state absorption and energy transfer in* Er^{3+} *doped* $LiYF_4$. J. Lumin. **36**, 39 (1986).

[Rus96] G. Rustad and K. Stenersen. *Modeling of laser-pumped Tm and Ho lasers accounting for upconversion and ground-state depletion.* IEEE J. Quantum Elect. **32**, 1645 (1996).

[Sal97] S. Salaün, M. T. Fornoni, A. Bulou, M. Rousseau, P. Simon, and J. Y. Gesland. *Lattice dynamics of fluoride scheelites: I. Raman and infrared study of* $LiYF_4$ *and* $LiLnF_4$ *(Ln = Ho, Er, Tm and Yb).* J. Phys-Condens. Mat. **9**, 6941 (1997).

[San96] T. Sandrock, E. Heumann, G. Huber, and B. H. T. Chai. *Continuous-wave Pr, Yb:*$LiYF_4$ *upconversion laser in the red spectral range at room temperature.* In: S. A. Payne and . Pollock (editors), *OSA Trends in Optics and Photonics on advanced solid-state lasers, TOPS*, volume 1, 550 (1996).

[San97] T. Sandrock, H. Scheife, E. Heumann, and G. Huber. *High-power continuous-wave upconversion fiber laser at room temperature.* Opt. Lett. **22**, 808 (1997).

[San04] E. Sani, A. Toncelli, M. Tonelli, and F. Traverso. *Growth and spectroscopic analysis of Tm, Ho:*KYF_4. J. Phys.- Condens. Mat. **16**, 241 (2004).

[San05] A. Santo, I. Ranieri, G. Brito, B. Epelbaum, S. Morato, N. V. Jr., and S. Baldochi. *Growth of* $LiYF_4$ *single-crystalline fibres by micro-pulling-down technique.* J. Cryst. Growth **275**, 528 (2005).

[San12] I. dos Santos, D. Klimm, S. Baldochi, and I. Ranieri. *Thermodynamic modeling of the LiF-*YF_3 *phase diagram.* J. Cryst. Growth **360**, 172 (2012).

[Sar95] N. Sarukura, M. A. Dubinskii, L. Zhenlin, V. V. Semashko, A. K. Naumov, S. L. Korableva, R. Y. Abdulsabirov, K. Edamatsu, Y. Suzuki, T. Itoh, and Y. Segawa. Ce^{3+}*-activated fluoride crystals as prospective active media for widely tunable ultraviolet ultrafast lasers with direct 10-ns pumping.* IEEE J. Sel. Top. Quant. **1**, 792 (1995).

[Sar02] E. Sarantopoulou, Z. Kollia, and A. Cefalas. *Vacuum ultraviolet emission bands of* $LiLuF_4$*:*Tb^{3+} *crystals in the spectral range from 157 to 200 nm.* Microelectron. Eng. **61**, 133 (2002).

[Sar12] C. J. Saraceno, O. H. Heckl, C. R. E. Baer, C. Schriber, M. Golling, K. Beil, C. Kränkel, T. Südmeyer, G. Huber, and U. Keller. *Sub-100 femtosecond pulses from a SESAM modelocked thin disk laser*. Appl. Phys. B-Lasers O. **106**, 559 (2012).

[Sch93] B. Schmaul, G. Huber, R. Clausen, B. Chai, P. LiKamWa, and M. Bass. Er^{3+}*:*$LiYF_4$ *continuous wave cascade laser operation at 1620 and 2810 nm at room temperature.* Appl. Phys. Lett. **62**, 541 (1993).

[Sch96] R. Scheps. *Upconversion laser processes.* Prog. Quant. Electron. **20**, 271 (1996).

[Sch04] H. Scheife, G. Huber, E. Heumann, S. Bär, and E. Osiac. *Advances in upconversion lasers based on* Er^{3+} *and* Pr^{3+}. Opt. Mater. **26**, 365 (2004).

[Sch09] M. Schellhorn, S. Ngcobo, and C. Bollig. *High-power diode-pumped Tm:YLF slab laser*. Appl. Phys. B-Lasers O. **94**, 195 (2009).

[Sch12] M. Schellhorn, L. Galecki, and M. Eichhorn. *Provision of a 0.5 at.% Er^{3+}:$LiLuF_4$ and a 0.5 at.% Er^{3+}:$BaYLuF_8$ crystals supplied by AC Materials* (2012). Collaboration with ISL - French-German Research Institute of Saint-Louis, Germany.

[Sch13] M. Schellhorn, D. Parisi, S. Veronesi, G. Bolognesi, M. Eichhorn, and M. Tonelli. *In-band pumped Ho^{3+}:KY_3F_{10} 2 µm laser*. Opt. Lett. **38**, 504 (2013).

[Sha69] W. Shand. *Single crystal growth and some properties of $LiYF_4$*. J. Cryst. Growth **5**, 143 (1969).

[Sha91] L. Shaw and R. Chang. *Rare earth doped YLF grown by laser-heated pedestal growth technique*. J. Cryst. Growth **112**, 731 (1991).

[Shi83] M. D. Shinn, W. A. Sibley, M. G. Drexhage, and R. N. Brown. *Optical transitions of Er^{3+} ions in fluorozirconate glass*. Phys. Rev. B **27**, 6635 (1983).

[Shi01] K. Shimamura, H. Sato, A. Bensalah, V. Sudesh, H. Machida, N. Sarukura, and T. Fukuda. *Crystal growth of fluorides for optical applications*. Cryst. Res. Technol. **36**, 801 (2001).

[Shi04] M. Shi and J. Xu. *Large size LaF_3:Eu:Ca crystal grown by Bridgman-Stockbarger method*. Mater. Lett. **58**, 3823 (2004).

[Sie10] J. Siebenmorgen, T. Calmano, K. Petermann, and G. Huber. *Highly efficient Yb:YAG channel waveguide laser written with a femtosecond-laser*. Opt. Express **18**, 16035 (2010).

[Sil87] A. J. Silversmith, W. Lenth, and R. M. Macfarlane. *Green infrared-pumped erbium upconversion laser*. Appl. Phys. Lett. **51**, 1977 (1987).

[Sil05] E. Silva, A. Ayala, J.-Y. Gesland, and R. Moreira. *Vibrational spectrum and lattice dynamics of KY_3F_{10} single crystals*. Vib. Spectrosc. **37**, 21 (2005).

[Sin66] S. Singh and J. E. Geusic. *Observation and saturation of a multiphoton process in $NdCl_3$*. Phys. Rev. Lett. **17**, 865 (1966).

[Sob76] B. Sobolev, P. Fedorov, D. Shteynberg, B. Sinitsyn, and G. Shakhkalamian. *On the problem of polymorphism and fusion of lanthanide trifluorides. I. The influence of oxygen on phase transition temperatures*. J. Solid State Chem. **17**, 191 (1976).

[Sob82] B. Sobolev and N. Tkachenko. *Phase diagrams of BaF_2-(Y, Ln)F_3 systems*. J. Less-Common Met. **85**, 155 (1982).

[Sob02] B. Sobolev. *Chemical aspects of crystal growth of multicomponent fluoride materials from the melt.* Crystallogr. Rep.+ **47**, S63 (2002).

[Sok00] I. Sokólska, E. Heumann, S. Kück, and T. Lukasiewicz. *Laser oscillation of* Er^{3+}*:*YVO_4 *and* Er^{3+}*,* Yb^{3+}*:*YVO_4 *crystals in the spectral range around 1.6 µm.* Appl. Phys. B-Lasers O. **71**, 893 (2000).

[Sok01] I. Sokólska and S. Kück. *Observation of photon cascade emission in the* Pr^{3+}*-doped perovskite* $KMgF_3$*.* Chem. Phys. **270**, 355 (2001).

[Sol63] R. Solomon and L. Mueller. *Stimulated emission at 5985 Å from* Pr^{3+} *in* LaF_3*.* Appl. Phys. Lett. **3**, 135 (1963).

[Som73] J. Sommerdijk. *Influence of host lattice on the infrared-excited visible luminescence in* Yb^{3+}*,* Er^{3+}*-doped fluorides.* J. Lumin. **6**, 61 (1973).

[Som74] J. Sommerdijk, A. Bril, and A. de Jager. *Luminescence of* Pr^{3+}*-activated fluorides.* J. Lumin. **9**, 288 (1974).

[Spi99] J. C. van 't Spijker, P. Dorenbos, C. W. E. van Eijk, J. M. Jacobs, H. W. den Hartog, and N. Korolev. *Luminescence and scintillation properties of* BaY_2F_8*:*Ce^{3+}*,* $BaLu_2F_8$ *and* $BaLu_2F_8$*:*Ce^{3+}*.* J. Lumin. **85**, 11 (1999).

[Sto12] G. Stoeppler, D. Parisi, M. Tonelli, and M. Eichhorn. *High-efficiency 1.9 µm* Tm^{3+}*:*$LiLuF_4$ *thin-disk laser.* Opt. Lett. **37**, 1163 (2012).

[Stu96] B. C. Stuart, M. D. Feit, S. Herman, A. M. Rubenchik, B. W. Shore, and M. D. Perry. *Nanosecond-to-femtosecond laser-induced breakdown in dielectrics.* Phys. Rev. B **53**, 1749 (1996).

[Suy05a] J. F. Suyver, A. Aebischer, D. Biner, P. Gerner, J. Grimm, S. Heer, K. W. Krämer, C. Reinhard, and H. U. Güdel. *Novel materials doped with trivalent lanthanides and transition metal ions showing near-infrared to visible photon upconversion.* Opt. Mater. **27**, 1111 (2005).

[Suy05b] J. F. Suyver, A. Aebischer, S. Garcia-Revilla, P. Gerner, and H. U. Güdel. *Anomalous power dependence of sensitized upconversion luminescence.* Phys. Rev. B **71**, 125123 (2005).

[Sve98] O. Svelto. *Principles of lasers* (Plenum Press, 1998), fourth edition edition.

[Syt91] J. Sytsma, S. J. Kroes, G. Blasse, and N. M. Khaidukov. *Spectroscopy of* Gd^{3+} *in* KYF_4*: a system with several luminescent sites.* J. Phys.- Condens. Mat **3**, 8959 (1991).

[Tay72] K. N. R. Taylor and M. I. Darby. *Physics of rare earth solids* (Chapman and Hall LTD, London, 1972).

[Ter12] N. Ter-Gabrielyan, V. Fromzel, W. Ryba-Romanowski, T. Lukasiewicz, and M. Dubinskii. *Spectroscopic properties and laser performance of resonantly-pumped cryo-cooled* Er^{3+}*:*$GdVO_4$. Opt. Express **20**, 6080 (2012).

[Tho61] R. E. Thoma, C. F. Weaver, H. Friedman, H. Insley, L. Harris, and H. A. Yakel. *Phase equilibria in the system LiF-*YF_3. J. Phys Chem.-US **65**, 1096 (1961).

[Tho66] R. E. Thoma and G. D. Brunton. *Equilibrium dimorphism of the lanthanide trifluorides.* Inorg. Chem. **5**, 1937 (1966).

[Tig01] P. Tigreat, J. Doualan, C. Budasca, and R. Moncorge. *Energy transfer processes in (*Yb^{3+}*,* Dy^{3+}*) and (*Tm^{3+}*,* Dy^{3+}*) codoped* $LiYF_4$ *and* KY_3F_{10} *single crystals.* J. Lumin. **94–95**, 23 (2001).

[Tin64] M. Tinkam. *Group theory and quantum mechanics* (McGraw-Hill, New York, 1964).

[Tka73] N. Tkachenko, L. Garashina, O. Izotova, V. Aleksandrov, and B. Sobolev. *Phase equilibria in* BaF_2*-(Y, Ln)*F_3 *systems.* J. Solid State Chem. **8**, 213 (1973).

[Toc07] V. Toccafondo, J. A. Cerqueira S., S. Faralli, E. Sani, A. Toncelli, M. Tonelli, and F. D. Pasquale. Er^{3+}*-doped* BaY_2F_8 *crystal waveguides for broadband optical amplification at 1.5 µm.* J. Appl. Phys. **101**, 023104 (2007).

[Tom07] O. Toma. *Emission regimes of a green Er:*$LiLuF_4$ *laser.* IEEE J. Quantum Elect. **43**, 519 (2007).

[Tom11] O. Toma and S. Georgescu. *Competition between green and infrared emission in Er:*$LiYF_4$ *upconversion lasers.* Opt. Commun. **284**, 388 (2011).

[Ton89] F. Tong, W. P. Risk, R. M. McFarlane, and W. Lenth. *551 nm diode-laser-pumped upconversion laser.* Electron. Lett. **25**, 1389 (1989).

[Ton10] A. Toncelli, F. Moglia, and M. Tonelli. *Optical properties of* Eu^{2+} *ions in* BaY_2F_8 *for completely-solid-state cw UV laser emission.* Opt. Mater. **33**, 22 (2010).

[TT61] K. Tchi-Tsu and A. V. Novocelova. Zh. Neorg. Khim. **9**, 2148 (1961).

[Tur11] G. Turri, C. Gorman, A. Cassanho, M. Bass, and H. P. Jenssen. *Spectroscopic comparison of Nd:*$BaYLuF_8$ *and Nd:*BaY_2F_8. J. Opt. Soc. Am. B **28**, 331 (2011).

[Tya10] N. Tyagi, A. A. Reddy, and R. Nagarajan. $KLaF_4$*:Er an efficient upconversion phosphor.* Opt. Mater. **33**, 42 (2010).

[Udo08] T. J. Udovic, Q. Huang, A. Santoro, and J. J. Rush. *The nature of deuterium arrangements in* YD_3 *and other rare-earth trideuterides.* Z. Crystallogr. **223**, 697 (2008).

[Uem00] S. Uemura and K. Torizuka. *Generation of 10 fs pulses from a diode-pumped Kerr-lens mode-locked Cr:LiSAF laser*. Jpn. J. Appl. Phys. **39**, 3472 (2000).

[Uhr77] R. Uhrin, R. Belt, and V. Rosati. *Preparation and crystal growth of lithium yttrium fluoride for laser applications*. J. Cryst. Growth **38**, 38 (1977).

[Veg21] L. Vegard. *Die Konstitution der Mischkristalle und die Raumfüllung der Atome*. Z. Phys. **5**, 17 (1921).

[Ver13] S. Veronesi and D. Parisi. *Melting temperature of* $BaYLuF_8$ (2013). Internal communication.

[Vie02] N. Vieira, I. Ranieri, L. Tarelho, N. Wetter, S. Baldochi, L. Gomes, P. de Matos, W. de Rossi, G. Nogueira, L. Courrol, E. Barbosa, E. Maldonado, and S. Morato. *Laser development of rare-earth doped crystals*. J. Alloy. Compd. **344**, 231 (2002).

[Vle37] J. H. van Vleck. *The puzzle of rare-earth spectra in solids*. J. Phys Chem.-US **41**, 67 (1937).

[Voß02] A. Voß. *Der Scheibenlaser: theoretische Grundlagen des Dauerstrichbetriebs und erste experimentelle Ergebnisse anhand von Yb:YAG*. Ph.D. thesis, Universität Stuttgart, Institut für Strahlwerkzeuge (2002).

[Wal97] B. M. Walsh, N. P. Barnes, and B. D. Bartolo. *On the distribution of energy between the Tm* $^3F_4$ *and Ho* $^5I_7$ *manifolds in Tm-sensitized Ho luminescence*. J. Lumin. **75**, 89 (1997).

[Wal98] B. M. Walsh, N. P. Barnes, and B. D. Bartolo. *Branching ratios, cross sections, and radiative lifetimes of rare earth ions in solids: Application to* Tm^{3+} *and* Ho^{3+} *ions in* $LiYF_4$. J. Appl. Phys. **83**, 2772 (1998).

[Wal04] B. M. Walsh, N. P. Barnes, M. Petros, J. Yu, and U. N. Singh. *Spectroscopy and modeling of solid state lanthanide lasers: Application to trivalent* Tm^{3+} *and* Ho^{3+} *in* $LiYF_4$ *and* $LiLuF_4$. J. Appl. Phys. **95**, 3255 (2004).

[Way85] R. W. Waynant and P. H. Klein. *Vacuum ultraviolet laser emission from* Nd^{3+}:LaF_3. Appl. Phys. Lett. **46**, 14 (1985).

[Web67a] M. J. Weber. *Probabilities for radiative and nonradiative decay of* Er^{3+} *in* LaF_3. Phys. Rev. **157**, 262 (1967).

[Web67b] M. J. Weber. *Selective excitation and decay of* Er^{3+} *fluorescence in* LaF_3. Phys. Rev. **156**, 231 (1967).

[Web73] M. J. Weber, T. E. Varitimos, and B. H. Matsinger. *Optical intensities of rare-earth ions in yttrium orthoaluminate*. Phys. Rev. B **8**, 47 (1973).

[Web75] M. J. Weber. *Handbook of optical materials* (Plenum Press, New York, USA, 1975).

[Web03] M. J. Weber. *Handbook of optical materials* (CRC Press LLC, Boca Raton, 2003).

[Weg95] R. T. Wegh and A. Meijerink. *Cooperative luminescence of ytterbium(III) in* La_2O_3. Chem. Phys. Lett. **246**, 495 (1995).

[Weg00] R. T. Wegh, A. Meijerink, R.-J. Lamminmäki, and J. Hölsä. *Extending Dieke's diagram.* J. Lumin. **87- 89**, 1002 (2000).

[Wel64] P. F. Weller and J. A. Kucza. *Single-crystal growth of* LaF_3. J. Appl. Phys. **35**, 1945 (1964).

[Wel99] J.-P. R. Wells, A. Sugiyama, T. Han, and H. Gallagher. *Laser site selective excitation of* KY_3F_{10}*-doped with samarium.* J. Lumin. **85**, 91 (1999).

[Wel00] J.-P. R. Wells, A. Sugiyama, T. P. Han, and H. G. Gallagher. *A spectroscopic comparison of samarium-doped* $LiYF_4$ *and* KY_3F_{10}. J. Lumin. **87-89**, 1029 (2000).

[Wen99] O. S. Wenger, D. R. Gamelin, H. U. Güdel, A. V. Butashin, and A. A. Kaminskii. *Site-selective optical spectroscopy and upconversion mechanisms of the laser material* $BaLu_2F_8$:Er^{3+}. Phys. Rev. B **60**, 5312 (1999).

[Wen00] O. S. Wenger, D. R. Gamelin, H. U. Güdel, A. V. Butashin, and A. A. Kaminskii. *Site-selective yellow to violet and near-infrared to green upconversion in* $BaLu_2F_8$:Nd^{3+}. Phys. Rev. B **61**, 16530 (2000).

[Whi91] T. J. Whitley, C. A. Millar, R. Wyatt, M. C. Brierley, and D. Szebesta. *Upconversion pumped green lasing in erbium doped fluorozirconate fibre.* Electron. Lett. **27**, 1785 (1991).

[Wil88] K.-T. Wilke and J. Bohm. *Kristallzüchtung* (Harri Deutsch, Frankfurt/Main, 1988).

[Wol13] U. Wolters. *Temperature behavior in either presence or absence of laser operation in* Yb^{3+}*:YAG thin disks.* (2013). Internal communication.

[Wyb65] B. G. Wybourne. *Spectroscopic properties of rare earths* (John Wiley & Sons, New York, 1965).

[Xie92a] P. Xie and S. C. Rand. *Visible cooperative upconversion laser in Er:*$LiYF_4$. Opt. Lett. **17**, 1198 (1992).

[Xie92b] P. Xie and S. C. Rand. *Visible cooperative upconversion laser in Er:*$LiYF_4$*: erratum.* Opt. Lett. **17**, 1822 (1992).

[Xu11] B. Xu, P. Camy, J.-L. Doualan, Z. Cai, and R. Moncorgé. *Visible laser operation of* Pr^{3+}*-doped fluoride crystals pumped by a 469 nm blue laser.* Opt. Express **19**, 1191 (2011).

[Yam00] M. Yamaga, M. Honda, J.-P. R. Wells, T. P. J. Han, and H. G. Gallagher. *An electron paramagnetic resonance study on* Sm^{3+} *and* Yb^{3+} *in* KY_3F_{10} *crystals.* J. Phys.- Condens. Mat **12**, 8727 (2000).

[Yan76] K. H. Yang and J. A. DeLuca. *VUV fluorescence of* Nd^{3+}*-,* Er^{3+}*, and* Tm^{3+}*-doped trifluorides and tunable coherent sources from 1650 to 2600 Å.* Appl. Phys. Lett. **29**, 499 (1976).

[Yan78] K. H. Yang and J. A. DeLuca. *Vacuum-ultraviolet excitation studies of* $5d^1 4f^{n-1}$ *to* $4f^n$ *and* $4f^n$ *to* $4f^n$ *transitions of* Nd^{3+}*-,* Er^{3+}*-, and* Tm^{3+}*-doped trifluorides.* Phys. Rev. B **17**, 4246 (1978).

[Yen64] W. M. Yen, W. C. Scott, and A. L. Schawlow. *Phonon-induced relaxation in excited optical states of trivalent praseodymium in* LaF_3*.* Phys. Rev. **136**, A271 (1964).

[Yin02] M. Yin, V. Makhov, N. Khaidukov, and J. Krupa. *Spectroscopic studies of* Er^{3+} *centers in* KYF_4*.* J. Alloy. Compd. **341**, 362 (2002).

[Yos05] A. Yoshikawa, K. Kamada, M. Nikl, K. Aoki, H. Sato, J. Pejchal, and T. Fukuda. *Growth and luminescent properties of Pr:*KY_3F_{10} *single crystal.* J. Christ. Growth **285**, 445 (2005).

[You04] Y. E. Young, S. D. Setzler, K. J. Snell, P. A. Budni, T. M. Pollak, and E. P. Chicklis. *Efficient 1645-nm Er:YAG laser.* Opt. Lett. **29** (10), 1075 (2004).

[Zac48] W. H. Zachariasen. *Double fluorides of potassium or sodium with uranium, thorium and lanthanum.* J. Am. Chem. Soc. **70**, 2147 (1948).

[Zal85] A. Zalkin and D. H. Templeton. *Refinement of the trigonal crystal structure of lanthanum trifluoride with neutron diffraction data.* Acta Crystallogr. B **41**, 91 (1985).

[Zie70] J. P. van der Ziel, F. W. Ostermayer, and L. G. V. Uitert. *Infrared excitation of visible luminescence in* $Y_{1\text{-}x}Er_xF_3$ *via resonant energy transfer.* Phys. Rev. B **2**, 4432 (1970).

[Zub97] D. A. Zubenko, M. Noginov, V. A. Smirnov, and I. A. Shcherbakov. *Different mechanisms of nonlinear quenching of luminescence.* Phys. Rev. B **55**, 8881 (1997).

[Zus77] L. D. Zusman. *Kinetics of luminescence damping in hopping mechanism of quenching.* Sov. Phys. JETP-USSR **46**, 347 (1977).

List of publications

Publications in scientific journals

- R. Faoro, F. Moglia, M. Tonelli, N. Magnani, and E. Cavalli. *Energy levels and emission parameters of the* Dy^{3+} *ion doped into the* YPO_4 *host lattice.* J. Phys. Condens. Matter **21**, 275501 (2009).
- A. Toncelli, F. Moglia, and M. Tonelli. *Optical properties of* Eu^{2+} *ions in* BaY_2F_8 *for completely-solid-state cw UV laser emission.* Optic. Mater. **33**, 22 (2010).
- F. Reichert, F. Moglia, D.-T. Marzahl, P. Metz, M. Fechner, N.-O. Hansen, and G. Huber. *Diode pumped laser operation and spectroscopy of* Pr^{3+}*:*LaF_3*.* Opt. Express **20**, 20387 (2012).
- P. W. Metz, S. Müller, F. Reichert, D.-T. Marzahl, F. Moglia, , C. Kränkel, and G. Huber. *Wide wavelength tunability and green laser operation of diode-pumped* Pr^{3+}*:*KY_3F_{10}*.* Opt. Express **21**, 31274 (2013).
- P. W. Metz, F. Reichert, F. Moglia, S. Müller, D.-T. Marzahl, , C. Kränkel, and G. Huber. *High power red, orange, and green* Pr^{3+}*:*$LiYF_4$ *lasers.* Opt. Lett. **39**, 3193 (2014).
- F. Moglia, S. Müller, F. Reichert, P. W. Metz, T. Calmano, C. Kränkel, E. Heumann, and G. Huber. *Upconversion lasers in* Er^{3+}*:*$LiLuF_4$ *crystals. In preparation* (2014).

International conferences

- R. Faoro, F. Moglia, M. Tonelli, and E. Cavalli. *Optical spectroscopy of the* Dy^{3+} *ion in* YPO_4 *crystals.* International Conference on Luminescence and Optical Spectroscopy of Condensed Matter (ICL 2008), Lyon, France, poster (2008).
- R. Faoro, F. Moglia, A. Toncelli, and M. Tonelli. *Investigation of rare earth doped* BaY_2F_8 *crystals as visible emitters.* Conference on Lasers and Electro-Optics (CLEO/Europe - EQEC) 2009, Munich, Germany, poster CE.P.18 (2009).
- F. Moglia, E. Heumann, R. Peters, and G. Huber. *Advances in semiconductor-laser-pumped high-power upconversion lasers.* 5th International Symposium on Laser, Scintillator and Non-Linear Optical Material, (ISLNOM 5) 2009, Pisa, Italy, oral presentation (2009).
- R. Faoro, F. Moglia, M. Tonelli, and E. Cavalli. *Luminescence properties of* $Ba_2NaNb_5O_{15}$ *crystals activated with* Pr^{3+}*.* 5th International Symposium on Laser,

Scintillator and Non-Linear Optical Material, (ISLNOM 5) 2009, Pisa, Italy, poster (2009).

- N.-O. Hansen, T. Gün, F. Moglia, and G. Huber. *Diode pumped Er- and Pr-lasers in the visible spectral range.* EOS Topical Meeting 2009, Capri, Italy, invited oral presentation.

- N.-O. Hansen, T. Gün, F. Moglia, and G. Huber. *Rare earth solid-state lasers in the visible spectral range.* Laser Medicine Conference (LASER Europe 2010), Tarragona, Spain, invited oral presentation.

- R. Kubrin, J. Huang, F. Moglia, K. Petermann and W. Bauhofer. *Photoluminescence of* $(YGd)_2O_3$*:Eu phosphors produced by nanoparticle-seeded flame-assisted spray pyrolysis.* ICC3: Symposium 7: Optical ceramics 2010, Osaka, Japan, oral presentation, in IOP Conf. Series: Materials Science Engineering **20**, 102018 (2011).

- F. Moglia, C. Brandt, and G. Huber. *Inband-pumped* Er^{3+}*:*$LiLuF_4$ *laser emitting in the 1.6 µm spectral range.* Advanced Solid-State Photonics (ASSP) 2012, San Diego, CA, USA, poster AM4.A.22 (2012).

- F. Moglia, F. Reichert, and G. Huber. Er^{3+}*:*LaF_3 *as potential material for upconversion lasers.* Advances in Optical Materials (AIOM) 2012, San Diego, CA, USA, oral presentation IW5D.6 (2012).

- F. Reichert, F. Moglia, M. Fechner, P. Koopmann, and G. Huber. *Diode pumped laser oscillation at 750 nm and excited state absorption measurements of* Ho^{3+}*:*$LiLuF_4$. Advances in Optical Materials (AIOM) 2012, San Diego, CA, USA, oral presentation IW3D.2 (2012).

- F. Reichert, F. Moglia, M. Fechner, N.-O. Hansen, and G. Huber. *Laser oscillation and spectroscopy of* Pr^{3+}*:*LaF_3*.* Conference on Lasers and Electro-Optics (CLEO/QELS) 2012, San José, CA, USA, oral presentation CM2D.2 (2012).

- F. Moglia, S. Müller, T. Calmano, C. Kränkel, and G. Huber. *Er:*$LiLuF_4$ *upconversion waveguide laser fabricated by femtosecond-laser writing.* 5th EPS-QUEOD Europhoton Conference - Solid state, fibre, and waveguide coherent light sources 2012, Stockholm, Sweden, poster TuP.25 (2012).

- F. Moglia, S. Müller, T. Calmano, C. Kränkel, and G. Huber. *Er:*$LiLuF_4$ *upconversion waveguide laser with femtosecond-laser written circular cladding structures.* Conference on Lasers and Electro-Optics (CLEO/Europe - EQEC) 2013, Munich, Germany, poster CJ.P.3 (2013).

German conferences

- C. Brandt, F. Moglia, K. Petermann, and G. Huber. Er^{3+}*-doped* YVO_4 *laser emitting around 1.6 µm.* Frühjahrstagung der Deutschen Physikalischen Gesellschaft 2011, Dresden, Germany, poster (2011).

- P. W. Metz, F. Moglia, S. Müller, F. Reichert, D.-T. Marzahl, N.-O. Hansen, M. Fechner, C. Kränkel, and G. Huber. *Spectroscopy and self-pulsed red and orange laser operation os Sm^{3+}-doped $LiLuF_4$ crystals.* Frühjahrstagung der Deutschen Physikalischen Gesellschaft 2011, Hannover, Germany, oral presentation Q43.3 (2013).

Contributions at seminars and workshops

- F. Moglia. *Growth and spectroscopic analysis of insulating ultraviolet-visible photoluminescent crystals.* LAS-F Workshop 2009, Lintrup, Denmark, oral presentation (2009).

- F. Moglia. *Beginning and future developments in Er-doped fluoride thin disk lasers.* LAS-F Workshop 2009, Lintrup, Denmark, oral presentation (2009).

- F. Moglia. *Towards semiconductor-laser-pumped erbium-doped fluoride thin disk laser.* LAS-F Workshop 2010, Vorbasse, Denmark, oral presentation (2010).

- F. Moglia, K. Beil, C. Kränkel, E. Heumann, K. Petermann, and G. Huber. *Towards semiconductor-laser-pumped erbium-doped fluoride thin disk laser.* GrK Workshop 2010, Lüneburg, Germany, oral presentation (2010).

- F. Moglia. *New investigation of erbium-doped fluorides and upconversion lasers.* LAS-F Workshop 2011, Lønborg, Denmark, oral presentation (2011).

- K. Beil, T. Calmano, M. Fechner, S. Heinrich, F. Moglia, F. Reichert, C. Kränkel, and G. Huber. *Project A3: Solid state lasers in the visible spectral range; Project A4: Waveguides fabricated with light.* GrK Workshop 2011, Amrum, Germany, oral presentation (2011).

- F. Moglia. *Upconversion-Laser in Erbium-dotierten Fluoriden.* LAS-F Workshop 2012, Lavensby, Denmark, oral presentation (2012).

- F. Reichert, K. Beil, F. Moglia. *Project A3: Short-wavelength solid-state lasers.* GrK Workshop 2012, Amrum, Germany, oral presentation (2012).

- F. Moglia, S. Müller, T. Calmano, C. Kränkel, and G. Huber. *Upconversion waveguide lasers fabricated by fs-laser-writing in Er:$LiLuF_4$ crystals.* 540 WE Heraeus-Seminar, Bad Honnef, Germany, poster (2013).

Further written publications

- F. Moglia. *I quasicristalli* Bachelor thesis, University of Pisa (2006)

- F. Moglia. *Crescita ed analisi spettroscopica di cristalli isolanti fotoluminescenti nel visibile e ultravioletto.* Master thesis, University of Pisa (2008).

Acknowledgements

This work was performed between 2009 and 2013 in the *Ferstkörperlaser* group of Prof. Günter Huber at the Institut für Laser-Physik at the Universität Hamburg. During these years, I had the possibility to collaborate and receive the support of different people to whom I would like to express my gratitude. Considering the number of pages of this thesis and my usual way to communicate, also the acknowledgements will not be just *long*, but *accurate*.

First, my gratitude goes to whom officially rendered this work possible, which means I would like to thank:

- Prof. Günter Huber, for the opportunity he offered me to join his working group and to widely extend my knowledge in the field of laser physics and also for effectively encouraging me in learning German
- Prof. Mauro Tonelli, for supporting my decision to pursue my Ph.D. studies in Hamburg and my work via a fruitful collaboration and for the evaluation of my thesis as second referee
- Prof. Henning Moritz, for being sympathetic about my time schedule and for being the second referee of my oral examination.

This work would have not been the same in terms of results and enjoyment in planning, carrying out and analyzing experiments if present and ex-members of the LAS-F group would have not contributed to create the general fruitful atmosphere in the past few years. Consequently, I continue with thanking:

- Prof. Ernst Heumann, for his support and very important advice regarding the fantastic but tricky world of upconversion lasers
- Klaus Petermann, for his consultancy about the crystal growth of good-quality fluoride crystals, in theory and in practice
- Christian Kränkel, for assuming the unbearable duty of proofreading my whole thesis and for precious suggestions which were even more effective during night shifts at the institute
- Sebastian Müller, for starting with an *interkulturellem Austausch* a fruitful collaboration (in German!) resulting in upconversion waveguide lasers and consequent proofreading of every publication (this thesis included), coffee together early in the morning when I was writing the thesis and further scientific and non-scientific adventures

- Fabian Reichert, for being the newcomer together with me in January 2009, for abandoning oxides for a while and joining the “fluoride crystal growers community”, for learning in Pisa how to drink coffee and sharing more than a few *espressi* with me at the institute talking not only about spectroscopy, for proofreading part of my thesis, for his technical and theoretical support, for “elping” me on business trips and also for sleep talking; but NOT for leaving my ballerinas on the Route 66

- Kolja Beil, for being my twin LEXI associate (even in pictures) and TU-Praktikum tutor, for going a million times through my rate equations and finding always something to be improved, for long sessions about theory and practice of thin disk lasers at any time of day and night and for starting with: “I have a short question” and finishing an hour later

- Philip Metz, for joining full-time the “fluoride crystal growers community” with the real *correct* attitude and for precious advice about my thesis, in the lab, in the office and at the Hurricane

- Philipp Koopmann, for organizing with me and Fabian Reichert the coolest LAS-F conference ever, for driving me to my first Hurricane, for giving me the LaTeX files of his thesis and proofreading one of my very first chapters, for being annoying asking me :“How many pages? “ but also for having always an encouraging word for me

- Sebastian Heinrich, for sharing the TU Praktikum responsibility of the solar cell and Peltier effect experiments, for proofreading the longest chapter of this thesis, for sleeping longer than me at the Hurricane, for being more or less easily convinced in choosing at some point a hotel room instead of a camping place during our trip in California and for cooking *Käse Spätzle*

- Thomas Calmano, for a pleasant co-work in the lab on the notes of Delta Radio confirmed on the same concert areas at the Hurricane, for sharing not only his extensive knowledge about waveguide lasers, but also the optimized back seat of the car on our trip in California and for helping by proofreading publications and part of this thesis

- Daniel Marzahl, for overtaking with extreme joy the responsibility of the OPOs and for eagerly sharing the duty with Philip Metz and for the lowest tone of :“Moin“ that a human being can emit

- Sven Waeselmann, for having enough troubles with the PLD facility, together with Sebastian Heinrich, to not let me feel alone with mine and for being “consciously nerd“, which means trying (sometimes. . .) to hide it instead of being proud of it

- Bastian Deppe for being both crazy and hyper-tidy, which actually is not a total contradiction

- Ulrike Wolters, for being my all-time-long office mate and showing me how people can be different and nevertheless get perfectly along with each other, for being my full-time consultant about English and German, not only about my thesis, for sharing night shifts in the last thrilling time before “the submission” and for our amusing internet investigations

- Alexander Heuer, for being two times office mate to confirm his devotion to us, for being nerd and proud of it, but also eager to IT-consult, for the *awesome* time in the office and for the non-scientific octopus- and non-octopus-related fun together
- Andreas Kahn, for his help in bureaucratic matters as the perfect oldest office member and for talking more and louder than me (officially proven)
- Rigo Peters, for being my scientific 360 °-guru in the first months and for calling me on the phone in the office from the lab on his last day pretending he could hear my voice from there (without the help of the phone. . .)
- Jörg Siebenmorgen, for misspelling in two different ways my first name and for being an example of successful scientist who still loves Hamburg and the old friends
- Nils-Owe Hansen, for being the chronologically first proofreader of this thesis, a reliable consultant about crystal growth of fluorides and an efficient coordinator of the Sneak Preview tickets distribution
- Teoman Gün, for being the shoulder to cry on when I had the first problems with the growth of crystals and for being just. . . Teo
- Matthias Fechner, for being the master of ESA measurements and making it looking like an accident, for showing that being responsible of the OPOs and the small Ti:sapphire laser is not such a big deal and for the good time together during scientific and non-scientific events
- Susanne Fredrich-Thornton, for being a V.I.P. of the institute, for organizing my first very-German baking session and for our super-funny walk in the Munich countryside
- Tao Li, for being the erbium-, non-German-speaker- colleague of the group
- Henning Kühn, for his support concerning theoretical aspects, even in Italian
- Christian Brandt, for his help and our collaboration about erbium-doped fluoride-based lasers at 1.6 µm and for reducing the frequency of his *Hirties* when I started to understand them
- André Richter, for the introduction in the labs on my first days and for his Ph.D. thesis: one of the few with a related topic to mine written in English
- Andrea Arcangeli, for joining our group twice and keeping the *Progetto Imbroglia* still alive along these years and for the tears spent in trying to understand German and interpret Chinese.

Furthermore, I would like to thank all the diploma, master, bachelor students and *HiWis* which have supported the work in our group and in particular JONATHAN THIELLMANN, BIANCA JESSEN, MANUEL KIRCHEN and JANNIS LEHMANN, for contributing to the nice atmosphere in our office, KORE HASSE for a post-deadline help, ANNA-GRETA PASCHKE for her laugh and UWE KELLING, for promoting scientific and non-scientific activities.

Working would have not been always productive without the help of other employees at the Institut für Laser-Physik and the Universität Hamburg. For this reason, a loud "Thank you!" goes also to the university workshop, administration and IT coordinators and in particular to:

- FRIEDJOF TELLKAMP, ROBERT FISCHER, STEPHAN GARBERS, REINHARD MIELCK and WOLFRAM KALB-ROTTMANN for their prompt technical support
- SILKE FRÖMMIG, especially for helping me with the first bureaucratic duties when my German was still not existing and together with JANINA DAHMS, ELLEN GLOY and NADJA WARDENBURG, for their organization work inside the institute.

During the work for this Ph.D. thesis, I had also the opportunity to collaborate and receive the support of many national and international scientists. In specific, I am very grateful to:

- STEFANO VERONESI, DANIELA PARISI and RAFFAELE FAORO from Prof. Tonelli's group at the University of Pisa, for continuing to be extremely helpful also after the conclusion of my master thesis and for being actively involved in the framework of the Vigoni Project with the procurement of erbium-doped fluoride crystals for my research
- CHRISTIAN FIEBIG, KATRIN PASCHKE and ERBERT GÖTZ from the Ferdinand-Braun Institut in Berlin, for their support and patience in the preparation of different DBR-TDLs for my dual-wavelength upconversion laser experiments
- MARC EICHHORN and MARTIN SCHELLHORN from the French-German Research Institute of Saint-Louis in France, for the possibility I had to perform experiments on their erbium-doped fluoride crystals
- DETLEF KLIMM from the Leibniz-Institut für Kristallzüchtung in Berlin, for the prompt support with his simulations of the crystal growth atmosphere
- ARLETE CASSANHO from the company *AC Materials* in the USA, for precious advice about the crystal growth of fluoride crystals
- DIETER BARLÖSIUS from the Institut für Laser-Physik, for the development and deposition of a special coating for the realization of a mirror for the dual-wavelength upconversion laser experiments
- PETER FJODOROW from the Institut für Laser-Physik, for consultancy about the *HITRAN Database*

- ORTWIN HELLMIG from the Institut für Laser-Physik, for being the good contact for any fiber-related issue
- KATRIN GROTH and REINHOLD MEISSNER from the Universität Hamburg, for the organization and the technical support for the TU-Praktikum.

My gratitude continues to be addressed to my family and my parents who maintained their support throughout all my studies, despite the kilometers which divide us.

I also would like to thank all my friends scattered in whole Europe (Italy, France, Switzerland, Belgium, England, Sweden, Spain, here in Hamburg and in other towns in Germany), in the US and in Latin America for the great time we had together but also for the friendship which will keep us together in the future.

Specifically related to my thesis, I am grateful to MENG LIANG, FRANZ TAVELLA, IVANKA GRGURAS, ROMAN MANKOWSKY, NIKOLA STOJANOVIC and JULIETTE SIMONET for proofreading part of my thesis, attending an informal defense-test-talk and taking active part in my oral examination.

Finally, I would like to express my gratitude to my boyfriend HAUKE HÖPPNER, for his support and help during the last years and hopefully in future, for being particularly patient during my 12 - 14 h-long writing sessions per day and for his advice.

I know I could still go on, that I am forgetting someone and that I could correct and add further reasons, but I better conclude here.

By the way, I thank all the “Doctors” I mentioned so far for not being offended by my omitting their Dr.-title...